Towards new means of performing multi T1-weighted contrast imaging and T1 mapping with the FLAWS magnetic resonance sequence

Jérémy Beaumont

UNIVERSITÉ DE RENNES 1

THESE DE DOCTORAT DE

L'UNIVERSITE DE RENNES 1

ECOLE DOCTORALE N° 601
Mathématiques et Sciences et Technologies de l'Information et de la Communication
Spécialité : *Image, Signal, Vision*

Par
Jérémy BEAUMONT

Towards new means of performing multi T1w contrast imaging and T1 mapping with the FLAWS magnetic resonance sequence.

En co-direction internationale avec The Australian e-Health Research Centre, Australia

Thèse présentée et soutenue à Rennes, le 10 décembre 2020
Unité de recherche : Laboratoire du Traitement du Signal et de l'Image, Inserm, UMR1099

Rapporteurs avant soutenance :

Rémy Guillevin	Professeur, CHU de Poitiers, Université de Poitiers
Jean-Philippe Ranjeva	Professeur, Université Aix-Marseille

Composition du Jury :

Président :	Virginie Callot	Directrice de recherche, CNRS, Marseille
Examinateurs :	Rémy Guillevin	Professeur, CHU de Poitiers, Université de Poitiers
	Jean-Philippe Ranjeva	Professeur, Université Aix-Marseille
	Alexandre Vignaud	Directeur de recherche, CEA, Université Paris-Saclay
Dir. de thèse :	Giulio Gambarota	Professeur, LTSI, Université de Rennes 1
Co-dir de thèse :	Jurgen Fripp	Group leader, The Australian e-Health Research Centre, Australia
	Oscar Acosta	Maître de conférences, LTSI, Université de Rennes 1
Invité(s)		
	Jean-Christophe Ferré	Professeur, CHU de Rennes, INRIA, Université de Rennes 1

Remerciements

Je tiens tout d'abord à remercier Professeur Rémi Guillevin et Professeur Jean-Philippe Ranjeva qui ont accepté d'être les rapporteurs de mes travaux de thèse. Merci également aux Docteur Virginie Callot, Professeur Jean-Christophe Ferré et Docteur Alexandre Vignaud d'avoir accepté de participer à mon jury de thèse. Vos différents retours m'ont permis de prendre un peu plus de recul sur mes travaux de thèse, de m'ouvrir à des aspects de l'imagerie par résonance magnétique (IRM) dans lesquels mes connaissances étaient limitées, mais également de m'éclaircir sur les points que je dois améliorer afin d'accroître mes compétences de chercheur. Je tiens également à remercier Docteur Pablo Alvarez, qui s'est assuré du bon déroulement de la diffusion en ligne de ma soutenance de thèse.

J'aimerai aussi remercier mes encadrants de thèse, sans lesquels je n'aurai pas pu mener ces travaux. Tout d'abord, merci au Docteur Oscar Acosta de m'avoir recruté en stage de master 2, puis de m'avoir proposé ce sujet de thèse. Oscar, comme tu le sais, j'étais réticent quant à l'idée de changer de sujet de recherche et de devoir partir un an et demi en Australie. Tu as su trouver les mots pour me convaincre d'accepter ce sujet de thèse et je t'en suis très reconnaissant. Sans toi, je serai passé à côté d'une vie qui me marquera à tout jamais, autant sur le plan scientifique que sur le plan humain. Je tiens également à remercier Docteur Jurgen Fripp, qui a pris l'encadrement de ma thèse du côté Australien en cours de route. Merci à toi qui m'as toujours suivi dans les différents projets d'imagerie que j'ai souhaité explorer durant ma thèse. Sans ton soutien, mes travaux à 3T et 7T n'auraient probablement jamais vu le jour. Je tiens finalement à remercier Professeur Giulio Gambarota, le « maestro » qui a su m'insuffler sa passion pour l'IRM et qui a dirigé mes travaux durant ces trois dernières années. Giulio, tu m'as fait découvrir tant de choses sur le monde de la physique de l'IRM et de la recherche scientifique, mais aussi sur la vie. Je te dois énormément ; notamment une initiation à la magie de la FLAWS, qui deviendra par la suite une séquence IRM dont je tomberai profondément amoureux.

Mes travaux de thèse n'auraient pu voir le jour sans la précieuse aide apportée par mes collègues du LTSI et du CSIRO. Je tiens particulièrement à remercier Professeur Hervé St Jalmes et Docteur Louis Marage qui m'ont initié à l'acquisition d'images IRM et à l'optimisation de séquences « en temps réel ». Vous avez aussi effectué des acquisitions à 1.5T pour moi lorsque j'étais en Australie. Je vous en remercie. Je tiens aussi à remercier Docteur Parnesh Raniga pour nos longues conversations sur la séquence MP2RAGE et pour m'avoir initié à des aspects de l'IRM qui m'étaient alors inconnus. J'aimerais également remercier Madame Julie Trinder, qui, avec Docteur Parnesh Raniga, m'a aidé sur les aspects éthiques et législatifs d'acquisition et de stockage de données IRM en Queensland (Australie). Merci à toi Julie d'avoir assuré les acquisitions FLAWS à 3T lorsque j'étais en France. Je remercie aussi Docteur Pierrick Bourgeat, qui m'a initié aux notions de segmentation d'images MP2RAGE, ainsi qu'à leurs problématiques et à l'utilisation du logiciel Neurotix, dont je me suis servi de nombreuses fois durant ma thèse. Je tiens finalement à remercier Docteur Lee Reid avec qui j'ai eu

l'opportunité de mener un projet de recherche annexe de simulation d'IRMs structurels afin d'éviter la perte de données dans des études d'imagerie de diffusion.

Je tiens à remercier les centres d'imagerie avec lesquels j'ai effectué les acquisitions d'images qui m'ont permis de réaliser mes travaux. Merci donc au service de radiologie de l'Hôpital Sud du CHU de Rennes et à son personnel pour la collaboration sur le projet FLAWS à 1.5T. Merci au Centre for Advanced Imaging de The University of Queensland (Australie) et à son personnel pour la collaboration sur le projet FLAWS à 7T. Enfin, je tiens à remercier The Herston Imaging Research Facility (Australie) pour la collaboration sur mes différents projets d'imagerie à 3T, et notamment le projet d'optimisation de la FLAWS avec « compressed sensing ». J'ai beaucoup apprécié votre investissement dans mes projets et c'est grâce au fait que vous m'ayez laissé travailler de nombreuses heures sur vos scanners lorsqu'ils étaient libres que j'ai pu mener mes projets d'imagerie à 3T à terme avant de quitter l'Australie. Je tiens particulièrement à remercier Professeur Katie McMahon et Mesdames Clare Berry, Peta Gray et Hilarie Richards pour leur accueil bienveillant au sein de The Herston Imaging Research Facility. J'aimerais aussi remercier toutes les personnes qui se sont portées volontaires pour les différents examens d'imagerie FLAWS que nous avons menés lors de ces travaux de thèse.

Je n'aurais pas pu effectuer mes travaux de thèse sans l'aide de différents collaborateurs que je tiens à remercier. Tout d'abord, merci au Docteur Tobias Kober, qui a mis à notre disposition la séquence FLAWS sur les IRMs sur lesquels nous avons travaillés. Tu nous as aussi fourni de précieux retours sur nos travaux. J'aimerais particulièrement te remercier pour le fait que tu aies implémenté une partie de nos travaux dans la dernière « Work-in-progress » version de la séquence MP2RAGE pour les IRMs Siemens. Je tiens également à remercier Professeur Jean-Christophe Ferré, qui a pris le temps de nous donner un retour clinique qui fût primordial pour valider nos travaux. J'aimerais aussi remercier Monsieur Mark Tanner pour ses précieux retours sur nos travaux d'optimisation de la séquence FLAWS à 1.5T. Enfin, je tiens à remercier Professeur Cristina Granziera, Docteur Meritxell Bach Cuadra, Monsieur Francesco La Rosa et Docteur Matthias Weigel pour la collaboration sur le projet d'imagerie FLAWS sur des patients atteints de sclérose en plaques.

Je tiens à remercier le personnel administratif du LTSI et du CSIRO pour leur précieuse aide concernant toutes les démarches qui furent nécessaires pour assurer le bon déroulement de ma thèse.

J'aimerai finalement remercier tous mes collègues de travail du LTSI et du CSIRO (dont certains sont devenus des amis), mes amis et ma famille pour le soutien qu'ils m'ont apporté durant ces trois années de thèse.

Table of contents

Résumé en Français

L'imagerie par résonance magnétique (IRM) est une technique d'imagerie non invasive utilisée pour visualiser le corps humain. Contrairement à d'autres méthodes d'imagerie du corps humain, telles que la tomodensitométrie ou la tomographie par émission de positons, l'IRM est une méthode d'imagerie non irradiante. De plus, l'IRM fourni un très bon contraste entre les tissus mous comparée aux méthodes d'imageries structurelles obtenues à partir de rayons X, telles que la tomodensitométrie. Par conséquent, l'IRM est la méthode de référence pour l'imagerie du cerveau, qui est l'organe d'intérêt dans cette thèse.

Il existe différentes séquences d'acquisition IRM qui fournissent différents contrastes entre les tissus cérébraux. Ces différents contrastes fournissent des informations sur les structures cérébrales, permettant entre autres de mieux visualiser les tissus (substance blanche, substance grise et liquide céphalorachidien) ou encore de faciliter la détection de lésions et de tumeurs cérébrales. Par exemple, certaines séquences IRM sont développées afin de fournir une visualisation détaillée de certaines structures cérébrales, telles que les noyaux gris centraux, pour des applications de chirurgie. Par conséquent, plusieurs séquences IRM sont acquises en routine clinique afin d'obtenir divers contrastes facilitant le diagnostic des différentes pathologies cérébrales.

L'IRM est une méthode d'imagerie qualitative. Cela signifie que les valeurs d'intensité des pixels volumétriques (voxels) ne fournissent pas d'information sur les tissus imagés. Ce sont les relations entre les intensités des voxels qui fournissent l'information nécessaire au diagnostic lors d'un examen IRM. Cependant, il existe certaines méthodes d'imagerie permettant l'obtention d'information quantitative en IRM. Ces informations quantitatives sont directement liées aux propriétés magnétiques des tissus imagés, qui peuvent elles-mêmes être liées à certaines pathologies cérébrales.

Dans le cadre de cette thèse, nous nous intéressons spécifiquement à la séquence IRM « fluid and white matter suppression » (FLAWS) dans le but de fournir des images avec différents contrastes ainsi que des images quantitatives des temps de relaxation T1 en une seule acquisition.

La séquence FLAWS est une séquence IRM fournissant deux images pondérées T1 en une seule acquisition : la première image FLAWS, FLAWS1, possède un contraste avec une suppression du signal de la substance blanche, tandis que la deuxième image, FLAWS2, est caractérisée par un contraste avec une suppression du signal du liquide céphalorachidien. La séquence FLAWS fourni des images d'intérêt pour la visualisation des noyaux gris centraux dans un contexte de chirurgie (stimulation cérébrale profonde). Les images FLAWS sont aussi utilisées pour mieux visualiser les lésions cérébrales, particulièrement les lésions corticales, pour des pathologies telles que l'épilepsie.

Lorsque cette thèse a débutée, la séquence FLAWS était uniquement disponible pour des scanners IRM possédants un champ magnétique de 3T. Nous nous sommes donc consacrés à

l'optimisation de la séquence FLAWS afin de fournir des paramètres permettant son acquisition sur des scanners possédants un champ magnétique de 1.5T et 7T. Pour ce faire, nous proposons une méthode d'optimisation consistant à maximiser une fonction de profit sous contraintes afin de maximiser le rapport contraste sur bruit entre les tissus cérébraux, tout en assurant une suppression des signaux de la substance blanche et du liquide céphalorachidien dans les images FLAWS1 et FLAWS2, respectivement. La valeur du profit utilisé pour l'optimisation est déterminée à partir des valeurs des signaux FLAWS1 et FLAWS2 en fonction des paramètres de la séquence et des propriétés magnétiques des tissus cérébraux. Cette méthode d'optimisation nous a permis de déterminer des paramètres pour l'acquisition d'images FLAWS à 1.5T et 7T. Ces paramètres furent validés par des acquisitions d'images FLAWS sur des volontaires sains. Les résultats obtenus montrent que les images FLAWS acquises à 1.5T et 7T avec les paramètres proposés sont caractérisées par une bonne suppression des signaux de la substance blanche et du liquide céphalorachidien dans FLAWS1 et FLAWS2, respectivement. De plus, une bonne visualisation des noyaux gris centraux est obtenue avec FLAWS1, ce qui valide la méthode d'optimisation de manière qualitative. Les valeurs de contraste entre les tissus cérébraux mesurées dans les images FLAWS obtenues à 1.5T et 7T sont proches des valeurs de contraste obtenues pour l'optimisation originale de la séquence FLAWS à 3T, ce qui valide la méthode d'optimisation d'un point de vue quantitatif.

L'IRM à très haut champ magnétique, telle que l'imagerie à 7T, permet d'obtenir des images haute résolution qui fournissent d'avantage de détails sur les différent tissus cérébraux comparé à de l'imagerie à haut champ magnétique telle que l'imagerie à 3T. Cependant, l'imagerie à 7T est fortement impactée par les inhomogénéités du champ magnétique B1, ce qui rend la lecture des images plus difficile pour les radiologues et complique l'obtention d'images quantitatives. Inspirés par le principe de la séquence « Magnetization Prepared with 2 Rapid Gradient Echoes » (MP2RAGE) qui fournit des images IRM peu sensibles aux inhomogénéités de champ magnétique B1, nous proposons une nouvelle combinaison des signaux FLAWS afin de fournir des images peu sensibles aux inhomogénéités du champ magnétique B1. Ces nouvelles images FLAWS, nommées *FLAWS-hc* et *FLAWS-hco*, furent comparées à l'image obtenue en divisant les signaux FLAWS (*FLAWS-div*), qui est utilisée empiriquement dans certaines études de planification de chirurgie pour des applications de stimulation cérébrale profonde. Les images *FLAWS-div* sont utilisées pour des étapes de planification de chirurgie car elles fournissent un très haut contraste entre les différents tissus cérébraux. De plus, ces images sont caractérisées par une sensibilité réduite aux inhomogénéités du champ magnétique B1. Nous avons démontré mathématiquement que les images *FLAWS-hc et FLAWS-hco* sont également caractérisées par une sensibilité réduite aux inhomogénéités du champ magnétique B1, tout en fournissant respectivement des images avec suppression des signaux de substance blanche et de liquide céphalorachidien. De plus, nous avons également démontré mathématiquement que ces images fournissent un meilleur rapport signal sur bruit que les images *FLAWS-div* tout en maintenant un haut contraste entre les tissus cérébraux. Les présomptions théoriques concernant les caractéristiques des images *FLAWS-hc* et *FLAWS-hco* furent validées par des acquisitions d'images sur des volontaires sains à 1.5T et 7T. Les résultats obtenus montrent que les images *FLAWS-hc* et *FLAWS-hco* sont caractérisées par une sensibilité réduite aux inhomogénéités de champ magnétique B1 et fournissent un meilleur rapport contraste sur bruit entre les tissus cérébraux que les images *FLAWS-div.* Ces résultats suggèrent que les images *FLAWS-hc* et *FLAWS-hco* soient utilisées à la place des images *FLAWS-div* pour des applications de planification chirurgicale en

stimulation cérébrale profonde. Ces images peuvent également être utilisées pour toute application visant à obtenir des images pondérées T1 à très haut champ magnétique.

La séquence FLAWS est une séquence dérivée de la séquence MP2RAGE. La séquence MP2RAGE fut développée afin de fournir des images IRM avec pondération T1 peu sensibles aux inhomogénéités du champ magnétique B1. Ces images IRM, appelées *MP2RAGE-uni*, sont obtenues à partir de combinaison des signaux MP2RAGE mesurés lors de l'acquisition de la séquence. La séquence MP2RAGE fournit également des images quantitatives des temps de relaxation T1 des tissus. La mesure des temps de relaxation T1 à l'aide de la séquence MP2RAGE est effectuée en construisant des tables de correspondances entre le signal *MP2RAGE-uni* et les temps de relaxation T1 en fonction des paramètres d'acquisition de la séquence. Dans le paragraphe précédent, nous avons mentionné que nos travaux permettent de fournir des images IRM pondérées T1 peu sensibles aux inhomogénéités du champ magnétique B1 à partir de la séquence FLAWS. Compte tenu de la similarité entre les séquences FLAWS et MP2RAGE, nous avons cherché à obtenir des images quantitatives des temps de relaxation T1 à partir de la séquence FLAWS. Le signal *uni* ne peut pas être directement utilisé pour mesurer les temps de relaxation T1 à partir de la séquence FLAWS. Nous avons donc proposé une nouvelle méthode de mesure des temps de relaxation T1 à partir de la séquence FLAWS. Cette méthode consiste à construire des tables de correspondances entre le signal *FLAWS-hc* et les temps de relaxation T1 en fonction des paramètres de la séquence. La méthode de mesure des temps de relaxation T1 proposée dans cette thèse fut validée par des expériences menées sur un fantôme à 3T : les temps de relaxation T1 mesurés avec la séquence FLAWS sont proches des temps de relaxation T1 fournis par le fantôme et des temps de relaxation T1 mesurés avec la séquence écho de spin avec inversion récupération, qui est la méthode de référence en terme de mesure des temps de relaxation T1.

Les images quantitatives des temps de relaxation T1 fournies par la séquence MP2RAGE sont affectées par les inhomogénéités du champ magnétique de transmission $\mathrm{B1}^{+}$. La séquence MP2RAGE fut donc optimisée afin de minimiser la sensibilité de ses cartes des temps de relaxation T1 aux inhomogénéités du champ magnétique $B1^{+}$. Les inhomogénéités du champ $B1^{+}$ sont très élevées à 7T. Afin de limiter la sensibilité aux inhomogénéités de champ magnétique $B1^{+}$, l'optimisation de la séquence MP2RAGE proposée à 7T possède une faible résolution et un faible rapport contraste sur bruit pour une séquence d'imagerie acquise à 7T. Une seconde optimisation de la séquence MP2RAGE fut donc proposée à 7T afin de fournir des images pondérées T1 caractérisées par une haute résolution et un rapport contraste sur bruit élevé. Une méthode de correction des cartographies T1 de la séquence MP2RAGE fut proposée afin de réduire la sensibilité de la séquence MP2RAGE optimisée pour une haute résolution aux inhomogénéités du champ $B1^{+}$. Cette méthode de correction repose sur l'utilisation d'une carte des inhomogénéités du champ $B1^{+}$ acquise à l'aide de la séquence SA2RAGE. L'utilisation de cette méthode de correction est peu conseillée pour des études multicentriques d'imagerie du cerveau menées à 7T car elle peut affecter la reproductibilité des résultats obtenus entre les différents centres d'imagerie.

Dans cette thèse, nous montrons que la cartographie T1 fournie par la séquence FLAWS à 7T est peu sensible aux inhomogénéités du champ $B1^{+}$, tout en permettant d'obtenir des images pondérées T1 avec une haute résolution et un rapport contraste sur bruit élevé. Cette propriété de la séquence FLAWS fut validée par des expériences de simulations (expériences de Monte-Carlo) ainsi que par de l'imagerie effectuée sur des volontaires sains à 7T. Les

résultats obtenus lors de l''étude menée à 7T suggèrent que la séquence FLAWS pourrait remplacer la séquence MP2RAGE pour des applications d'imagerie IRM à 7T car 1) elle fournit plus de contrastes pondérés T1 avec une faible sensibilité aux inhomogénéités de champ magnétique B1 que la séquence MP2RAGE ; et 2) elle permet de surpasser les contraintes imposées à la séquence MP2RAGE en termes de résolution et de rapport contraste sur bruit pour obtenir des cartographies des temps de relaxation T1 peu sensibles aux inhomogénéités du champ magnétique $B1^+$.

Les contributions proposées dans cette thèse ont quelques limitations. En effet, la méthode d'optimisation proposée pour la séquence FLAWS dépend du choix de la résolution des images et des informations à priori concernant propriétés magnétiques des tissus du cerveau. Par conséquent, plusieurs jeux de paramètres peuvent être obtenus en fonction de la résolution et des propriétés magnétiques utilisées pour effectuer l'optimisation. De plus, la résolution des images FLAWS dans le plan sagittal est limitée car un important nombre d'excitations par temps de répétition de la séquence ne permet pas une suppression correcte du signal de la substance blanche dans FLAWS1. La sensibilité des cartographies des temps de relaxation T1 fournies par la séquence FLAWS aux inhomogénéités du champ magnétique $B1^+$ croît avec le temps de relaxation T1 des tissus. Par conséquent, les cartographies des temps de relaxation T1 obtenues avec la séquence FLAWS doivent être corrigées post-acquisition à l'aide de cartographies $B1^+$ afin de permettre une mesure précise dans les tissus caractérisés par un long temps de relaxation T1, telles que les lésions cérébrales. Les travaux présentés dans cette thèse furent uniquement validés sur des volontaires sains. Une validation sur des données de patients est nécessaire avant de considérer l'inclusion de ces travaux en routine clinique. Finalement, le temps d'acquisition de la séquence FLAWS est long (8 à 10 mins), ce qui limite son utilisation en routine clinique.

Les contributions proposées dans cette thèse mènent à des perspectives intéressantes en termes de recherche sur la séquence FLAWS. La génération des images *FLAWS-hc* et *FLAWS-hco* est désormais directement disponible sur les IRM de recherche Siemens (Work-in-progress package #925B-VE11C), ce qui facilitera leur utilisation dans des études de neuro-imagerie. Suite à nos travaux, la séquence FLAWS fut inclue dans le protocole d'imagerie de l'étude « Prospective Imaging Study of Ageing: Genes, Brain and Behavior » (PISA) en Australie et sera acquise sur 30 sujets de l'étude possédant des lésions cérébrales dues à l'âge. Les images FLAWS acquise seront comparées à des images FLAIR afin d'évaluer le potentiel de la séquence FLAWS en termes de détection et segmentation de lésions. Les images FLAWS seront également comparées à des images MP2RAGE afin de valider les contributions de cette thèse avec des données de patients. De plus, une collaboration avec l'école Polytechnique Fédérale de Lausanne fut créée afin d'évaluer le potentiel de la séquence FLAWS en termes de détection et segmentation de lésions dues à la sclérose en plaques. Enfin, nous travaillons en collaboration avec Siemens Healthineers afin de fournir un protocole d'imagerie FLAWS plus rapide à 3T dans le but de faciliter l'utilisation de la séquence en routine clinique. Ce protocole d'imagerie repose sur l'acquisition d'images en parallèle à l'aide de méthodes de compressed sensing. Ce projet consiste à combiner la méthode d'optimisation de la séquence FLAWS présentée dans cette thèse avec des méthodes d'imagerie parallèle avec compressed sensing développées par Siemens Healthineers. Les résultats préliminaires que nous avons obtenus permettent d'acquérir la séquence FLAWS à 3T en 6 mins (le temps d'acquisition standard de la séquence FLAWS est actuellement de 8 à 10 mins à 3T). Plus d'expériences

seront cependant nécessaires afin de valider ce nouveau protocole d'acquisition de la séquence FLAWS.

Cette thèse est composée de 5 chapitres. Le premier chapitre présente brièvement les notions d'anatomie du cerveau nécessaires à la compréhension de cette thèse. Ce chapitre introduit également les principes fondamentaux de l'IRM. Le second chapitre présente le principe d'inversion récupération et les séquences qui l'utilisent, telles que les séquences MP2RAGE et FLAWS. Ce chapitre présente également différentes méthodes d'imagerie quantitative des temps de relaxation T1 (cartographie des temps de relaxation T1 à partir de la séquence écho de spin avec inversion récupération et cartographie des temps de relaxation T1 à partir de la séquence MP2RAGE). Ce chapitre expose aussi les difficultés liées à l'imagerie quantitative des temps de relaxation T1 à l'aide de la séquence MP2RAGE à 7T. Enfin, il présente une validation de la méthode d'imagerie quantitative proposée dans cette thèse pour la mesure des temps de relaxation T1 à partir de la séquence FLAWS sur un fantôme à 3T. Le troisième chapitre introduit la combinaison des signaux FLAWS proposée dans cette thèse pour fournir des images peu sensibles aux inhomogénéités de champs magnétiques. Ce chapitre fourni également des résultats préliminaires quant à l'optimisation de la séquence FLAWS à 1.5T. Les paramètres finaux permettant d'acquérir des images FLAWS à 1.5T sont fournis dans le chapitre 4. Ce chapitre présente aussi la méthode proposée dans cette thèse pour optimiser la séquence FLAWS. Le chapitre 5 propose une optimisation de la séquence FLAWS à 7T à partir de la méthode développée dans le chapitre 4. De plus, le chapitre 5 présente la méthode d'imagerie quantitative des temps de relaxation T1 à partir de la séquence FLAWS proposée dans cette thèse.

Cette thèse fut effectuée en co-direction internationale entre le Laboratoire du Traitement du Signal et de l'Image (LTSI INSERM UMR 1099), Université de Rennes 1, France (18 mois de recherche dans ce laboratoire) et The Australian e-Health Research Centre (AEHRC), Commonwealth Scientific and Industrial Research Organisation (CSIRO), Australie (21 mois de recherche dans ce laboratoire). Cette collaboration entre le LTSI et the AEHRC a facilité le développement des travaux proposés dans cette thèse grâce à : 1) l'expertise de la séquence FLAWS et de l'imagerie IRM quantitative des membres du LTSI ; 2) l'expertise en imagerie IRM du cerveau des membres de the AEHRC ; 3) la facilitation d'accès à un scanner IRM 1.5T au LTSI ; et 4) la facilitation d'accès à des scanners IRM 3T et 7T à the AEHRC.

Cette thèse fut co-financée par la Région Bretagne, France (bourse ARED n° 127504 – projet BITRAST) et le CSIRO, Australie (collaborative project agreement). Afin de permettre la lecture de ce manuscrit de thèse aux co-financeurs Australiens de ce projet, la suite de ce manuscrit est rédigée en anglais.

Introduction

Magnetic resonance imaging (MRI) is a non-invasive imaging technique used to visualize the human body. Thanks to its high soft tissue contrast, MRI is the gold standard imaging technique when it comes to the study of the brain. This thesis focuses on the fluid and white matter suppression (FLAWS) sequence. The FLAWS sequence provides two co-registered T1-weighted contrasts, named *FLAWS1* and *FLAWS2*. *FLAWS1* provides an image with a suppression of the white matter (WM) signal, allowing for the visualization of deep gray matter structures. *FLAWS2* provides a cerebrospinal fluid (CSF) suppressed image that is of interest for the study of the brain anatomy thanks to its high brain tissue contrast. A gray matter specific image, *FLAWS-min*, is obtained by computing the minimum between the *FLAWS1* and *FLAWS2* images. The *FLAWS1*, *FLAWS2* and *FLAWS-min* images are of interest for a wide range of clinical applications, from deep brain stimulation surgery planning to brain lesion detection.

When this thesis started, the FLAWS sequence was only available for 3T imaging. We then decided to propose an optimization method in order to provide FLAWS sequence parameters for 1.5T and 7T imaging. We also proposed a new combination of the FLAWS signals to provide a T1-weighted contrast characterized by a reduced sensitivity to the $B1$ magnetic field inhomogeneities. Finally, we proposed a method allowing for the measurement of the T1 relaxation times with the FLAWS sequence. We showed that this FLAWS T1 mapping method is characterized by a reduced sensitivity to the transmitted magnetic field ($B1^+$) inhomogeneities, which allows for the use of this T1 mapping method at 7T since $B1^+$ inhomogeneities are very high at this field strength.

This thesis is composed of 5 chapters. The first chapter introduces the basics of brain anatomy that are required to understand the work presented in this thesis. This chapter also presents the fundamental notions of MRI. The second chapter introduces the inversion recovery principle and the MRI sequences using this principle, such as the MP2RAGE and FLAWS sequences. The second chapter also presents T1 mapping techniques based on the spin echo inversion recovery and MP2RAGE sequences. This chapter exposes the difficulties arising when performing T1 mapping at ultra-high field (7T and above). Finally, the second chapter presents a validation of the FLAWS T1 mapping method presented in this thesis on phantom data acquired at 3T. The third chapter introduces the FLAWS signals combinations proposed in this thesis for the generation of T1-weighted images with reduced $B1$ sensitivity. The data used in this chapter was acquired with the preliminary results of the FLAWS optimization at 1.5T. The final FLAWS parameters proposed for 1.5T imaging and the FLAWS optimization method proposed in this thesis are presented in the fourth chapter. Finally, the fifth chapter presents the FLAWS sequence parameters proposed for 7T imaging. The fifth chapter also introduces the FLAWS T1 mapping technique proposed in this thesis.

The work presented in the third chapter was published as a conference paper at the IEEE International Symposium on Biomedical Imaging (ISBI). Venice, Italy, 2019. The work

presented in the fourth chapter was published in the journal Magnetic Resonance Imaging and the work presented in the fifth chapter was published in the journal Magnetic Resonance in Medicine.

This thesis was internationally co-supervised by the Laboratoire du Traitement du Signal et de l'Image (LTSI INSERM UMR 1099), Université de Rennes 1, France (18 month spent in this laboratory) the Australian e-Health Research Centre (AEHRC), Commonwealth Scientific and Industrial Research Organization (CSIRO), Australia (21 month spent in this laboratory). This collaboration between the LTSI and the AEHRC facilitated the development of the work proposed in this thesis thanks to: 1) the FLAWS sequence and quantitative MRI expertise of the LTSI members; 2) the brain MRI expertise of the AEHRC members; 3) the facilities to access to a 1.5T MRI scanner through the LTSI; and 4) the facilities to access to 3T and 7T MRI scanners through the AEHRC. This thesis was co-funded by the Region Bretagne, France (grant ARED n° 127504 – BITRAST project) and the CSIRO, Australia (collaborative project agreement).

Chapter 1
Introduction to brain magnetic resonance imaging

1.1 Why is MRI of interest for brain imaging?

Magnetic resonance imaging is a non-invasive imaging technique that can be used to visualize the human body. As opposed to other *in-vivo* imaging techniques like computed tomography (CT) or positron emission tomography (PET), MRI is non irradiant. In addition, MRI displays a high contrast between soft tissues compared to structural images obtained with X-rays, such as CT scans. Multiple images displaying different soft tissue contrasts can be acquired by varying the MR pulse sequences as well as their acquisition parameters, thus providing many scans of clinical interest using a single scanner. In addition to the provision of structural images, MRI allows to map the diffusion of water molecules within the brain and can even provide functional images that detect the brain regions activated when performing a task inside the scanner. Thanks to its properties, MRI appeared to be of interest for a wide range of clinical applications and quickly became the gold standard for *in-vivo* brain imaging.

MRI has however some limitations. One of them is its long acquisition time. For example, a brain imaging session can last more than an hour in research protocols. In addition, MRI cannot provide images of the bones. Furthermore, the use of a strong magnet makes MRI unsafe for people having metal in their bodies, like patients with a metal prosthesis or a penetrating eye injury. Finally, since the MR imaging process requires the subject to enter a tube, MRI is difficult to perform on people suffering from claustrophobia.

1.2 Brain anatomy

The brain is mainly composed of neurons. Neurons are cells that can be excited and can transmit a bioelectric signal allowing the brain to function. Neurons are composed of a cell body, dendrites and an axon (Figure 1.1). The dendrites receive the bioelectric signals from other neurons. When enough signal is received, the neuron transmits a bioelectric signal through its axon whose terminals are connected to the dendrites of other neurons. Axons are covered of myelin to speed up the bioelectric signal transmission.

The brain is composed of approximately 86 billion of neurons [1] that makes the brain work in a similar way as computers work with transistors. At the macroscopic scale, the cell bodies of the neurons are gathered to form the grey matter (GM) while the axons are gathered to form the white matter (WM). The GM is classified in two categories: the cortical GM, which is located at the surface of the brain and forms the cortex; and the deep GM, located near the center of the brain. The brain is immersed in the cerebrospinal fluid (CSF) to be protected from shock injuries and ischemia. The CSF, which is also present in the ventricles of the brain, removes the brain wastes and also ensures homeostasis. The brain is composed of 3 areas (Figure 1.2): the cerebrum, divided in the left and the right hemispheres that ensure the majority of the cognitive functions such as the vision, the language and the memory; the cerebellum, which is responsible for the motor movements and is involved in other functions

such as the language and attention; and the brainstem, which transmits the motor and sensory information between the brain and the spinal cord and regulates the respiratory and cardiac functions.

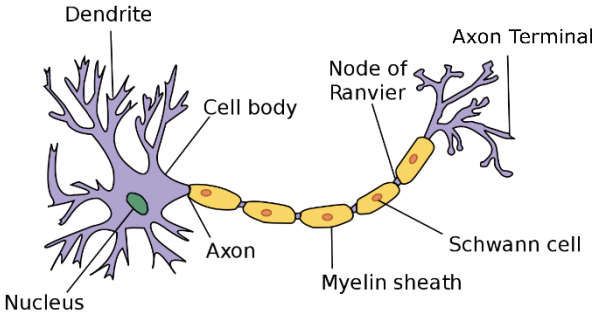

Figure 1.1. Anatomy of a neuron. Image from simple.wikipedia.org.

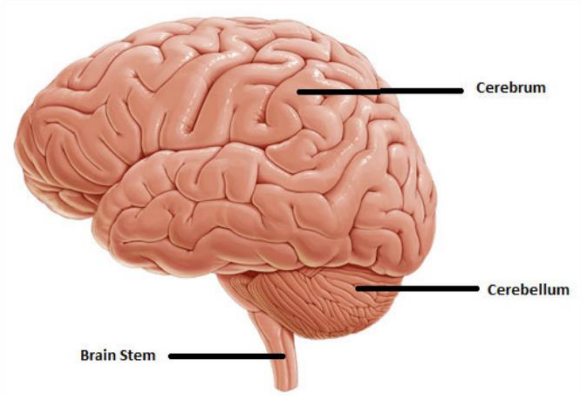

Figure 1.2. The three areas of the brain: cerebrum, cerebellum and brainstem. Image from the website myshepherdconnection.org.

The right and left hemispheres are each composed of lobes (Figures 1.3 and 1.4): the frontal lobe is responsible for the control of the movements, short term memory tasks, as well as the planning and attention functions; the parietal lobe controls the sensory information and is involved in the language function; the temporal lobe, responsible for the memory and emotions functions, is involved in the language comprehension; and finally the occipital lobe processes the visual information.

The deep gray matter –involved in cognition, emotions, learning, as well as the control of motor movements– is located near the center of the brain and is composed of multiple structures including the caudate nucleus, the putamen, the globus pallidus and the thalamus (Figure 1.5).

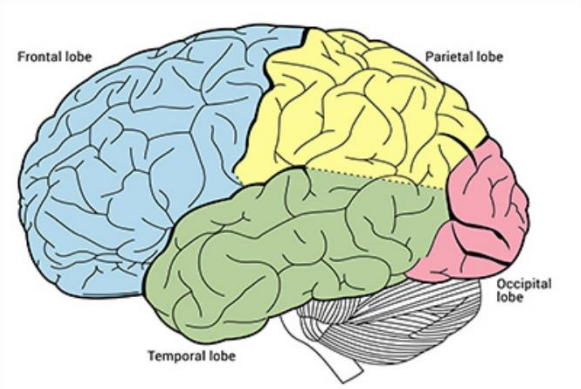

Figure 1.3. Location of the frontal, parietal, temporal and occipital lobes in the brain. Image from qbi.uq.edu.au.

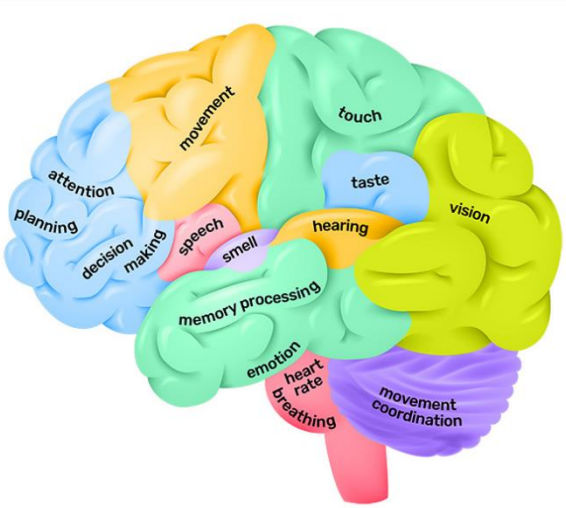

Figure 1.4. Location of the different functions in the brain. Image from qbi.uq.edu.au.

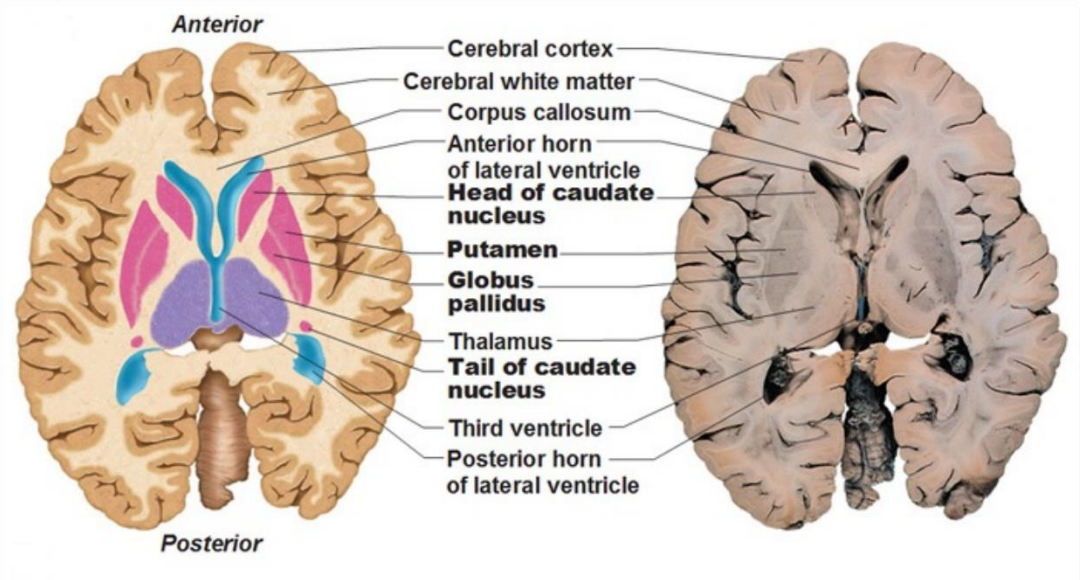

Figure 1.5. Anatomy of the brain. Image from neurovascularmedicine.com.

1.3 Clinical applications of brain MR imaging

MRI can provide structural images of the brain. These structural images are used to detect oedemas, tumors, lesions due to brain diseases such as multiple sclerosis and epilepsy, as well as the shrinking of brain structures due to ageing or diseases like the Alzheimer's disease. Structural brain MRIs can be used for surgery and/or radiotherapy planning for cancer treatments. The structural information provided by brain MRI is also used for surgery planning in deep brain stimulation (DBS) applications dedicated to the treatment of diseases such as the Parkinson disease or dystonia.

The MRI techniques allowing the visualization of the water molecules diffusion within the brain are used to detect ischemia and tumors. Diffusion MRI can also be used to perform tractography, allowing the visualization of the nerve tracts within the brain for surgery applications.

1.4 MRI basics: introducing the notion of magnetic resonance

According to quantum mechanics, the hydrogen proton has a spin of $\frac{1}{2}$, and as such, the hydrogen proton possesses its own magnetic moment. Magnetic Resonance Imaging aims at measuring the spatial variation and the strength of the magnetic moments of given protons to generate *in-vivo* images. In practice, most of the current MRI applications are performed by measuring the magnetic moment of the hydrogen proton since Avogadro numbers of hydrogen protons can be found in the human body.

In normal conditions, the magnetic fields of the hydrogen protons are associated with a random direction, and as such, the sum of the magnetic fields generated by the hydrogen protons is null (Figure 1.6a). In the presence of a magnet, the magnetization generated by the hydrogen protons will precess about the magnet axis (Figure 1.6b). Let $\overrightarrow{B_0}$ be the vector representing the magnetic field of the magnet used to align the hydrogen spins, then the precession angular frequency of the hydrogen spin, called the Larmor frequency, is computed as follow:

$$\omega_0 = \gamma \left|\overrightarrow{B_0}\right| \qquad 1.1$$

With γ the gyromagnetic ratio of the hydrogen proton, which value approximately $2.68 \,.\, 10^8 \, rad \,.\, s^{-1} \,.\, T^{-1}$ [2]. The energy difference (ΔE) associated to the resonance frequency ω_0 is computed as $\Delta E = \hbar \, \omega_0$, with $\hbar = h/2\pi$ and h the Planck constant which is equal to $6.6 \,.\, 10^{-34} \, m^2 . kg \,.\, s^{-1}$.

Basic MRI principle 1: From equation 1, we deduce that the higher the strength of the magnetic field $\overrightarrow{B_0}$, the higher the precession angular frequency ω_0 of the hydrogen spin.

In this situation, the hydrogen spins can have two directions: in the direction of the magnetic field, corresponding to a low energy state, and in the opposite direction of the magnetic field, corresponding to a high energy state (Figure 1.6c). Since it requires more energy for the hydrogen spins to be in the opposite direction of the magnetic field B_0, there is an excess number of hydrogen spins in the direction parallel to B_0. From the Boltzmann distribution, the excess number can be approximated by the following equation:

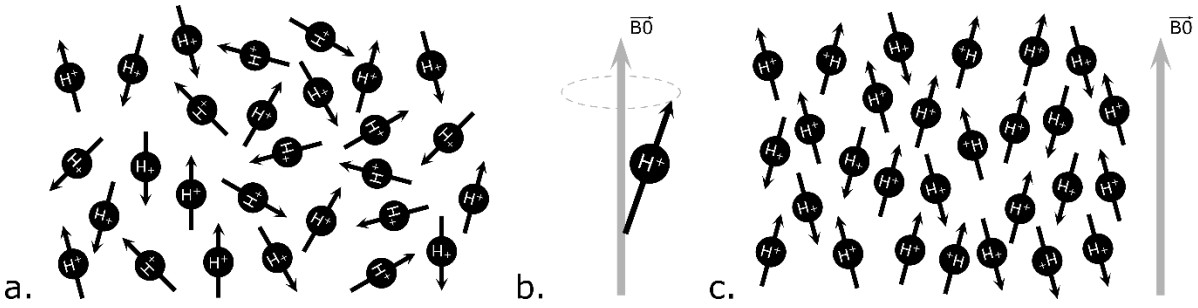

Figure 1.6. Effect of an external magnetic field B_0 on the orientation of the spins of the hydrogen protons H^+. In the absence of an external magnetic field (a), the hydrogen spins can have any orientation and the sum of their magnetization is null. In the presence of an external magnetic field, the hydrogen spins start to precess about the field (b) and can have two orientations: one in the direction of the magnetic field $\overrightarrow{B_0}$ and the other in the opposite direction of the magnetic field $\overrightarrow{B_0}$ (c).

$$N_{excess} = \frac{\hbar\,\omega_0}{2\,k\,T} N_{total} \qquad 1.2$$

when $\Delta E \ll kT$, which is the case of MRI, with N_{total} the total number of spins contained in the volume of interest, k the Boltzmann constant and T the absolute temperature in the volume of interest. By injecting equation 1.1 in equation 1.2, we obtain:

$$N_{excess} = \frac{\hbar\,\gamma}{2\,k\,T} \left|\overrightarrow{B_0}\right| N_{total} \qquad 1.3$$

Considering that $h = 6.6\,.\,10^{-34}\,m^2.kg\,.s^{-1}$ and $k = 1.4\,.\,10^{-23}\,m^2\,.kg\,.s^{-2}\,.K^{-1}$, the excess number of hydrogen spins in the direction of B_0 at $310\ K$ ($37.5\ °C$, i.e. the temperature of the human body) is approximately equal to:

$$N_{excess} \cong\ 3.3\,.\,10^{-6} \left|\overrightarrow{B_0}\right| N_{total} \qquad 1.4$$

This result indicates that the spin excess in the B_0 direction is very low compared to the total number of spins. For example, the spin excess is about 3 parts-per-million (ppm) for a B_0 magnetic field with a magnitude of $1\ T$. Since the magnetization induced by the hydrogen spins in the spin down position cancels out the magnetization induced by the hydrogen spins in the spin up position, only the excess number of hydrogen spins in the spin-up position provides the magnetization that we aim at measuring to generate magnetic resonance images. Equation 1.4 indicates that the amount of hydrogen spins that produces the MRI signal is very low compared to the total amount of hydrogen spins. However, images can still be produced thanks to the huge amount of hydrogen spins present in human tissues.

Basic MRI principle 2: From equation 1.4, we deduce that increasing the strength of the magnetic field B_0 increases the excess number of hydrogen spins in the B_0 direction, thus increasing the strength of the magnetization that we aim at measuring in MRI.

Basic MRI principle 3: From equation 1.4, we deduce that increasing the total number of hydrogen spins –this can be achieved by increasing the volume in which the magnetization is measured– increases the excess number of hydrogen spins in the B_0 direction, thus increasing the strength of the magnetization that we aim at measuring in MRI.

The total magnetization M_0 induced by the excess of hydrogen spins along the B_0 magnetic field is computed as follows:

$$\left|\overrightarrow{M_0}\right| = \frac{\hbar^2\,\gamma^2}{4\,k\,T}\,\left|\overrightarrow{B_0}\right|\,\rho_0 \qquad 1.5$$

With ρ_0 the number of protons per unit volume, also called the spin density. For a temperature of $310\ K$, we obtain:

$$\left|\overrightarrow{M_0}\right| \cong 4.7\ 10^{-32}\,\left|\overrightarrow{B_0}\right|\,\rho_0 \qquad 1.6$$

Equation 1.6 indicates that the magnetization M_0 is proportional to the spin density ρ_0. Therefore, if it is possible to measure M_0 throughout multiple adjacent volumes, it is possible to create an image that maps the distribution of hydrogen in the human tissues. However, equation 1.6 shows that the magnetization M_0 is insignificant compared to the strength of the magnetic field B_0, rendering its measurement almost impossible when $\overrightarrow{M_0}$ is aligned with $\overrightarrow{B_0}$. However, the transversal component of the M_0 magnetic field can be measured since there is no external magnetization in the orthogonal plane relative to $\overrightarrow{B_0}$. When the magnetic field B_0 is the only external field impacting the magnetization M_0 of the hydrogen spins, the spins of the hydrogen precess with different phases. Thus, the magnetization measured in the transversal plane in null (Figure 1.7). It is then necessary to tip the M_0 magnetization in the transversal plane to allow its measurement. This can be achieved by generating a second magnetic field, $\overrightarrow{B_1}$, in the transversal direction from the magnetization vector $\overrightarrow{B_0}$. The $\overrightarrow{B1}$ field is created using a radio-frequency (RF) pulse at the resonance frequency of the hydrogen spins, which happen to be equal to the Larmor frequency ω_0. The B_1 field allows the tip of the magnetization M_0 towards the transversal plane with a flip angle α as described by the following equation:

$$\alpha = \gamma\ t\ \left|\overrightarrow{B_1}\right| \qquad 1.7$$

With t equal to the duration of the RF pulse.

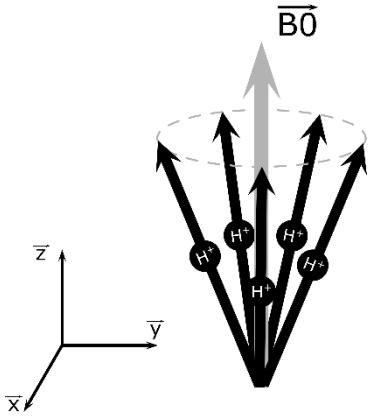

Figure 1.7. The excess hydrogen spins in the direction of the magnetic field $\overrightarrow{B_0}$ that creates the magnetization M_0 tend to repel each other. As such, the components of the magnetization M_0 in the transversal plane $(\vec{x}, \vec{y})$ are out of phase, resulting in a null transversal magnetization.

In Magnetic Resonance physics, we define the term longitudinal magnetization as the component of the magnetization $\overrightarrow{M_0}$ in the $\vec{z}$ direction, i.e. in the direction of the magnetic field $\overrightarrow{B_0}$, while the transversal magnetization is defined as the $\overrightarrow{M_0}$ component measured in the $(\vec{x}, \vec{y})$ plane (please refer to Figure 1.7 for more information about the axis orientation).

As depicted in Figure 1.8a, the visualization of the tipping of the magnetization $\overrightarrow{M_0}$ towards the transversal plane is difficult to represent and analyze in the scanner reference frame. As such, the magnetization M_0 is usually represented in a rotating reference frame whose transversal axis are rotated at the Larmor frequency (Figure 1.8b).

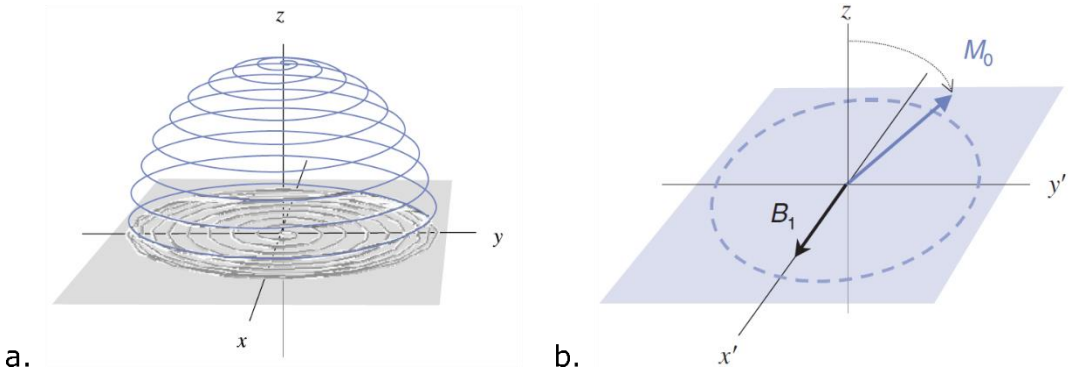

Figure 1.8. Tipping of the M_0 magnetization in the transversal plane. As depicted in a. the tipping of the magnetization is difficult to study in the fix reference frame of the scanner used for the measurement. However, the tipping of the magnetization is easy to study in a rotating reference frame, when its angular frequency matches the Larmor frequency of the hydrogen spins, as depicted in b. Images from [3].

1.5 Longitudinal and transversal relaxation, introduction to the Bloch equations

To be able to measure the transversal component of the magnetization M_0, it is necessary to remove the B_1 field. Once the B_1 field disappears, the hydrogen spins will dephase, thus suppressing the transversal component of the magnetization M_0. This phenomenon is called the spin-spin relaxation, transversal relaxation or T2 relaxation. In addition, the hydrogen spins will exchange energy with their surroundings in order to come back to their steady-state, where the excess number of hydrogen spins in the direction of the B_0 magnetic field is defined as in equation 1.3. This phenomenon is called the spin-lattice relaxation, longitudinal relaxation or T1 relaxation.

1.5.1 The longitudinal relaxation and the T1 relaxation time

The rate of change of the longitudinal magnetization $M_{\parallel}$ growths according to the following equation:

$$\frac{d\, M_{\parallel}(t)}{dt} = \frac{\left|\overrightarrow{M_0}\right| - M_{\parallel}(t)}{T1} \qquad 1.8$$

With $T1$ defined as the longitudinal relaxation time. The solution of equation 1.8 allows to describe the evolution of the longitudinal magnetization over time as follows:

$$M_{\parallel}(t) = M_{\parallel}(0)\, e^{-\frac{t}{T1}} + \left|\overrightarrow{M_0}\right| \left(1 - e^{-\frac{t}{T1}}\right) \qquad 1.9$$

With $M_{\parallel}(0)$ the longitudinal magnetization at the time $t = 0\, ms$, which correspond to the time from when the relaxation phenomenon begins. By definition, the T1 relaxation time is

defined as the time for which $t = T1$ after tipping the magnetization $\overrightarrow{M_0}$ by $90°$, i.e. after completely tipping the magnetization $\overrightarrow{M_0}$ in the transversal plane ($M_{\parallel}(0) = 0$):

$$M_{\parallel}(T1) = \left|\overrightarrow{M_0}\right| \left(1 - e^{-\frac{T1}{T1}}\right) \cong 0.66\, \overrightarrow{M_0} \qquad 1.10$$

The result of equation 1.10 indicates that the $T1$ relaxation time corresponds to the time required to obtain a longitudinal magnetization $M_{\parallel}$ that is equal to approximately $66\ \%$ of the original magnetization M_0. It is clear, from equations 1.8-1.10, that the $T1$ relaxation time is directly linked to the speed at which the hydrogen spins come back to their steady state after a perturbation by the B_1 magnetic field. An interesting characteristic of the $T1$ relaxation time is that it varies according to the properties of the molecule in which the hydrogen spins are located, thus allowing to visualize and measure differences between the tissues that compose the human body.

It was shown from experimentation [3] that the $T1$ relaxation time increases with the B_0 magnetic field:

$$T1 \propto \left|\overrightarrow{B_0}\right|^b \qquad 1.11$$

With b a factor approximately equal to 0.3. In this thesis, we focus on the imaging of the brain, i.e. on the imaging of the WM and GM tissues whose T1 relaxation times are presented in Table 1.1. It should be noted that the measure of the T1 relaxation time is highly dependent on the method used to measure it [4]. Since the CSF is a fluid that is flowing at a high speed that cannot be neglected during T1 measurements, its T1 is usually not measured with standard T1 measurements techniques. The T1 of the CSF is usually assumed to be longer than $2.5\ sec$. The recovery of the longitudinal magnetization of sets of hydrogen spins belonging to WM, cortical GM and CSF at 3T is presented in Figure 1.9.

Basic MRI principle 4: From equation 1.11, we deduce that the T1 relaxation time increases when the strength of the B_0 magnetic field increases.

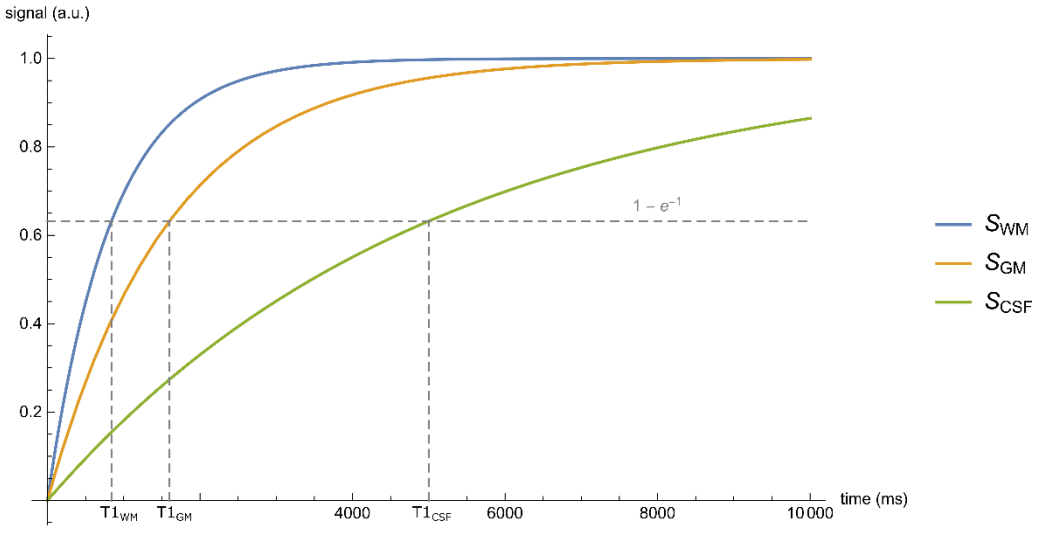

Figure 1.9. Recovery of the longitudinal magnetization $M_{\parallel}$ as a function of time after a $90°$ flip angle for WM, GM and CSF, with an original magnetization $M_0 = 1$ and with $B_0 = 3\ T$.

Table 1.1. T1 relaxation times of the brain tissues measured by Wright et al. [4] for a B_0 field strength of $1.5\ T$, $3\ T$ *and* $7\ T$.

	T1 relaxation time (ms)			
Field	White matter	Putamen	Caudate Head	Cortical Gray matter
1.5 T	650 ± 30	1084 ± 63	1109 ± 66	1197 ± 135
3 T	840 ± 50	1332 ± 68	1395 ± 49	1607 ± 112
7 T	1130 ± 100	1643 ± 167	1684 ± 76	1939 ± 150

1.5.2 The transversal relaxation, the $T2$ and the $T2^*$ relaxation time

In the rotating reference frame, the rate of change of the transversal magnetization $M_\perp$ is defined as:

$$\frac{d\,\vec{M}_\perp(t)}{dt} = -\frac{\vec{M}_\perp(t)}{T2} \qquad 1.12$$

With $T2$ defined as the transversal relaxation time. The solution of equation 1.12 allows to describe the evolution of the transversal magnetization as follows:

$$\vec{M}_\perp(t) = \vec{M}_\perp(0)\, e^{-\frac{t}{T2}} \qquad 1.13$$

With $M_\perp(0)$ the transversal magnetization at the time $t = 0\ ms$, which corresponds to the time from when the relaxation phenomenon begins. By definition, the $T2$ relaxation time is defined as the time for which $t = T2$ after tipping the magnetization $\overrightarrow{M_0}$ by an angle of $90°$, i.e. after completely projecting the magnetization $\overrightarrow{M_0}$ in the transversal plane:

$$\vec{M}_\perp(T2) = \vec{M}_0(0)\, e^{-\frac{T2}{T2}} \cong 0.33\, \vec{M}_0(0) \qquad 1.14$$

The result of equation 1.14 indicates that the $T2$ relaxation time corresponds to the time required to obtain a transversal magnetization $M_\perp$ that is equal to approximately $33\ \%$ of the magnetization M_0. It is clear, from equations 1.12-1.14, that the $T2$ relaxation time is directly linked to the speed at which the hydrogen spins dephase in the transversal plane. Similarly to the T1 relaxation time, the $T2$ relaxation time varies according to the properties of the molecule in which the hydrogen spins are located, thus allowing to visualize and measure differences between the tissues that compose the human body. However, the T2 relaxation time is different from the T1 relaxation time in the sense that it is roughly independent from the B_0 magnetic field [3]. Wansapura et al. reported the following $T2$ measurements of brain tissues: $79.6 \pm 0.6\ ms$ for WM and $110.0 \pm 2.0\ ms$ for GM (including the putamen, the caudate head and cortical GM) [5]. Similarly to the measure of the T1 relaxation time, the T2 relaxation time of the CSF cannot be measured with standard T2 measurement techniques. The decay of the transversal magnetization of sets of hydrogen spins belonging to WM, GM and CSF at 3T is presented in Figure 1.10, with the T2 relaxation time of CSF assumed to be equal to $1\ sec$.

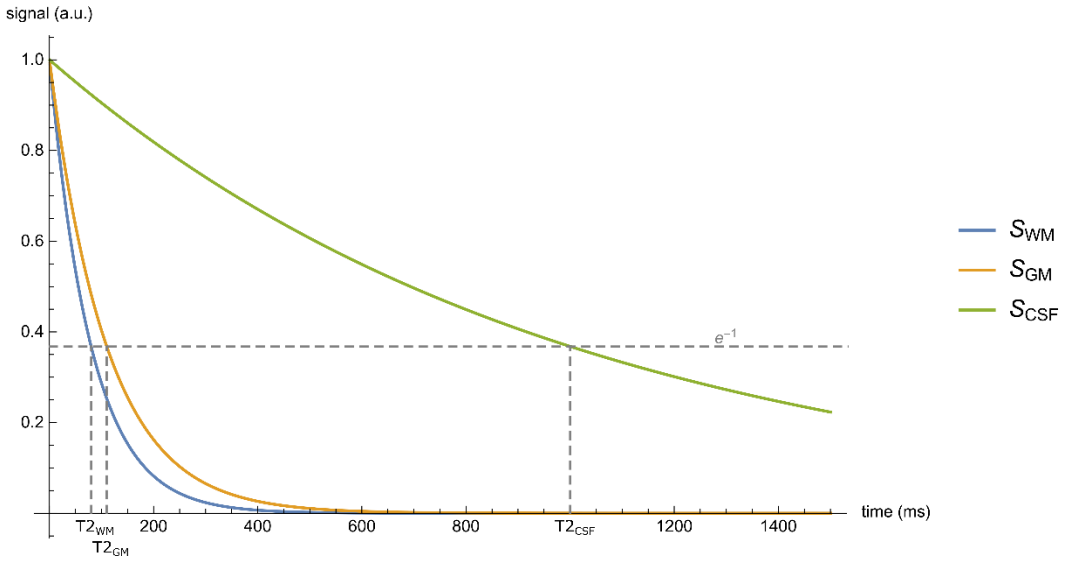

Figure 1.10. Decay of the transversal magnetization $M_\perp$ as a function of time after a $90°$ flip angle for WM, GM and CSF, with an original magnetization $M_0 = 1$ and with $B_0 = 3\ T$.

As shown in equation 1.1, the precessional frequency of the hydrogen spins about the B_0 magnetic field depends on B_0. Thus, two neighboring sets of spins experiencing some local differences ΔB_0 in the B_0 magnetic field will have different precessional frequencies:

$$\omega_0^1 = \gamma\, B_0 \qquad 1.15$$

$$\omega_0^2 = \gamma\, (B_0 + \Delta B_0) = \omega_0^1 + \Delta B_0\, \gamma \qquad 1.16$$

With ω_0^1 the precessional frequency of a set of spins 1, non affected by B_0 inhomogeneities and ω_0^2 the precessional frequency of a set of spins 2, affected by local B_0 inhomogeneities ΔB_0.

In practice, the difference between the precessional frequencies of the set of spin 1 and the set of spin 2 (i.e. $\Delta B_0\, \gamma$) will induce an additional dephasing of the spins. By convention, the relaxation time of the dephasing induced by the B_0 inhomogeneities is named the $T2'$ relaxation time. The $T2^*$ relaxation time, characterizing the decay of the magnetization in the transversal plane, is computed as follows:

$$\frac{1}{T2^*} = \frac{1}{T2} + \frac{1}{T2'} \qquad 1.17$$

Then, the decay of the transverse magnetization is computed with the following equation:

$$\vec{M}_\perp(t) = \vec{M}_\perp(0)\, e^{-\frac{t}{T2^*}} \qquad 1.18$$

With $T2^*$ defined as the time required to obtain a transversal magnetization $M_\perp$ that is equal to approximately $33\,\%$ of the original magnetization M_0 in the presence of local B_0 field inhomogeneities. Equations 1.17 and 1.18 indicate that the dephasing induced by B_0 inhomogeneities decreases the $T2^*$ relaxation time, and as such, increases the speed at which the magnetization $M_\perp$ decays in the transversal plane. The $T2^*$ relaxation is of interest in MRI applications since a change in tissue compositions may locally introduce some bias in the B_0 field that can be useful for the study of certain pathologies.

Increasing the strength of the magnetic field B_0 also tends to increase its local inhomogeneities ΔB_0 and, as such, decreases the $T2^*$ relaxation time. The $T2^*$ values measured in brain tissues are presented as a function of the B_0 magnetic field in Table 1.2. Similarly to the measure of the T1 and T2 relaxation times, the $T2^*$ relaxation time of the CSF cannot be measured with standard $T2^*$ measurement techniques. The decay of the apparent transversal magnetization of sets of hydrogen spins belonging to WM, cortical GM and CSF at 3T is presented in Figure 1.11, with the CSF $T2^*$ relaxation time assumed to be equal to $250\ ms$.

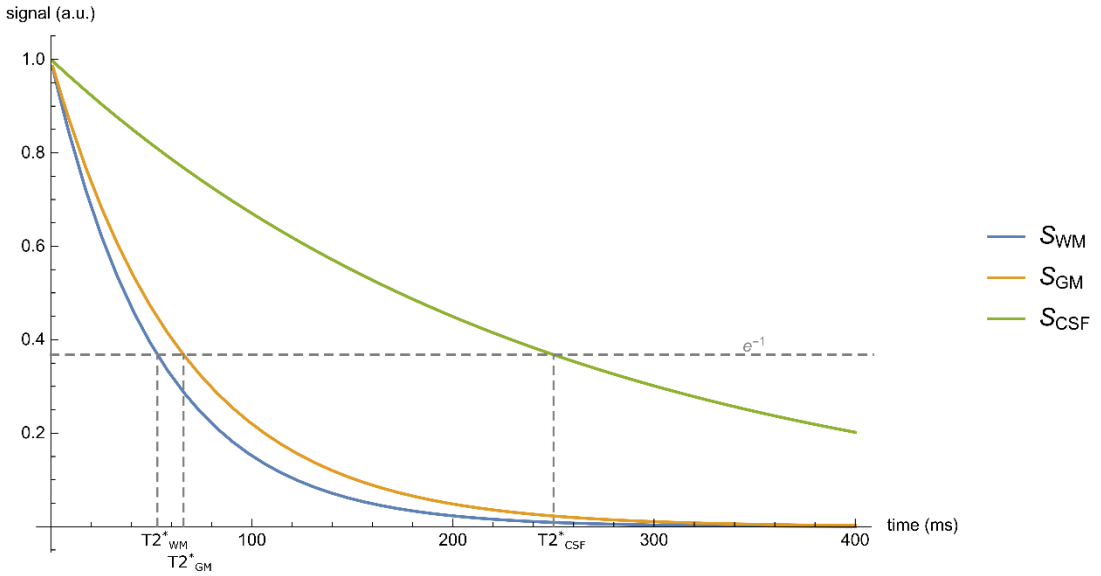

Figure 1.11. Decay of the apparent transversal magnetization $M_\perp$ as a function of time after a $90°$ flip angle for WM, GM and CSF, with an original magnetization $M_0 = 1$ and with $B_0 = 3\ T$.

Table 1.2. $T2^*$ relaxation times of the brain tissues measured by Peters et al. [6] for a B_0 field strength of $1.5\ T$, $3\ T$ and $7\ T$.

	$T2^*$ relaxation time (ms)			
Field	White matter	Putamen	Caudate Head	Cortical GM
1.5 T	62.2 ± 1.9	55.5 ± 2.3	58.8 ± 2.4	84.0 ± 0.8
3 T	53.2 ± 1.2	31.5 ± 2.5	41.3 ± 2.3	66.0 ± 1.4
7 T	26.8 ± 1.2	16.1 ± 1.6	19.9 ± 2.0	33.2 ± 1.3

1.5.3 The Bloch equations

In the sections above, the rate of change of the magnetization as a function of time was defined in two separated equations, with equation 1.8 defining the rate of change of the longitudinal magnetization, while equation 1.12 defines the rate of change of the transversal magnetization.

These rates of changes can be combined in a single vectorial equation called the Bloch equation (or Bloch equations when decomposed along the $\vec{x}$, $\vec{y}$ and $\vec{z}$ axis in a three dimensional reference space):

$$\frac{d\,\vec{M}(t)}{dt} = \gamma\,\vec{M}(t) \times \vec{B}_{ext}(t) + \frac{M_0\,\vec{z} - \overrightarrow{M_{\parallel}}(t)}{T1} + \frac{\overrightarrow{M_{\perp}}(t)}{T2} \qquad 1.19$$

With $\vec{B}_{ext}$ the sum of the external bias fields affecting the spins producing the magnetization $\vec{M}$ and $\vec{z}$ the unit vector in the direction of the magnetic field $\overrightarrow{B_0}$. The Bloch equations are very handy to describe the change of the longitudinal and transversal magnetizations as a function of time during the MR signal acquisition, allowing to describe the signal evolution as a function of the pulse sequences that modulates it. Solving the Bloch equations is of crucial interest for the development and optimization of new MR pulse sequences, as well as for the study of the magnetic behavior of human tissues, especially in quantitative imaging.

1.6 Basic MR sequences: spin echo, gradient echo

In this section, we focus on the measurement of the M_0 magnetization. As explained in the previous sections, the M_0 magnetization must be tipped in the transversal plane by a second magnetic field, $B1$, in order to be measured. In practice, the decay of the transversal magnetization $M_{\perp}$ is too fast to allow its direct measurement. It is then necessary to rephase the transversal magnetization $M_{\perp}$ in order to create an echo that allows its measurement. This rephasing of $M_{\perp}$ can be performed with two different MR pulse sequences: the spin echo and the gradient echo sequences.

1.6.1 The spin echo sequence

The scheme of the spin echo pulse sequence is presented in Figure 1.12a. First, the M_0 magnetization is tipped in the transversal plane with a $90°$ flip angle (Figure 1.12b). After the $90°$ flip angle, the hydrogen spins start to dephase due to the spin-spin interactions and the local B_0 field inhomogeneities (Figure 1.12c). After a given time $TE/2$, a $180°$ RF pulse is applied to reverse the magnetization in the transversal plane (Figure 1.12d). The spins that were precessing faster (resp. slower) than the Larmor frequency, ω_0, due to local B_0 field inhomogeneities had a negative (resp. positive) phase compared to the spins precessing at the Larmor frequency. After the inversion of the magnetization in the transversal plane, these spins end up having a positive (resp. negative) phase (Figure 1.12d). Since the B_0 inhomogeneities remain unchanged before and after the RF pulse, the spins start to rephase (Figure 1.12e). After a given time $TE/2$, the rephasing of the spins generates an echo allowing the measurement of the magnetization in the transversal plane (Figure 1.12f). Finally, the spins dephase again to reach their steady-state (Figure 1.12g). Due to the method used to spatially sample the magnetization (please refer to the section 1.9 for more information), the spin echo pattern is repeated multiple times with TR defined as the repetition time between two $90°$ pulses. The time between the $90°$ pulse and the measurement of the magnetization is called the echo time TE. The Bloch equations were solved for the spin echo sequence, allowing to describe the spin echo signal with the following equation:

$$S_{SE} = M_0\,e^{-\frac{TE}{T2}}\left(1 - e^{-\frac{TR}{T1}}\right) \qquad 1.20$$

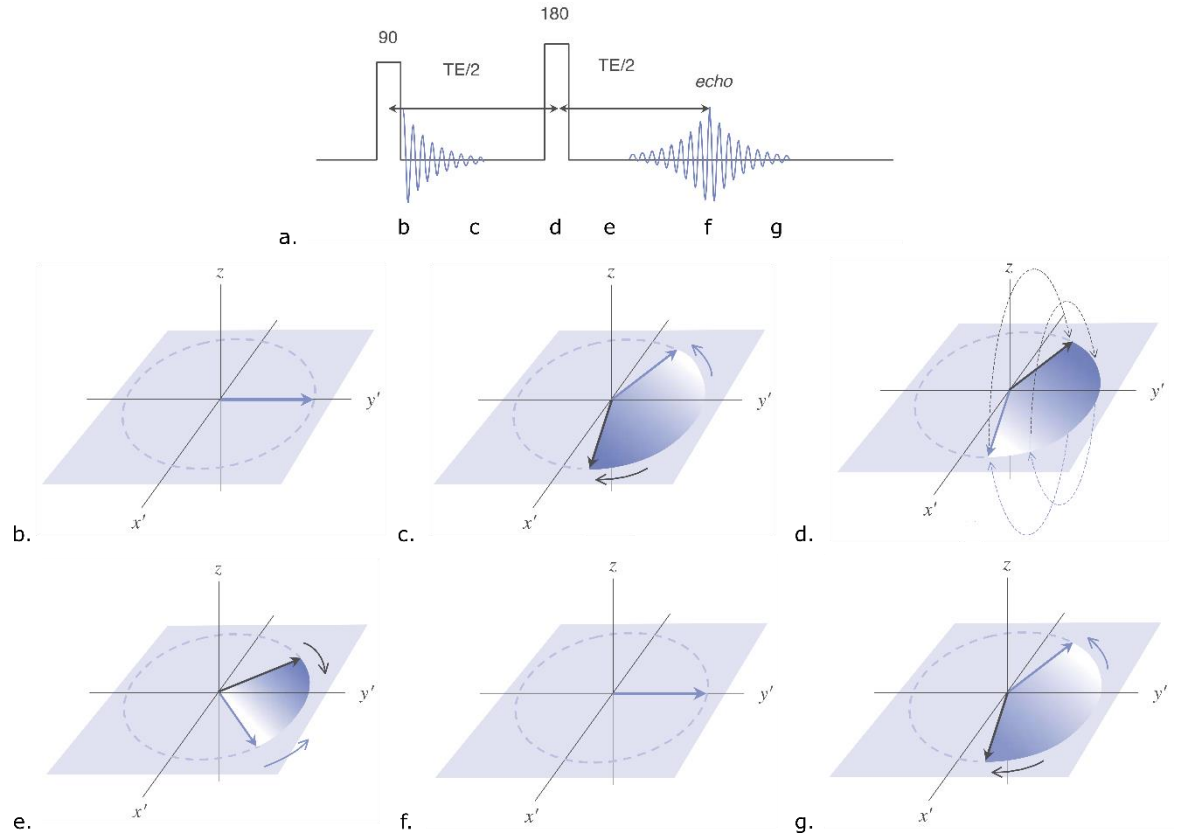

Figure 1.12. Acquisition scheme of the spin echo pulse sequence. Images from [3].

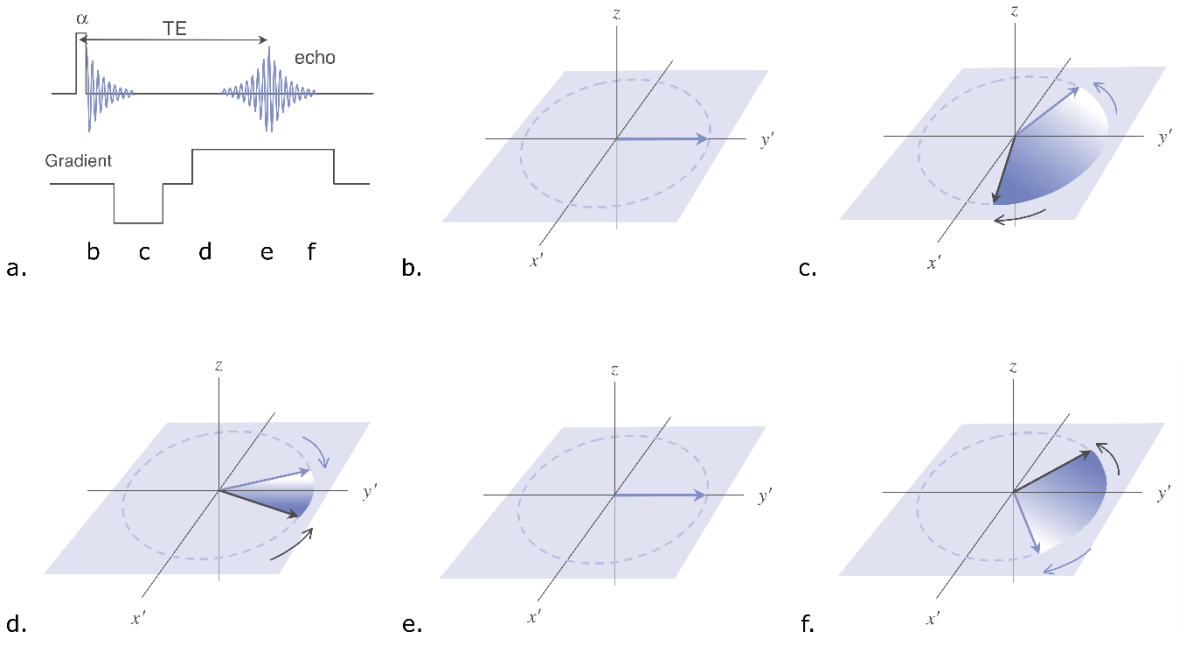

Figure 1.13. Acquisition scheme of the gradient echo pulse sequence. Images from [3].

1.6.2 The gradient echo sequence

The gradient echo (GRE) sequence proposes a different way of rephasing the spins to create the echo of the transversal magnetization $M_{\perp}$. The scheme of the gradient echo sequence is presented in Figure 1.13a. First, the longitudinal magnetization is tipped towards the transversal plane with a given flip angle α (Figure 1.13b). Immediately after tipping the magnetization, a spatially varying gradient ∇B_0 is applied for a given time $TE/2$. This gradient is used to increase the dephasing of the transversal magnetization. During this time, the spins with a positive (resp. negative) gradient will precess faster (resp. slower) than the spins precessing at the Larmor frequency, thus introducing a negative (resp. positive) dephasing between them (Figure 1.13c). After the time $TE/2$, the gradient is reversed. Then, the precession frequencies are reversed, which rephases the spins (Figure 1.13d). After a given time $TE/2$, the rephasing of the spins generates an echo allowing the measurement of the transversal magnetization (Figure 1.13e). Finally, the spins dephase again to reach their steady-state (Figure 1.13f).

The gradient echo sequence has the advantage that any flip angle can be used to tip a part of the M_0 magnetization in the transversal plane and get a signal, as opposed to the spin echo sequence that is restricted to a flip angle of $90°$. However, there is no compensation for the dephasing of the spins induced by B_0 field inhomogeneities. Therefore, the gradient echo signal is sensitive to B_0 field inhomogeneities, as opposed to the spin echo sequence which is exclusively sensitive to the transversal magnetization of the tissues.

The solution of the Bloch equations for the gradient echo pulse sequence allows to describe the gradient echo signal with the following equation:

$$S_{GRE} = \sin\alpha \; M_0 \, e^{-\frac{TE}{T2^*}} \frac{1 - e^{-\frac{TR}{T1}}}{1 - \cos\alpha \; e^{-\frac{TR}{T1}}} \tag{1.21}$$

Similarly to the spin echo sequence, the gradient echo pattern needs to be acquired multiple times to generate MR images, with the repetition time TR being defined as the time between two RF pulses and the echo time TE defined as the time between the tipping of the magnetization and its measurement in the transversal plane.

It should be noted that the equations 1.20 and 1.21 are solved assuming that there is no transversal magnetization $M_{\perp}$ at the beginning of the pulse sequence, i.e. $T2 \ll TR$ for the spin echo pulse sequence and $T2^* \ll TR$ for the gradient echo pulse sequence. In practice, this is ensured by adding spoiling gradients that accelerate the spins dephasing in the transverse plane after the transversal magnetization measurement. In addition, the equation 1.21 is solved assuming that the longitudinal magnetization $M_{\parallel}$ at the beginning of the pulse sequence is equal to M_0, while in the case where $TR < 5\,T1$, the longitudinal magnetization does not have enough time to reach its steady-state. The evolution of the longitudinal magnetization for a gradient echo pulse sequence with $TR < 5\,T1$ is the following according to the solution of the Bloch equations:

$$S_{\parallel gre} = M_{\parallel}(0) \left(\cos\alpha \; e^{-\frac{TR}{T1}}\right)^n + M_0 \left(1 - e^{-\frac{TR}{T1}}\right) \frac{1 - \left(\cos\alpha \, e^{-\frac{TR}{T1}}\right)^n}{1 - \cos\alpha \, e^{-\frac{TR}{T1}}} \tag{1.22}$$

With n the number of consecutive gradient echo pulses. In this situation, the gradient echo signal measured in the transversal plane values:

$$S_{GRE} = \sin\alpha\, e^{-\frac{TE}{T2^*}} S_{\parallel gre} \quad 1.23$$

1.7 Assessing the visual quality of Magnetic Resonance Images

This section presents the quantitative metrics commonly used to assess the visual quality of structural brain MRIs. The first metric is the signal to noise ratio (SNR). The SNR represents the corruption of the structures imaged by random noise, as displayed in Figure 1.14. In practice, the SNR is computed as follows:

$$SNR_A = \frac{\mu_A}{\sigma_n} \quad 1.24$$

With μ_A the average signal intensity of a given tissue A and σ_n the standard deviation measured in the background of the image (usually the air in MRI). However, equation 1.24 cannot be used when MRIs are acquired with parallel imaging techniques (section 1.9.5). Then, the SNR can be approximated by acquiring twice the same image and using the following equation:

$$SNR_A \cong \frac{\mu_A}{\sigma_{A[I1-I2]}} \quad 1.25$$

With $\sigma_{A[I1-I2]}$ the standard deviation of the difference between the images 1 and 2 measured for a given tissue A. Another way to compute the SNR is to acquire a single image and to use the following equation:

$$SNR_A \cong \frac{\mu_A}{\sigma_A} \quad 1.26$$

With σ_A the standard deviation of the a given tissue A. It is clear from equations 1.24-1.26 and Figure 1.14 that the higher the SNR, the higher the visual quality of the associated structure in the MRI.

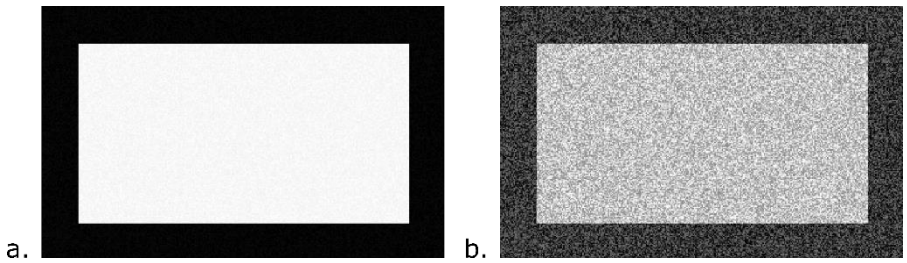

Figure 1.14. Example of images with a high SNR (a) and a low SNR (b). The visualization of the structure of interest is clearly impacted by the SNR.

It can be deduced from the Basic MRI principles 2 and 3 (section 1.4) that both increasing the strength of the B_0 magnetic field and increasing the volume of the voxel increase the SNR. It can be deduced from the spin echo and the gradient echo signal equations (equations 1.20 and 1.21) that decreasing the echo time TE and increasing the repetition time TR allows to

increase the SNR. In the case of the gradient echo pulse sequence, increasing the part of the longitudinal magnetization that is tipped in the transversal plane, i.e. setting-up the value of the flip angle α to be close to $90°$, also increases the SNR. Finally, the SNR can be increased by lowering the bandwidth used to acquire the signal, since lowering the bandwidth corresponds to increase the time used to measure the signal.

The SNR is not the only metric of importance to represent the visual quality of MRIs. For example, images with a low contrast provide very few information about the structures imaged, as shown in Figure 1.15. In practice, we measure the contrast with the following equation:

$$CN_{A/B} = \frac{|\mu_A - \mu_B|}{\mu_A + \mu_B} \quad 1.27$$

With μ_A and μ_B the average signal intensities of the given tissues A and B. The contrast takes values within $[0,1]$ with the value 1 (resp. 0) representing a good (resp. poor) contrast.

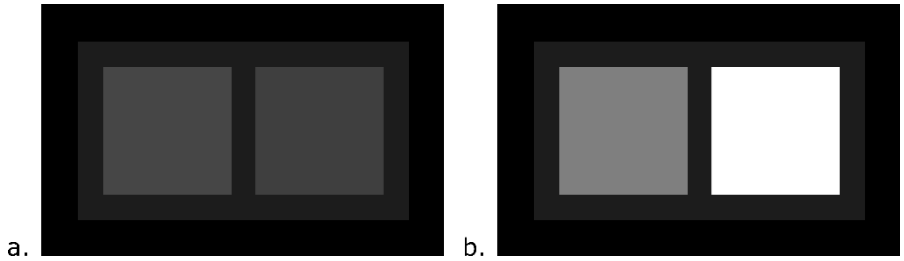

Figure 1.15. Example of images with a low CN (a) and a high CN (b). The differentiation between the three structures of interest is easier in images with a high CN.

In the case of structural brain imaging, it is clear that we aim at acquiring images with both a good SNR and a good contrast for the structures of interest. This can be measured with the contrast to noise ratio (CNR), defined as follows:

$$CNR_{A/B} = \frac{|\mu_A - \mu_B|}{\sqrt{\frac{\sigma_A^2 + \sigma_B^2}{2}}} \quad 1.28$$

With a high CNR value representing an image of good visual quality, as shown in Figure 1.16. In practice, we aim at obtaining the best compromise between the maximization of the CNR and the minimization of the sequence acquisition time. The definition of the CNR is then modified to also account for the sequence acquisition time, which directly depends on the sequence repetition time. This new definition of the CNR is called the CNR per unit of time, with:

$$CNR_{A/B} = \frac{|\mu_A - \mu_B|}{\sqrt{\frac{\sigma_A^2 + \sigma_B^2}{2}}} \times \frac{1}{\sqrt{TR}} \quad 1.29$$

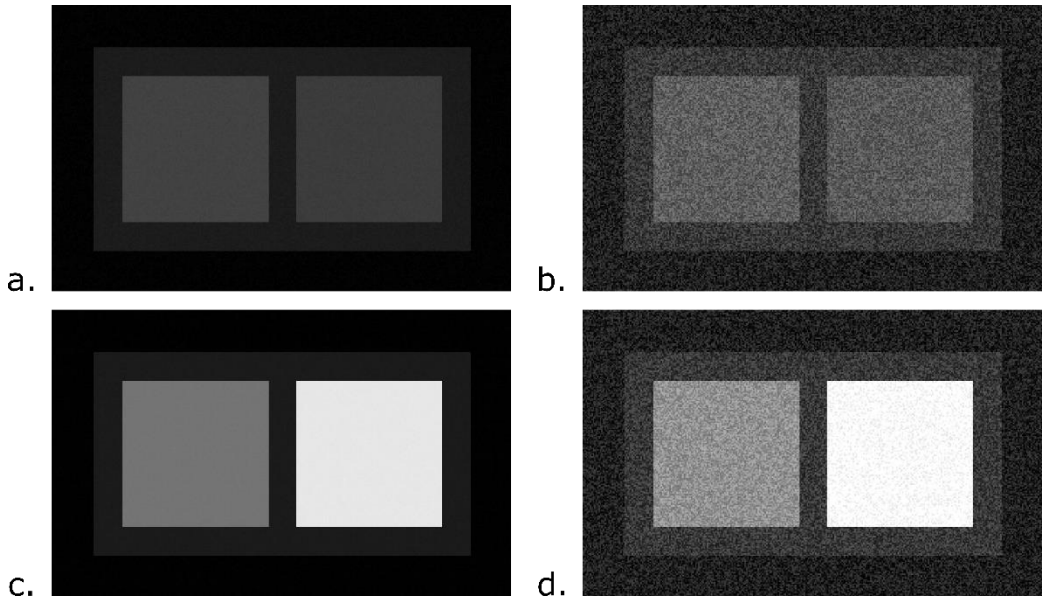

Figure 1.16. Example of images with a low CNR (a,b,d) and a high CNR (c). a. Image with a low CN and a high SNR. b. Image with a low CN and a low SNR. c. Image with a high CN and a high SNR. d. Image with a high CN and a low SNR. It is clear by comparing the different images that images with a high CNR allow to better differentiate the three structures of interest.

1.8 Basic MR contrast

1.8.1 Proton density-weighted imaging

Let us consider two sets of hydrogen spins, s_1 and s_2, with different magnetic properties. We then obtain the following equations for the spin echo signal:

$$S_{SE}^{s1} = M_{01}\ e^{-\frac{TE}{T2_1}}\left(1 - e^{-\frac{TR}{T1_1}}\right) \quad 1.30$$

$$S_{SE}^{s2} = M_{02}\ e^{-\frac{TE}{T2_2}}\left(1 - e^{-\frac{TR}{T1_2}}\right) \quad 1.31$$

With M_{01} (resp. M_{02}) the magnetization at equilibrium, $T1_1$ (resp. $T2_1$) the $T1$ relaxation time and $T2_1$ (resp. $T2_2$) the $T2$ relaxation time of the set of spins s_1 (resp. s_2). Then, by tuning the TE and TR parameters of the spin echo sequence so that $e^{-\frac{TE}{T2_1}} \cong e^{-\frac{TE}{T2_2}} \cong 1$ and $e^{-\frac{TR}{T1_1}} \cong e^{-\frac{TR}{T1_2}} \cong 0$, we obtain:

$$S_{SE}^{s1} = M_{01} \quad 1.32$$

$$S_{SE}^{s2} = M_{02} \quad 1.33$$

Considering that the set of spins s_1 and s_2 are located in different tissues, the contrast between those tissues can be computed using equation 1.27:

$$CN_{s_1/s_2} = \frac{|M_{01} - M_{02}|}{M_{01} + M_{02}} \quad 1.34$$

The same result can be derived from the gradient echo pulse sequence (equation 1.21) in the case where $e^{-\frac{TE}{T2_1^*}} \cong e^{-\frac{TE}{T2_2^*}} \cong 1$ and $e^{-\frac{TR}{T1_1}} \cong e^{-\frac{TR}{T1_2}} \cong 0$.

Basic MRI principle 5: It can be deduced from equation 1.34 that an MRI with a proton density-weighted contrast can be acquired with a spin-echo (resp. gradient echo) sequence when its TE is sufficiently short and its TR is sufficiently long to ignore the effects of the $T1$ and $T2$ (resp. $T2^*$) relaxation times on the signal.

In brain imaging, the proton densities of the tissues of interest are very close to each other, with $\rho_{WM} \cong 0.7$, $\rho_{GM} \cong 0.8$ and $\rho_{CSF} \cong 1.0$ –it should be noted that the reported proton densities are relative measures compared to the CSF proton density–, thus leading to a poor contrast in proton density-weighted images. This poor contrast limits the interest of proton density-weighted imaging for structural brain imaging.

1.8.2 T1-weighted imaging

Let us now focus on the signal of the two sets of hydrogen spins s_1 and s_2, measured with a spin echo sequence with its TE and TR parameters tuned so that $e^{-\frac{TE}{T2_1}} \cong e^{-\frac{TE}{T2_2}} \cong 1$, $e^{-\frac{TR}{T1_1}} \neq 0$ and $e^{-\frac{TR}{T1_2}} \neq 0$:

$$S_{SE}^{s1} = M_{01}\left(1 - e^{-\frac{TR}{T1_1}}\right) \quad 1.35$$

$$S_{SE}^{s2} = M_{02}\left(1 - e^{-\frac{TR}{T1_2}}\right) \quad 1.36$$

The contrast between the tissues corresponding to the sets of spins s_1 and s_2 values:

$$CN_{s_1/s_2} = \frac{\left| M_{01}\left(1 - e^{-\frac{TR}{T1_1}}\right) - M_{02}\left(1 - e^{-\frac{TR}{T1_2}}\right)\right|}{M_{02}\left(1 - e^{-\frac{TR}{T1_1}}\right) + M_{02}\left(1 - e^{-\frac{TR}{T1_2}}\right)} \quad 1.37$$

We notice that the contrast obtained in equation 1.37 does not only depend on the proton-density, but also on the T1 relaxation times of the tissues corresponding to the sets of spins s_1 and s_2. A similar behavior is observed when deriving the contrast obtained from the gradient echo sequence when $e^{-\frac{TE}{T2_1^*}} \cong e^{-\frac{TE}{T2_2^*}} \cong 1$, $e^{-\frac{TR}{T1_1}} \neq 0$ and $e^{-\frac{TR}{T1_2}} \neq 0$.

Basic MRI principle 6: It can be deduced from equation 1.37 that an MRI with a T1-weighted contrast can be acquired with a spin-echo (resp. gradient echo) sequence when its TE is sufficiently short to ignore the effects of the $T2$ (resp. $T2^*$) relaxation time on the signal, while its TR is sufficiently short to account for the effects of the $T1$ relaxation time on the signal.

1.8.3 T2-weighted imaging

We now focus on the signal of the two sets of hydrogen spins s_1 and s_2 measured with a spin echo sequence with its parameters setup so that $e^{-\frac{TE}{T2_1}} \neq 1$, $e^{-\frac{TE}{T2_2}} \neq 1$ and $e^{-\frac{TR}{T1_1}} \cong e^{-\frac{TR}{T1_2}} \cong 0$:

$$S_{SE}^{s1} = M_{01}\ e^{-\frac{TE}{T2_1}} \tag{1.38}$$

$$S_{SE}^{s2} = M_{02}\ e^{-\frac{TE}{T2_2}} \tag{1.39}$$

The contrast between the tissues corresponding to the sets of spins s_1 and s_2 values:

$$CN_{s_1/s_2} = \frac{\left| M_{01}\, e^{-\frac{TE}{T2_1}} - M_{02}\, e^{-\frac{TE}{T2_2}} \right|}{M_{01}\, e^{-\frac{TE}{T2_1}} + M_{02}\, e^{-\frac{TE}{T2_2}}} \tag{1.40}$$

We notice that the contrast obtained in equation 1.40 does not only depend on the proton-density, but also on the T2 relaxation times of the tissues corresponding to the sets of spins s_1 and s_2.

Basic MRI principle 7: It can be deduced from equation 1.40 that an MRI with a T2-weighted contrast can be acquired with a spin-echo sequence when its TE is sufficiently long to account for the effects of the $T2$ relaxation time on the signal, while its TR is sufficiently long to ignore the effects of the $T1$ relaxation time on the signal.

1.8.4 T2*-weighted imaging

Similarly to the $T2$-weighted imaging method, a $T2^*$-weighted contrast can be obtained by acquiring a gradient echo sequence when its parameters are tuned so that $e^{-\frac{TE}{T2_1^*}} \neq 1$, $e^{-\frac{TE}{T2_2^*}} \neq 1$ and $e^{-\frac{TR}{T1_1}} \cong e^{-\frac{TR}{T1_2}} \cong 0$:

$$S_{GRE}^{s1} = M_{01} \sin\alpha\ e^{-\frac{TE}{T2_1^*}} \tag{1.41}$$

$$S_{GRE}^{s2} = M_{02} \sin\alpha\ e^{-\frac{TE}{T2_2^*}} \tag{1.42}$$

The contrast between the tissues corresponding to the sets of spins s_1 and s_2 values:

$$CN_{s_1/s_2} = \frac{\left| M_{01}\, e^{-\frac{TE}{T2_1^*}} - M_{02}\, e^{-\frac{TE}{T2_2^*}} \right|}{M_{01}\, e^{-\frac{TE}{T2_1^*}} + M_{02}\, e^{-\frac{TE}{T2_2^*}}} \tag{1.43}$$

We notice that the contrast obtained in equation 1.43 does not only depend on the proton-density, but also on the $T2^*$ relaxation times of the tissues corresponding to the sets of spins s_1 and s_2.

Basic MRI principle 8: It can be deduced from equation 1.43 that an MRI with a $T2^*$-weighted contrast can be acquired with a gradient echo sequence when its TE is sufficiently long to account for the effects of the $T2^*$ relaxation time on the signal, while its TR is sufficiently long to ignore the effects of the $T1$ relaxation time on the signal.

1.8.5 Choosing the appropriated pulse sequence

From the sections above, it is clear that a choice between the spin echo sequence and the gradient echo sequence has to be made to determine how to acquire MRIs. In this section, we discuss the advantages and the flaws of the two sequences and we summarize what is the appropriated sequence to use for a given contrast.

The first and main difference between the spin echo and the gradient echo pulse sequences is related to the contrasts they provide. As the spin echo signal depends on the $T2$ relaxation time, while the gradient echo signal depends on the $T2^*$ relaxation time, only the spin echo (resp. gradient echo) sequence can be used to acquire a $T2$-weighted (resp. $T2^*$-weighted) contrast. Since the spin echo signal depends on the $T2$ relaxation time, the SNR obtained with this sequence is theoretically higher than the one obtained with the gradient echo sequence. This is explained by the fact that the $T2^*$ relaxation time is always shorter than the $T2$ relaxation time, and as such, the transversal magnetization $M_\perp$ decays faster when measured with a gradient echo sequence. However, an additional $180°$ RF pulse is required to acquire images with the spin echo sequence. This induces an increase in the specific absorption rate (SAR). The SAR is a standard metric measuring the energy per Kg sent by RF pulses to the human body. The SAR is limited in MRI applications for safety purposes, justifying the preference for gradient echo sequences over spin echo sequences. In addition, the freedom provided by the choice of the flip angle in the gradient echo sequence allows to better control the SAR in scanning sessions since low flip angles lowers the energy sent to the human body. The acquisition of gradient echo sequences with low flip angles also allows to decrease the sequence acquisition time since shorter TR are required to allow for the magnetization M_0 to recover in the longitudinal direction. For the aforementioned reasons, gradient echo sequences are preferred for the acquisition of proton density-weighted and $T1$-weighted contrasts.

It should be noted that, nowadays, more advanced sequences are used in clinical practice for the acquisition of brain MR images. However, all of those sequences are based on the spin echo and gradient echo principles and can be differentiated using the aforementioned arguments, with spin echo-based sequences used for $T2$-weighted imaging and gradient echo-based sequences used for proton density-weighted, $T1$-weighted and $T2^*$-weighted imaging. Examples of proton density-weighted, $T1$-weighted, $T2$-weighted and $T2^*$-weighted MRIs of the brain, obtained with the spin echo and gradient echo sequences, are presented in Figures 1.17 and 1.18.

a. b. c.

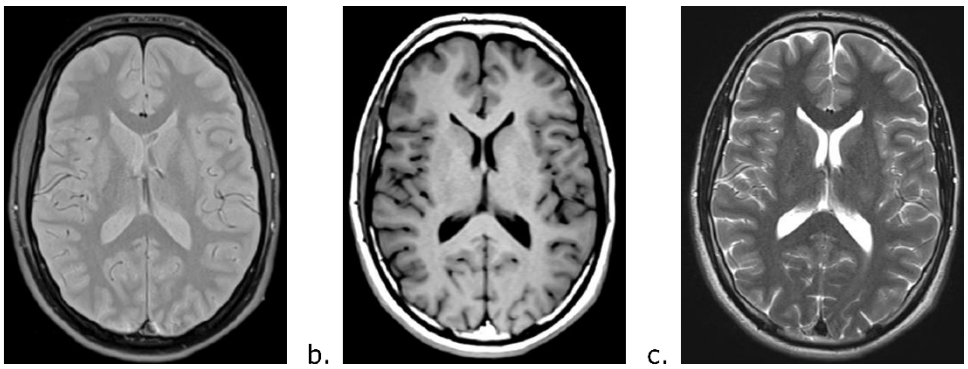

Figure 1.17. Examples of proton-density-weighted (a), T1-weighted (b) and T2-weighted (c) contrasts of the brain obtained with the spin echo sequence at 1.5T.

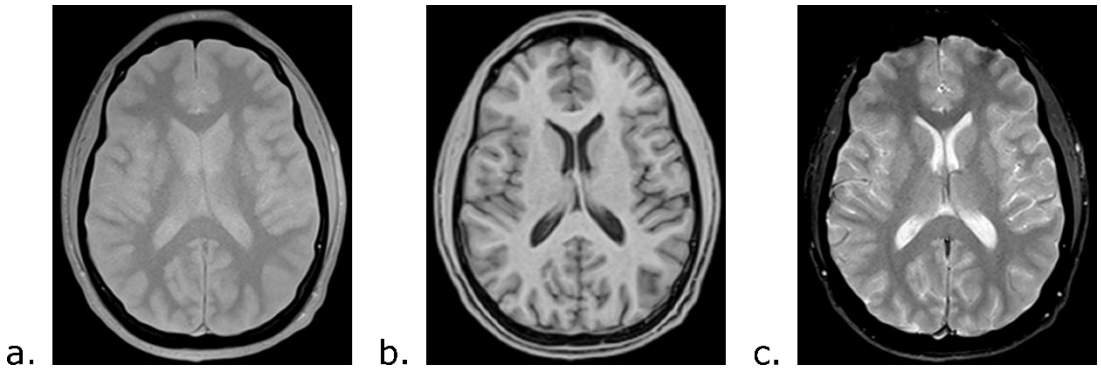

Figure 1.18. Examples of proton-density-weighted (a), T1-weighted (b) and T2-weighted (c) contrasts of the brain obtained with the gradient echo sequence at 1.5T.*

1.9 MRI spatial encoding

In the previous sections, we focused on the measure of the M_0 magnetization within a given volume. However, in practice, the M_0 magnetization must be measured in multiple adjacent volumes to allow for the generation of an image. This section describes the methods used to spatially measure the M_0 magnetization within the human body. These methods are mainly based on the Basic MRI principle 1, which is introduced in section 1.4 and indicates that the Larmor frequency of the hydrogen spins is proportional to the strength of the B_0 magnetic field.

1.9.1 Slice excitation principle

Let us introduce two sets of spins s_1 and s_2 with a different location along the $\vec{z}$ axis (this method works for any axis, with $\vec{z}$ used here as an example). By applying a spatially varying gradient to the B_0 magnetic field in the $\vec{z}$ direction, we obtain:

$$\omega_0(z_1) = \omega_0 + \gamma \, \nabla B_0(z_1) \qquad 1.44$$

$$\omega_0(z_2) = \omega_0 + \gamma \, \nabla B_0(z_2) \qquad 1.45$$

With z_1 and z_2 the positions of the sets of spins s_1 and s_2 along the $\vec{z}$ axis. It is clear from equations 1.44 and 1.45 that if the value of the gradient ∇B_0 varies along the $\vec{z}$ direction, then the sets of spins s_1 and s_2 will precess at different Larmor frequencies. Therefore, generating a B_1 magnetic field in the transversal plane with the frequency $\omega_0(z_1)$ (resp. $\omega_0(z_2)$) is only tipping the magnetization of the set of spins s_1 (resp. s_2) in the transversal plane. This method is used to select the slice from which the M_0 magnetization is measured. The acquisition of consecutive slices is performed by repeating a pulse sequence (spin echo or gradient echo for example) for every slice by varying the frequency of the B_1 magnetic field.

1.9.2 Frequency encoding

As mentioned in section 1.5.2, any local change of the B_0 magnetic field strength induces some dephasing of the hydrogen spins in the transversal plane. By applying spatially varying gradients along the $\vec{x}$ axis, it is possible to induce a specific dephasing to the hydrogen spins according to their $\vec{x}$ location (here $\vec{x}$ is used as an example, but the method works along any given axis). It can be shown mathematically [2] that the signal measured in the transversal plane corresponds to the spatial Fourier transform of the transversal magnetization $M_\perp$ in the $\vec{x}$ direction. It is then possible to obtain the spatial variation of the transversal magnetization $M_\perp$ in the $\vec{x}$ direction by computing the inverse Fourier transform of the signal measured in

the transversal plane. It should be noted that the frequency encoding step in the pulse sequence acquisition must be performed in a very short amount of time compared to the $T2^*$ relaxation time of the tissues of interest in order to avoid spatial distortions due to the $T2^*$ relaxation.

Let us define the k-space as the frequency space in which MR images are acquired (Figure 1.19). The center of the k-space contains the low frequency information of the image, i.e. the average signal intensity of the image. The sides of the k-space contain the high frequency information of the image, i.e. the high levels of details and the noise. In practice, the frequency encoding gradient is used to acquire one line of the k-space at each repetition of the pulse sequence (Figure 1.20).

In standard spatial encoding techniques, like Cartesian sampling, one line of the k-space is acquired along one direction ($\vec{x}$, $\vec{y}$ or $\vec{z}$). Then, the data contains information in 1 dimension only. The number of dimensions of the image is increased by increasing the number of phase encoding directions.

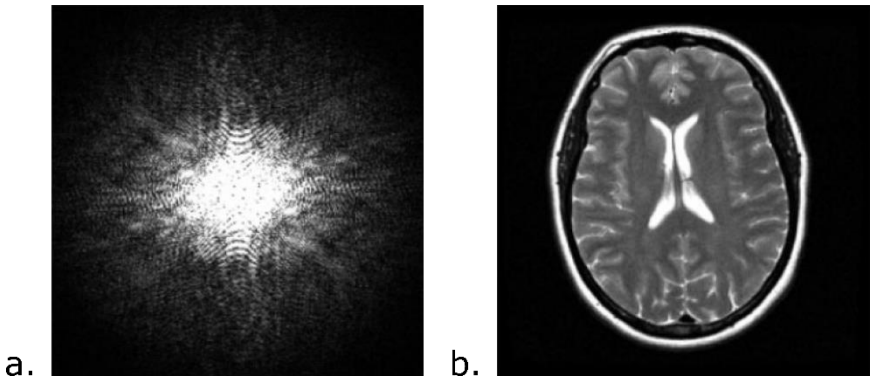

Figure 1.19. Example of k-space (a) MRI data acquired for brain imaging. The inverse Fourier transform of the k-space data (a) is shown in b. Images from [7].

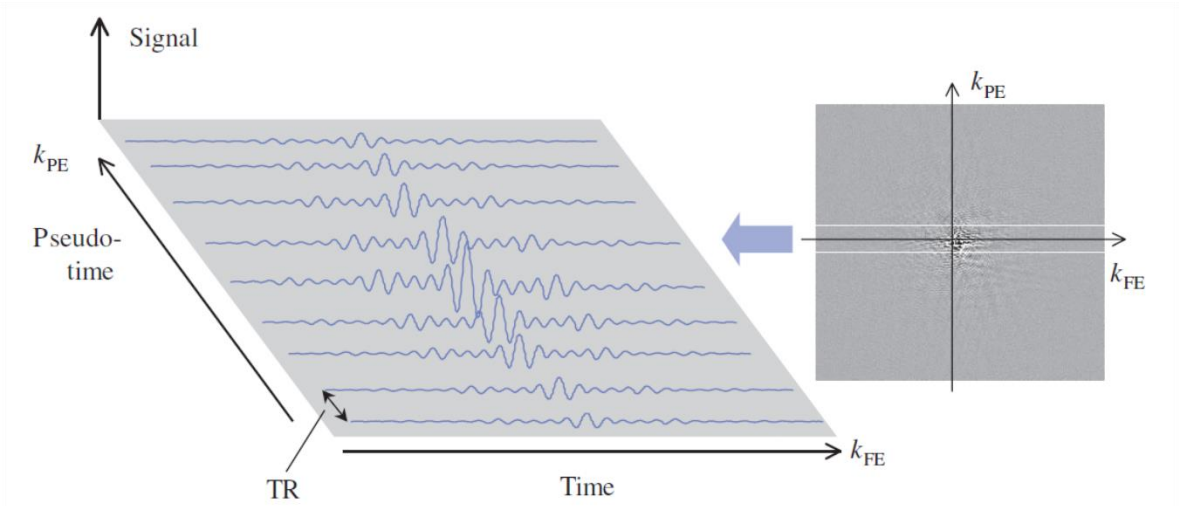

Figure 1.20. Acquisition of the k-space MRI data. A line of the k-space is acquired in the frequency encoding direction (k_{FE}) at each repetition of the pulse sequence. The pulse sequence is repeated multiple times to fill the phase encoding direction (K_{PE}), with TR the time between two repetitions of the pulse sequence. Images from [3].

1.9.3 Phase encoding

The frequency encoding method is only used to sample the k-space in one direction in standard sampling methods. Then, phase encoding methods are used to sample the k-space in the other directions. Let us consider that the magnetization M_0 has been fully tipped in the transversal plane. Providing that the B_0 magnetic field is homogeneous within the volume imaged, the hydrogen spins are precessing in phase within this volume (Figure 1.21a). As mentioned above, the application of a spatially varying gradient of the B_0 magnetic field makes the hydrogen spins dephase according to their spatial location. A phase encoding gradient is applied along the $\vec{y}$ direction ($\vec{y}$ is used as an example here, but the method works along any given axis) to induce a dephasing between the hydrogen spins (Figure 1.21b). After a given time, the phase encoding gradient is removed and the spins conserve their dephasing. Then, a frequency encoding gradient is applied along the $\vec{x}$ direction during the signal measurement step (Figure 1.21c). It can be shown mathematically [2] that the signal measured corresponds to the 2D Fourier transform of the spatial distribution of the transversal magnetization $M_\perp$. Therefore, an image can be reconstructed by computing the inverse Fourier transform of the signal measured. It should be noted that one pulse sequence acquisition allows to acquire data from only one k-space frequency in the phase encoding direction. The pulse sequence is then repeated to acquire the full k-space data in the phase encoding direction.

1.9.4 2D and 3D imaging

In practice, MRIs can be acquired in either two dimensions or three dimensions. The acquisition of 2D images is performed by exciting slices (section 1.9.1) prior to encode the transversal magnetization $M_\perp$ using the frequency and phase encoding principles described above. A 3D image can be reconstructed with the 2D sampling method by stacking up 2D images acquired with different slice positions. The acquisition of 3D images is performed by exciting the whole volume prior to apply phase encoding gradients in two different directions and finally apply a frequency encoding gradient during data sampling (allowing the acquisition of the k-space in three dimensions).

1.9.5 MR sequence acquisition time

As mentioned above, the pulse sequence is repeated for every phase encoding steps. The sequence acquisition time is then computed as:

$$TA = N_{ex} \times N_{PE} \times N_A \times TR \qquad 1.46$$

With N_{ex} the number of slice excitations, N_{PE} the number of phase encoding steps and N_A the number of signal averages (in certain acquisitions, the same pulse sequence is acquired multiple times and averaged to increase the SNR). Equation 1.46 represents the acquisition time for 2D spatial sampling methods. The 3D sequence acquisition time is computed as follows:

$$TA = N_{PE1} \times N_{PE2} \times N_A \times TR \qquad 1.47$$

With N_{PE1} and N_{PE2} the number of phase encoding steps along the given directions 1 and 2. In practice, 2D spatial sampling methods are mainly used for spin echo pulse sequences since their acquisition time would be too long in the 3D sampling case. It should be noted that some spin echo based-sequences (SPACE, CUBE, VISTA) were developed to allow for the acquisition

of spin echo signals in 3D [8]. Since gradient echo pulse sequences can have a short TR, they are usually acquired in 3D.

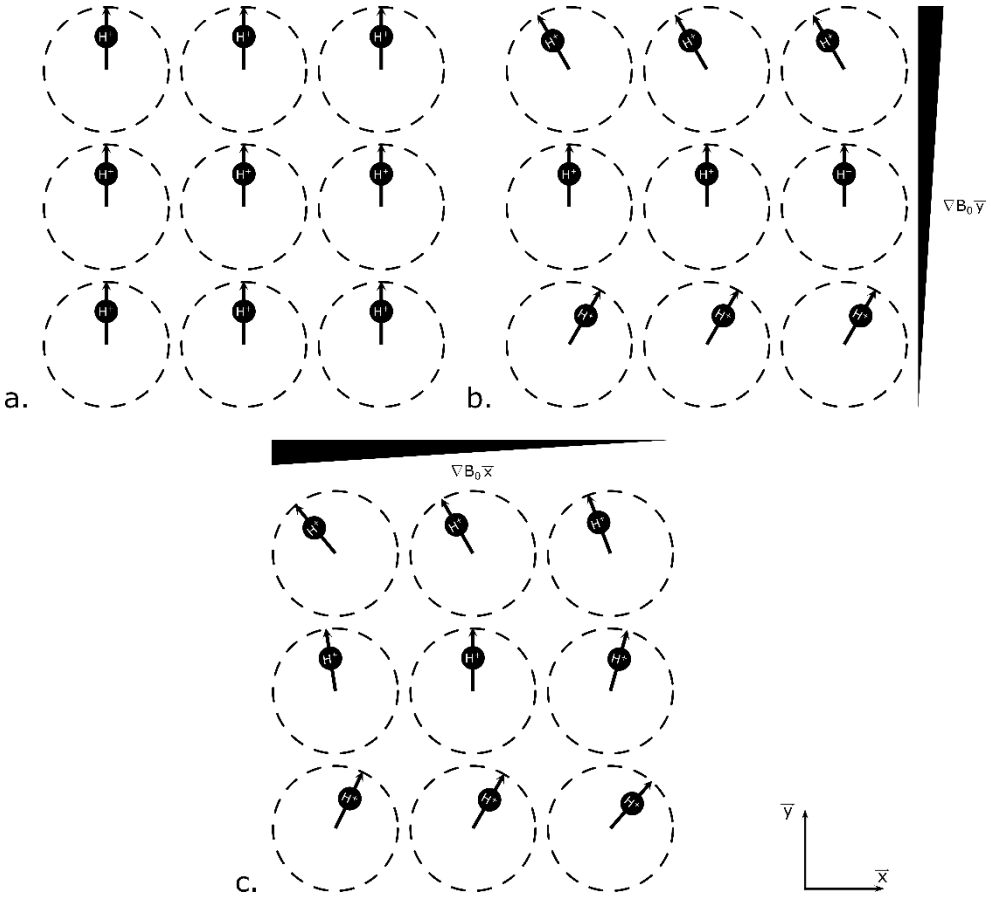

Figure 1.21. Example a spatial encoding using spatially varying gradients of the B_0 magnetization. After tipping the magnetization M_0 in the transversal plane, all the hydrogen spins are in phase (a). Then, a dephasing is introduced in the phase encoding direction (here $\vec{y}$) using a spatially varying gradient (b). Once the gradient is removed, the spins preserve their dephasing. Applying a frequency encoding gradient along the $\vec{x}$ direction then allows to fully differentiate the spins in two dimensions according to their dephasing (c).

As shown in equations 1.46 and 1.47, the sequence acquisition time depends on the number of phase encoding steps used to sample the k-space. The sequence acquisition time can then be reduced by decreasing the number of phase encoding steps required to generate the MR images. Since the k-space is symmetrical (Figures 1.19a and 1.22), the number of phase encoding steps can be decreased by acquiring a part of the k-space only and reconstructing the missing part mathematically with symmetrical constraints on the signal. This method is called partial Fourier and allows for a k-space sampling reduction by up to $6/8$ of the full k-space in a given direction. Since the k-space sampling in the frequency encoding direction is very fast, partial Fourier techniques are used in the phase encoding directions only.

In practice the MR signal is often measured with multi-channel received coils. These receiving coils have different spatial sensitivities (Figure 1.23) that allows for the reconstruction of the full k-space from a sub-sampled k-space with parallel imaging techniques such as SENSE [9], GRAPPA [10] or compressed sensing [11].

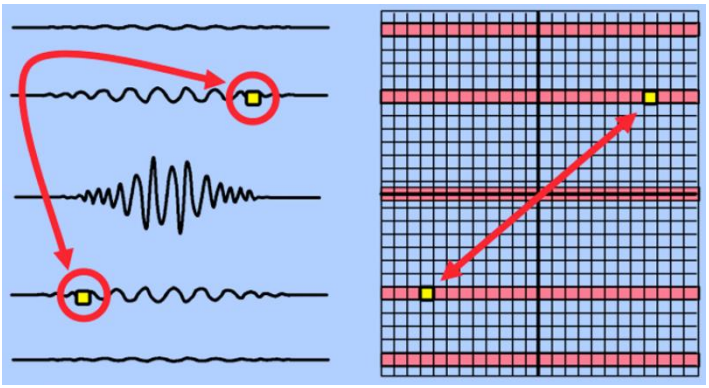

Figure 1.22. Illustration of the k-space symmetry. In this example, the yellow dots contain the same signal information, suggesting that it is possible to acquire only one of them and reconstruct the other by symmetry. Image from mri-q.com.

1.9.6 Field of view and spatial resolution

The field of view (FOV) is defined as the volume imaged. The resolution directly depends on the size of the voxel imaged. The voxel size depends on the choice of the FOV as well as on the number of k-space encoding steps, with:

$$\Delta x = \frac{FOV_{frequency}}{N_{frequency}} \quad 1.48$$

$$\Delta y = \frac{FOV_{phase1}}{N_{phase1}} \quad 1.49$$

$$\Delta z = \frac{FOV_{phase2}}{N_{phase2}} \quad 1.50$$

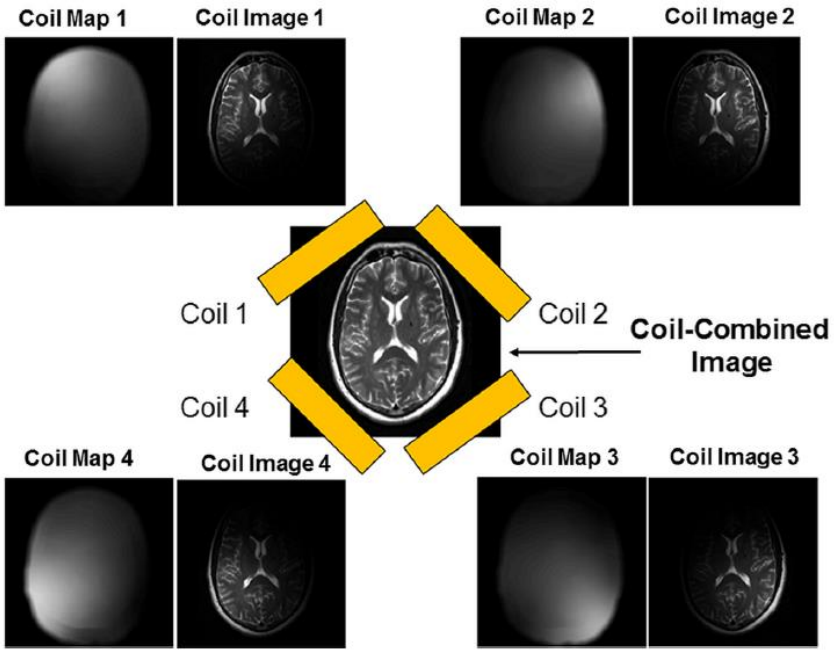

Figure 1.23. Example of the spatial sensitivity of a 4-channel coil. Image from [12].

With Δx, Δy and Δz the voxel size along the $\vec{x}$, $\vec{y}$ and $\vec{z}$ axis; $FOV_{frequency}$, FOV_{phase1} and FOV_{phase2} the size of the FOV in the frequency and phase encoding directions; and $N_{frequency}$, N_{phase1} and N_{phase2} the number of steps used to acquire the k-space in the frequency and phase encoding directions. In the case of a two dimensional MRI acquisition, Δz is equal to the thickness of the slice excited to acquire the signal. The equations 1.48-1.50 can be swapped according to the axis on which the frequency and phase encodings are performed.

As MR images are acquired in the frequency domain, the spatial encoding of the information is sensitive to aliasing. Due to the way that phase encoding is performed, the spins outside of the phase encoding FOV are dephased with an angle outside of the $0° - 360°$ range. This dephasing is then projected back in the $0° - 360°$ range during the signal measurement, leading to the generation of wrap-around artifacts (Figure 1.24). Examples of images with phase wrapping artifacts are presented in Figure 1.25.

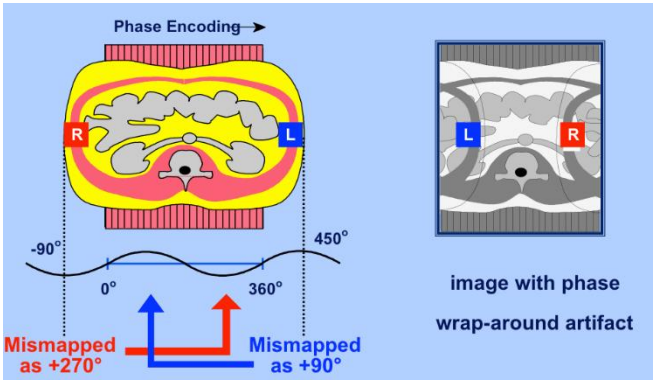

Figure 1.24. Generation of wrap-around artifacts in the phase encoding direction. The signal outside of the field of view in the phase encoding direction possess a dephasing outside of the $0° - 360°$ range (left). This signal is wrapped into the $0° - 360°$ dephasing range during the signal measurement, leading to the generation of wrap-around artifacts (right). Image from mri-q.com

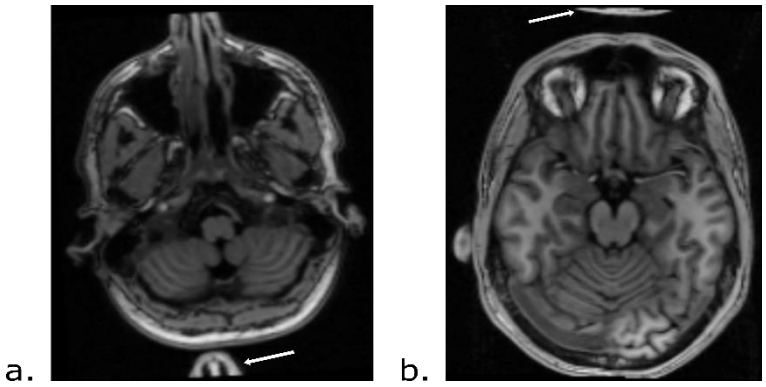

Figure 1.25. Example of wrap-around artifacts. a. The nose of the subject is wrapped at the back of his head, as highlighted by the white arrow. b. The back of the subject is wrapped in front of his eyes, as highlighted by the white arrow.

Increasing the resolution corresponds to decreasing the voxel size, allowing for a better visualization of the structures of interest. To avoid the generation of phase wrapping artifacts, the resolution is usually increased by increasing the number of frequency and phase encoding

steps, thus increasing the sequence acquisition time. It can be deduced from Basic MRI principle 3 (section 1.4) that increasing the resolution decreases the strength of the magnetization M_0 and as such, decreases the SNR. This decrease in SNR can be compensated by increasing the strength of the B_0 magnetic field, as explained in the Basic MRI principle 2 (section 1.4). Examples of T1-weighted MRI of the brain acquired with different resolution and at different magnetic fields are displayed in Figure 1.26. The increase in resolution allowed by the increase in the magnetic field is noteworthy.

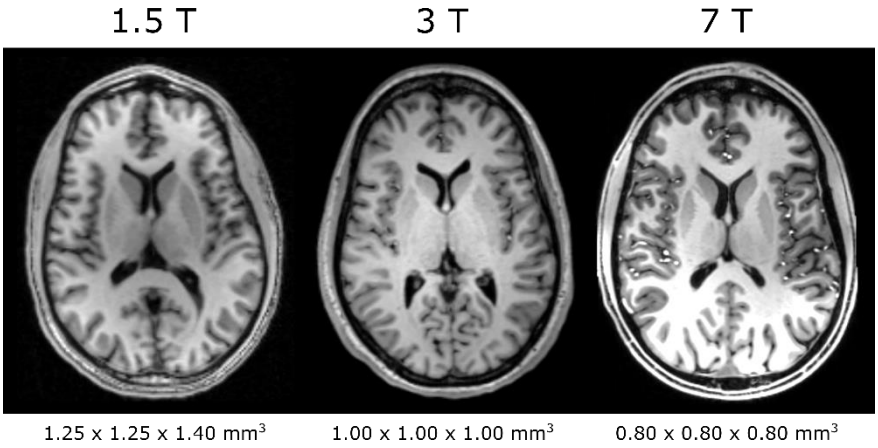

Figure 1.26. Example of T1-weighted images acquired at different resolutions and B_0 magnetic field strengths. The increase in the image resolution allows for a better visualization of brain structures. The resolution can be increased by increasing the strength of the B_0 magnetic field. However, at higher fields, new challenges related to $B1$ magnetic field inhomogeneities arise.

1.10 Magnetic field inhomogeneities

The inhomogeneities of the magnetic fields used to acquire MR images have an impact on the images obtained. Magnetic field inhomogeneities can be distinguished as: the inhomogeneities of the static B_0 magnetic field and the inhomogeneities of the radiofrequency magnetic field (transmitted and received, $B1^+$ and $B1^-$ respectively). As shown in the equations 1.15 and 1.16, the inhomogeneities of the B_0 magnetic field induce a dephasing of the hydrogen spins which changes their precession frequencies. This phenomenon can induce spatial distortion in the MR images due to frequency shifting in the k-space (see section 1.9). The change of the spins precessional frequency also changes the efficiency of the M_0 magnetization tipping towards the transversal plane when the frequency associated to the B_1 magnetic field differs from the hydrogen spins precessional frequency. This phenomenon is called off-resonance frequency.

The inhomogeneities of the transmitted magnetic field, $B1^+$, impact the M_0 magnetization tipping towards the transversal plane by generating a flip angle α that is different from the nominal flip angle. The inhomogeneities of the received magnetic field, $B1^-$, are due to the spatial sensitivity of the coil used to measure the transversal magnetization. Let us consider the signal of the gradient echo sequence (equation 1.21). In real conditions, this signal is affected by the transmitted and received bias fields as follows:

$$S_{GRE} = M_0 \, e^{-\frac{TE}{T2^*}} \, \mathrm{B1}^- \sin(B1^+\alpha) \, f_{gre} \qquad 1.51$$

With $B1^+$ the ratio between the real and the desired flip angle, $B1^-$ a coefficient corresponding to the spatial sensitivity of the received coil and f_{gre} the longitudinal magnetization measured at the center of the gradient echo k-space in the presence of B1 inhomogeneities:

$$f_{gre} = \left(\cos(B1^+\alpha)\ e^{-\frac{TR}{T1}}\right)^n + \left(1 - e^{-\frac{TR}{T1}}\right)\frac{1 - \left(\cos(B1^+\alpha)\, e^{-\frac{TR}{T1}}\right)^n}{1 - \cos(B1^+\alpha)\, e^{-\frac{TR}{T1}}} \qquad 1.52$$

The effect of the $B1^+$ and $B1^-$ inhomogeneities on T1-weighted MR imaging is shown in Figure 1.26.

1.11 References

[1] Azevedo FAC, Carvalho LRB, Grinberg LT, Farfel JM, Ferretti REL, Leite REP, et al. Equal numbers of neuronal and nonneuronal cells make the human brain an isometrically scaled-up primate brain. J Comp Neurol 2009;513:532–41. doi:10.1002/cne.21974.

[2] Brown RW, Cheng YCN, Haacke EM, Thompson MR, Venkatesan R. Magnetic Resonance Imaging. vol. 9780471720850. Chichester, UK: John Wiley & Sons Ltd; 2014. doi:10.1002/9781118633953.

[3] McRobbie DW, Moore EA, Graves MJ, Prince MR. MRI from picture to proton. Cambridge University Press; 2006. doi:10.1017/CBO9780511545405.

[4] Wright PJ, Mougin OE, Totman JJ, Peters AM, Brookes MJ, Coxon R, et al. Water proton T 1 measurements in brain tissue at 7, 3, and 1.5T using IR-EPI, IR-TSE, and MPRAGE: results and optimization. Magn Reson Mater Physics, Biol Med 2008;21:121–30. doi:10.1007/s10334-008-0104-8.

[5] Wansapura JP, Holland SK, Dunn RS, Ball WS. NMR relaxation times in the human brain at 3.0 Tesla. J Magn Reson Imaging 1999;9:531–8. doi:10.1002/(SICI)1522-2586(199904)9:4<531::AID-JMRI4>3.0.CO;2-L.

[6] Peters AM, Brookes MJ, Hoogenraad FG, Gowland PA, Francis ST, Morris PG, et al. T2* measurements in human brain at 1.5, 3 and 7 T. Magn Reson Imaging 2007;25:748–53. doi:10.1016/j.mri.2007.02.014.

[7] Paschal CB, Morris HD. K-space in the clinic. J Magn Reson Imaging 2004;19:145–59. doi:10.1002/jmri.10451.

[8] Mugler Iii JP. Optimized Three-Dimensional Fast-Spin-Echo MRI n.d. doi:10.1002/jmri.24542.

[9] Pruessmann KP, Weiger M, Scheidegger MB, Boesiger P. SENSE: Sensitivity encoding for fast MRI. Magn Reson Med 1999;42:952–62. doi:10.1002/(SICI)1522-2594(199911)42:5<952::AID-MRM16>3.0.CO;2-S.

[10] Griswold MA, Jakob PM, Heidemann RM, Nittka M, Jellus V, Wang J, et al. Generalized Autocalibrating Partially Parallel Acquisitions (GRAPPA). Magn Reson Med 2002;47:1202–10. doi:10.1002/mrm.10171.

[11] Lustig M, Donoho D, Pauly JM. Sparse MRI: The application of compressed sensing for rapid MR imaging. Magn Reson Med 2007;58:1182–95. doi:10.1002/mrm.21391.

[12] Hamilton J, Franson D, Seiberlich N. Recent advances in parallel imaging for MRI. Prog Nucl Magn Reson Spectrosc 2017;101:71–95. doi:10.1016/j.pnmrs.2017.04.002.

Chapter 2
Inversion recovery and T1 mapping

2.1 Inversion recovery principle

The inversion recovery principle is often used in brain MR imaging applications to suppress the signal of a given tissue in order to provide a better contrast between the tissues of interest. This principle is also useful to measure the T1 relaxation time of tissues. The inversion recovery consists in tipping the magnetization M_0 at $180°$, i.e. fully reversing the M_0 magnetization in the longitudinal direction (Figure 2.1). The evolution of the longitudinal magnetization after its inversion is the following:

$$M_{\parallel}(t) = M_0 \left(1 - 2\, e^{-\frac{t}{T1}}\right) \qquad 2.1$$

As shown in Figure 2.2, after the inversion of the longitudinal magnetization $M_{\parallel}$, the longitudinal magnetization of a given tissue is null at a given time t. Then, acquiring an image at this time t allows to obtain an image with a suppression of the given tissue. In brain imaging applications, the inversion recovery principle is of interest to suppress the CSF signal to better visualize the WM and GM structures.

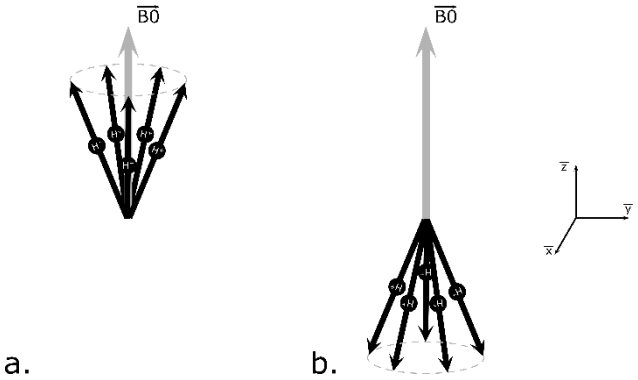

Figure 2.1. Inversion of the longitudinal magnetization M_0. The excess number of spins that generate the M_0 magnetization and that were precessing about the $\vec{z}$ axis in the direction of $\overrightarrow{B_0}$ (a) are precessing about the $\vec{z}$ axis in the opposite direction of $\overrightarrow{B_0}$ (b) after a tipping of the magnetization with a $180°$ RF pulse.

2.2 Spin echo inversion recovery

The diagram of the spin echo inversion recovery pulse sequence is presented in Figure 2.3. The spin echo inversion recovery pulse sequence consists in first inverting the longitudinal magnetization $M_{\parallel}$ with a $180°$ pulse. Then the longitudinal magnetization recovers for a time TI, defined as the inversion time, prior to acquire a spin echo pulse sequence. The definition of the echo time TE for the spin echo inversion recovery pulse sequence is the same as the one defined for the standard spin echo pulse sequence (see section 1.6.1). The repetition time

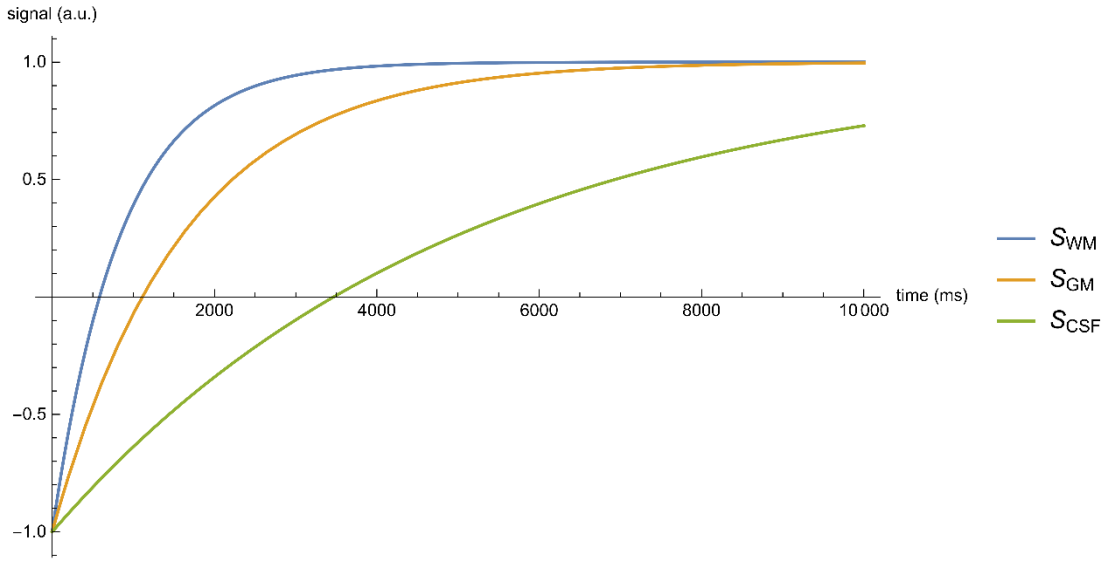

Figure 2.2. Recovery of the longitudinal magnetization $M_{\parallel}$ as a function of time after a $180°$ flip angle for WM, GM and CSF, with an original magnetization $M_0 = 1$ and with $B_0 = 3\ T$.

TR of the spin echo inversion recovery pulse sequence is defined as the time between to inversion pulses. The signal of the spin echo inversion recovery is computed as follow:

$$S_{IRSE} = M_0\, e^{-\frac{TE}{T2}} \left(1 - 2\, e^{-\frac{TI}{T1}} + e^{-\frac{TR-TE}{T1}}\right) \qquad 2.2$$

It should be noted that, in practice, more advanced spin echo pulse sequences are employed to reduce the acquisition time. The fluid attenuated inversion recovery (FLAIR) sequence is a spin echo inversion recovery sequence for which the parameters TE, TI and TR were optimized to deliver a T2-weighted contrast with a suppression of the CSF signal. This sequence is widely used in clinical practice for the detection of brain lesions. Indeed, the CSF suppression in the FLAIR sequence provides a good contrast between brain lesions and CSF, while brain lesions and CSF have a very low contrast in standard T2-weighted images. An example of FLAIR images is shown in Figure 2.4.

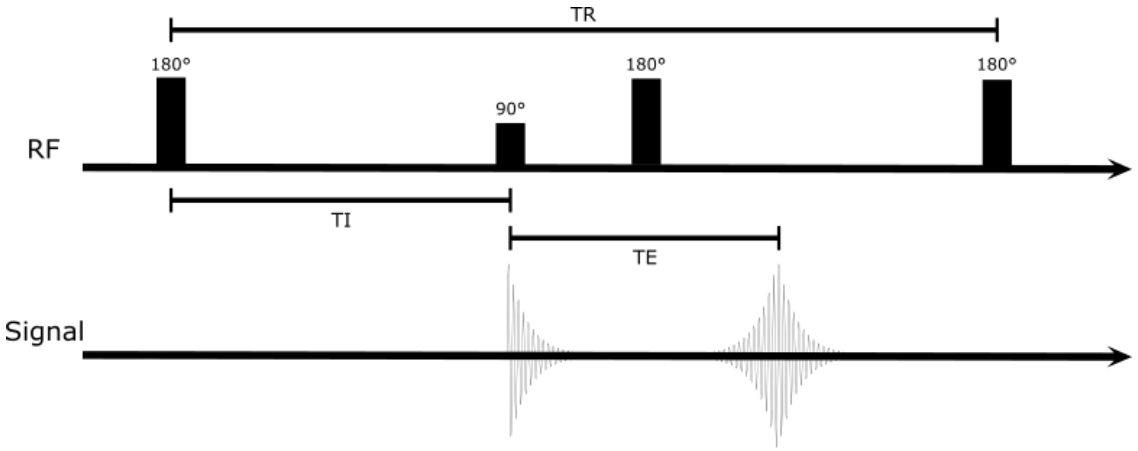

Figure 2.3. Diagram of the Spin echo inversion recovery pulse sequence.

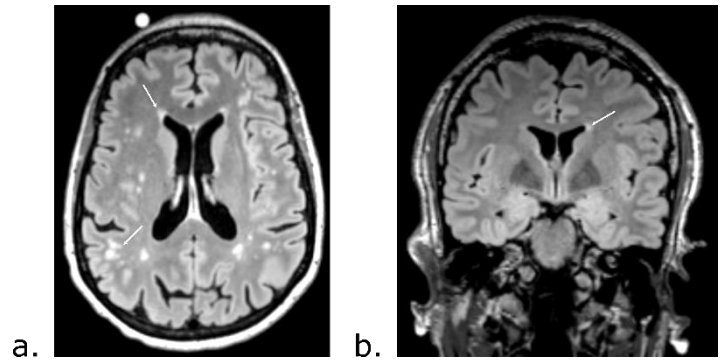

Figure 2.4. Example of axial (a) and coronal (b) FLAIR images. FLAIR images are of interest to detect brain lesions (white arrows), especially for lesions located near the ventricles since the CSF signal is suppressed.

It is possible to suppress the signal of two different tissues with spin echo inversion recovery sequences by adding a second inversion pulse prior to the acquisition of the spin echo signal. The use of this sequence, called the double inversion recovery (DIR) sequence, is limited because of its high SAR. The DIR sequence is sometimes used in brain imaging applications to provide images with a GM-specific contrast, i.e. images with a suppression of the WM and CSF signals (Figure 2.5).

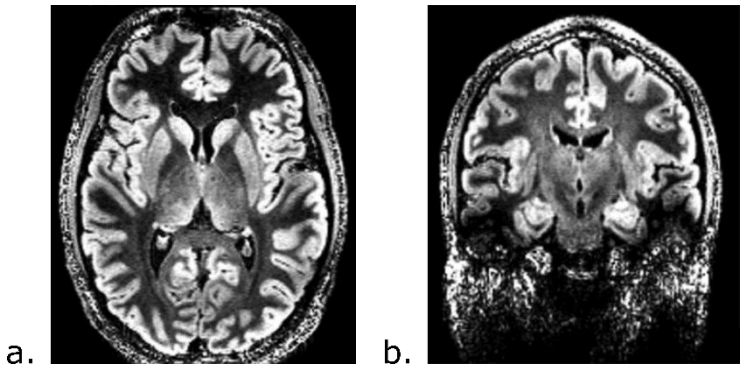

Figure 2.5. Example of axial (a) and coronal (b) DIR images. DIR images provide a GM-specific T2-weighted contrast. Images from [1].

2.3 T1 mapping with the spin echo inversion recovery sequence

T1 mapping consists in measuring the value of the T1 relaxation time for each voxel of the image. T1 mapping methods are of interest for brain imaging applications since the T1 of brain tissues changes according to certain pathologies [2,3]. In this section, we focus on the most straightforward mean of obtaining T1 maps. Let us consider a spin echo inversion recovery pulse sequence with parameters optimized so that $e^{-\frac{TE}{T2}} \cong 1$ and $e^{-\frac{TR-TE}{T1}} \cong 0$. The signal of the spin echo inversion recovery pulse sequence is then computed as:

$$S_{IRSE} \cong M_0 \left(1 - 2\, e^{-\frac{TI}{T1}}\right) \qquad 2.3$$

By acquiring multiple spin echo inversion recovery pulse sequences with varying TI and fixed TE and TR determined so that $e^{-\frac{TE}{T2}} \cong 1$ and $e^{-\frac{TR-TE}{T1}} \cong 0$, it is possible to fit the signal of the images obtained to the following equation in order to measure the T1 relaxation time:

$$S_{IRSE}(TI) = A + B\, e^{-\frac{TI}{T1}} \quad 2.4$$

With A and B coefficients used for the curve fitting. The analogy between equations 2.3 and 2.4 renders the initialization of the fitting coefficients simple, with:

$$A = S_{IRSE}(TI_L) \quad 2.5$$

$$B = -2\,A \quad 2.6$$

$$T1 = \mu T1_{brain} \quad 2.7$$

With TI_L the longest inversion time TI for which the spin echo inversion recovery pulse sequence was acquired (a long TI allows to obtain a spin echo signal with $e^{-\frac{TI}{T1}} \cong 0$) and $\mu T1_{brain}$ the average T1 relaxation time measured in brain tissues. An example of T1 curve fitting of spin echo inversion recovery signals acquired on a phantom (for further information about the phantom, please refer to section 2.9) is shown in Figure 2.6. Many acquisitions are required to obtain a good T1 curve fitting, thus leading to a long acquisition time that renders the spin echo inversion recovery T1 mapping method unusable in practice. The spin echo inversion recovery T1 mapping method is however used as a reference for validation of advanced T1 mapping techniques.

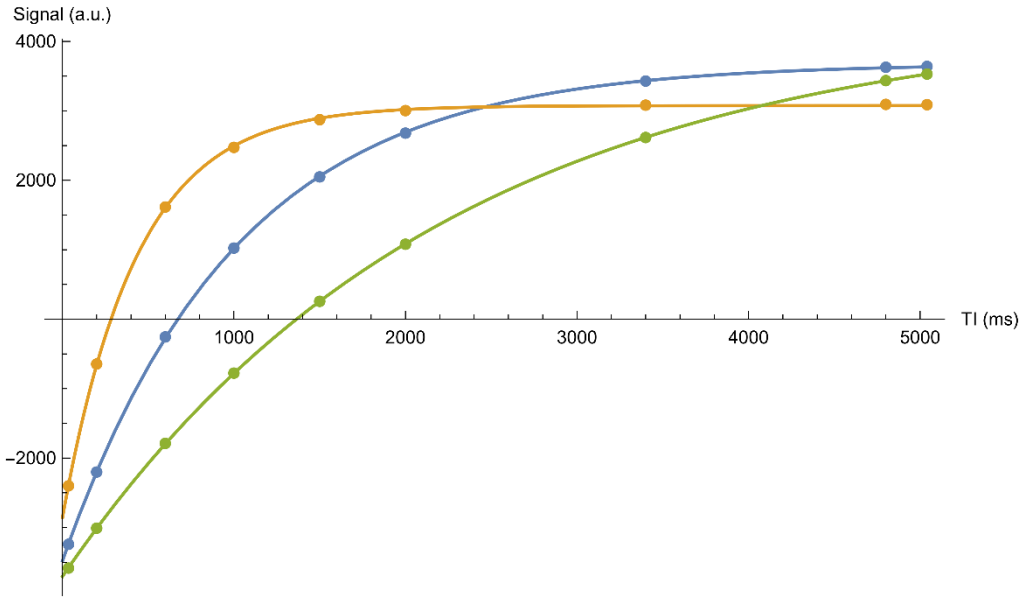

Figure 2.6. Nine spin echo recovery pulse sequences with different inversion times TI were acquired on a phantom characterized by three different relaxation times. The dots represent the average signal intensities measured in ROIs manually drawn to extract the spin echo signal from the three different relaxation times (orange, blue and green). It is clear that the signals measured follow the inversion recovery curve as a function of TI, allowing to fit equation 2.4 to measure the T1 relaxation times (continuous lines).

2.4 Gradient echo inversion recovery

The inversion recovery principle can also be applied to gradient echo pulse sequences. In practice, the sequence used to acquire gradient echo inversion recovery images is called the magnetization prepared rapid gradient echo (MPRAGE) sequence [4]. The three dimensional

MPRAGE sequence diagram is presented in Figure 2.7. First, a $180°$ inversion pulse is used to reverse the longitudinal magnetization. Then, a rapid gradient echo pulse sequence –the term rapid gradient echo designs here a gradient echo sequence with a spoiling of the transversal magnetization (see section 1.6.2)– is acquired to sample the magnetization along the first phase encoding direction. The rapid gradient echo pulse sequence starts after a delay allowing to sample the center of the k-space after a given inversion time TI. The inversion time TI is defined as the time between the inversion pulse and the sampling of the k-space center (the k-space center carries the average signal intensity of the image). After a delay TR, the MPRAGE pulse sequence is repeated to sample the k-space along the second phase encoding direction. The evolution of the MPRAGE signal is computed as follows:

$$S_{MP} = M_0 \, e^{-\frac{TE}{T2^*}} \, B1^- \sin(B1^+\alpha) \; f_{mp} \qquad 2.8$$

With α the flip angle of the gradient echo sequence, $B1^+$ and $B1^-$ the inhomogeneities of the transmitted- and received-B1 fields and f_{mp} the longitudinal magnetization measured at the center of the gradient echo k-space (the f_{mp} equation is presented in section 2.10).

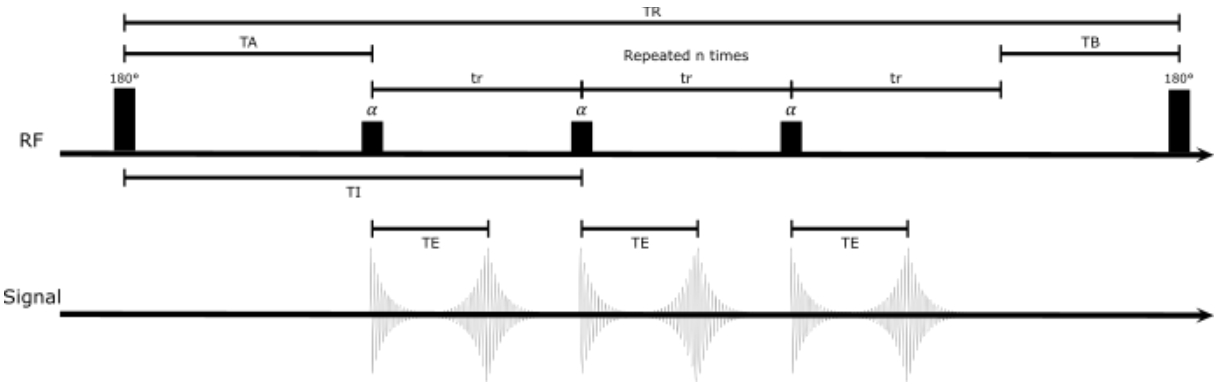

Figure 2.7. Diagram of the gradient echo inversion recovery pulse sequence.

The MPRAGE sequence is widely used in brain imaging applications to provide structural T1-weighted images of the brain with suppression of the CSF signal (Figures 2.8 and 2.9). Another optimization of the MPRAGE sequence, called the fast gray matter acquisition T1 inversion recovery (FGATIR) sequence, has been proposed to suppress the WM signal. The FGATIR sequence provides a good visualization of the deep gray matter structures for deep brain surgery (DBS) planning applications (Figures 2.10 and 2.11) [5]. Like the spin echo inversion recovery pulse sequence, the MPRAGE sequence can be used for T1 mapping by acquiring multiple MPRAGE scans with fixed α, TE, tr, TR, and varying inversion times TI [6]. The acquisition time of the MPRAGE T1 mapping method is very long. Thus, T1 mapping methods requiring less image acquisitions, such as the variable flip angle method [7,8] or the MP2RAGE method [9], are preferred in practice.

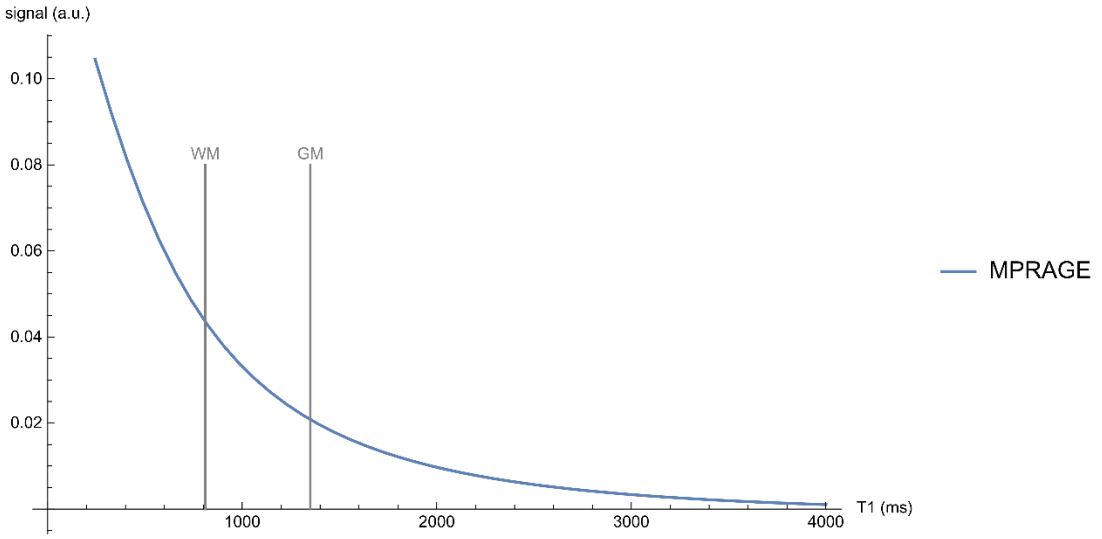

Figure 2.8. MPRAGE signal intensity optimized for CSF suppression as a function of the T1 relaxation time at 3T. The MPRAGE signal displays a high intensity for WM. The signal decreases for GM and is suppressed for CSF (T1 relaxation time around $4-5$ *sec).*

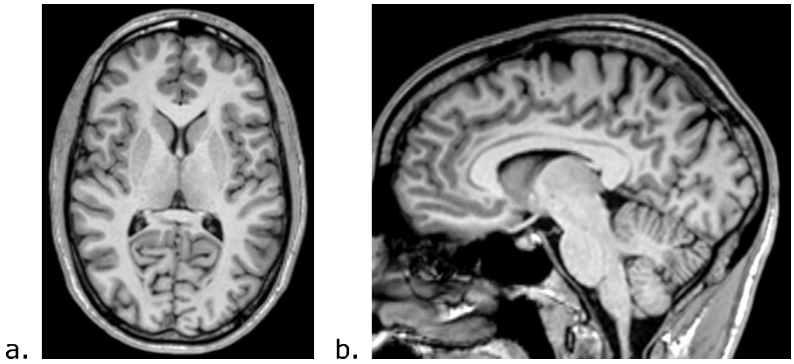

Figure 2.9. Examples of axial (a) and sagittal (b) MPRAGE images of the brain. In accordance with the signal simulation presented in Figure 2.8, the MPRAGE images are characterized by a suppression of the CSF signal. This CSF signal suppression provides a good contrast between brain tissues, allowing for the study of brain structures.

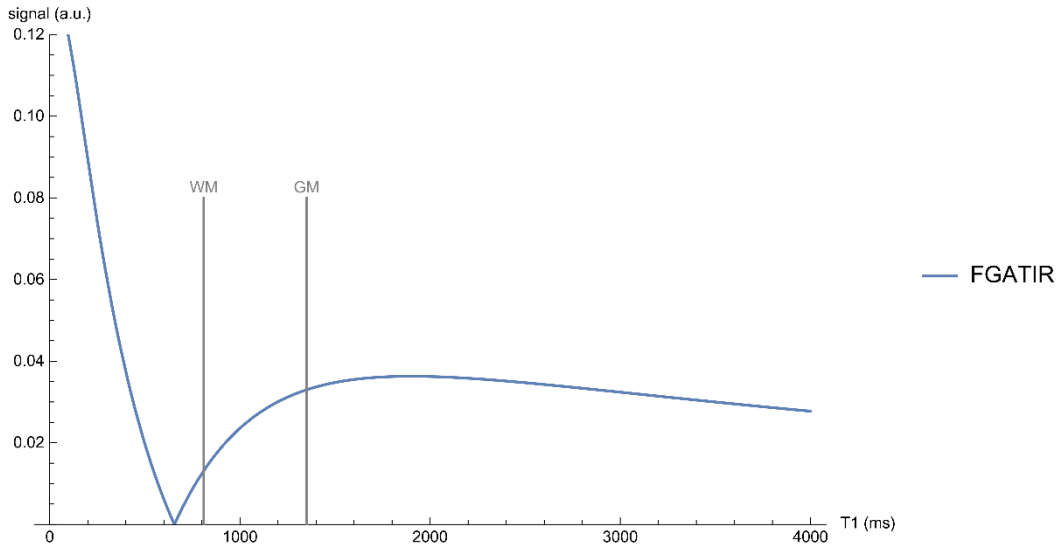

Figure 2.10. Simulation of the FGATIR signal as a function of the T1 relaxation time at 3T. The FGATIR signal is characterized by a low WM signal. The WM signal is purposely not fully suppressed to provide a good visualization of deep GM structures.

a. 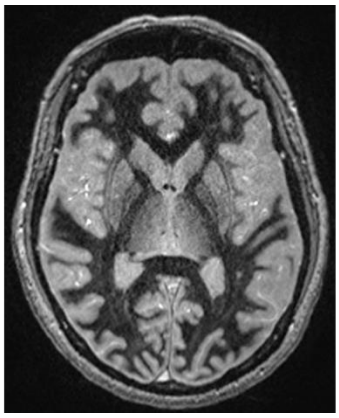 b. 

Figure 2.11. Examples of axial (a) and sagittal (b) FGATIR images. The low WM intensity allows to better visualize deep GM structures compared to the deep GM visualization provided by standard MPRAGE imaging. Image a from mriquestions.com. Image b from [10].

2.5 The MP2RAGE sequence

The inhomogeneities of the received- and transmitted-$B1$ magnetic field induce a bias in the intensity distribution of MR images (Figure 1.24). This bias increases with the strength of the B_0 magnetic field, while increasing the B_0 field strength is of interest to increase image resolution (see section 1.9.6). Although some post-processing techniques such as the N4 algorithm [11] allow to correct the effect of the $B1$ magnetic field inhomogeneities, the bias induced at ultra-high fields (7T and above) still hampers the generation of high quality MR images. To tackle this problem, Van de Moortele et al. [12] proposed to acquire two MR images in order to provide a T1-weighted contrast with a reduced sensitivity to the $B1$ magnetic field inhomogeneities. The first image is acquired with the MPRAGE sequence to provide the T1-weighted contrast. The second image is acquired with a gradient echo sequence parameterized to obtain a proton-density weighted contrast. Then, the division of the MPRAGE signal by the gradient echo signal leads to:

$$S_{ratio} = \frac{M_0\, e^{-\frac{TE_{mp}}{T2^*}} B1^- \sin\left(B1^+\alpha_{mp}\right) f_{mp}}{M_0\, e^{-\frac{TE_{gre}}{T2^*}} \mathrm{B1}^- \sin(B1^+\alpha_{gre})\, f_{gre}} \qquad 2.9$$

With α_{mp} and TE_{mp} the flip angle and echo time of the MPRAGE sequence; α_{gre} and TE_{gre} the flip angle and echo time of the proton-density-weighted gradient echo sequence; f_{mp} and f_{gre} the longitudinal magnetizations measured at the k-space center of the MPRAGE and proton-density-weighted gradient echo sequences (the f_{mp} and f_{gre} equations are respectively presented in sections 2.10 and 1.10); and $B1^+$ and $B1^-$ the transmitted- and received-$B1$ field inhomogeneities. When $TE_{mp} = TE_{gre}$, we obtain:

$$S_{ratio} = \frac{\sin\left(B1^+\alpha_{mp}\right) f_{mp}}{\sin(B1^+\alpha_{gre})\, f_{gre}} \qquad 2.10$$

Equation 2.10 shows that the division of an MPRAGE signal by a proton-density-weighted gradient echo signal provides a *ratio* signal that is independent of the proton density (the proton-density component of the signal is contained in M_0, see section 1.4), the $T2^*$ relaxation time, as well as the $B1^-$ inhomogeneities. The reduced $B1$ sensitivity provided by the division image is noteworthy when compared to the $B1$ sensitivity of the MPRAGE image (Figure 2.12),

suggesting that this method is of interest for ultra-high field imaging. The *ratio* principle introduced by Van de Moortele et al. [12] led to the creation of a new MR pulse sequence called the magnetization prepared two rapid gradient echoes (MP2RAGE) sequence.

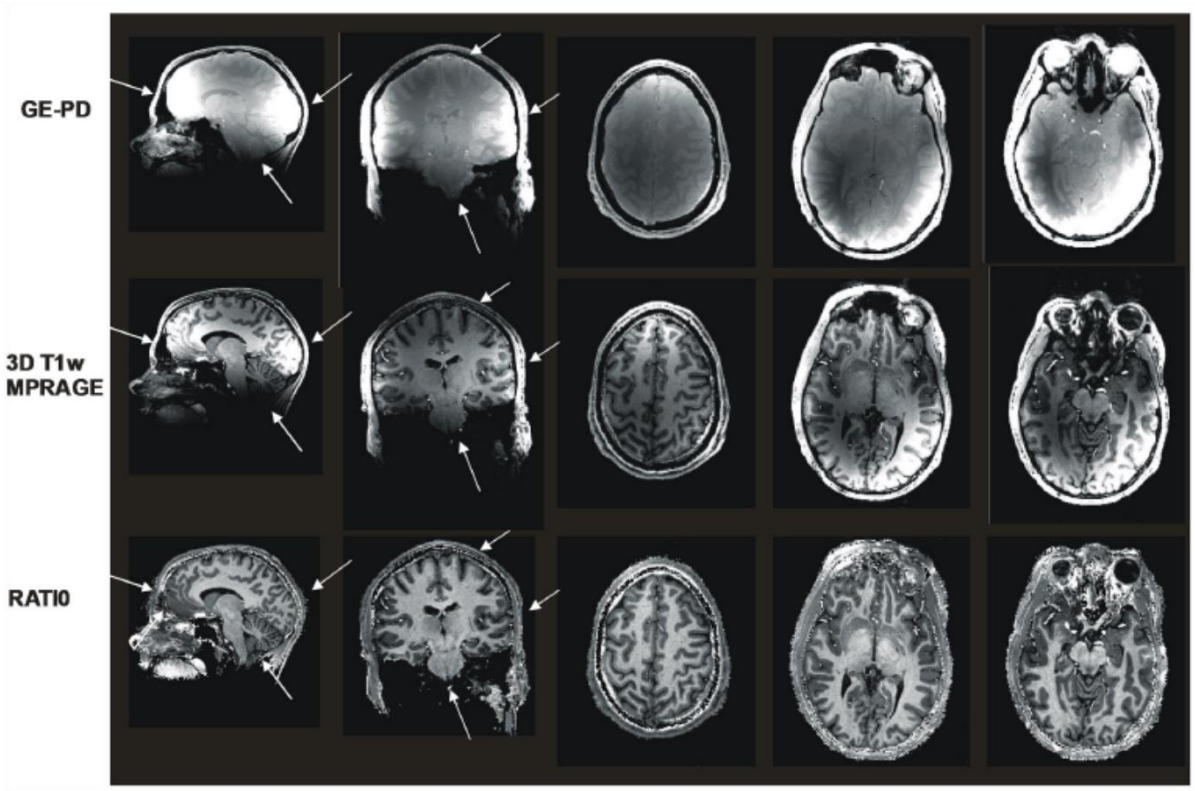

Figure 2.12. Examples of proton-density-weighted (GE-PD) and magnetization prepared rapid gradient echo (MPRAGE) images acquired at 7T. The effect of the $B1$ magnetic field inhomogeneities on the GE-PD and MPRAGE signal intensity is noteworthy, as highlighted by the white arrows. A T1-weighted image with reduced $B1$ sensitivity is obtained by dividing the MPRAGE signal by the GE-PD signal (ratio). The reduced $B1$ sensitivity of the ratio image allows to increase its visual quality, improving the structures visualization. Figure from [12].

The diagram of the MP2RAGE sequence is presented in Figure 2.13. First, a $180°$ inversion pulse is used to reverse the longitudinal magnetization. Then, two rapid gradient echo pulse sequences are acquired to sample the magnetization along the first phase encoding direction at two different inversion times TI_1 and TI_2. The inversion time TI_1 (resp. TI_2) is defined as the time between the inversion pulse and the sampling of the first (resp. second) gradient echo k-space center. After a delay TR, the MP2RAGE pulse sequence is repeated to sample the k-space along the second phase encoding direction. Since the two gradient echo images are acquired simultaneously, they are natively co-registered. The signals of the MP2RAGE sequence are computed as follows:

$$S1 = M_0\, e^{-\frac{TE}{T2^*}}\, B1^-\, \sin(B1^+\alpha_1)\; f_{mp1} \qquad 2.11$$

$$S2 = M_0\, e^{-\frac{TE}{T2^*}}\, B1^-\; \sin(B1^+\alpha_2)\; f_{mp2} \qquad 2.12$$

With TE the echo time of the gradient echoes (the two gradient echoes are acquired with the same echo time), α_1 and α_2 the flip angles of the first and second gradient echoes, and f_{mp1} and f_{mp2} the longitudinal magnetization measured during the acquisition of the k-space

center of the first and second gradient echoes, respectively (the f_{mp1} and f_{mp2} equations are presented in section 2.10).

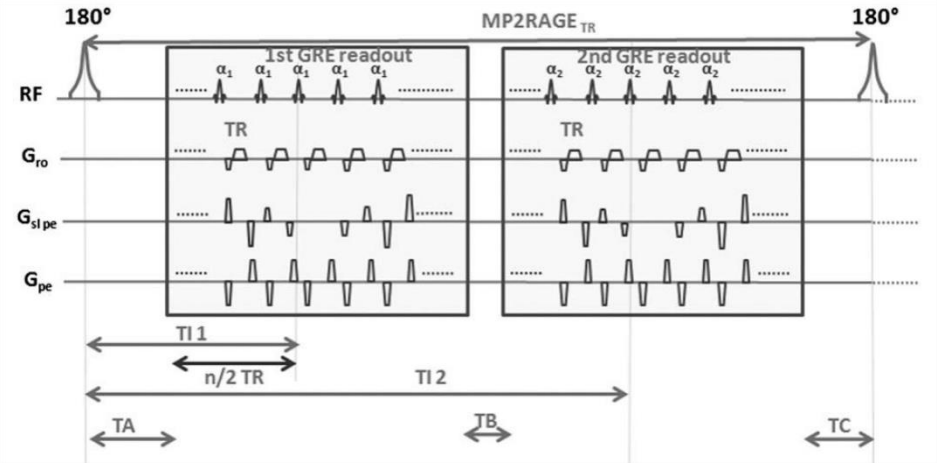

Figure 2.13. Diagram of the MP2RAGE sequence. Figure from [9].

The MP2RAGE sequence parameters can be setup to acquire a T1-weighted contrast with CSF signal suppression in the first gradient echo and a proton-density weighted contrast in the second gradient echo, allowing to use the method introduced by Van de Moortele et al. [12] to obtain T1-weighted images with a reduced $B1$ sensitivity. Marques et al. [9] proposed a new combination of the MP2RAGE signals:

$$S_{uni} = \frac{Real(S1_C^* \, S2_C)}{\|S1_C\|^2 + \|S2_C\|^2} \qquad 2.13$$

With $S1_C$ and $S2_C$ the complex signals of the first and second gradient echoes and $*$ the complex conjugate operator. The gradient echoes complex signals are defined so that the $\vec{x}$ component of the transversal magnetization $M_\perp$ corresponds to the real part of the signal while the $\vec{y}$ component of the transversal magnetization $M_\perp$ corresponds to its imaginary part (Figure 2.14). Let us consider that the imaginary part of the transversal magnetization $M_\perp$ is null, we obtain:

$$S_{uni} = \frac{S1 \, S2}{S1^2 + S2^2} \qquad 2.14$$

$$S_{uni} = \frac{\sin(B1^+\alpha_1) \; f_{mp1} \times \sin(B1^+\alpha_2) \, f_{mp2}}{\left(\sin(B1^+\alpha_1) \; f_{mp1}\right)^2 + \left(\sin(B1^+\alpha_2) \, f_{mp2}\right)^2} \qquad 2.15$$

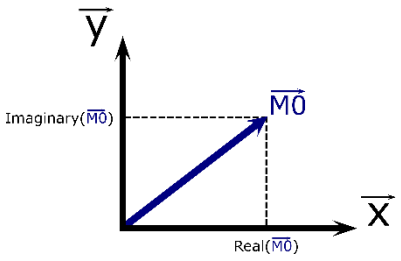

Figure 2.14. Real and imaginary parts of the M_0 magnetization tipped in the transversal plane.

Equation 2.15 indicates that, like the *ratio* signal, the *uni* signal is independent of the proton-density, the $T2^*$ relaxation time and the received bias field $B1^-$. By optimizing the MP2RAGE sequence parameters, the *uni* signal can provide a T1-weighted contrast, as shown in Figure 2.15. It can be deduced from equation 2.16 that the *uni* signal takes its values in the $[-0.5; 0.5]$ range, except when the $S1_C$ and $S2_C$ signals magnitudes are equal to 0, i.e. except when no signal is measured. This leads to the generation of a salt and pepper noise in the background (Figure 2.15c). O 'brien et al. proposed a new combination of the gradient echo signals to remove the background noise [13]:

$$S_{uni-den} = \frac{Real(S1_C^* \, S2_C) - \beta}{\|S1_C\|^2 + \|S2_C\|^2 + 2\beta} \qquad 2.16$$

With β a denoising parameter determined empirically to remove the background noise without impacting the signal of the brain structures. An example of denoised *uni* image is presented in Figure 2.15d. Since the SNR provided by the *uni* signal is higher than the SNR provided by the *ratio* signal [9], the MP2RAGE sequence acquired in practice is optimized to provide a T1-weighted contrast from the *uni* signal instead of the *ratio* signal.

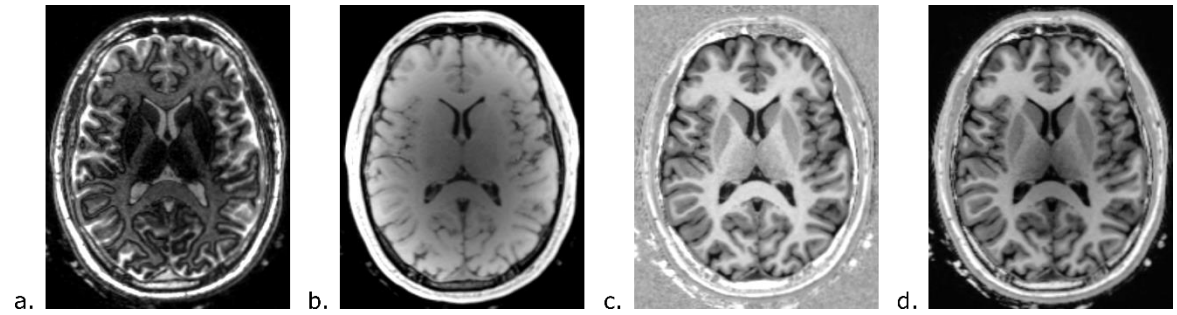

Figure 2.15. Example of MP2RAGE images acquired at 3T. a. first MP2RAGE gradient echo image (MP2RAGE1); b. second MP2RAGE gradient echo image (MP2RAGE2); c. MP2RAGE-uni; d. MP2RAGE-uni-den. MP2RAGE1 and MP2RAGE2 have a limited clinical interest. However, their image combination leads to a T1-weighted contrast with reduced $B1$ sensitivity in MP2RAGE-uni. The denoising of the uni signal is noteworthy when comparing MP2RAGE-uni with MP2RAGE-uni-den.

2.6 $B1^+$ mapping with the SA2RAGE sequence

The saturation prepared with two rapid gradient echoes acquisition (SA2RAGE) sequence is an MRI sequence allowing for $B1^+$ inhomogeneities mapping. The diagram of the SA2RAGE sequence is presented in Figure 2.16. First, a $90°$ saturation pulse is used to suppress the longitudinal magnetization $M_{\parallel}$. Following the $90°$ pulse, a spoiled gradient is applied to suppress the transversal magnetization $M_{\perp}$. Then, two rapid gradient echo pulse sequences are acquired to sample the magnetization along the first phase encoding direction at two different delay times $TD1$ and $TD2$. The delay times $TD1$ and $TD2$ are defined as the time between the saturation pulse and the sampling of the first and second gradient echo k-space center, respectively. After a delay TR, the SA2RAGE pulse sequence is repeated to sample the k-space in the second phase encoding direction. The two gradient echo images acquired are naturally co-registered and their signals can be computed as follows:

$$S_{SA1} = M_0 \, e^{-\frac{TE}{T2^*}} \, B1^- \sin(B1^+ \alpha_1) \; f_{sa1} \qquad 2.17$$

$$S_{SA2} = M_0 \, e^{-\frac{TE}{T2^*}} \, B1^- \, \sin(B1^+\alpha_2) \, f_{sa2} \qquad 2.18$$

With TE the echo time of the gradient echoes (the two gradient echoes are acquired with the same echo time), α_1 and α_2 the flip angles of the first and second gradient echoes, and f_{sa1} and f_{sa2} the longitudinal magnetization measured at the k-space center acquisition of the first and second gradient echoes, respectively (the f_{sa1} and f_{sa2} equations are presented in section 2.10).

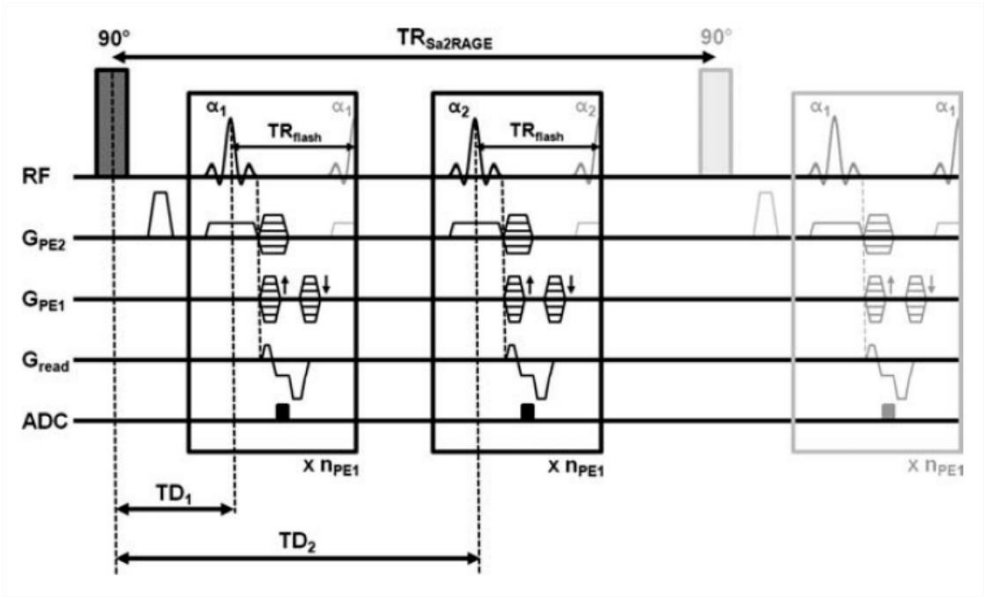

Figure 2.16. Diagram of the SA2RAGE sequence. Figure from [14].

Similarly to the MP2RAGE sequence, the ratio of the SA2RAGE gradient echoes leads to a signal that is independent from the proton-density, the $T2^*$ relaxation time and the received bias field $B1^-$:

$$SA2RAGE_{ratio} = \frac{\sin(B1^+\alpha_1) \, f_{sa1}}{\sin(B1^+\alpha_2) \, f_{sa2}} \qquad 2.19$$

By optimizing the SA2RAGE sequence parameters so that the delay time of the first gradient echo $TD1$ is very short and the delay time of the second gradient echo $TD2$ is very long, it is possible to greatly reduce the T1-weighting of the SA2RAGE signals. This provides an SA2RAGE ratio that is only sensitive to $B1^+$ inhomogeneities, allowing for the generation of $B1^+$ maps by building lookup tables of the $SA2RAGE_{ratio}$ signal as a function of the SA2RAGE sequence parameters (Figure 2.17). Since the $B1^+$ inhomogeneities are varying slowly according to their spatial location, the SA2RAGE sequence is usually acquired at very low resolution (about 4 mm isotropic) to reduce its acquisition time and SAR. Examples of SA2RAGE images and $B1^+$ maps are presented in Figure 2.18.

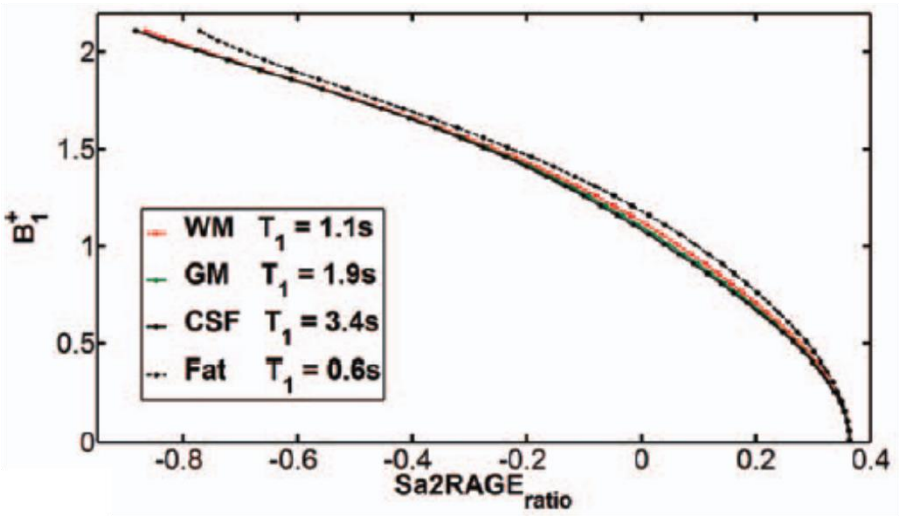

Figure 2.17. $B1^+$ *inhomogeneities measured by the SA2RAGE sequence as a function of the* $SA2RAGE_{ratio}$ *signal for different tissues (WM, GM, CSF and Fat). The* $SA2RAGE_{ratio}$ *signal is characterized by a reduced sensitivity to the* $T1$ *relaxation times of brain tissues. The* $B1^+$ *inhomogeneities values are reported in percent of the nominal flip angles. Figure from* [14].

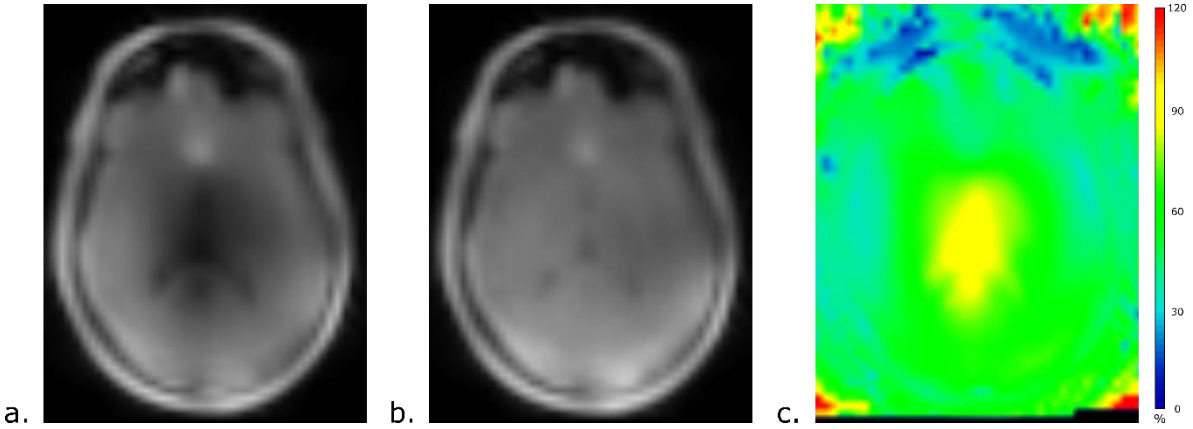

Figure 2.18. Example of images obtained with the SA2RAGE sequence. a. first gradient echo image; b. second gradient echo image; c. $B1^+$ *map in percent of the nominal flip angle.*

2.7 T1 mapping with the MP2RAGE sequence

According to equation 2.15, the *MP2RAGE-uni* signal depends only on the T1 relaxation times, the $B1^+$ inhomogeneities and the MP2RAGE sequence parameters. Marques et al. [9] showed that the T1 relaxation times can be measured by building a lookup table of the *uni* signal (Figure 2.19) when the effect of the $B1^+$ inhomogeneities on the *uni* signal is neglected. In practice, the $B1^+$ is varying by up to $\pm$ 20 % and $\pm$ 40 % of the nominal flip angle at 3T and 7T, respectively [9]. This variation of the $B1^+$ field introduces T1 mapping errors (Figure 2.20). Thus, the MP2RAGE sequence parameters have to be optimized to provide a T1-weighted contrast in the *uni* image, while ensuring that the *uni* signal is characterized by a reduced sensitivity to the $B1^+$ inhomogeneities. Marques et al. assessed the sensitivity of the *uni* signal to $B1^+$ inhomogeneities as a function of the MP2RAGE sequence parameters and reported that the *uni* $B1^+$ sensitivity increases when the flip angles increase and when the number of gradient echo excitations n increases [9,15]. The outcomes of the *uni* signal properties in terms of $B1^+$ sensitivity are twofold: 1) the SNR of the MP2RAGE signals is limited by the use

of low flip angles to obtain a low $B1^+$ sensitivity; 2) the number of gradient echo excitations is limited to ensure a reduced $B1^+$ sensitivity, thus limiting the image resolution to avoid the generation of wrap-around artifacts (see section 1.9.6). Therefore, the MP2RAGE sequence parameters must be chosen to reach a compromise between 1) SNR and resolution maximization and 2) $B1^+$ sensitivity minimization.

Different MP2RAGE optimizations were proposed by Marques et al. at 7T [15]. First, an MP2RAGE optimization was proposed to obtain a *uni* signal characterized by a reduced $B1^+$ sensitivity (Figure 2.20b). This MP2RAGE sequence is characterized by a low CNR and a low resolution compared to other 7T sequences because of its low flip angles and its low number of excitations n. A second optimization was proposed to acquire MP2RAGE signals with a higher CNR and resolution. This high resolution MP2RAGE sequence is characterized by a high $B1^+$ sensitivity (Figure 2.20c). The parameters corresponding to these two different MP2RAGE optimizations are presented in Table 2.1. Examples of images acquired with these two different optimizations are presented in Figure 2.21.

Marques et al. proposed a method to correct the $B1^+$ inhomogeneities of the *MP2RAGE-uni* signal to reduce the $B1^+$ sensitivity of the MP2RAGE T1 mapping [15]. This method consists in acquiring a $B1^+$ map with the SA2RAGE sequence and a T1 map with the MP2RAGE sequence. After registering the SA2RAGE data on the MP2RAGE data, it is possible to correct the MP2RAGE T1 mapping by building two dimensional lookup tables that map the *SA2RAGE-ratio* and the *MP2RAGE-uni* signals to the T1 relaxation times and $B1^+$ inhomogeneities (Figure 2.22). First, the $B1^+$ map provided by the SA2RAGE sequence is corrected for the change in T1 relaxation times. Then, the T1 map provided by the MP2RAGE sequence is corrected for the change in $B1^+$ inhomogeneities. After a few iterations, the variation in the T1 relaxation times and $B1^+$ inhomogeneities is lower than 10^{-3}, allowing to provide $B1^+$-corrected T1 maps and T1-corrected $B1^+$ maps [15]. The convergence of the T1 maps and $B1^+$ maps correction method is due to the very low T1 sensitivity of the *SA2RAGE-ratio* signal (Figure 2.22b). This $B1^+$ correction method allows for the acquisition of high resolution T1 maps with the MP2RAGE sequence at 7T [15]. However, MP2RAGE protocols with reduced $B1^+$ sensitivities are preferred to increase the robustness of multi-center studies [16]. Examples of T1 maps acquired with the MP2RAGE sequence are presented in Figure 2.23.

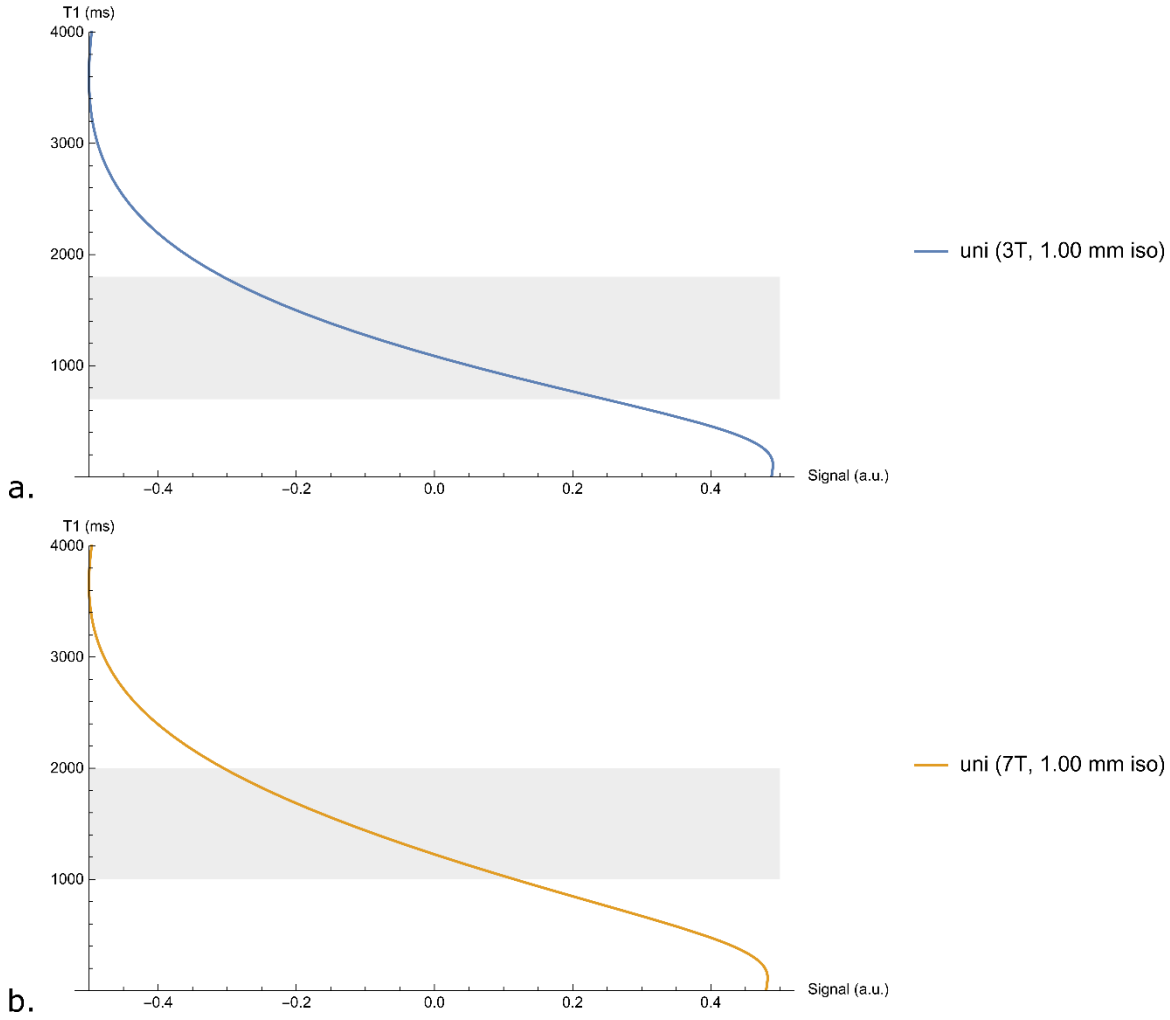

Figure 2.19. T1 relaxation times measured with the MP2RAGE sequence as a function of the uni signal intensity for a 3T MP2RAGE protocol (a) and a 7T MP2RAGE protocol (b) when $B1^+$ inhomogeneities are neglected. The gray zone represents the T1 relaxation times of the WM and GM tissues.

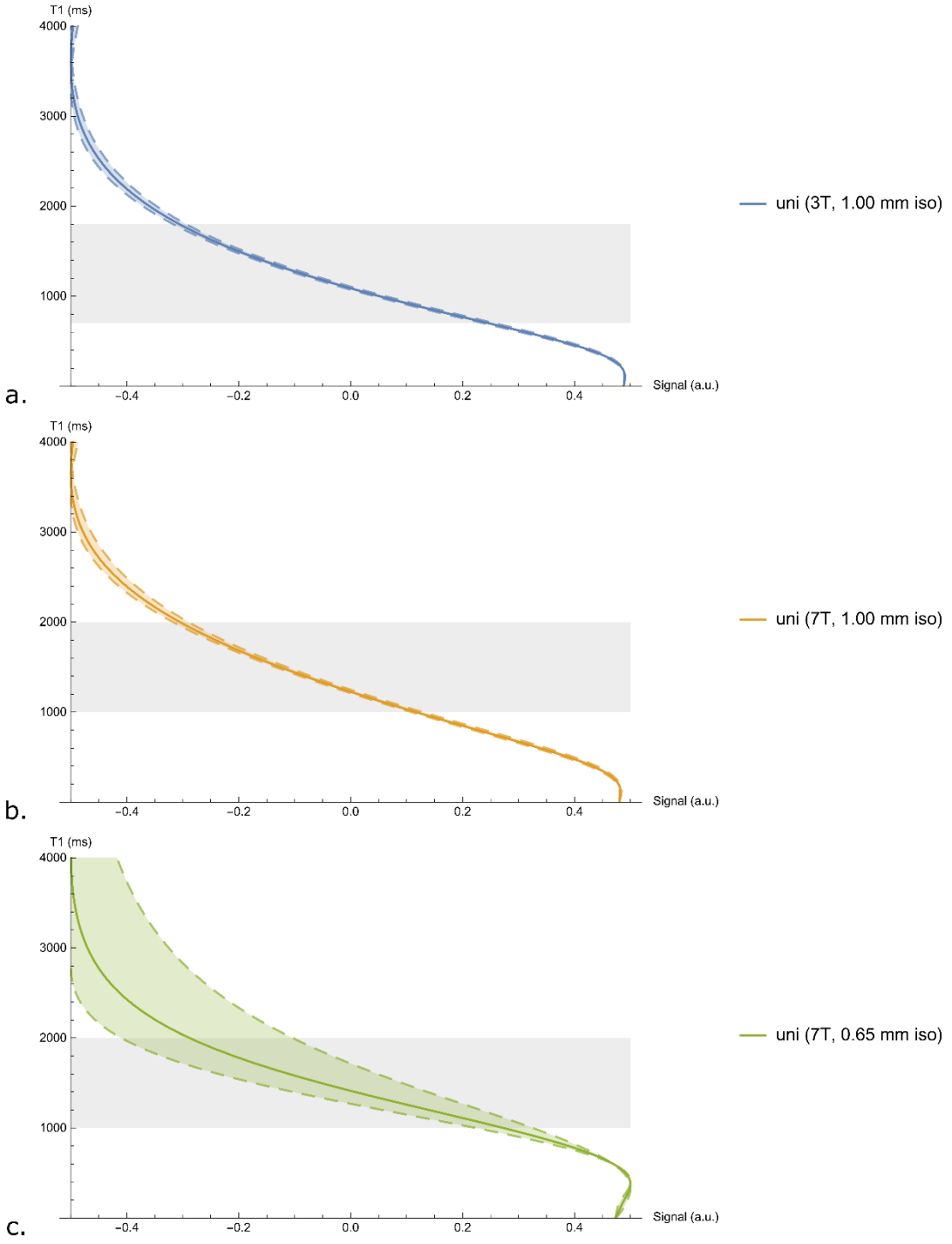

Figure 2.20. Effect of the $B1^+$ magnetic field inhomogeneities on the MP2RAGE-uni signal at 3T (a) and 7T (b,c). The plain lines represent the MP2RAGE-uni signal in the absence of $B1^+$ inhomogeneities. The dashed lines represent the MP2RAGE-uni signals affected by $\pm 20\%$ $B1^+$ inhomogeneities at 3T (a) and $\pm 40\%$ $B1^+$ inhomogeneities at 7T (b,c). The gray zone represents the T1 relaxation times of the WM and GM tissues. The MP2RAGE parameters proposed by Marques et al. [9] *at 3T provide an MP2RAGE-uni signal characterized by a reduced $B1^+$ sensitivity, allowing for T1 mapping with the MP2RAGE sequence. Different optimizations were proposed by Marques et al. for 7T imaging* [15]*. A low resolution and low contrast optimization was proposed to obtain an MP2RAGE-uni signal characterized by a reduced $B1^+$ sensitivity (b). An optimization that is highly sensitive to $B1^+$ inhomogeneities was proposed to obtain high resolution and high contrast MP2RAGE-uni images (c).*

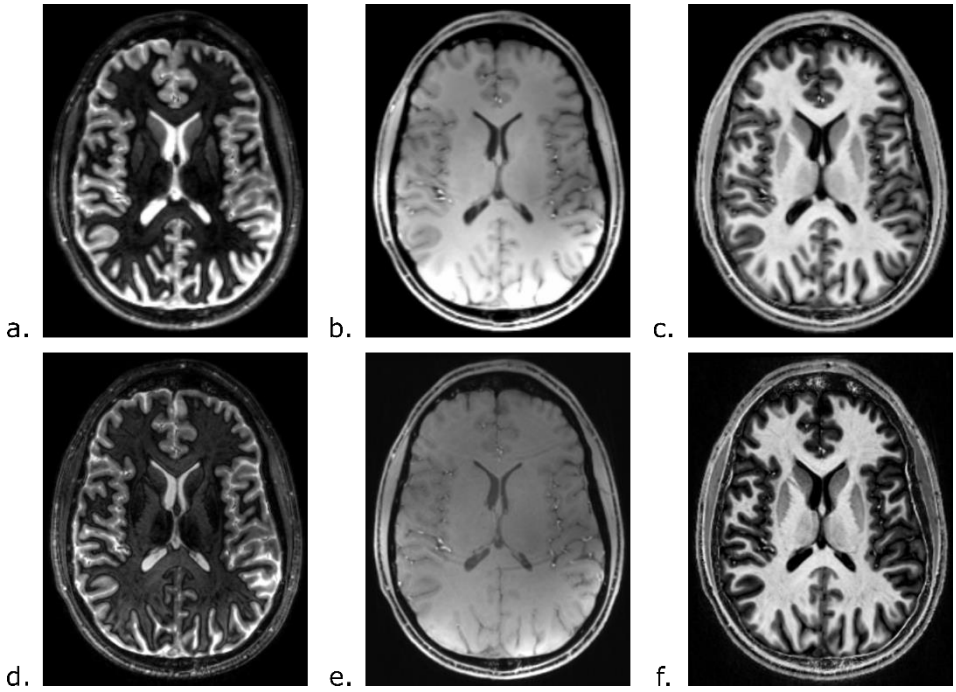

Figure 2.21. Examples of MP2RAGE images acquired at 7T. Images a, b and c were acquired with the MP2RAGE protocol proposed for reduced $B1^+$ sensitivity, while images d, e and f were acquired with the high resolution MP2RAGE protocol [15]*. a,d: first gradient echo images; b,e: second gradient echo images; c,f: uni images. By comparing image c with image f, it is clear that the MP2RAGE-uni image of the high resolution protocol (f) is characterized by a higher contrast and resolution than the MP2RAGE-uni image of the reduced $B1^+$ sensitivity protocol (c).*

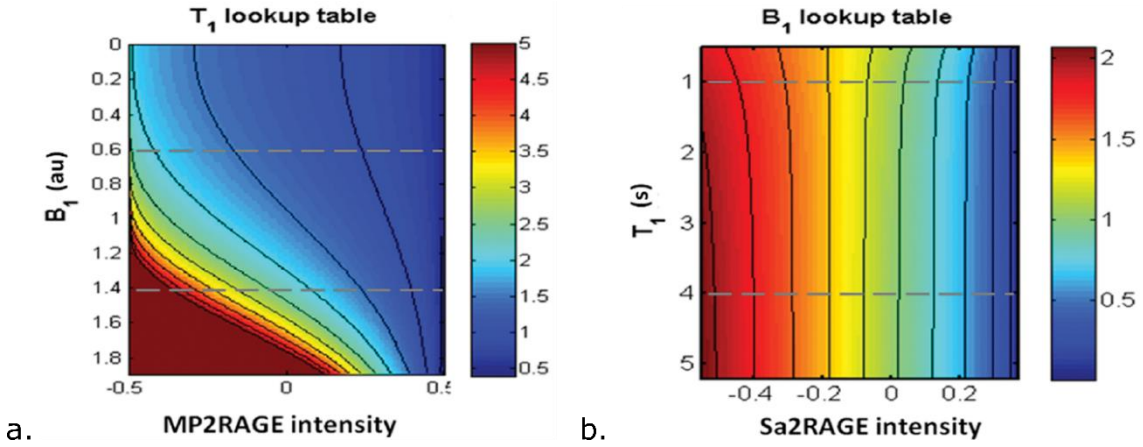

Figure 2.22. Lookup table of the MP2RAGE-uni (a) and SA2RAGE-ratio signal intensities as a function of the T1 relaxation times and $B1^+$ inhomogeneities in percent of the nominal flip angles.

Table 2.1. Parameters used to acquire the MP2RAGE sequence at 3T [9] *and the reduced $B1^+$ and high resolution MP2RAGE sequences at 7T* [15].

Sequence	MP2RAGE 3T	Reduced $B1^+$ MP2RAGE 7T	High resolution MP2RAGE 7T
TR/TE ($msec$)	$5000/2.96$	$6000/2.16$	$6000/2.30$
TI ($msec$)	$701/2500$	$800/2700$	$800/2700$
Flip angles	$4°/5°$	$3°/4°$	$7°/5°$
Matrix	256×240	240×240	320×320
Slices	192	160	256
Number of GRE excitations	144	120	192
Resolution (mm^3)	$1.0 \times 1.0 \times 1.0$	$1.0 \times 1.0 \times 1.0$	$0.65 \times 0.65 \times 0.65$
BW (Hz/px)	240	300	300
Orientation	$Sagittal$	$Sagittal$	$Sagittal$
FOV (mm^2)	256×240	240×240	208×208
$GRAPPA$	3	3	3
Slice partial Fourier	$6/8$	$6/8$	$6/8$
Phase partial Fourier	$None$	$None$	$6/8$
Scan time ($min: sec$)	$8: 20$	$10: 02$	$10: 08$

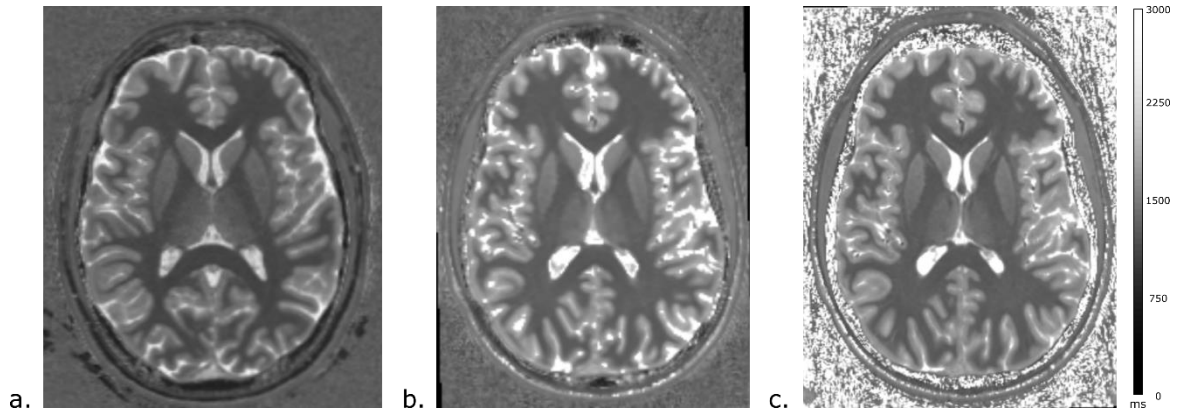

Figure 2.23. Examples of T1 maps obtained with the MP2RAGE sequence at 3T (a) and 7T (b,c). The 7T T1 maps were acquired with protocols optimized for reduced $B1^+$ sensitivity (b) and high resolution (c). MR images were acquired at 3T at the Herston imaging Research Facility (HIRF) and at 7T at the Centre for Advanced Imaging (CAI), Brisbane, Australia.

2.8 FLAWS: the Queen of the T1-weighted sequences

As shown in Figures 2.15a and 2.15b, the gradient echo images acquired by the MP2RAGE sequence (MP2RAGE1 and MP2RAGE2, see Figure 2.15a and 2.15b) do not provide good qualitative information about the brain structures. Therefore, their interest for clinical imaging is limited. Tanner et al. proposed a new optimization of the MP2RAGE sequence to provide gradient echo images with a high clinical interest [10]. This new optimization of the MP2RAGE sequence is called the fluid and white matter suppression (FLAWS) sequence. It consists in optimizing the MP2RAGE sequence to obtain a contrast similar to the FGATIR contrast in the first gradient echo image (FLAWS1) and a contrast similar to the MPRAGE contrast in the second gradient echo image (FLAWS2). The FLAWS sequence optimization was performed by fine tuning the sequence parameters with signal simulations to obtain theoretical FLAWS1 and FLAWS2 signals that are closed to the FGATIR and MPRAGE signals (Figure 2.24). Examples of FLAWS images are shown in Figure 2.25. The FLAWS contrasts provide co-registered images with a good visualization of the deep GM structures in FLAWS1 (Figure 2.25a) and a standard anatomical T1-weighted contrast in FLAWS2 (Figure 2.25b). Tanner et al proposed to compute the minimum of the FLAWS signals to obtain a GM-specific signal:

$$S_{min} = \min(S1, S2) \qquad 2.20$$

The GM-specific contrast provided in the *FLAWS-min* image is similar to the DIR contrast (Figure 2.25c) [1]. The FLAWS1, FLAWS2 and GM-specific images provided by the FLAWS sequence are of interest for a wide range of clinical applications, including deep brain stimulation (DBS) surgery planning [17] and brain lesion detection [18]. However, the FLAWS sequence optimization does not provide a *uni* image characterized by a T1-weighted contrast (Figures 2.26 and 2.27), and as such, does not provide T1 maps of the brain tissues.

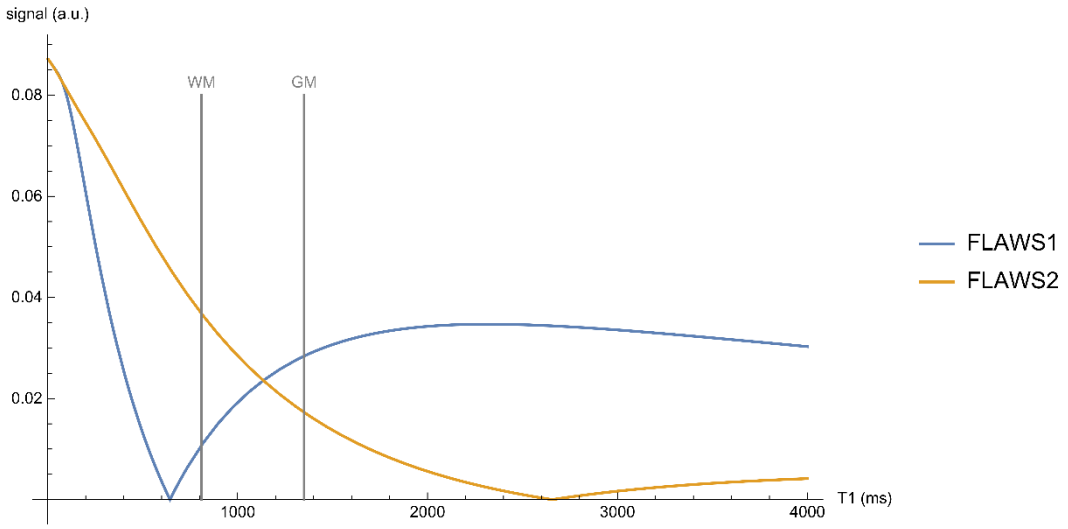

Figure 2.24. FLAWS1 and FLAWS2 signals intensities as a function of the T1 relaxation time at 3T. The FLAWS1 signal displays a contrast similar to the FGATIR contrast (Figure 2.10), with a low WM intensity. Like the FGATIR signal, the FLAWS1 signal does not provide a perfect WM suppression to allow for a good visualization of deep GM structures. The FLAWS2 signal provides a contrast similar to the MPRAGE contrast (Figure 2.8), with a high WM signal intensity and a suppression of the CSF signal (T1 relaxation time around $4 - 5$ *sec).*

The work presented in this thesis focuses on the FLAWS sequence. At the beginning of this thesis, FLAWS sequence parameters were only provided for 3T imaging. We then developed an optimization method based on numerical simulations with the Bloch equations to provide

FLAWS sequence parameters at 1.5T (see Chapter 4) and 7T (see Chapter 5). The 3T FLAWS sequence was also re-optimized with the method presented in Chapter 4 to provide sequence parameters allowing imaging with an increased FOV in the sagittal direction. The FLAWS sequence parameters proposed at 3T by Tanner et al. and the FLAWS sequence parameters proposed at 1.5T, 3T and 7T in the current thesis are presented in Table 2.2. The work presented in this thesis also proposes a new combination of the FLAWS signals to provide a T1-weighted signal that is independent to the proton density, the $T2^*$ relaxation time and the $B1^-$ inhomogeneities (see Chapters 3-5). This new FLAWS signal, named *FLAWS-hc*, allows to measure the T1 relaxation times in a similar way as the *uni* signal allows T1 mapping with the MP2RAGE sequence (see Chapter 5).

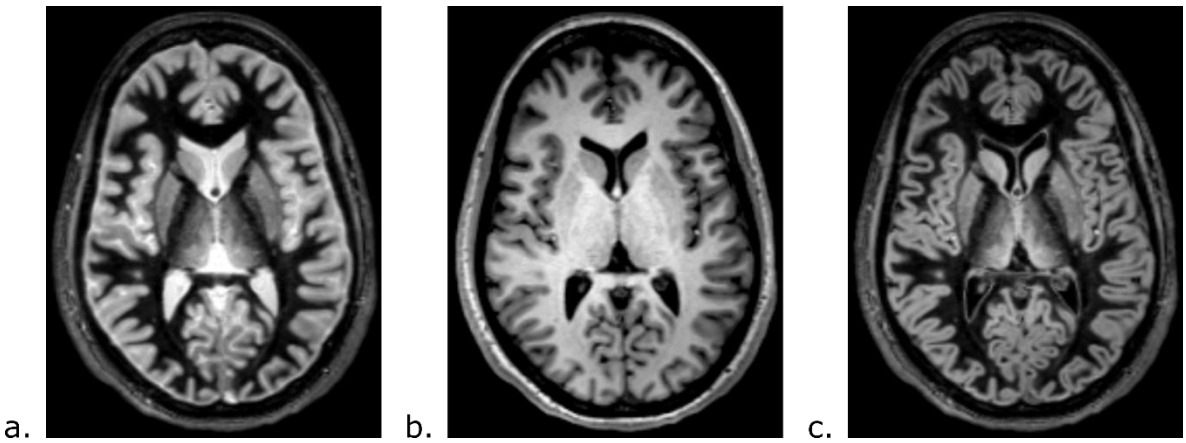

Figure 2.25. Example of FLAWS images acquired at 3T. The first gradient echo image, FLAWS1, provides WM-suppressed contrast (a) similar to the FGATIR contrast. The second gradient echo image, FLAWS2, provides a CSF-suppressed contrast (b) similar to the MPRAGE contrast. The minimum of the two gradient echo images, FLAWS-min, provides a GM specific contrasts (c) similar to the DIR contrast.

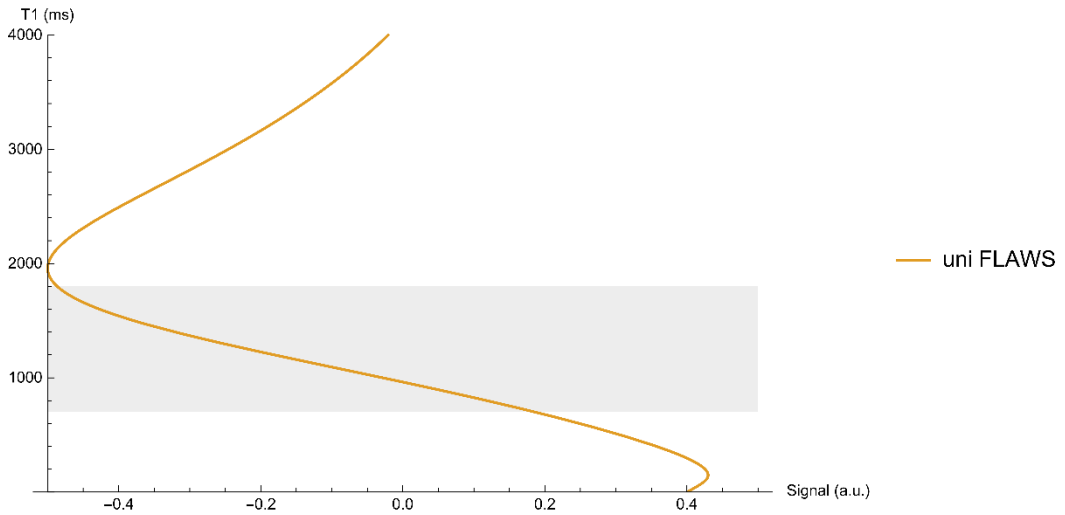

Figure 2.26. Lookup table of the T1 relaxation time as a function of the FLAWS-uni signal at 3T. Since one FLAWS-uni intensity corresponds to two different T1 relaxation times, the FLAWS-uni signal cannot provide T1 maps. The gray zone represents the T1 relaxation times of the WM and GM tissues.

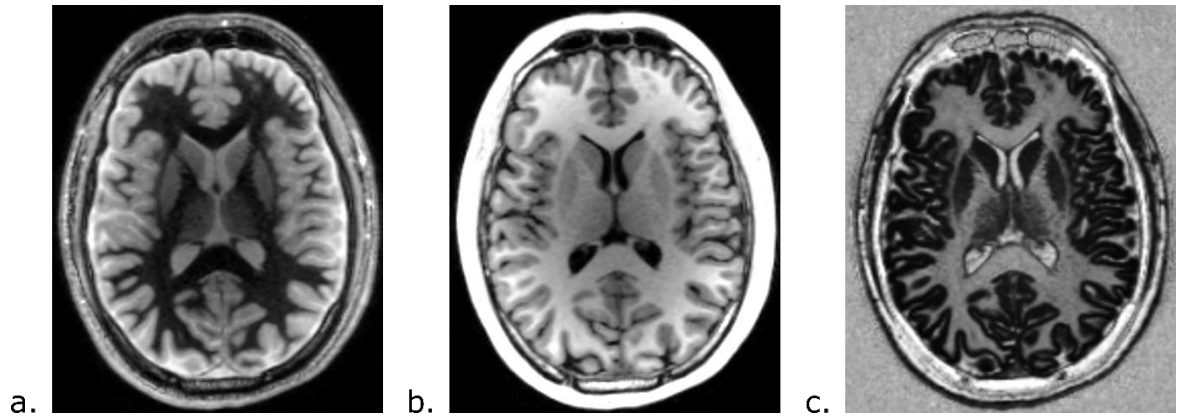

Figure 2.27. Example of FLAWS1 (a), FLAWS2 (b) and FLAWS-uni (c) images acquired at 3T. As seen in image c, the FLAWS-uni image does not provide a standard T1-weighted contrast.

Table 2.2. FLAWS sequence parameters originally proposed by Tanner et al. [10] at 3T and FLAWS sequence parameters proposed in this thesis at 1.5T, 3T and 7T.

Sequence	FLAWS 1.5T	FLAWS 3T Tanner et al.	FLAWS 3T	FLAWS 7T
TR/TE ($msec$)	$3500/2.32$	$5000/2.94$	$5000/2.19$	$5000/2.04$
TI ($msec$)	$403/1030$	$409/1100$	$449/1270$	$620/1430$
Flip angles	$6°/10°$	$5°/5°$	$5°/6°$	$4°/8°$
Matrix	192×180	256×240	256×240	300×300
Slices	128	160	192	192
Number of GRE excitations	96	120	144	144
Resolution (mm^3)	$1.25 \times 1.25 \times 1.40$	$1.0 \times 1.0 \times 1.0$	$1.0 \times 1.0 \times 1.0$	$0.8 \times 0.8 \times 0.8$
BW (Hz/px)	240	240	400	370
Orientation	$Sagittal$	$Sagittal$	$Sagittal$	$Sagittal$
FOV (mm^2)	240×225	256×240	256×240	240×240
$GRAPPA$	$None$	2	3	3
Slice partial Fourier	$6/8$	$6/8$	$6/8$	$6/8$
Phase partial Fourier	$None$	$None$	$None$	$None$
Scan time ($min: sec$)	$10: 27$	$10: 57$	$8: 20$	$10: 02$

2.9 Validation of the FLAWS T1 mapping method on a caliber phantom

2.9.1 Materials and methods

The measure of the T1 relaxation times with the FLAWS sequence was validated with experiments performed on an MRI caliber phantom (QalibreMD System Standard Model 130, https://qmri.com/system-phantom, Figure 2.28) at 3T. The MRI caliber phantom provides 14 spheres with known T1 and T2 relaxation times (Table 2.3).

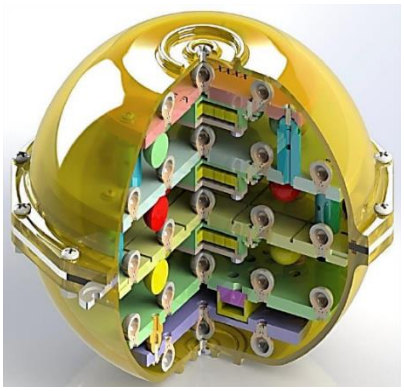

Figure 2.28. Picture of the MRI caliber phantom QalibreMD System Standard Model 130. Image from https://qmri.com.

Table 2.3. T1 and T2 relaxation times of the 14 spheres provided by the MRI caliber phantom Qalibre MD System Standard Model 130.

	$T1\ (ms)$	$T2\ (ms)$
Sphere 1	87	5
Sphere 2	122	8
Sphere 3	171	11
Sphere 4	238	15
Sphere 5	300	20
Sphere 6	444	31
Sphere 7	590	45
Sphere 8	782	63
Sphere 9	1017	94
Sphere 10	1341	134
Sphere 11	1552	185
Sphere 12	1961	286
Sphere 13	2281	424
Sphere 14	2756	646

The caliber phantom was imaged with a 3T scanner (Magnetom Prisma, Siemens Healthcare, Erlangen, Germany) equipped with a 20-receiver channel head and neck matrix coil. Nine inversion recovery turbo spin echo (IRTSE) images were acquired with the following parameters: $TE = 8.2\,ms, TR = 6000\,ms, TIs = 35/500/1000/1500/2000/2500/3000/4000/5000\,ms$, $1\,mm$ isotropic resolution, total acquisition time: $52{:}30$ mins. MP2RAGE images were acquired with the 3T parameters presented in Table 2.1. FLAWS images were acquired with the 3T parameters proposed in this thesis (Table 2.2). The IRTSE was used as a reference for the measure of the T1 relaxation times. The measure of the T1 relaxation times with the IRTSE data was performed by curve fitting as described in section 2.3. The average signal intensity of the 14 phantom spheres was measured for each IRTSE images by manually drawing ROIs within the spheres. The same ROIs were used for the measurement of the 9 IRTSE images. T1 maps were generated with the MP2RAGE and FLAWS sequences using the methods described in section 2.7 and Chapter 5, respectively. The average T1 relaxation times of the phantom spheres were then measured by manually selecting ROIs in the T1 maps. The ground truth T1 relaxation times and the T1 measurements provided by the IRTSE, MP2RAGE and FLAWS methods were compared by computing the mean absolute error:

$$\hat{e}_{A/B} = \frac{1}{N}\sum_{i=0}^{N-1}\left|T1_{A,i} - T1_{B,i}\right| \qquad 2.21$$

With N the number of phantom spheres and $T1_{A,i}$ (resp. $T1_{B,i}$) the T1 measurement performed in the sphere i with the T1 mapping method A (resp. B).

2.9.2 Results and discussion

Examples of images acquired on the caliber phantom with the IRTSE sequence, the MP2RAGE sequence and the FLAWS sequence are presented in Figures 2.29-2.31. Examples of T1 maps obtained with the MP2RAGE and FLAWS sequences are presented in Figure 2.32. The T1 values measured with the FLAWS sequence were in agreement with the IRTSE and MP2RAGE T1 measurements as well as with the T1 values provided for the caliber phantom (Figure 2.33 and Table 2.4).

The error measured between the T1 values provided for the caliber phantom and the T1 values measured with the IRTSE method tends to increase with the T1 relaxation time (Figure 2.34a). This error increase is potentially due to the short IRTSE repetition time, which may not allow for the full recovery of the longitudinal magnetization for spheres with a long T1 relaxation time. The IRTSE sequence repetition time was purposely not increased to limit the acquisition time. The T1 measurement error starts to increase for T1 relaxation times higher than the T1 relaxation times of tissues of interest for brain imaging at 3T ($700\,ms - 2000\,ms$), thus further justifying the choice of a short IRTSE repetition time. A similar increase in T1 measurement errors was found for the MP2RAGE and FLAWS T1 mapping methods. The error between the T1 values provided for the caliber phantom and the T1 values measured with the FLAWS sequence was found to be close to the error obtained with the T1 mapping method of reference (IRTSE), as shown in Figure 2.34a. The mean absolute errors between the caliber phantom T1 values and the T1 values measured with the IRTSE, MP2RAGE and FLAWS methods were equal to $41\,ms$, $58\,ms$ and $50\,ms$, respectively. The mean absolute error in the T1 range of brain tissues of interest (spheres 7 to 12) was equal to $24\,ms$ for the IRSTE method, $57\,ms$ for the MP2RAGE method and $34\,ms$ for the FLAWS method.

The error measured between the IRTSE and FLAWS T1 mapping methods tends to be lower than the error measured between the IRTSE and MP2RAGE methods (Figure 2.34b), with mean absolute errors equal to $23\ ms$ and $46\ ms$, respectively. The mean absolute error computed within the T1 range of brain tissues of interest (spheres 7 to 12) was equal to $41\ ms$ between the IRTSE and MP2RAGE methods, and $17\ ms$ between the IRTSE and FLAWS methods. The T1 mapping results obtained at 3T on the caliber phantom then validate the FLAWS T1 mapping method, which will be presented in more details in Chapter 5.

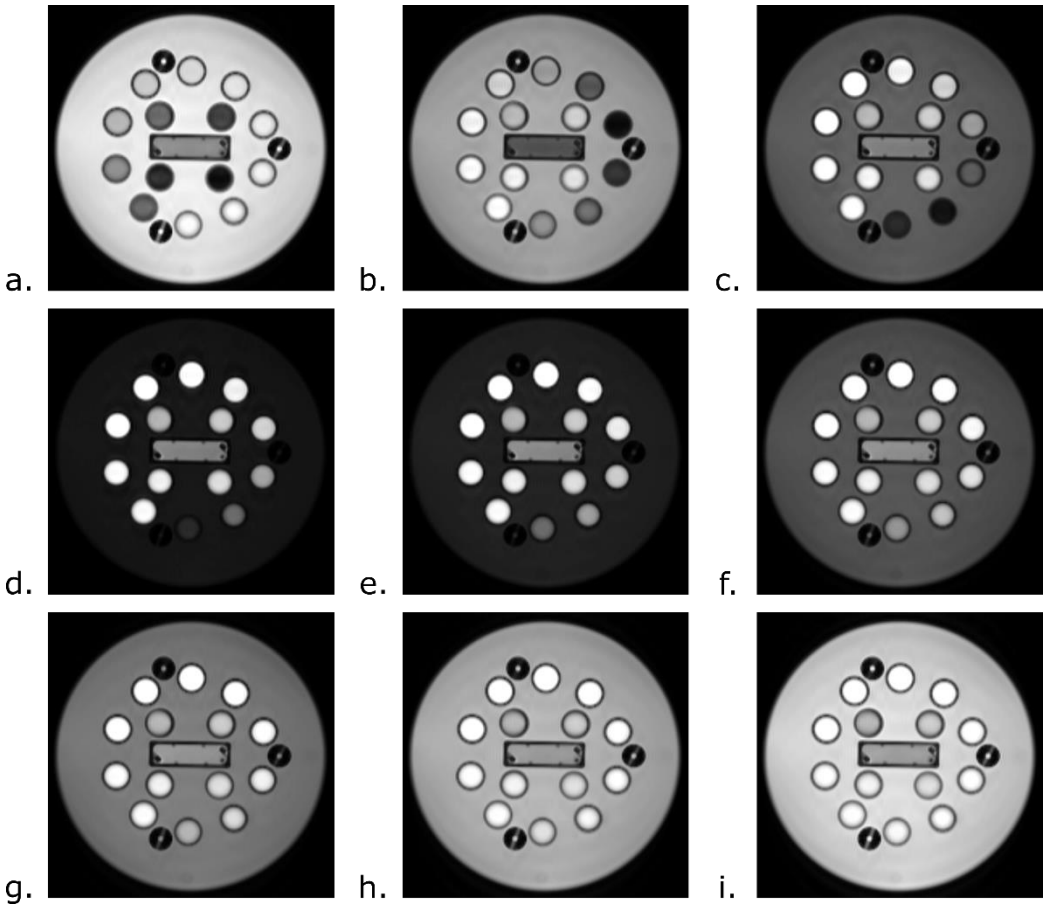

Figure 2.29. Example of inversion recovery spin echo images acquired on a caliber phantom at 3T. a. $TI = 36\ ms$; b. $TI = 500\ ms$; c. $TI = 1000\ ms$; d. $TI = 1500\ ms$; e. $TI = 2000\ ms$; f. $TI = 2500\ ms$; g. $TI = 3000\ ms$; h. $TI = 4000\ ms$; i. $TI = 5000\ ms$.

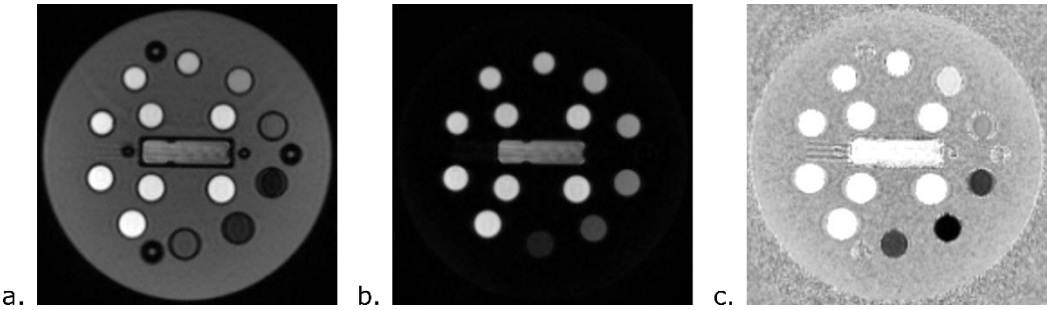

Figure 2.30. Example of MP2RAGE images acquired on a caliber phantom at 3T. a. MP2RAGE1; b. MP2RAGE2; c. MP2RAGE-uni.

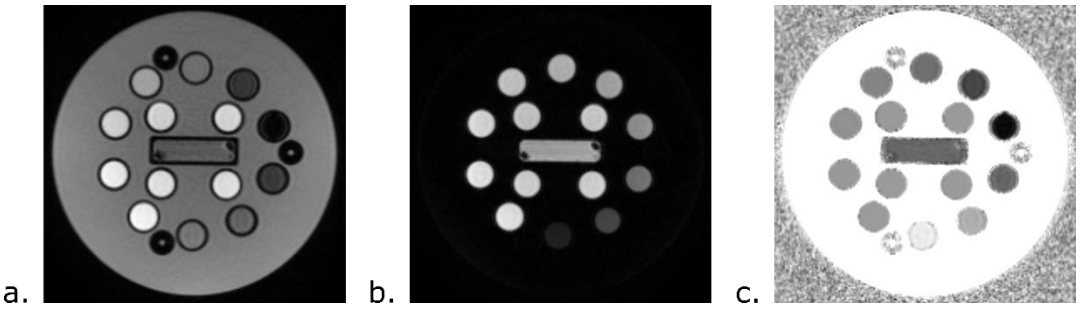

Figure 2.31. Example of FLAWS images acquired on a caliber phantom at 3T. a. FLAWS1; b. FLAWS2; c. FLAWS-hc.

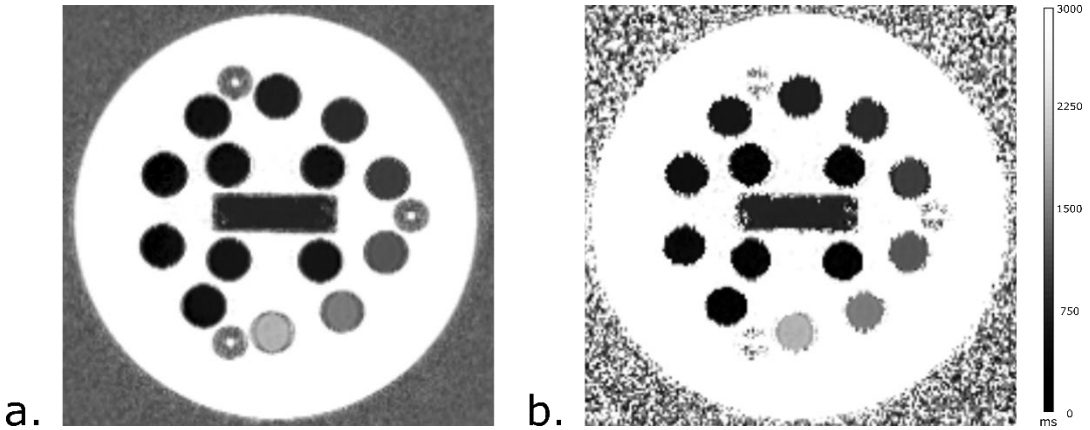

Figure 2.32. Examples of MP2RAGE (a) and FLAWS (b) T1 maps acquired on a caliber phantom at 3T.

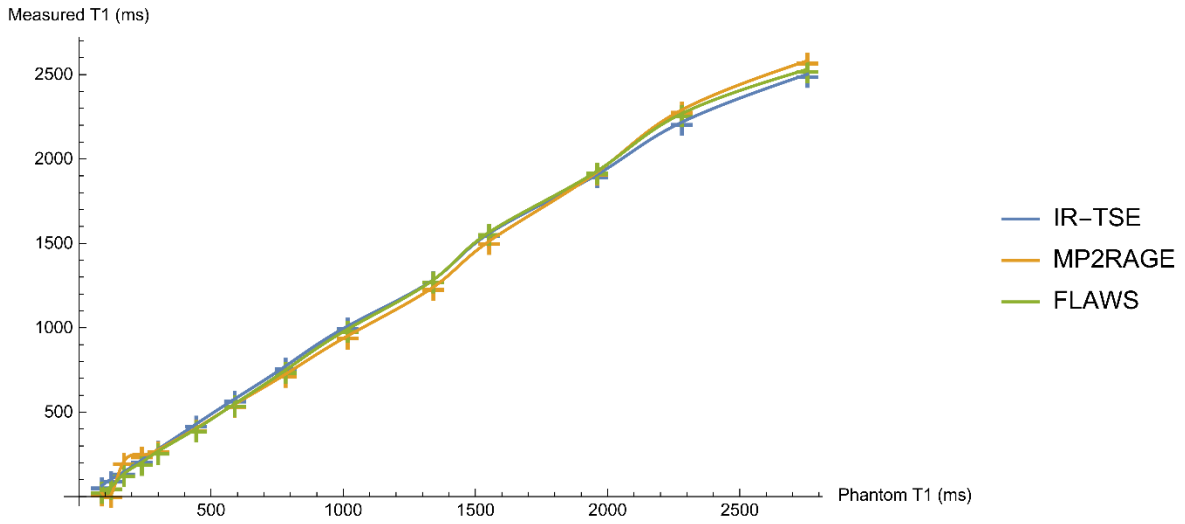

Figure 2.33. T1 relaxation times measured with the inversion recovery turbo spin echo sequence (IR-TSE), the MP2RAGE sequence and the FLAWS sequence as a function of the caliber phantom T1 relaxation times. The crosses represent the measures of the T1 relaxation times on the 14 spheres of the caliber phantom.

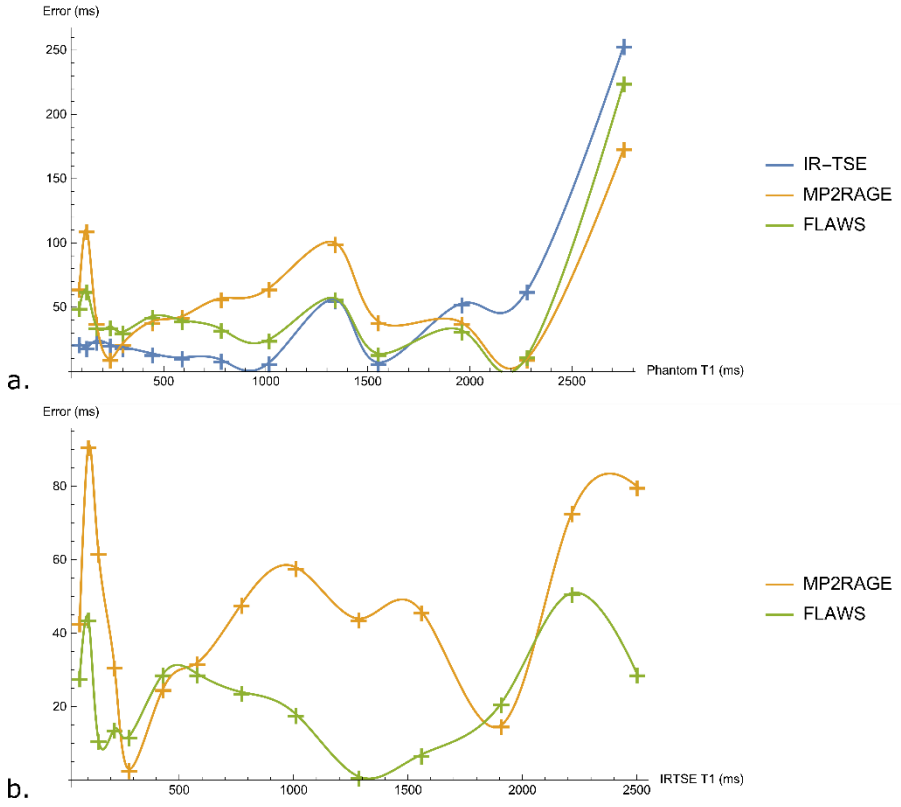

Figure 2.34. Comparison of the FLAWS T1 mapping performance with the performances of the reference T1 mapping methods on caliber phantom data at 3T. a. Absolute error between the T1 values provided for the caliber phantom and the T1 values measured with the inversion recovery turbo spin echo method (IRTSE), the MP2RAGE method and the FLAWS method. The FLAWS T1 mapping error is in the range of the T1 mapping errors of the reference methods (IRTSE and MP2RAGE). b. Absolute error between the T1 values measured with the IRTSE

method and the T1 values measured with the MP2RAGE and FLAWS method. The FLAWS T1 mapping method tends to provide closer results to the T1 mapping reference method (IRTSE) than the MP2RAGE T1 mapping method.

Table 2.4. T1 values of the 14 spheres provided by the caliber phantom and T1 values measured within these 14 spheres with the inversion recovery turbo spin echo method (IRTSE), the MP2RAGE method and the FLAWS method. The comparison between the different T1 mapping methods is presented in Figure 2.33.

T1 caliber phantom (ms)	T1 IRTSE (ms)	T1 MP2RAGE (ms)	T1 FLAWS (ms)
87	65	22	37
122	103	12	59
171	147	209	136
238	217	248	203
300	281	278	269
444	430	405	401
590	579	547	550
782	773	725	749
1017	1010	952	992
1341	1285	1241	1284
1552	1559	1513	1566
1961	1908	1923	1929
2281	2218	2291	2269
2756	2502	2582	2531

2.10 Signal equations

2.10.1 MPRAGE signal

The longitudinal magnetization measured at the center of the k-space for the MPRAGE sequence is computed as follows:

$$f_{mp} = \frac{\begin{array}{c} e^{\frac{\mathrm{TA+TB}}{\mathrm{T1}}}\left(-1+e^{-\frac{\mathrm{tr}}{\mathrm{T1}}}\right)+I_{\mathrm{eff}}\left(-1+e^{-\frac{\mathrm{tr}}{\mathrm{T1}}}\right)\left(e^{-\frac{\mathrm{tr}}{\mathrm{T1}}}\cos(B1^{+}\alpha)\right)^{\mathrm{n}} \\ +\left(e^{\frac{\mathrm{TA+TB}}{\mathrm{T1}}}+I_{\mathrm{eff}}-e^{\frac{\mathrm{TB}}{\mathrm{T1}}}(1+I_{\mathrm{eff}})\right)\left(e^{-\frac{\mathrm{tr}}{\mathrm{T1}}}\cos(B1^{+}\alpha)\right)^{1+a\mathrm{n}} \\ +\left(-e^{\frac{\mathrm{TA+TB}}{\mathrm{T1}}}-I_{\mathrm{eff}}+e^{\frac{\mathrm{TB+tr}}{\mathrm{T1}}}(1+I_{\mathrm{eff}})\right)\left(e^{-\frac{\mathrm{tr}}{\mathrm{T1}}}\cos(B1^{+}\alpha)\right)^{1+a\mathrm{n}}\sec(B1^{+}\alpha) \end{array}}{\left(-1+e^{-\frac{\mathrm{tr}}{\mathrm{T1}}}\cos(B1^{+}\alpha)\right)\left(e^{\frac{\mathrm{TA+TB}}{\mathrm{T1}}}+I_{\mathrm{eff}}\left(e^{-\frac{\mathrm{tr}}{\mathrm{T1}}}\cos(B1^{+}\alpha)\right)^{\mathrm{n}}\right)} \quad 2.22$$

With α the gradient echo flip angle, TE the echo time of the gradient echo, TA the time between the inversion pulse and the first gradient echo pulse, TB the time between the last

gradient echo pulse and the next inversion pulse, tr the gradient echo repetition time –not to confuse with TR the gradient echo inversion recovery repetition time, equal to the time between to inversion pulses–, I_{eff} the efficiency of the inversion pulse, an the number of gradient echo excitations before the sampling of the k-space center, n the total number of gradient echo excitations (Figure 2.7) and $B1^+$ and $B1^-$ the inhomogeneities of the transmitted- and received-B1 fields.

2.10.2 MP2RAGE signals

The longitudinal magnetization measured at the acquisition of the k-space center of the first and second MP2RAGE gradient echoes is computed as follows:

$$f_{mp1} = \frac{e^{\frac{TA+TB+TC}{T1}}\left(\begin{array}{c}\left(e^{-\frac{tr}{T1}}\cos(B1^+\alpha_1)\right)^{an} - e^{-\frac{TA}{T1}}\left(e^{-\frac{tr}{T1}}\cos(B1^+\alpha_1)\right)^{an} - I_{eff}\,e^{-\frac{TA}{T1}}\left(e^{-\frac{tr}{T1}}\cos(B1^+\alpha_1)\right)^{an} \\ +I_{eff}\,e^{-\frac{TA+TC}{T1}}\left(e^{-\frac{tr}{T1}}\cos(B1^+\alpha_1)\right)^{an} - \frac{\left(-1+e^{\frac{tr}{T1}}\right)\left(-1+\left(e^{-\frac{tr}{T1}}\cos(B1^+\alpha_1)\right)^{an}\right)}{e^{\frac{tr}{T1}}-\cos(B1^+\alpha_1)} \\ -I_{eff}\,e^{-\frac{TA+TC}{T1}}\left(e^{-\frac{tr}{T1}}\cos(B1^+\alpha_1)\right)^{an}\left(e^{-\frac{tr}{T1}}\cos(B1^+\alpha_2)\right)^{n} \\ +I_{eff}\,e^{-\frac{TA+TB+TC}{T1}}\left(e^{-\frac{tr}{T1}}\cos(B1^+\alpha_1)\right)^{an}\left(e^{-\frac{tr}{T1}}\cos(B1^+\alpha_2)\right)^{n} \\ +\frac{\left(\begin{array}{c}I_{eff}\,e^{-\frac{TA+TB+TC}{T1}}\left(-1+e^{\frac{tr}{T1}}\right)\left(e^{-\frac{tr}{T1}}\cos(B1^+\alpha_1)\right)^{an} \\ \left(-1+\left(e^{-\frac{tr}{T1}}\cos(B1^+\alpha_1)\right)^{bn}\right)\left(e^{-\frac{tr}{T1}}\cos(B1^+\alpha_2)\right)^{n}\end{array}\right)}{e^{\frac{tr}{T1}}-\cos(B1^+\alpha_1)} \\ +\frac{I_{eff}\,e^{-\frac{TA+TC}{T1}}\left(-1+e^{\frac{tr}{T1}}\right)\left(e^{-\frac{tr}{T1}}\cos(B1^+\alpha_1)\right)^{an}\left(-1+\left(e^{-\frac{tr}{T1}}\cos(B1^+\alpha_2)\right)^{n}\right)}{e^{\frac{tr}{T1}}-\cos(B1^+\alpha_2)}\end{array}\right)}{e^{\frac{TA+TB+TC}{T1}} + I_{eff}\left(e^{-\frac{tr}{T1}}\cos(B1^+\alpha_1)\right)^{n}\left(e^{-\frac{tr}{T1}}\cos(B1^+\alpha_2)\right)^{n}} \quad 2.23$$

$$f_{mp2} = \frac{e^{\frac{TA+TB+TC}{T1}}\left(\begin{array}{c}\left(e^{-\frac{tr}{T1}}\cos(B1^+\alpha_2)\right)^{an} - e^{-\frac{TB}{T1}}\left(e^{-\frac{tr}{T1}}\cos(B1^+\alpha_2)\right)^{an} \\ +e^{-\frac{TB}{T1}}\left(e^{-\frac{tr}{T1}}\cos(B1^+\alpha_1)\right)^{n}\left(e^{-\frac{tr}{T1}}\cos(B1^+\alpha_2)\right)^{an} \\ -e^{-\frac{TA+TB}{T1}}\left(e^{-\frac{tr}{T1}}\cos(B1^+\alpha_1)\right)^{n}\left(e^{-\frac{tr}{T1}}\cos(B1^+\alpha_2)\right)^{an} \\ -I_{eff}\,e^{-\frac{TA+TB}{T1}}\left(e^{-\frac{tr}{T1}}\cos(B1^+\alpha_1)\right)^{n}\left(e^{-\frac{tr}{T1}}\cos(B1^+\alpha_2)\right)^{an} \\ +I_{eff}\,e^{-\frac{TA+TB+TC}{T1}}\left(e^{-\frac{tr}{T1}}\cos(B1^+\alpha_2)\right)^{n}\left(e^{-\frac{tr}{T1}}\cos(B1^+\alpha_2)\right)^{an} \\ -\frac{e^{-\frac{TB}{T1}}\left(-1+e^{\frac{tr}{T1}}\right)\left(-1+\left(e^{-\frac{tr}{T1}}\cos(B1^+\alpha_1)\right)^{n}\right)\left(e^{-\frac{tr}{T1}}\cos(B1^+\alpha_2)\right)^{an}}{e^{\frac{tr}{T1}}-\cos(B1^+\alpha_1)} \\ -\frac{\left(-1+e^{\frac{tr}{T1}}\right)\left(-1+\left(e^{-\frac{tr}{T1}}\cos(B1^+\alpha_2)\right)^{an}\right)}{e^{\frac{tr}{T1}}-\cos(B1^+\alpha_2)} \\ +\frac{\left(\begin{array}{c}I_{eff}\,e^{-\frac{TA+TB+TC}{T1}}\left(-1+e^{\frac{tr}{T1}}\right)\left(e^{-\frac{tr}{T1}}\cos(B1^+\alpha_1)\right)^{n} \\ \left(e^{-\frac{tr}{T1}}\cos(B1^+\alpha_2)\right)^{an}\left(-1+\left(e^{-\frac{tr}{T1}}\cos(B1^+\alpha_2)\right)^{bn}\right)\end{array}\right)}{e^{\frac{tr}{T1}}-\cos(B1^+\alpha_2)}\end{array}\right)}{e^{\frac{TA+TB+TC}{T1}} + I_{eff}\left(e^{-\frac{tr}{T1}}\cos(B1^+\alpha_1)\right)^{n}\left(e^{-\frac{tr}{T1}}\cos(B1^+\alpha_2)\right)^{n}} \quad 2.24$$

With α_1 the first gradient echo flip angle, α_2 the second gradient echo flip angle, TA the time between the inversion pulse and the first pulse of the first gradient echo, TB the time between the last pulse of the first gradient echo and the first pulse of the second gradient echo, TC the time between the last pulse of the second gradient echo and the next inversion pulse, tr the gradient echo repetition time (the two gradient echoes are acquired with the same repetition time), I_{eff} the efficiency of the inversion pulse, an the number of gradient echo excitations

before the sampling of the k-space center, bn the number of gradient echo excitations after the sampling of the k-space center, n the total number of gradient echo excitations (the two gradient echoes are acquired with the same number of excitations an, bn and n) and $B1^+$ the transmitted-inhomogeneities of the $B1$ magnetic field.

2.10.3 SA2RAGE signals

The longitudinal magnetization measured at the acquisition of the k-space center of the first and second SA2RAGE gradient echoes is computed as follows:

$$f_{SA1} = \frac{e^{\frac{TA+TB+TC}{T1}} \begin{pmatrix} \left(e^{-\frac{tr}{T1}}\cos(B1^+\alpha_1)\right)^{an} - e^{-\frac{TA}{T1}}\left(e^{-\frac{tr}{T1}}\cos(B1^+\alpha_1)\right)^{an} \\ -\frac{\left(-1+e^{\frac{tr}{T1}}\right)\left(-1+\left(e^{-\frac{tr}{T1}}\cos(B1^+\alpha_1)\right)^{an}\right)}{e^{\frac{tr}{T1}}-\cos(B1^+\alpha_1)} + e^{-\frac{TA}{T1}}\left(e^{-\frac{tr}{T1}}\cos(B1^+\alpha_1)\right)^{an}\cos\left(B1^+\frac{\pi}{2}\right) \\ -e^{-\frac{TA+TC}{T1}}\left(e^{-\frac{tr}{T1}}\cos(B1^+\alpha_1)\right)^{an}\cos\left(B1^+\frac{\pi}{2}\right) \\ +e^{-\frac{TA+TC}{T1}}\left(e^{-\frac{tr}{T1}}\cos(B1^+\alpha_1)\right)^{an}\left(e^{-\frac{tr}{T1}}\cos(B1^+\alpha_2)\right)^{n}\cos\left(B1^+\frac{\pi}{2}\right) \\ -e^{-\frac{TA+TB+TC}{T1}}\left(e^{-\frac{tr}{T1}}\cos(B1^+\alpha_1)\right)^{an}\left(e^{-\frac{tr}{T1}}\cos(B1^+\alpha_2)\right)^{n}\cos\left(B1^+\frac{\pi}{2}\right) \\ -\frac{\begin{pmatrix} e^{-\frac{TA+TB+TC}{T1}}\left(-1+e^{\frac{tr}{T1}}\right)\left(e^{-\frac{tr}{T1}}\cos(B1^+\alpha_1)\right)^{an} \\ \left(-1+\left(e^{-\frac{tr}{T1}}\cos(B1^+\alpha_1)\right)^{bn}\right)\left(\begin{pmatrix}\left(e^{-\frac{tr}{T1}}\cos(B1^+\alpha_2)\right)^{n} \\ \cos\left(B1^+\frac{\pi}{2}\right)\end{pmatrix}\right)\end{pmatrix}}{e^{\frac{tr}{T1}}-\cos(B1^+\alpha_1)} \\ -\frac{e^{-\frac{TA+TC}{T1}}\left(-1+e^{\frac{tr}{T1}}\right)\left(e^{-\frac{tr}{T1}}\cos(B1^+\alpha_1)\right)^{an}\left(-1+\left(e^{-\frac{tr}{T1}}\cos(B1^+\alpha_2)\right)^{n}\right)\cos\left(B1^+\frac{\pi}{2}\right)}{e^{\frac{tr}{T1}}-\cos(B1^+\alpha_2)} \end{pmatrix}}{e^{\frac{TA+TB+TC}{T1}} - \left(e^{-\frac{tr}{T1}}\cos(B1^+\alpha_1)\right)^{n}\left(e^{-\frac{tr}{T1}}\cos(B1^+\alpha_2)\right)^{n}\cos\left(B1^+\frac{\pi}{2}\right)} \quad 2.35$$

$$f_{SA2} = \frac{e^{\frac{TA+TB+TC}{T1}} \begin{pmatrix} \left(e^{-\frac{tr}{T1}}\cos(B1^+\alpha_2)\right)^{an} - e^{-\frac{TB}{T1}}\left(e^{-\frac{tr}{T1}}\cos(B1^+\alpha_2)\right)^{an} \\ +e^{-\frac{TB}{T1}}\left(e^{-\frac{tr}{T1}}\cos(B1^+\alpha_1)\right)^{n}\left(e^{-\frac{tr}{T1}}\cos(B1^+\alpha_2)\right)^{an} \\ -e^{-\frac{TA+TB}{T1}}\left(e^{-\frac{tr}{T1}}\cos(B1^+\alpha_1)\right)^{n}\left(e^{-\frac{tr}{T1}}\cos(B1^+\alpha_2)\right)^{an} \\ -\frac{e^{-\frac{TB}{T1}}\left(-1+e^{\frac{tr}{T1}}\right)\left(-1+\left(e^{-\frac{tr}{T1}}\cos(B1^+\alpha_1)\right)^{n}\right)\left(e^{-\frac{tr}{T1}}\cos(B1^+\alpha_2)\right)^{an}}{e^{\frac{tr}{T1}}-\cos(B1^+\alpha_1)} \\ -\frac{\left(-1+e^{\frac{tr}{T1}}\right)\left(-1+\left(e^{-\frac{tr}{T1}}\cos(B1^+\alpha_2)\right)^{an}\right)}{e^{\frac{tr}{T1}}-\cos(B1^+\alpha_2)} \\ +e^{-\frac{TA+TB}{T1}}\left(e^{-\frac{tr}{T1}}\cos(B1^+\alpha_1)\right)^{n}\left(e^{-\frac{tr}{T1}}\cos(B1^+\alpha_2)\right)^{an}\cos\left(B1^+\frac{\pi}{2}\right) \\ -e^{-\frac{TA+TB+TC}{T1}}\left(e^{-\frac{tr}{T1}}\cos(B1^+\alpha_1)\right)^{n}\left(e^{-\frac{tr}{T1}}\cos(B1^+\alpha_2)\right)^{an}\cos\left(B1^+\frac{\pi}{2}\right) \\ -\frac{\begin{pmatrix} e^{-\frac{TA+TB+TC}{T1}}\left(-1+e^{\frac{tr}{T1}}\right)\left(e^{-\frac{tr}{T1}}\cos(B1^+\alpha_1)\right)^{n} \\ \left(e^{-\frac{tr}{T1}}\cos(B1^+\alpha_2)\right)^{an}\left(-1+\left(e^{-\frac{tr}{T1}}\cos(B1^+\alpha_2)\right)^{bn}\right)\cos\left(B1^+\frac{\pi}{2}\right)\end{pmatrix}}{e^{\frac{tr}{T1}}-\cos(B1^+\alpha_2)} \end{pmatrix}}{e^{\frac{TA+TB+TC}{T1}} - \left(e^{-\frac{tr}{T1}}\cos(B1^+\alpha_1)\right)^{n}\left(e^{-\frac{tr}{T1}}\cos(B1^+\alpha_2)\right)^{n}\cos\left(B1^+\frac{\pi}{2}\right)} \quad 2.36$$

With α_1 the first gradient echo flip angle, α_2 the second gradient echo flip angle, TA the time between the saturation pulse and the first pulse of the first gradient echo, TB the time between the last pulse of the first gradient echo and the first pulse of the second gradient echo, TC the time between the last pulse of the second gradient echo and the next saturation pulse, tr the gradient echo repetition time (the two gradient echoes are acquired with the same repetition time), an the number of gradient echo excitations before the sampling of the k-space center, bn the number of gradient echo excitations after the sampling of the k-space

center, n the total number of gradient echo excitations (the two gradient echoes are acquired with the same number of excitations an, bn and n) and $B1^{+}$ the transmitted-inhomogeneities of the $B1$ magnetic field.

2.11 References

[1] Urushibata Y, Kuribayashi H, Fujimoto K, Kober T, Grinstead JW, Isa T, et al. Advantages of fluid and white matter suppression (FLAWS) with MP2RAGE compared with double inversion recovery turbo spin echo (DIR-TSE) at 7T. Eur J Radiol 2019;116:160–4. doi:10.1016/j.ejrad.2019.04.019.

[2] Tang X, Cai F, Ding DX, Zhang LL, Cai XY, Fang Q. Magnetic resonance imaging relaxation time in Alzheimer's disease. Brain Res Bull 2018;140:176–89. doi:10.1016/j.brainresbull.2018.05.004.

[3] Manfredonia F, Ciccarelli O, Khaleeli Z, Tozer DJ, Sastre-Garriga J, Miller DH, et al. Normal-appearing brain T1 relaxation time predicts disability in early primary progressive multiple sclerosis. Arch Neurol 2007;64:411–5. doi:10.1001/archneur.64.3.411.

[4] Mugler JP, Brookeman JR. Three-dimensional magnetization-prepared rapid gradient-echo imaging (3D MP RAGE). Magn Reson Med 1990;15:152–7.

[5] Sudhyadhom A, Haq IU, Foote KD, Okun MS, Bova FJ. A high resolution and high contrast MRI for differentiation of subcortical structures for DBS targeting: The Fast Gray Matter Acquisition T1 Inversion Recovery (FGATIR). Neuroimage 2009;47:T44–52. doi:10.1016/j.neuroimage.2009.04.018.

[6] Wright PJ, Mougin OE, Totman JJ, Peters AM, Brookes MJ, Coxon R, et al. Water proton T 1 measurements in brain tissue at 7, 3, and 1.5T using IR-EPI, IR-TSE, and MPRAGE: results and optimization. Magn Reson Mater Physics, Biol Med 2008;21:121–30. doi:10.1007/s10334-008-0104-8.

[7] Christensen KA, Grant DM, Schulman EM, Walling C. Optimal determination of relaxation times of Fourier transform nuclear magnetic resonance. Determination of spin-lattice relaxation times in chemically polarized species. J Phys Chem 1974;78:1971–6. doi:10.1021/j100612a022.

[8] Wang HZ, Riederer SJ, Lee JN. Optimizing the precision in T1 relaxation estimation using limited flip angles. Magn Reson Med 1987;5:399–416. doi:10.1002/mrm.1910050502.

[9] Marques JP, Kober T, Krueger G, van der Zwaag W, Van de Moortele P-F, Gruetter R. MP2RAGE, a self bias-field corrected sequence for improved segmentation and T1-mapping at high field. Neuroimage 2010;49:1271–81. doi:10.1016/j.neuroimage.2009.10.002.

[10] Tanner M, Gambarota G, Kober T, Krueger G, Erritzoe D, Marques JP, et al. Fluid and white matter suppression with the MP2RAGE sequence. J Magn Reson Imaging 2012;35:1063–70. doi:10.1002/jmri.23532.

[11] Tustison NJ, Avants BB, Cook PA, Zheng Y, Egan A, Yushkevich PA, et al. N4ITK: improved N3 bias correction. IEEE Trans Med Imaging 2010;29:1310–20. doi:10.1109/TMI.2010.2046908.

[12] Van de Moortele P-F, Auerbach EJ, Olman C, Yacoub E, Uğurbil K, Moeller S. T1 weighted brain images at 7 Tesla unbiased for Proton Density, T2 contrast and RF coil receive B1 sensitivity with simultaneous vessel visualization. Neuroimage 2009;46:432–46.

doi:10.1016/J.NEUROIMAGE.2009.02.009.

[13] O ’brien KR, Kober T, Hagmann P, Maeder P, Marques J, Lazeyras F, et al. Robust T1-Weighted Structural Brain Imaging and Morphometry at 7T Using MP2RAGE 2014;9:e99676. doi:10.1371/journal.pone.0099676.

[14] Eggenschwiler F, Kober T, Magill AW, Gruetter R, Marques JP. SA2RAGE: A new sequence for fast B1+-mapping. Magn Reson Med 2012;67:1609–19. doi:10.1002/mrm.23145.

[15] Marques JP, Gruetter R. New Developments and Applications of the MP2RAGE Sequence - Focusing the Contrast and High Spatial Resolution R1 Mapping. PLoS One 2013;8:e69294. doi:10.1371/journal.pone.0069294.

[16] Haast RA, Lau JC, Ivanov D, Menon RS, Uludağ K, Khan AR. Effects of MP2RAGE B1+ sensitivity on inter-site T1 reproducibility and morphometry at 7T. BioRxiv 2020:2020.02.13.947382. doi:10.1101/2020.02.13.947382.

[17] Bannier E, Gambarota G, Ferre J-C, Kober T, Nica A, Chabardes S, et al. FLAWS imaging improves depiction of the thalamic subregions for DBS planning in epileptic patients. Int. Soc. Magn. Reson. Med., 2018.

[18] Chen X, Qian T, Kober T, Zhang G, Ren Z, Yu T, et al. Gray-matter-specific MR imaging improves the detection of epileptogenic zones in focal cortical dysplasia: A new sequence called fluid and white matter suppression (FLAWS). NeuroImage Clin 2018;20:388–97. doi:10.1016/J.NICL.2018.08.010.

Chapter 3
High Contrast T1-weigthed MRI with fluid and white matter suppression using the MP2RAGE sequence

3.1 Foreword

In this chapter we describe the work presented at the ISBI 2019 conference in Venice, Italy. The major novelty of this work was the introduction of new FLAWS images combinations for high contrast imaging. A detailed analysis of the contrast and signal to noise ratio of these novel images was performed. The 1.5T FLAWS sequence parameters proposed in this chapter were optimized with a preliminary version of the FLAWS optimization method presented in Chapter 4. We then advise to use the parameters presented in Chapter 4 for 1.5T FLAWS acquisitions.

3.2 Abstract

A novel magnetic resonance imaging (MRI) sequence called fluid and white matter suppression (FLAWS) was recently proposed for brain imaging at 3T. This sequence provides two co-registered 3D-MRI datasets of T1-weighted images. The voxel-wise division of these two datasets yields contrast-enhanced images that have been used in preoperative Deep Brain Stimulation (DBS) planning. In the current study, we propose a new way of combining the two 3D-MRI FLAWS datasets to increase the contrast-to-noise ratio of the resulting images. Furthermore, since many centers performing DBS are equipped with 1.5T MRI systems, we also optimized the FLAWS sequence parameters for data acquisition at the field strength of 1.5T.

3.3 Introduction

In a previous study, a new magnetic resonance imaging (MRI) sequence called fluid and white matter suppression (FLAWS) was proposed for brain imaging at 3T [1]. This sequence, derived from the MP2RAGE sequence [2], provides two co-registered 3D MRI datasets of T1-weighted images. In one dataset (*FLAWS1*), the signal of white matter (WM) is suppressed; the *FLAWS1* images yield an improved visualization of basal ganglia structures and are characterized by an excellent sensitivity to WM lesions. In the other dataset (*FLAWS2*), the signal of the cerebrospinal fluid (CSF) is suppressed; these images provide a standard anatomical MRI delineation of the brain, similar to that obtained with the classical MPRAGE [1].

Two applications of the FLAWS sequence to clinical settings were very recently published [3], [4]. One study [3] showed that FLAWS is beneficial in preoperative Deep Brain Stimulation (DBS) planning; specifically, the authors of this study used -in an empirical way- the images obtained by combining the two datasets (*FLAWS1*, *FLAWS2*). These images (*FLAWS-Div*) were calculated by the voxel-wise division of *FLAWS1* by *FLAWS2*. *FLAWS-Div* provided an enhanced brain-tissue contrast, improving the planning of electrode trajectory for DBS. The other study

showed that FLAWS improves the detection of epileptogenic lesions in focal cortical dysplasia [4].

Motivated by these recent developments and applications to clinical settings of the FLAWS MRI sequence, we i) investigated the signal properties inherent to the *FLAWS-Div* image [3], and ii) developed a novel image combination that could further enhance the brain-tissue contrast.

The current study was performed at 1.5T, since most of the centers performing DBS are equipped with 1.5T MRI systems [5]. To the best of our knowledge, no studies have been previously conducted with FLAWS at 1.5T; therefore, an optimization of the FLAWS sequence parameters was also necessary, as a prerequisite to acquire FLAWS MRI data.

3.4 Materials and methods

3.4.1 Sequence optimization

The acquisition parameters of the FLAWS sequence (repetition time TR, echo time TE, inversion times TI_1 and TI_2, flip angles, α_1 and α_2 , etc.) were optimized using the Bloch equations. Six healthy volunteers (6 males, age 24–32) were scanned on a 1.5T Aera system (Siemens Healthcare, Erlangen, Germany) with a 20-receiver channel head and neck matrix coil. The FLAWS sequence parameters were those obtained by the sequence optimization study. All the experiments were performed according to procedures approved by the Institutional Review Board.

The quality of the acquired images was assessed by measuring the contrast (CN) and the contrast to noise ratio (CNR) between brain tissues:

$$CN_{A/B} = \frac{|S_A - S_B|}{|S_A| + |S_B|} \quad 3.1$$

$$CNR_{A/B} = \frac{|S_A - S_B|}{\sqrt{\frac{\sigma_A^2 + \sigma_B^2}{2}}} \quad 3.2$$

where S_A and σ_A^2 (resp. S_B and σ_B^2) are the mean and the variance of signal intensities of a given tissue A (resp. B). The mean and variance of signal intensities were determined by manually drawing regions of interests (ROI) in the corpus callosum (splenium) for WM, caudate nucleus (head) for GM and lateral ventricle for CSF. The size of the ROI was $46\ mm^3$ for each tissue, across all the datasets.

A qualitative assessment was also performed to ensure that the separation between the internal Globus Pallidus (GPi) and the external Globus Pallidus (GPe) was clearly visible in *FLAWS1*.

3.4.2 Image combination

In this section, the combination of two sets of images (*FLAWS1* and *FLAWS2*) acquired with FLAWS is investigated in order to obtain an enhanced contrast between brain tissues. The image combination is computed by voxel-wise operations. It should be emphasized that voxel-wise operations with *FLAWS1* and *FLAWS2* are effective and readily usable, without any

(additional) pre- or post-processing, since the FLAWS images are naturally co-registered due to the design of the sequence [1], [2].

Two combinations are investigated: 1) *FLAWS-Div*, calculated by the voxel-wise division of *FLAWS1* by *FLAWS2* and applied in an empirical way for preoperative DBS planning and 2) *FLAWS-HC* (high contrast), a novel image combination that we propose here for the first time. The theoretical comparison between *FLAWS-Div* and *FLAWS-HC* was performed using two features directly linked with the CNR: 1) the contrast between brain tissues; and 2) the signal to noise ratio (SNR), defined as $SNR_A = S_A/\vartheta$, where S_A is the mean signal of a given tissue A and ϑ is the noise level in the image.

The noise level of an image combination was determined by computing the error propagation of the noise levels in the acquired images *FLAWS1* and *FLAWS2*. The noise level in *FLAWS1* was assumed to be the same as in *FLAWS2*, thus, the error propagation of the FLAWS image combinations was computed as follows:

$$\vartheta_{prop} = \vartheta \sqrt{\left(\frac{\partial}{\partial S1} S_{combi}\right)^2 + \left(\frac{\partial}{\partial S2} S_{combi}\right)^2} \quad 3.3$$

With ϑ the noise measured in *FLAWS1* and *FLAWS2*, S_{combi} the signal of the combination image and $S1$ and $S2$ the *FLAWS1* and *FLAWS2* signals, respectively. For sake of clarity, in the formulas we will use *W*, *G and C* as abbreviations for white matter, gray matter and cerebrospinal fluid.

3.4.2.1 Properties of the division image (FLAWS-Div)

The signal of the division image is computed as $S_A = S1_A/S2_A$, where $S1_A$ (resp. $S2_A$) is the voxel signal intensity of a given tissue A in *FLAWS1* (resp. *FLAWS2*). Therefore, the contrast between WM and GM in the division image can be computed as:

$$CN_{W/G} = \frac{\left|\frac{S1_W}{S2_W} - \frac{S1_G}{S2_G}\right|}{\left|\frac{S1_W}{S2_W}\right| + \left|\frac{S1_G}{S2_G}\right|} \quad 3.4$$

Since the signal of WM is suppressed in *FLAWS1*, the signal of WM in the division image should tend towards zero and thus:

$$CN_{W/G} \xrightarrow[S1_W \ll S2_W]{} 1 \quad 3.5$$

Similarly, the WM/CSF and GM/CSF contrasts in the division image should tend towards 1 when the WM and CSF signals are respectively suppressed in *FLAWS1* and *FLAWS2*. The *FLAWS-div* error propagation is equal to:

$$\theta_{div} = \vartheta \sqrt{\frac{S1^2 + S2^2}{S2^4}} \quad 3.6$$

The SNR of WM in the division image is then computed as follows:

$$SNR_W = \frac{S1_W}{S2_W} \times \frac{1}{\vartheta\sqrt{\frac{S1_W^2 + S2_W^2}{S2_W^4}}} \quad 3.7$$

which leads to:

$$SNR_W \xrightarrow[S1_W \ll S2_W]{} \frac{S1_W}{S2_W} \times \frac{1}{\vartheta\sqrt{\frac{S2_W^2}{S2_W^4}}} = \frac{S1_W}{\vartheta} \quad 3.8$$

Likewise, the SNR of CSF in the division image will tend towards $S2_{CSF}/\vartheta$ when $S1_{CSF} \gg S2_{CSF}$. The SNR of WM (resp. CSF) in the division image equals the SNR of WM in *FLAWS1* (resp. CSF in *FLAWS2*). As a result, the SNR of both WM and CSF would be low in the division image, as the signals of WM and CSF are suppressed in *FLAWS1* and *FLAWS2,* respectively.

3.4.2.2 Properties of the novel image combination (FLAWS-HC)

Since the *FLAWS-div* SNR is low for both WM and CSF, new combinations of FLAWS signals were investigated in order provide a T1-weighted image characterized by a low $B1$ sensitivity and a high CNR between brain tissues. A new FLAWS combination image, named *FLAWS-HC*, was found. The signal of this novel FLAWS image is defined as:

$$S_A = \frac{S1_A - S2_A}{S1_A + S2_A} \quad 3.9$$

Computing *FLAWS-HC* corresponds to measuring the voxel-wise signed contrast between *FLAWS1* and *FLAWS2*. Therefore, the signal intensity of *FLAWS-HC* is in the range of [-1, 1], except when $S1_A = S2_A = 0$. To avoid zero division, voxels with values $S1_A = S2_A = 0$ are set to -1.

The WM/GM contrast of the FLAWS image combination is computed using the following equation:

$$CN_{W/G} = \frac{\left|\frac{S1_W - S2_W}{S1_W + S2_W} - \frac{S1_G - S2_G}{S1_G + S2_G}\right|}{\left|\frac{S1_W - S2_W}{S1_W + S2_W}\right| + \left|\frac{S1_G - S2_G}{S1_G + S2_G}\right|} \quad 3.10$$

which leads to:

$$CN_{W/G} \xrightarrow[S1_W \ll S2_W]{} \left|\frac{S1_G}{S2_G}\right| \quad 3.11$$

when the signal of WM is suppressed in *FLAWS1*.

Similarly,

$$CN_{G/C} \xrightarrow[S1_C \gg S2_C]{} \left|\frac{S2_G}{S1_G}\right| \quad 3.12$$

when the signal of CSF is suppressed in *FLAWS2*.

Since the signal intensity of GM in *FLAWS1* ($S1_G$) is close to the signal intensity of GM in *FLAWS2* ($S2_G$) –this is one of the characteristics of the FLAWS sequence– both the WM/GM and GM/CSF contrast will be high (i.e., it will tend towards 1). This is also the case for the WM/CSF contrast, because of the WM suppression in *FLAWS1* and CSF suppression in *FLAWS2*. As a result, the contrast between all the brain tissues will be high in the *FLAWS-HC*.

The *FLAWS-div* error propagation is equal to:

$$\vartheta_{hc} = \frac{2\vartheta\sqrt{S1^2 + S2^2}}{(S1 + S2)^2} \tag{3.13}$$

The SNR of WM in the *FLAWS-HC* is computed as follows:

$$SNR_W = \left|\frac{S1_W - S2_W}{S1_W + S2_W} \times \frac{(S1_W + S2_W)^2}{2\vartheta\sqrt{S1_W^2 + S2_W^2}}\right| \tag{3.14}$$

Then, in case WM is suppressed in *FLAWS1*:

$$SNR_W \xrightarrow[S1_W \ll S2_W]{} \left|\frac{S2_W}{2\vartheta}\right| \tag{3.15}$$

Likewise,

$$SNR_C \xrightarrow[S1_C \gg S2_C]{} \left|\frac{S1_{CSF}}{2\vartheta}\right| \tag{3.16}$$

These two formulas show that the SNR of WM (resp. CSF) in the *FLAWS-HC* will tend towards half the SNR of WM (resp. CSF) in *FLAWS2* (resp. *FLAWS1*). Thus, since WM (resp. CSF) is the tissue with the higher SNR in *FLAWS2* (resp. *FLAWS1*), the SNR of the *FLAWS-HC* will be higher than that of the *FLAWS-Div*, for both WM and CSF.

3.5 Results

Signal simulations for the optimization of the FLAWS sequence at 1.5T yielded the following parameters: $TR/TI_1/TI_2 = 3.50/0.37/1.03\,s$, $TE = 2.08\,ms$, $\alpha_1/\alpha_2 = 6°/9°$. FLAWS images were acquired with a $1.25 \times 1.25 \times 1.4\,mm$ resolution and a $300\,Hz/px$ bandwidth, for a total scan time of 10:26 mins.

An example of axial head *FLAWS1* and *FLAWS2* images acquired on one of the six volunteers is shown in Figure 3.1. A good suppression of the WM signal and CSF signal was noticeable in *FLAWS1* and *FLAWS2* respectively.

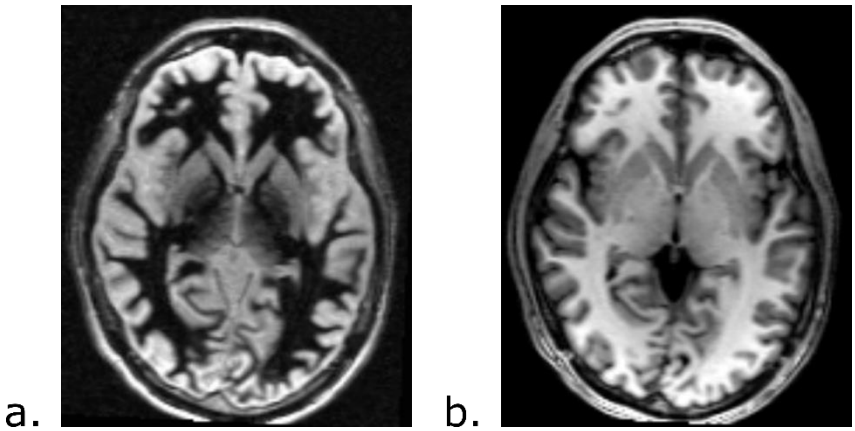

Figure 3.1. MRI axial brain images acquired with the FLAWS sequence. a. FLAWS1; b. FLAWS2.

Figure 3.2 shows a zoom-in of a *FLAWS1* image at the level of the globus pallidus; the separation between the GPi and the GPe is clearly identifiable (oblique, continuous arrow), similarly to the original study performed at 3T. The quality of the WM suppression in *FLAWS1* and CSF suppression in *FLAWS2*, combined with the good visualization of the GPi and GPe, demonstrates that the FLAWS sequence parameters were well optimized for data acquisition at 1.5T. In Figure 3.2, the novel image combination *FLAWS-HC* is also illustrated. The enhanced contrast between GM and CSF (dashed, vertical arrow) is noteworthy.

The results of the quantitative analysis are presented Table 3.1. In the acquired images, i.e., *FLAWS1* and *FLAWS2*, the values of the CNR between brain tissues are similar to those obtained in the work performed at 3T, where the FLAWS sequence was introduced. Thus, the results of Table 3.1 further validate the optimization of FLAWS sequence parameters at 1.5 T, carried out in the current study. In addition, the results of Table 3.1 show that the *FLAWS-HC* yields an enhanced CNR between brain tissues when compared to the previously proposed image combination, *FLAWS-Div.*

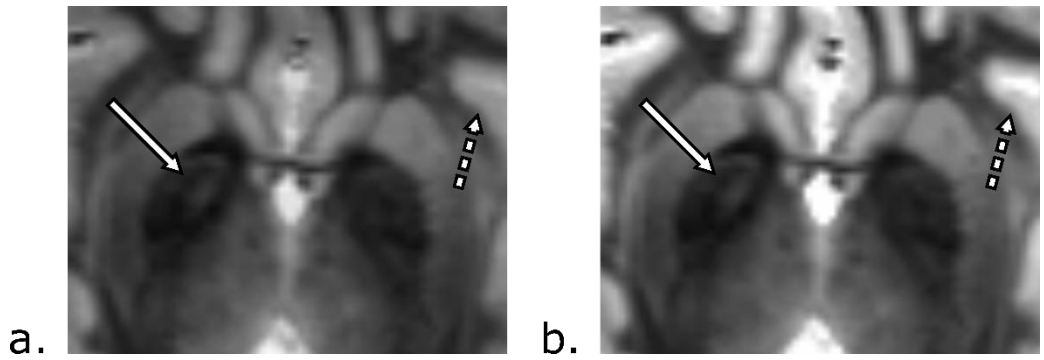

Figure 3.2. Zoom-in of the Basal Ganglia. The acquired image FLAWS1 (a) is shown on the left and the novel image combination FLAWS-HC (b) is illustrated on the right. The oblique, continuous arrow indicates the separation between the internal and the external Globus Pallidus. The dashed, vertical arrow shows the enhanced GM/CSF contrast in the FLAWS-HC.

Axial head images of the *FLAWS-Div* and *FLAWS-HC* are presented in Figure 3.3. This figure also shows that MPRAGE-like contrasts can be obtained by computing the inverse of *FLAWS-Div* and the opposite of *FLAWS-HC.*

Table 3.1. Mean contrast (CN) and contrast-to-noise ratio (CNR) between brain tissues for both acquired (FLAWS1 and FLAWS2) and combined FLAWS images (FLAWS-Div and FLAWS-HC). Data were acquired on six healthy volunteers.

	FLAWS1	*FLAWS2*	*FLAWS-Div*	*FLAWS-HC*
			CN	
WM/GM	0.81 (0.77 – 0.84)	0.24 (0.22 – 0.27)	0.88 (0.85 – 0.90)	0.71 (0.62 – 0.83)
WM/CSF	0.84 (0.81 – 0.86)	0.84 (0.80 – 0.91)	0.99 (0.99 – 0.99)	1.00 (1.00 – 1.00)
GM/CSF	0.09 (0.00 – 0.15)	0.76 (0.70 – 0.86)	0.85 (0.79 – 0.92)	1.00 (1.00 – 1.00)
			CNR	
WM/GM	13.0 (10.7 – 14.9)	10.3 (7.5 – 13.2)	11.2 (6.5 – 15.0)	14.8 (11.2 – 17.7)
WM/CSF	17.6 (14.1 – 19.2)	22.3 (15.6 – 35.3)	2.0 (0.8 – 3.5)	19.6 (13.9 – 26.9)
GM/CSF	2.9 (0.1 – 5.3)	13.3 (9.3 – 21.0)	1.9 (0.7 – 3.1)	10.3 (7.0 – 16.4)

WM: white matter; GM: gray matter; CSF: cerebrospinal fluid. *In-vivo* measurements were performed in the corpus callosum (splenium) for WM, caudate nucleus (head) for GM and lateral ventricles for the CSF. Ranges of *in-vivo* CN and CNR are presented in parenthesis.

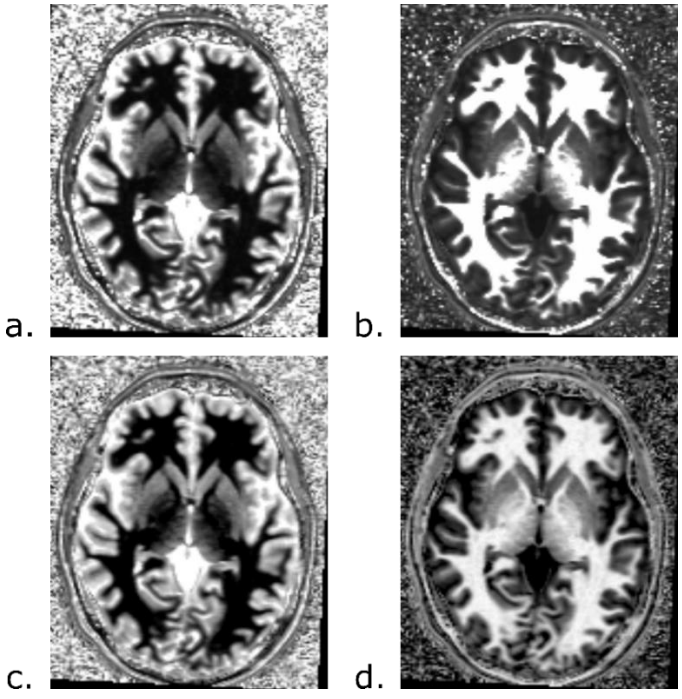

Figure 3.3. The image combination FLAWS-Div (a) and FLAWS-HC (c). The inverse of FLAWS-Div (b) and the opposite of FLAWS-HC (d) is also shown.

3.6 Discussion

In this paper, we propose a set of parameters for FLAWS imaging of the brain at 1.5T, which is of interest for preoperative DBS planning as most of the centers performing DBS are equipped with 1.5T scanners [3], [5]. This set of parameters was optimized to provide a good visualization of the Basal Ganglia in FLAWS1 and a good CNR between brain tissues in FLAWS2, and was validated by both qualitative and quantitative analysis.

In the current work we have also introduced a novel image combination, *FLAWS-HC*. The previously proposed *FLAWS-Div*, which is currently used for preoperative DBS planning [3], is characterized by a low CNR, despite its enhanced CN between brain tissues. The *FLAWS-HC* allows to overcome this limitation, obtaining both an enhanced CN and CNR. The theoretical arguments and quantitative measurements illustrated in the current study indicate that the *FLAWS-HC* may improve preoperative DBS planning. The CNR of *FLAWS-HC* is similar to the one of *FLAWS2*. However, the separation between the GPe and the GPi cannot be clearly identified in *FLAWS2*, due to the low WM/GM CN of *FLAWS2*. In addition, *FLAWS-HC* images are free of received bias field, T2* and proton density, similar to the MP2RAGE combination image [2]. This suggests that FLAWS could be of interest for ultra-high field imaging, especially for detection of epileptogenic zones in focal cortical dysplasia [4].

Computing the opposite of the *FLAWS-HC* provides an MPRAGE-like contrast, potentially allowing automated segmentation methods designed for MPRAGE to be used from FLAWS scans. This feature, in combination with the contrast enhancement and bias field independence, strongly indicates that the *FLAWS-HC* could be exploited for brain segmentation at ultra-high field.

3.7 References

[1] M. Tanner *et al.*, “Fluid and white matter suppression with the MP2RAGE sequence,” *J. Magn. Reson. Imaging*, vol. 35, no. 5, pp. 1063–1070, May 2012.

[2] J. P. Marques, T. Kober, G. Krueger, W. van der Zwaag, P.-F. Van de Moortele, and R. Gruetter, “MP2RAGE, a self bias-field corrected sequence for improved segmentation and T1-mapping at high field,” *Neuroimage*, vol. 49, no. 2, pp. 1271–1281, Jan. 2010.

[3] E. Bannier *et al.*, “FLAWS imaging improves depiction of the thalamic subregions for DBS planning in epileptic patients,” in *The International Society for Magnetic Resonance in Medicine (ISMRM)*, 2018.

[4] X. Chen *et al.*, “Gray-matter-specific MR imaging improves the detection of epileptogenic zones in focal cortical dysplasia: A new sequence called fluid and white matter suppression (FLAWS),” *NeuroImage Clin.*, vol. 20, pp. 388–397, Jan. 2018.

[5] E. Jiltsova *et al.*, “Imaging of Anterior Nucleus of Thalamus Using 1.5T MRI for Deep Brain Stimulation Targeting in Refractory Epilepsy,” *Neuromodulation Technol. Neural Interface*, vol.19, pp. 812–817, Dec. 2016.

Chapter 4
Multi T1-weighted contrast MRI with Fluid and White matter Suppression (FLAWS) at 1.5T

4.1 Foreword

In this chapter we describe the work published in the journal Magnetic Resonance Imaging in 2019. The major novelty of this work was the presentation of a profit function, which fully models the MP2RAGE signals, to find the optimal FLAWS parameters at 1.5T. These parameters improved the quality of the images compared to the parameters presented at the ISBI conference (Chapter 3).

4.2 Abstract

Introduction: The fluid and white matter suppression sequence (FLAWS) provides two T1-weighted co-registered datasets: a white matter (WM) suppressed contrast (*FLAWS1*) and a cerebrospinal fluid (CSF) suppressed contrast (*FLAWS2*). FLAWS has the potential to improve the contrast of the subcortical brain regions that are important for Deep Brain Stimulation surgery planning. However, to date FLAWS has not been optimized for 1.5T.

In this study, the FLAWS sequence was optimized for use at 1.5T. In addition, the contrast-enhancement properties of FLAWS image combinations were investigated using two voxel-wise FLAWS combined images: the division (*FLAWS-div*) and the high contrast (*FLAWS-hc*) image.

Methods: FLAWS sequence parameters were optimized for 1.5T imaging using an approach based on the use of a profit function under constraints for brain tissue signal and contrast maximization. MR experiments were performed on eleven healthy volunteers (age 18-30). Contrast (CN) and contrast to noise ratio (CNR) between brain tissues were measured in each volunteer. Furthermore, a qualitative assessment was performed to ensure that the separation between the internal globus pallidus (GPi) and the external globus pallidus (GPe) is identifiable in *FLAWS1*.

Results: The optimized set of sequence parameters for FLAWS at 1.5T provided contrasts similar to those obtained in a previous study at 3T. The separation between the GPi and the GPe was clearly identified in *FLAWS1*. The CN of *FLAWS-hc* was higher than that of *FLAWS1* and *FLAWS2*, but was not different from the CN of *FLAWS-div*. The CNR of *FLAWS-hc* was higher than that of *FLAWS-div*.

Conclusion: Both qualitative and quantitative assessments validated the optimization of the FLAWS sequence at 1.5T. Quantitative assessments also showed that *FLAWS-hc* provides an enhanced contrast compared to *FLAWS1* and *FLAWS2*, with a higher CNR than *FLAWS-div*.

4.3 Introduction

The acquisition of magnetic resonance (MR) images with different contrasts (T1, T2, diffusion, …) is today a standard procedure in both research and clinical practice. Typically, images are acquired in separate measurements and then pre-processing steps -such as co-registration- are needed to spatially normalize the data before analysis. In this context, magnetic resonance imaging (MRI) sequences that provide, in a single acquisition, co-registered datasets with different contrasts are of interest to reduce the amount of data processing and to minimize loss of information due to interpolation and other possible confounding effects.

The fluid and white matter suppression (FLAWS) sequence [1], derived from the magnetization-prepared two rapid gradient-echoes (MP2RAGE) sequence [2], was introduced to provide two co-registered T1-weighted images of the brain with different contrasts in a single acquisition. The first contrast (*FLAWS1*) is characterized by the suppression of the white matter (WM) signal, yielding an image with a contrast similar to the one provided by the fast gray matter acquisition T1 inversion recovery (FGATIR) sequence [3]. The WM-suppressed contrast can be used to improve the visualization of basal ganglia structures such as the globus pallidus [4–6] and to detect epileptogenic lesions in focal cortical dysplasia [7]. The second contrast (*FLAWS2*) is similar to the contrast obtained with the magnetization-prepared rapid gradient-echo (MPRAGE) sequence [8]. This contrast is considered as being the standard T1-weighted anatomical contrast of the brain, with a suppression of the cerebrospinal fluid (CSF) signal.

A recent study performed at 3T showed that FLAWS imaging allows for a good visualization of basal ganglia structures and facilitates deep brain stimulation (DBS) surgery planning [6]. However, most of the centers performing DBS employ 1.5T MR systems [9,10]. These centers would benefit from the use of FLAWS for surgery planning, but to the best of our knowledge there is no study reporting the optimization of FLAWS imaging at 1.5T.

The co-registration properties of the MP2RAGE and FLAWS images allow to perform voxel-wise operations for generating new sets of images characterized by new T1 contrasts. Van de Moortele et al. [11] and Marques et al. [2] investigated the properties of the voxel-wise division of MP2RAGE images. They determined that the result of this image combination was free of signal variations induced by the received bias field ($B1^-$), proton density (M_0) and $T2^*$. Division images were also used by Bannier et al. [6] in the case of FLAWS, but the signal properties of the FLAWS division image were not investigated. Another image combination was proposed by Tanner et al. [1] to provide a gray matter specific contrast by computing the voxel-wise minimum of FLAWS images. FLAWS image combinations were also used by Wang et al. to develop a fast brain tissue segmentation method [12].

In this context, the aim of the current study was twofold. The first aim was to determine the optimal sequence parameters of FLAWS for 1.5T MR imaging. Given the complexity and the multi-parametric nature of this sequence optimization, an approach based on the use of a profit function was employed. The second aim of this study was to investigate the properties of FLAWS voxel-wise division images and to propose an improved approach for combining FLAWS images for tissue contrast enhancement.

4.4 Materials and methods

4.4.1 Sequence optimization

The goal of this optimization was to obtain FLAWS images at 1.5T with a contrast similar to that obtained at 3T by Tanner et al. [1], that is, a WM-suppressed contrast in *FLAWS1* and a CSF-suppressed contrast in *FLAWS2*. The quality of the optimization was assessed using the standard definition of the contrast (CN) and contrast-to-noise ratio (CNR) [1].

The signal of *FLAWS1* and *FLAWS2* depends on the following set of sequence parameters (Φ):

$$\Phi = [\alpha_1, \alpha_2, TI_1, TI_2, TR_{GRE}, TR_{Seq}, N_{Ex}] \quad 4.1$$

where α_1 and α_2 are the flip angles of the Gradient Echo (GRE) modules, acquired at two different inversion times, TI_1 and TI_2, TR_{GRE} is the repetition time of the GRE modules, TR_{Seq} is the sequence repetition time, corresponding to the time interval between two consecutive inversion pulses and N_{Ex} is the number of excitations per GRE module. We define as Φ_{opt} the set of parameters which provides the optimal contrasts for FLAWS at 1.5T, i.e. contrasts similar to those obtained at 3T by Tanner et al. [1].

Given the complexity and the multi-parametric nature of the FLAWS signal, we proposed a novel strategy for the optimization of the FLAWS sequence. The optimization was performed in two steps. In the first step, an approach based on the use of a profit function was employed to determine pre-optimal parameter sets. In the second step, the optimal set was selected among the pre-optimal sets by maximizing the contrast between brain tissues.

In the following formulae, we will use the subscripts *W*, *G*, *GP* and *C* to denote white matter, grey matter, the globus pallidus and cerebrospinal fluid, respectively.

4.4.1.1 Profit function

The profit function P was defined to: (1) suppress the WM signal in *FLAWS1* ($S1_W$) while facilitating the visualization of the globus pallidus -this is accomplished by increasing the profit when $(S1_{GP} - S1_W)$ increases; (2) suppress the CSF signal in *FLAWS2* ($S2_C$) by decreasing the profit when $S2_C$ increases; (3) maximize the CNR between brain tissues by increasing the profit when the sum $S1_G + S1_C + S2_W + S2_G$ is increasing. Based on the aforementioned criteria, the profit function P was written as:

$$P_m^k(\Phi) = k\big(S1_{GP}(\Phi) - S1_W(\Phi)\big) - m\,S2_C(\Phi) + S1_G(\Phi) + S1_C(\Phi) + S2_W(\Phi) + S2_G(\Phi) \quad 4.2$$

where k and m are regularization parameters allowing to adjust the importance of the globus pallidus visualization and WM and CSF suppression in the optimization.

Profits were computed for every pair of regularization parameters (k, m), with both k and m varying between 0 and 100 (step-size: 1). Each couple (k, m) is associated to a pre-optimal set of parameters $\Phi_{opt}^{k,m}$ that maximizes the profit $P_m^k(\Phi)$.

4.4.1.2 Contrast maximization

Among all the pre-optimal parameter sets $\Phi_{opt}^{k,m}$, the optimal parameter set Φ_{opt} was defined as the one maximizing the sum of the simulated contrast between the tissues ($\sum CN = CN1_{W/G} + CN1_{W/C} + CN1_{G/C} + CN2_{W/G} + CN2_{W/C} + CN2_{G/C}$).

4.4.1.3 Signal simulations

The signal of *FLAWS1* and *FLAWS2* was simulated using the Bloch equations, implemented in *Mathematica (Wolfram Research, Inc, Champaign, IL, USA)*. Signal simulations were performed using 1.5T tissue properties reported in the literature [13–15]: T1 relaxation times were fixed to $0.65\ sec$ for WM, $0.75\ sec$ for the globus pallidus, $1.2\ sec$ for GM and $4\ sec$ for CSF; proton densities of WM, the globus pallidus, GM and CSF were respectively fixed to 0.7, 0.72, 0.8 and 1.

Based on preliminary MRI experiments, a voxel size of $1.25 \times 1.25 \times 1.4\ mm^3$ was considered to be the best compromise between SNR maximization and spatial resolution within a maximum acquisition time of 10 minutes. Consequently, the number of slices (N_{Slices}) was set to 128 and the matrix size was set to 180×192 to obtain a spatial coverage sufficiently large to avoid artefacts due to aliasing. The slice partial Fourier was set to $6/8$ to allow for the acquisition of FLAWS images with WM signal suppression [1]. According to the size of the matrix and the constraints on the acquisition time, the maximum sequence repetition time should not exceed $3.5\ sec$.

The optimization was performed on a wide range of parameter combinations, with α_1 and α_2 ranging from $3°$ to $13°$ (step-size $1°$); TI_1 ranging from $0.37\ sec$ to $1.41\ sec$ (step-size $0.02\ sec$); TI_2 ranging from $1\ sec$ to $3.2\ sec$ (step-size $0.02\ sec$); TR_{GRE} equals to $4.16\ msec$; TR_{Seq} ranging from $2.5\ sec$ to $3.5\ sec$ (step-size $0.1\ sec$); N_{Ex} equals to $6/8 * N_{Slices}$. With this choice of parameter combinations, we obtained 9×10^6 parameter sets Φ. Out of this pool, we selected 4×10^4 parameter sets Φ that provided the typical contrasts of the FLAWS, i.e. WM suppression in *FLAWS1* and CSF suppression in *FLAWS2*. From these 4×10^4 combinations, 10^4 pre-optimal parameter sets $\Phi_{opt}^{k,m}$ were determined using the profit function. Among these parameter sets $\Phi_{opt}^{k,m}$, the optimal parameter set Φ_{opt} was defined as the one maximizing the sum of the contrast $\sum CN$ between brain tissues.

4.4.2 Voxel-wise image combination

Voxel-wise image combinations of *FLAWS1* and *FLAWS2* were investigated to enhance the contrast between brain tissues. The metrics used to analytically compare different types of combinations were the contrast (CN) and the signal to noise ratio (SNR).

First, the properties of the FLAWS division image (*FLAWS-div*) were investigated. Then, a FLAWS-dedicated image-combination, denoted here as FLAWS high contrast image (*FLAWS-hc)*, was proposed.

For sake of clarity, mathematical demonstrations associated to the work presented in the following sections are provided in supplementary materials.

4.4.2.1 Properties of the division image (FLAWS-div)

FLAWS-div is computed using the voxel-wise operation:

$$Sdiv_A = \frac{S1_A}{S2_A} \qquad 4.3$$

where $S1_A$ ($S2_A$) is the signal of a given tissue A in *FLAWS1* (*FLAWS2*). It can be shown that the WM/GM, WM/CSF and GM/CSF contrasts are close to 1 in the division image (see supplementary materials). Additionally, mathematical demonstrations show that the SNR of WM and CSF is low in *FLAWS-div*.

4.4.2.2 Properties of the high contrast image (FLAWS-hc)

The high contrast image, *FLAWS-hc*, is obtained by computing the voxel-wise signed contrast between *FLAWS1* and *FLAWS2*:

$$Shc_A = \frac{S1_A - S2_A}{S1_A + S2_A} \quad 4.4$$

Therefore, *FLAWS-hc* values are included within the [-1,1] interval. It should be noted that *FLAWS-hc* is free of signal variations due to the received bias field, T2* relaxation and proton density [2].

It can be shown that the WM/CSF contrast is close to 1 in *FLAWS-hc.* In addition, either the WM/GM contrast or the GM/CSF contrast tends towards 1, according to the sign of $(S1_G - S2_G)$ (see supplementary materials). Mathematical demonstrations showed that the SNR of WM and CSF is higher in *FLAWS-hc* than in *FLAWS-div*.

Similarly to the *FLAWS-div* and the MP2RAGE-dedicated combination image [2,11], *FLAWS-hc* is characterized by the appearance of a salt and pepper noise in its background. This noise can be removed by adding coefficients in the voxel-wise operations [16]. A preliminary investigation on the high-contrast image was recently proposed for presentation at a conference [17] using a dataset of FLAWS images that, however, were not fully optimized.

4.4.3 MRI experiments and data analysis

To assess the results of the optimization, MR imaging was performed on eleven healthy volunteers (four females, age 18-30yo) with a 1.5T scanner (MAGNETOM Aera, Siemens Healthcare, Erlangen, Germany) equipped with a 20-receiver channel head and neck matrix coil, using the optimal parameter set Φ_{opt}. MR acquisitions were performed without parallel imaging for all the volunteers and with parallel imaging ($2x\ GRAPPA\ acelleration$) on a subset of four volunteers. All experiments were approved by the Institutional Review Board and the volunteers signed an informed consent form to be included in the study.

To compare the results of the current study with those obtained at 3T by Tanner et al. [1], the CN and CNR between brain tissues were measured in regions of interests (ROI) manually drawn in the corpus callosum (splenium) for WM, caudate nucleus (head) for GM and lateral ventricle for CSF. The size of the ROI was $46\ mm^3$ for each tissue, across all datasets. A qualitative assessment of the acquired images was performed to ensure that the separation between the internal globus pallidus (GPi) and the external globus pallidus (GPe) was identifiable in *FLAWS1*.

4.5 Results

The sum of the six simulated contrast ($\sum CN$), computed for each pre-optimal parameter set $\Phi_{opt}^{k,m}$, is illustrated in Figure 4.1. In this figure, we observe different plateaus, that is, regions where multiple pairs (k, m) yield the same value of $\sum CN$. A low value of $\sum CN$ was observed within the plateau around $(k = 0, m = 0)$, illustrated in dark blue color. A high value of $\sum CN$ was found within the plateau illustrated in orange color, containing the pair $(k = 100, m = 100)$. The maximum value of $\sum CN$ was found within the plateau illustrated in red color corresponding to the pair $(k = 44, m = 77)$. The associated set of parameters ($\Phi_{\text{opt}} = [\alpha_1, \alpha_2, TI_1, TI_2, TR_{GRE}, TR_{Seq}, N_{Ex}]$) is presented in Table 4.1.

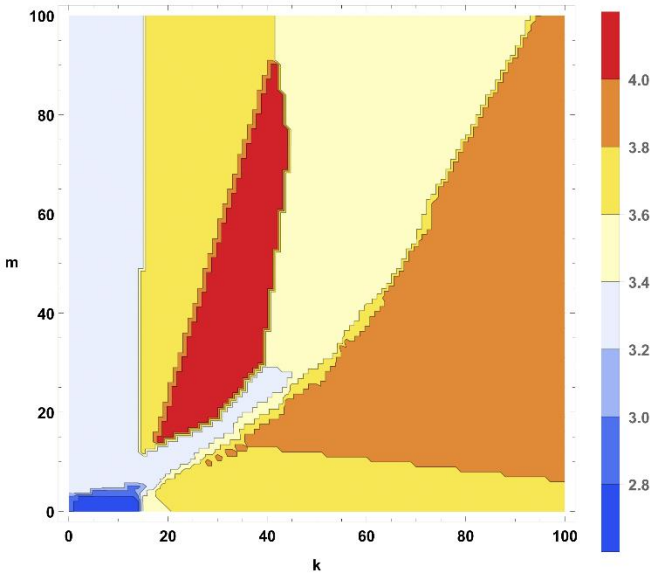

Figure 4.1. Sum of the simulated contrast between brain tissues for the pre-optimal parameter sets $\Phi_{opt}^{k,m}$ according to the pair of regularization parameters (k,m).

Table 4.1. Optimal parameters of the FLAWS sequence at 1.5T.

TR/TE ($msec$)	$3500/2.32$
TI ($msec$)	$403/1030$
Flip angles	$6°/10°$
Matrix	180×192
Slices	128
Resolution (mm^3)	$1.25 \times 1.25 \times 1.4$
BW (Hz/px)	240
Orientation	$Sagittal$
FOV (mm^2)	225×240
GRAPPA	$None$ (or $2x\ acceleration$)
Slice partial Fourier	$6/8$
Scan time ($min{:}\ sec$)	$10{:}\ 27$ (or $05{:}\ 50$)

Figure 4.2 shows the signal of *FLAWS1* and *FLAWS2* for pre-optimal sets of parameters associated to three different pairs of regularization parameters $(k,m{:}\ 0{,}0;\ 44{,}77;\ 100{,}100)$. The signal corresponding to the pair $(k = 0, m = 0)$ is characterized by a poor WM suppression in *FLAWS1* (dashed blue line) and a poor CSF suppression in *FLAWS2* (continuous blue line). The pair $(k = 100, m = 100)$ yields WM and GM signals with a very low intensity in *FLAWS2* (continuous orange line).

As opposed to the case of the two pairs presented above, the signal of the pair $(k = 44, m = 77)$ does not suffer from the aforementioned disadvantages. On the contrary, this signal is characterized by a good WM suppression in *FLAWS1* (dashed red line) and a good CSF suppression in *FLAWS2* (continuous red line). Moreover, the signals of WM and GM in *FLAWS2* have a high intensity (continuous red line).

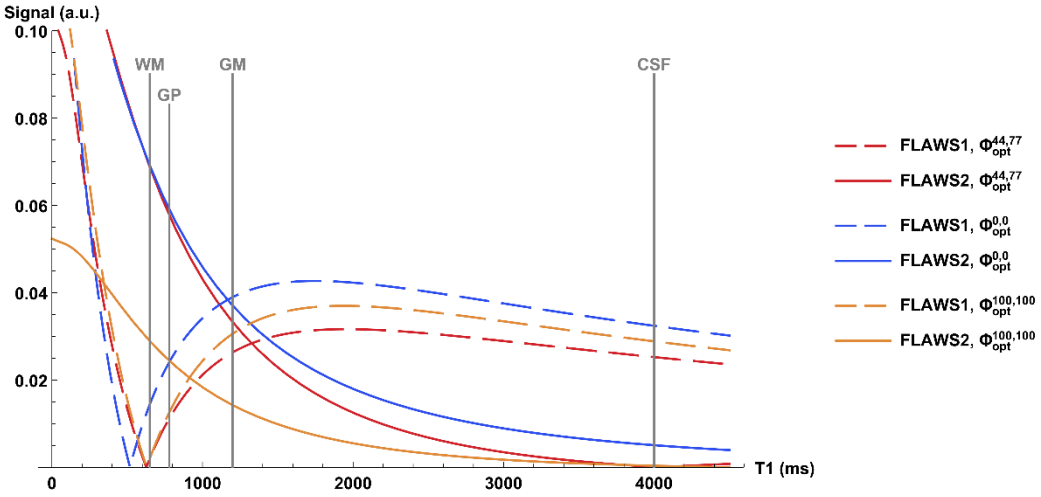

Figure 4.2. Signal simulation of FLAWS1 and FLAWS2 for the pre-optimal parameter sets $\Phi_{opt}^{k,m}$ corresponding to the pair of regularization parameters $(k = 44, m = 77)$, $(k = 0, m = 0)$ and $(k = 100, m = 100)$. WM: white matter; GP: globus pallidus; GM: gray matter; CSF: cerebrospinal fluid.

Figure 4.3 shows 1.5T FLAWS images acquired with the optimal set of parameters, corresponding to the pair $(k = 44, m = 77)$ and presented in Table 4.1. *FLAWS1* is characterized by an excellent WM suppression, as easily visualized on the sagittal view. An excellent CSF suppression was observed in *FLAWS2*. These images displayed a strong bias, as particularly evident in the sagittal views. For every set of FLAWS images, the separation between the GPe and the GPi was identified in *FLAWS1*, whereas it could not be identified in *FLAWS2*, as shown in Figure 4.4.

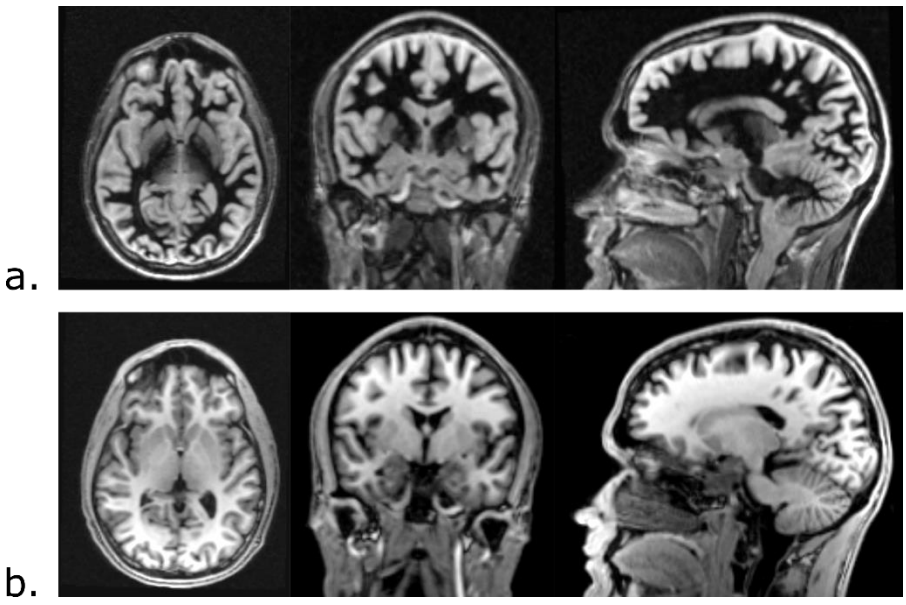

Figure 4.3. Axial (left), coronal (center) and sagittal (right) 1.5T FLAWS images acquired with the optimal set of parameters Φ_{opt}, presented in Table 4.1.

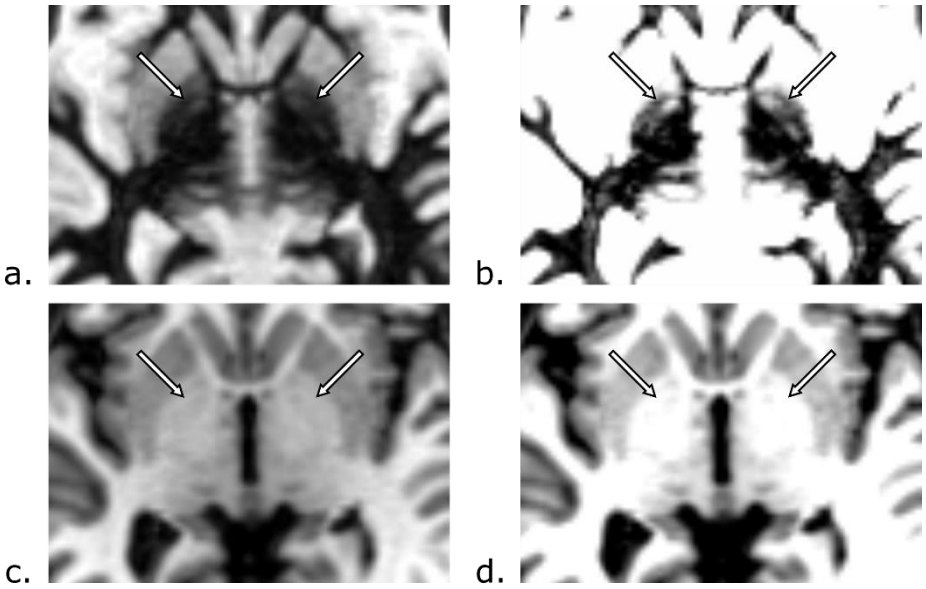

Figure 4.4. Visualization of the basal ganglia with FLAWS at 1.5T. The arrows indicate the location of the separation between the internal and the external globus pallidus. The identification of globus pallidus structures is easier in FLAWS1 (a) than in FLAWS2 (c). FLAWS1 and FLAWS2 images are also displayed with a saturated signal window (b, d) to better visualize the separation between the internal and the external globus pallidus in the printed version of the paper.

Table 4.2 presents the simulated and *in-vivo* values of contrast obtained at 1.5T with the optimal set of parameters indicated in Table 4.1. Results obtained at 3T by Tanner et al. [1] are also reported. The simulated contrast was consistent with the contrast measured *in-vivo* at 1.5T. A good agreement between the contrast reported at 1.5T and 3T was also found.

Table 4.2. Simulated and in-vivo values of contrast at 1.5T in FLAWS1 and FLAWS2. For reference, the values obtained at 3T by Tanner et al. are also shown [1].

	FLAWS1			*FLAWS2*		
Contrast	Simulation 1.5T	*In-vivo* 1.5T	*In-vivo* 3T [1]	Simulation 1.5T	*In-vivo* 1.5T	*In-vivo* 3T [1]
WM/GM	0.88	0.69 (0.59-0.84)	0.59 (0.51-0.69)	0.29	0.23 (0.19-0.28)	0.15 (0.13-0.16)
WM/CSF	0.90	0.75 (0.67-0.89)	0.68 (0.62-0.77)	1.00	0.88 (0.82-0.93)	0.83 (0.68-0.89)
GM/CSF	0.09	0.12 (0.08-0.19)	0.16 (0.13-0.17)	0.99	0.81 (0.72-0.89)	0.78 (0.60-0.86)
Total*	1.87	1.56 (1.39-1.91)	-	2.28	1.92 (1.77-2.04)	-

WM: White Matter, GM: Gray Matter, CSF: Cerebrospinal Fluid. *In-vivo* contrast measurements were performed in the corpus callosum (splenium) for WM, caudate nucleus (head) for GM and lateral ventricle for CSF. Ranges of *in-vivo* contrasts are presented in parentheses.

*Total is the mean sum of the contrast WM/GM, WM/CSF and GM/CSF calculated for each volunteer.

Figure 4.5 shows the image combinations *FLAWS-div* and *FLAWS-hc*. These images display an excellent WM suppression, similarly to *FLAWS1*. Furthermore, *FLAWS-div* and *FLAWS-hc* are also characterized by a high signal intensity of the CSF. Figure 4.6 highlights the contrast enhancement provided by *FLAWS-hc* compared to *FLAWS1*. For example, the enhanced GM/CSF contrast provides a clear separation between the cerebellum and the CSF. This separation is not identifiable in *FLAWS1*. Furthermore, *FLAWS-hc* provides an image with reduced bias compared to *FLAWS1*. This is noticeable when comparing the CSF signal in the cortical regions to the CSF signal nearby the cerebellum. Contrast-enhanced images with a contrast similar to *FLAWS2* can be obtained by computing the opposite of *FLAWS-hc* (*FLAWS-hco*), that is, multiplying *FLAWS-hc* by -1. As observed in *FLAWS-hc*, *FLAWS-hco* displays a contrast enhancement and a bias field reduction.

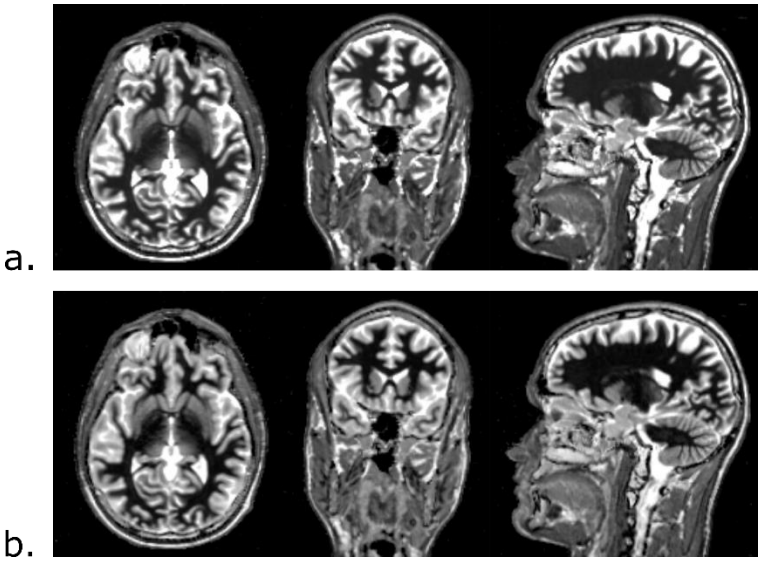

Figure 4.5. Axial (left), coronal (center) and sagittal (right) image combination FLAWS-div (first row) and FLAWS-hc (second row). These images were denoised by adding coefficients in the voxel-wise combinations [16].

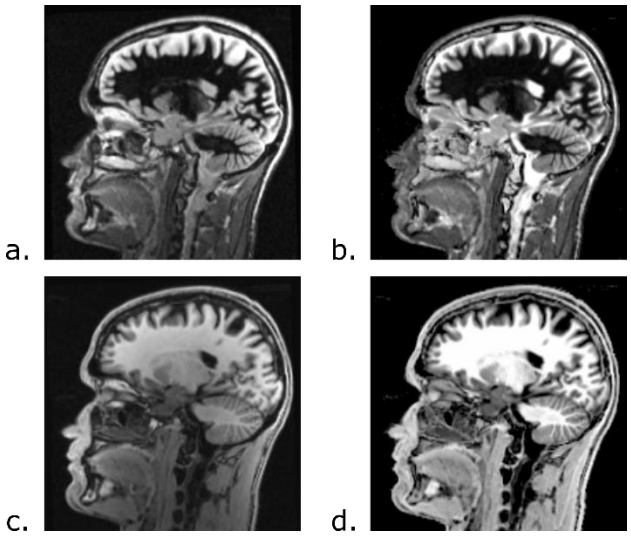

Figure 4.6. Sagittal views of FLAWS1 and FLAWS-hc (first row) and FLAWS2 and FLAWS-hco, the opposite of FLAWS-hc (second row).

Table 4.3 presents the CN and CNR of *FLAWS1, FLAWS2*, *FLAWS-div* and *FLAWS-hc*. The minimum total CN of *FLAWS-div* is higher than the maximum total CN of *FLAWS1* and *FLAWS2*. The minimum total CN of *FLAWS-hc* is also higher than the maximum total CN of *FLAWS1* and *FLAWS2*. The total CN of *FLAWS-hc* is not different from the total CN of *FLAWS-div*. However, the minimum total CNR of *FLAWS-hc* is higher than the maximum total CNR of *FLAWS-div*. *FLAWS-hc* is also characterized by a higher total CNR than *FLAWS1*. No difference was found between the total CNR of *FLAWS2* and *FLAWS-hc*.

Table 4.3. Average values of contrast (CN) and contrast to noise ratio (CNR) for the FLAWS sequence acquired with optimal parameters at 1.5T.

	FLAWS1	*FLAWS2*	*FLAWS-div*	*FLAWS-hc*
		CN		
WM/GM	0.69 (0.59-0.84)	0.23 (0.19-0.28)	0.80 (0.73-0.89)	0.58 (0.48-0.64)
WM/CSF	0.75 (0.67-0.89)	0.88 (0.82-0.93)	0.98 (0.97-0.99)	1.00 (1.00-1.00)
GM/CSF	0.12 (0.08-0.19)	0.81 (0.72-0.89)	0.87 (0.77-0.93)	1.00 (1.00-1.00)
TotalCN*	1.56 (1.39-1.91)	1.92 (1.77-2.04)	2.65 (2.51-2.77)	2.58 (2.48-2.64)
		CNR		
WM/GM	12.4 (8.6-15.7)	13.2 (10.4-17.7)	13.5 (9.0-18.4)	16.0 (11.8-22.1)
WM/CSF	19.2 (13.8-30.5)	33.7 (22.9-45.8)	3.1 (1.2-6.4)	27.4 (17.3-36.2)
GM/CSF	4.2 (1.9-7.0)	22.5 (14.2-29.5)	2.9 (1.1-5.9)	16.4 (10.0-22.8)
TotalCNR**	35.8 (25.5-52.0)	69.3 (49.2-87.6)	19.5 (12.7-30.8)	59.8 (39.2-79.0)

WM: White Matter, GM: Gray Matter, CSF: Cerebrospinal Fluid. CN and CNR measurements were performed in the corpus callosum (splenium) for WM, caudate nucleus (head) for GM and lateral ventricle for CSF. Ranges of *CN and CNR* are presented in parentheses.

*TotalCN is the mean sum of the contrast WM/GM, WM/CSF and GM/CSF calculated for each volunteer.

**TotalCNR is the mean sum of the contrast to noise ratios WM/GM, WM/CSF and GM/CSF calculated for each volunteer.

FLAWS images acquired with parallel imaging are characterized by a contrast similar to the one obtained without parallel imaging, as presented in Figure 4.7 and Supporting Information Table 4.1. Supporting Information Table 4.1 shows that the CNR between brain tissues remains high in parallel FLAWS images. However, the CNR provided by the parallel imaging FLAWS was slightly lower than the CNR of the standard FLAWS. This decrease in CNR hampered the visualization of basal ganglia structures in parallel imaging FLAWS images, as shown in Supporting Information Figure 4.1.

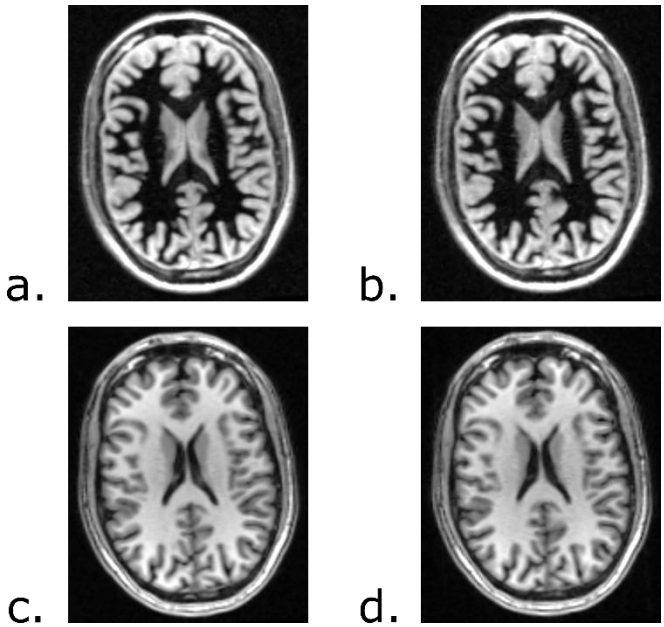

Figure 4.7. Examples of FLAWS1 (top row) and FLAWS2 (bottom row) images acquired at 1.5T without parallel imaging (a, c) and with parallel imaging (b, d).

An incidental finding (periventricular GM heterotopia) was found in one of the volunteers. The contrast enhancement provided by *FLAWS-hc* allowed to better identify the incidental finding compared to *FLAWS1* and *FLAWS2* (Figure 4.8). This incidental finding was also clearly identified in the FLAWS minimum image (*FLAWS-min*). FLAWS images acquired with parallel imaging also allowed to identify the periventricular GM heterotopia, as shown in Supporting Information Figure 4.2.

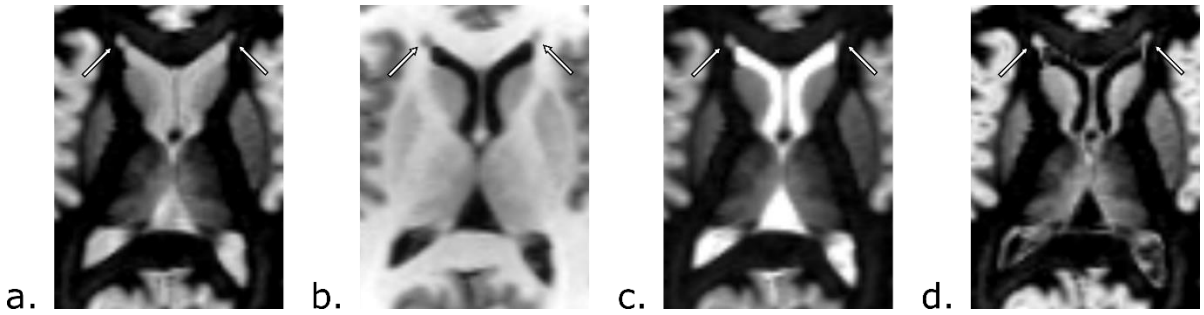

Figure 4.8. Axial FLAWS images showing an incidental finding (periventricular GM heterotopia) observed in one volunteer. The contrast enhancement provided by FLAWS-hc allows to better identify the incidental finding. This incidental finding was also clearly identified in the FLAWS minimum image (FLAWS-min).

4.6 Discussion

In this study, we optimized FLAWS imaging at the field strength of 1.5T. The optimization was carried out by performing signal simulations using the Bloch equations and applying a strategy that employs a profit function. FLAWS images were acquired *in vivo*, with the most favorable set of sequence parameters obtained by the optimization procedure. Qualitative and quantitative assessment of FLAWS images at 1.5T validated the optimization approach proposed in this study. Furthermore, the co-registration properties of *FLAWS1* and *FLAWS2* provided us the opportunity of investigating image combinations (*FLAWS-div* and *FLAWS-hc*).

The choice of a novel MRI optimization approach, relying on the use of a profit function, was driven by the multiparametric nature of the problem. As a matter of fact, the signal intensity in FLAWS depends on seven parameters $[\alpha_1, \alpha_2, TI_1, TI_2, TR_{GRE}, TR_{Seq}, N_{Ex}]$; moreover, the same set of parameters has to provide different targeted contrasts in two sets of images, *FLAWS1* and *FLAWS2*.

The optimization consisted of three steps: (i) the sequence parameters providing a simulated contrast similar to FLAWS at 3T were extracted from a wide range of sets; (ii) among the sets of parameters extracted in step (i), pre-optimal sets were selected by maximizing a profit function aimed at tailoring the WM and CSF signal suppression in the optimization; and (iii) the optimal set was chosen from the pre-optimal sets to maximize the simulated contrast between brain tissues. To obtain *FLAWS1* images where the separation between the GPe and the GPi is identifiable, the profit function was designed to suppress the WM and, at the same time, to maximize the difference between the globus pallidus and WM.

The MRI experiments performed on healthy volunteers at 1.5T validated the results of our optimization procedure. An excellent WM and CSF signal suppression was observed in *FLAWS1* and *FLAWS2*, respectively. The values of the contrast measured *in-vivo* at 1.5T were consistent with the simulated values and with the values reported at 3T [1]. From a qualitative point of view, the optimal parameters of FLAWS at 1.5T allowed to identify the separation between the GPe and the GPi in *FLAWS1*. This could be of interest for DBS surgery planning at 1.5T, which is the field strength employed by most of the centers performing DBS [9,10].

In the current study, we investigated FLAWS-dedicated image combinations. First, the properties of the division image *FLAWS-div* were presented. It was shown, by theoretical arguments and quantitative measurements, that the contrast between brain tissues in *FLAWS-div* tends towards 1. A previous study investigated the use of FLAWS imaging, and specifically *FLAWS-div,* at 3T for DBS surgery planning. In this study, the authors exploited the enhanced contrast of *FLAWS-div* to visualize the basal ganglia. However, we showed in the current study that *FLAWS-div* is characterized by a poor SNR in both WM and CSF, leading to a low CNR between brain tissues.

To overcome the CNR limitation of *FLAWS-div*, a new combination image, *FLAWS-hc,* was proposed. Mathematical demonstrations and quantitative measurements showed that *FLAWS-hc* is characterized by a high CN and CNR between brain tissues. Furthermore, *FLAWS-hc* has a contrast similar to *FLAWS1*, but provides a better differentiation of GM structures from the CSF thanks to its contrast-enhancement properties. In addition, the incidental periventricular GM heterotopia observed in the FLAWS images of a volunteer highlights the interest of FLAWS for clinical applications. In particular, the contrast provided by the FLAWS combination images, *FLAWS-hc* and *FLAWS-min*, represents an added value in clinical settings.

FLAWS-hc images are characterized by a signal free of T2* relaxation, proton density and received bias field, similarly to the MP2RAGE combination image [2]. The comparison between *FLAWS1* and *FLAWS-hc* highlights the bias field reduction obtained in *FLAWS-hc*. The opposite of *FLAWS-hc* (*FLAWS-hco*) provides a CSF signal suppression, as the MPRAGE images and the MP2RAGE combination images. Like the MP2RAGE combination image, *FLAWS-hco* is free of T2* relaxation, proton density and received bias field and thus could be of interest for brain segmentation at ultra-high fields.

A previous study performed at 3T showed the relevance of FLAWS imaging for the detection of epileptogenic zones in focal-cortical dysplasia [7] and suggested that 7T FLAWS imaging might improve the detection of epileptogenic zones. Our investigation of the combination-images indicates that the contrast-enhancement and bias field reduction of *FLAWS-hc* provide an added value for FLAWS imaging at ultra-high fields. It should be noted that the transmitted-bias field affects the signal of *FLAWS-hc.* This aspect should be carefully taken into account for the optimization and implementation of FLAWS at ultra-high fields.

In the current study, in addition to the 10-min FLAWS protocol without parallel imaging, a 6-min protocol ($2x\ GRAPPA\ acceleration$) was tested. The shorter protocol yielded images of diagnostic quality similar to the long protocol, as highlighted by the unequivocal observation of the incidental finding. As such, the 6-min FLAWS protocol is of potential interest for diagnostic purposes; however, the CNR decrease induced by the use of *GRAPPA* acceleration techniques hampered the identification of the different basal ganglia structures. Thus, the 6-min protocol cannot be used for DBS surgery planning, where an accurate basal ganglia structures identification is required.

The current study has some limitations. First, MRI experiments were performed only on a small number of young volunteers. In future studies, it will be necessary to acquire data on a large cohort of patients, in order to assess the impact of FLAWS imaging on DBS surgery planning at 1.5T. Furthermore, as opposed to the division image *FLAWS-div*, the newly proposed combination image *FLAWS-hc* is not readily available on the MRI console, that is, is not yet reconstructed online on the user interface of the MR systems; as such, the combination image *FLAWS-hc* needs to be computed offline. The FLAWS protocol proposed in the current study for DBS surgery planning takes 10 minutes. Compressed sensing techniques could be employed to decrease the protocol acquisition time. However, these techniques were not readily available on the clinical system used in the current study.

In conclusion, we optimized FLAWS brain imaging at 1.5T for a potential application to DBS surgery planning. In addition, the co-registration properties of FLAWS images were exploited to generate the combination image *FLAWS-hc*, which is characterized by an enhanced contrast between brain tissues. With a signal free of T2* relaxation, proton density and received bias field, *FLAWS-hc* can be of interest for ultra-high field imaging.

4.7 Supplementary materials

Voxel-wise image combinations of *FLAWS1* and *FLAWS2* were investigated to enhance the contrast between brain tissues. The metrics used to analytically compare different types of combinations were the contrast (CN):

$$CN_{A/B} = \frac{|S_A - S_B|}{|S_A| + |S_B|} \qquad 4.5$$

and the signal to noise ratio (SNR):

$$SNR_A = \frac{S_A}{\vartheta} \tag{4.6}$$

where S_A (S_B) is the mean signal of a given tissue A (B), and ϑ is the noise level of the image. The noise level of combination images was determined using the error propagation of the noise levels in *FLAWS1* and *FLAWS2*, which were assumed to be equal.

4.7.1 Properties of the division image (*FLAWS-div*)

The *FLAWS-div* image is computed using the voxel-wise operation:

$$Sdiv_A = \frac{S1_A}{S2_A} \tag{4.7}$$

where $S1_A$ ($S2_A$) is the signal of a given tissue A in *FLAWS1* (*FLAWS2*). The contrast between WM and GM in the division image is defined as:

$$CNdiv_{W/G} = \frac{\left|\frac{S1_W}{S2_W} - \frac{S1_G}{S2_G}\right|}{\left|\frac{S1_W}{S2_W}\right| + \left|\frac{S1_G}{S2_G}\right|} \tag{4.8}$$

Considering that WM is suppressed in *FLAWS1*, the ratio $S1_W/S2_W$ is close to zero:

$$CNdiv_{W/G} \xrightarrow[S1_W \ll S2_W]{} 1 \tag{4.9}$$

Following the same principle and considering that the CSF is suppressed in *FLAWS2*, the WM/CSF and GM/CSF contrasts are close to one.

Error propagation allowed to compute the SNR of WM in the division image:

$$SNRdiv_W = \frac{S1_W}{S2_W} \times \frac{1}{\vartheta\sqrt{\frac{S1_W^2 + S2_W^2}{S2_W^4}}} \tag{4.10}$$

with ϑ the noise level in *FLAWS1* and *FLAWS2*. The WM signal is suppressed in *FLAWS1*, leading to:

$$SNRdiv_W \xrightarrow[S1_W \ll S2_W]{} \frac{S1_W}{S2_W} \times \frac{1}{\vartheta\sqrt{\frac{S2_W^2}{S2_W^4}}} = \frac{S1_W}{\vartheta} \tag{4.11}$$

Similarly, the SNR of CSF in the division image is close to $S2_C/\vartheta$ as the CSF is suppressed in *FLAWS2*. The SNR of WM (resp. CSF) is low in the division image as its value is close to the value of the SNR of WM in *FLAWS1* (resp. CSF in *FLAWS2*), while WM (resp. CSF) is suppressed in *FLAWS1* (resp. *FLAWS2*).

4.7.2 Properties of the high contrast image (*FLAWS-hc*)

The high contrast image, *FLAWS-hc*, is computed by measuring the voxel-wise signed contrast between *FLAWS1* and *FLAWS2*:

$$Shc_A = \frac{S1_A - S2_A}{S1_A + S2_A} \tag{4.12}$$

The WM/GM contrast of *FLAWS-hc* is computed as:

$$CNhc_{W/G} = \frac{\left|\frac{S1_W - S2_W}{S1_W + S2_W} - \frac{S1_G - S2_G}{S1_G + S2_G}\right|}{\left|\frac{S1_W - S2_W}{S1_W + S2_W}\right| + \left|\frac{S1_G - S2_G}{S1_G + S2_G}\right|} \tag{4.13}$$

Leading to:

$$CNhc_{W/G} \xrightarrow[S1_W \ll S2_W]{} \frac{\left|-1 - \frac{S1_G - S2_G}{S1_G + S2_G}\right|}{1 + \left|\frac{S1_G - S2_G}{S1_G + S2_G}\right|} \tag{4.14}$$

Case $S1_G \geq S2_G$:

$$CNhc_{W/G} \xrightarrow[S1_W \ll S2_W]{} \frac{\left|\frac{-S1_G - S2_G - S1_G + S2_G}{S1_G + S2_G}\right|}{\frac{S1_G + S2_G + S1_G - S2_G}{S1_G + S2_G}} \tag{4.15}$$

$$CNhc_{W/G} \xrightarrow[S1_W \ll S2_W]{} \frac{|-2S1_G|}{2S1_G} = 1 \tag{4.16}$$

Case $S1_G < S2_G$:

$$CNhc_{W/G} \xrightarrow[S1_W \ll S2_W]{} \frac{\left|\frac{-S1_G - S2_G - S1_G + S2_G}{S1_G + S2_G}\right|}{\frac{S1_G + S2_G + S2_G - S1_G}{S1_G + S2_G}} \tag{4.17}$$

$$CNhc_{W/G} \xrightarrow[S1_W \ll S2_W]{} \frac{|-2S1_G|}{2S2_G} = \frac{S1_G}{S2_G} \tag{4.18}$$

The GM/CSF contrast of *FLAWS-hc* is computed as:

$$CNhc_{G/C} = \frac{\left|\frac{S1_C - S2_C}{S1_C + S2_C} - \frac{S1_G - S2_G}{S1_G + S2_G}\right|}{\left|\frac{S1_C - S2_C}{S1_C + S2_C}\right| + \left|\frac{S1_G - S2_G}{S1_G + S2_G}\right|} \tag{4.19}$$

Leading to:

$$CNhc_{G/C} \xrightarrow[S1_C \gg S2_C]{} \frac{\left|1 - \frac{S1_G - S2_G}{S1_G + S2_G}\right|}{1 + \left|\frac{S1_G - S2_G}{S1_G + S2_G}\right|} \quad 4.20$$

Case $S1_G \geq S2_G$:

$$CNhc_{G/C} \xrightarrow[S1_C \gg S2_C]{} \frac{\left|\frac{S1_G + S2_G}{S1_G + S2_G} - \frac{S1_G - S2_G}{S1_G + S2_G}\right|}{\frac{S1_G + S2_G + S1_G - S2_G}{S1_G + S2_G}} \quad 4.21$$

$$CNhc_{G/C} \xrightarrow[S1_C \gg S2_C]{} \frac{2S2_G}{2S1_G} = \frac{S2_G}{S1_G} \quad 4.22$$

Case $S1_G < S2_G$:

$$CNhc_{G/C} \xrightarrow[S1_C \gg S2_C]{} \frac{\left|\frac{S1_G + S2_G}{S1_G + S2_G} - \frac{S1_G - S2_G}{S1_G + S2_G}\right|}{\frac{S1_G + S2_G + S2_G - S1_G}{S1_G + S2_G}} \quad 4.23$$

$$CNhc_{W/C} \xrightarrow[S1_W \ll S2_W]{} \frac{2S2_G}{2S2_G} = 1 \quad 4.24$$

The WM/CSF contrast is always close to 1 in *FLAWS-hc* when WM is suppressed in *FLAWS1* and CSF is suppressed in *FLAWS2*. The SNR of WM in *FLAWS-hc* is defined as:

$$SNRhc_W = \left| \frac{S1_W - S2_W}{S1_W + S2_W} \times \frac{1}{2\vartheta \sqrt{\frac{S1_W^2 + S2_W^2}{(S1_W + S2_W)^4}}} \right| \quad 4.24$$

$$SNRhc_W = \left| \frac{S1_W - S2_W}{2\vartheta} \times \frac{1}{\sqrt{\frac{S1_W^2 + S2_W^2}{(S1_W + S2_W)^2}}} \right| \quad 4.24$$

Leading to:

$$SNRhc_W \xrightarrow[S1_W \ll S2_W]{} \left| \frac{S2_W}{2\vartheta} \times \frac{1}{\sqrt{\frac{S2_W^2}{(S2_W)^2}}} \right| = \left| \frac{S2_W}{2\vartheta} \right| \quad 4.24$$

Similarly:

$$SNRhc_C \xrightarrow[S1_C \gg S2_C]{} \left|\frac{S1_C}{2\vartheta}\right| \qquad 4.24$$

The SNR of WM (CSF) in *FLAWS-hc* is close to half the SNR of WM (CSF) in *FLAWS2* (*FLAWS1*). Then, considering that the signal of WM is suppressed in *FLAWS1* and that the signal of CSF is suppressed in *FLAWS2*, the SNR of WM and CSF is lower in *FLAWS-div* than in *FLAWS-hc.*

Supporting Information Table 4.1. Average values of contrast (CN) and contrast to noise ratio (CNR) for the FLAWS sequence acquired without parallel imaging ($no\ GRAPPA$) and with parallel imaging ($2x\ GRAPPA\ acceleration$) on a subset of 4 volunteers. No difference was noticed between the contrast of FLAWS images acquired with and without parallel imaging. The CNR remains high in the case of parallel imaging, but was slightly lower than the one provided by images acquired without parallel imaging.

	FLAWS1		*FLAWS2*		*FLAWS-hc*	
	$no\ GRAPPA$	$2x\ GRAPPA$	$no\ GRAPPA$	$2x\ GRAPPA$	$no\ GRAPPA$	$2x\ GRAPPA$
			CN			
WM/GM	0.66 (0.61 – 0.75)	0.68 (0.63 – 0.80)	0.22 (0.18 – 0.26)	0.21 (0.19 – 0.24)	0.58 (0.51 – 0.65)	0.57 (0.51 – 0.65)
WM/CSF	0.72 (0.68 – 0.79)	0.74 (0.69 – 0.83)	0.86 (0.79 – 0.92)	0.86 (0.83 – 0.88)	1.00 (1.00 – 1.00)	1.00 (1.00 – 1.00)
GM/CSF	0.11 (0.08 – 0.15)	0.12 (0.08 – 0.16)	0.79 (0.69 – 0.88)	0.79 (0.74 – 0.82)	1.00 (1.00 – 1.00)	1.00 (1.00 – 1.00)
			CNR			
WM/GM	10.8 (9.4 – 12.7)	10.1 (7.7 – 11.4)	10.9 (7.9 – 13.2)	9.9 (8.7 – 11.4)	13.5 (11.0 – 16.4)	12.8 (9.6 – 15.3)
WM/CSF	16.6 (14.9 – 19.3)	14.4 (11.9 – 16.4)	27.7 (20.6 – 36.2)	22.6 (16.4 – 27.6)	23.1 (17.5 – 31.4)	18.3 (15.3 – 20.4)
GM/CSF	3.4 (2.5 – 4.7)	3.0 (2.1 – 4.5)	21.5 (12.6 – 37.0)	15.9 (11.8 – 19.7)	13.9 (9.9 – 20.9)	10.9 (8.8 – 13.5)

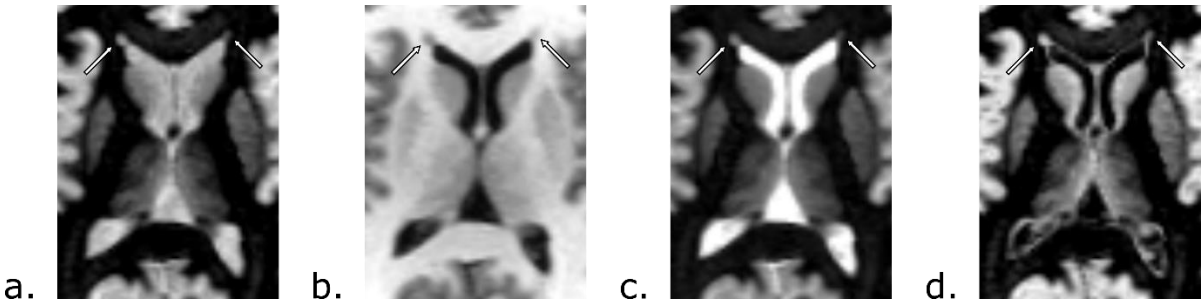

Supporting Information Figure 4.2. Axial FLAWS images –acquired with parallel imaging– showing an incidental finding (periventricular GM heterotopia) observed in one volunteer. The quality of the FLAWS parallel images was sufficient to clearly identify the incidental finding.

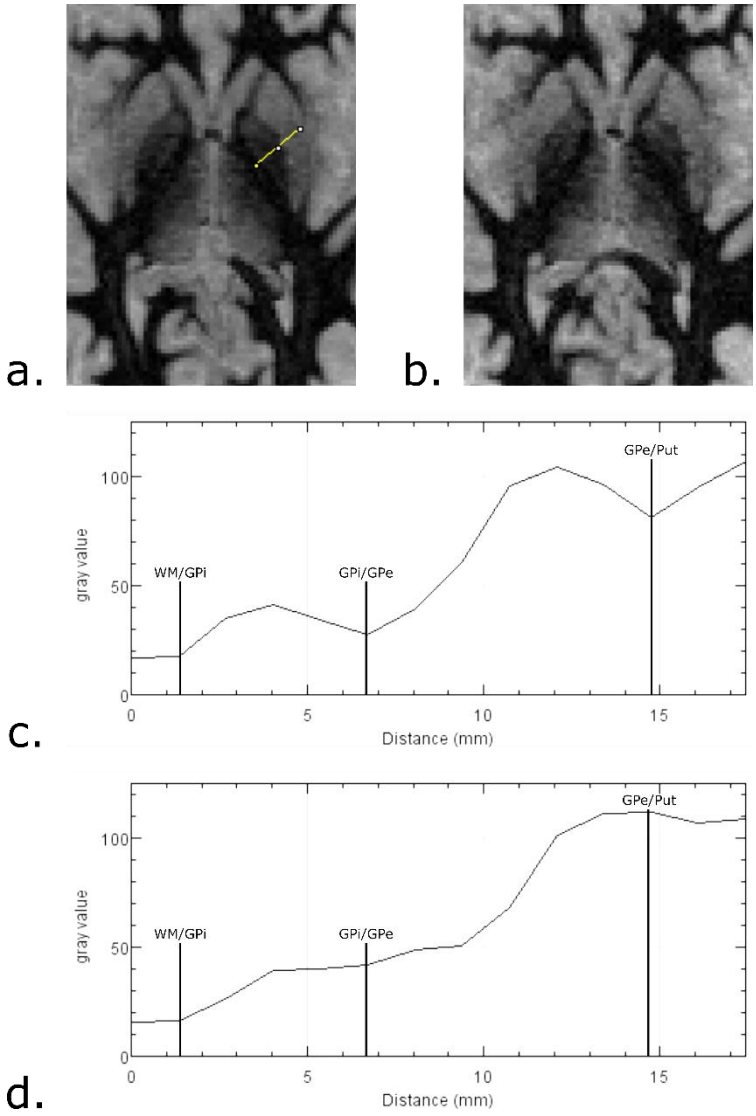

Supporting Information Figure 4.1. Visualization of the basal ganglia with FLAWS images acquired without parallel imaging (a) and with parallel imaging (b). Intensity profiles of the transition from white matter to the putamen (yellow line in Figure 4.1a.) are plotted for acquisitions performed without parallel imaging (c) and with parallel imaging (d). The separation between the white matter (WM), the internal globus pallidus (GPi), the external globus pallidus (GPe) and the putamen (Put) are clearly identifiable in FLAWS acquired without parallel imaging (a,c). The separation between these structures is more blurry in the images acquired with parallel imaging turned on (b,d).

4.8 References

[1] Tanner M, Gambarota G, Kober T, Krueger G, Erritzoe D, Marques JP, et al. Fluid and white matter suppression with the MP2RAGE sequence. J Magn Reson Imaging 2012;35:1063–70. doi:10.1002/jmri.23532.

[2] Marques JP, Kober T, Krueger G, van der Zwaag W, Van de Moortele P-F, Gruetter R. MP2RAGE, a self bias-field corrected sequence for improved segmentation and T1-mapping at high field. Neuroimage 2010;49:1271–81. doi:10.1016/j.neuroimage.2009.10.002.

[3] Sudhyadhom A, Haq IU, Foote KD, Okun MS, Bova FJ. A high resolution and high contrast MRI for differentiation of subcortical structures for DBS targeting: The Fast Gray Matter Acquisition T1 Inversion Recovery (FGATIR). Neuroimage 2009;47:T44–52. doi:10.1016/j.neuroimage.2009.04.018.

[4] Martin-Bastida A, Ward RJ, Newbould R, Piccini P, Sharp D, Kabba C, et al. Brain iron chelation by deferiprone in a phase 2 randomised double-blinded placebo controlled clinical trial in Parkinson's disease. Sci Rep 2017;7:1398. doi:10.1038/s41598-017-01402-2.

[5] Niccolini F, Haider S, Reis Marques T, Muhlert N, Tziortzi AC, Searle GE, et al. Altered PDE10A expression detectable early before symptomatic onset in Huntington's disease. Brain 2015;138:3016–29. doi:10.1093/brain/awv214.

[6] Bannier E, Gambarota G, Ferre J-C, Kober T, Nica A, Chabardes S, et al. FLAWS imaging improves depiction of the thalamic subregions for DBS planning in epileptic patients. Int. Soc. Magn. Reson. Med., 2018.

[7] Chen X, Qian T, Kober T, Zhang G, Ren Z, Yu T, et al. Gray-matter-specific MR imaging improves the detection of epileptogenic zones in focal cortical dysplasia: A new sequence called fluid and white matter suppression (FLAWS). NeuroImage Clin 2018;20:388–97. doi:10.1016/J.NICL.2018.08.010.

[8] Mugler JP, Brookeman JR. Three-dimensional magnetization-prepared rapid gradient-echo imaging (3D MP RAGE). Magn Reson Med 1990;15:152–7.

[9] Jiltsova E, Möttönen T, Fahlström M, Haapasalo J, Tähtinen T, Peltola J, et al. Imaging of Anterior Nucleus of Thalamus Using 1.5T MRI for Deep Brain Stimulation Targeting in Refractory Epilepsy. Neuromodulation Technol Neural Interface 2016;19:812–7. doi:10.1111/ner.12468.

[10] Larson PS, Richardson RM, Starr PA, Martin AJ. Magnetic Resonance Imaging of Implanted Deep Brain Stimulators: Experience in a Large Series. Stereotact Funct Neurosurg 2008;86:92–100. doi:10.1159/000112430.

[11] Van de Moortele P-F, Auerbach EJ, Olman C, Yacoub E, Uğurbil K, Moeller S. T1 weighted brain images at 7 Tesla unbiased for Proton Density, T2 contrast and RF coil receive B1 sensitivity with simultaneous vessel visualization. Neuroimage 2009;46:432–46. doi:10.1016/J.NEUROIMAGE.2009.02.009.

[12] Wang Y, Wang Y, Zhang Z, Xiong Y, Zhang Q, Yuan C, et al. Segmentation of gray matter, white matter, and CSF with fluid and white matter suppression using MP2RAGE. J Magn

Reson Imaging 2018. doi:10.1002/jmri.26014.

[13] Wright PJ, Mougin OE, Totman JJ, Peters AM, Brookes MJ, Coxon R, et al. Water proton T 1 measurements in brain tissue at 7, 3, and 1.5T using IR-EPI, IR-TSE, and MPRAGE: results and optimization. Magn Reson Mater Physics, Biol Med 2008;21:121–30. doi:10.1007/s10334-008-0104-8.

[14] Rooney WD, Johnson G, Li X, Cohen ER, Kim S-G, Ugurbil K, et al. Magnetic field and tissue dependencies of human brain longitudinal1H2O relaxation in vivo. Magn Reson Med 2007;57:308–18. doi:10.1002/mrm.21122.

[15] Vymazal J, Righini A, Brooks RA, Canesi M, Mariani C, Leonardi M, et al. T1 and T2 in the Brain of Healthy Subjects, Patients with Parkinson Disease, and Patients with Multiple System Atrophy: Relation to Iron Content. Radiology 1999;211:489–95. doi:10.1148/radiology.211.2.r99ma53489.

[16] O 'brien KR, Kober T, Hagmann P, Maeder P, Marques J, Lazeyras F, et al. Robust T1-Weighted Structural Brain Imaging and Morphometry at 7T Using MP2RAGE 2014. doi:10.1371/journal.pone.0099676.

[17] Beaumont J, Saint-Jalmes H, Acosta O, Kober T, Tanner M, Ferré J-C, et al. High Contrast T1-Weighted MRI with Fluid and White Matter Suppression Using MP2RAGE. IEEE Int. Symp. Biomed. Imaging, Venice, Italy: 2019.

Chapter 5
High resolution multi T1-weighted contrast and T1 mapping with low $\boldsymbol{B1^+}$ sensitivity using the Fluid And White matter Suppression (FLAWS) sequence at 7T

5.1 Foreword
In this chapter, we describe the work published in the journal Magnetic Resonance in Medicine. The major novelty of this work was to show that the FLAWS sequence allows for T1 mapping. Another novelty was the 7T FLAWS sequence parameters optimization using the profit function introduced in Chapter 4.

5.2 Abstract
Purpose: To demonstrate that FLAWS imaging can be used for high resolution T1 mapping with low transmitted bias field ($B1^+$) sensitivity at 7T.

Methods: The FLAWS sequence was optimized for $0.8\ mm$ isotropic resolution imaging. The theoretical accuracy and precision of the FLAWS T1 mapping was compared to the one of the MP2RAGE sequence optimized for low $B1^+$ sensitivity. FLAWS images were acquired at 7T on 6 healthy volunteers (age: 21-48 years old, 2 females). MP2RAGE and SA2RAGE datasets were also acquired to obtain T1 mapping references and $B1^+$ maps. The contrast to noise ratio (CNR) between brain tissues was measured in the *FLAWS-hco* and *MP2RAGE-uni* images. The Pearson correlation was measured between the MP2RAGE and FLAWS T1 maps. The effect of $B1^+$ on FLAWS T1 mapping was assessed using the Pearson correlation.

Results: The *FLAWS-hco* images are characterized by a higher brain tissue CNR ($CNR_{WM/GM} = 5.5, CNR_{WM/CSF} = 14.7, CNR_{GM/CSF} = 10.3$) than the *MP2RAGE-uni* images ($CNR_{WM/GM} = 4.9,\ CNR_{WM/CSF} = 6.6,\ CNR_{GM/CSF} = 3.7$). The theoretical accuracy and precision of the FLAWS T1 mapping ($acc = 91.9\%; prec = 90.2\%$) were in agreement with the ones provided by the MP2RAGE T1 mapping ($acc = 90.0\%; prec = 86.8\%$). A good agreement was found between *in-vivo* T1 values measured with the MP2RAGE and FLAWS sequences ($r = 0.91$). A weak correlation was found between the FLAWS T1 map and the $B1^+$ map within cortical GM and white matter segmentations ($r_{WM} = -0.026; r_{GM} = 0.081$).

Conclusion: The results from this study suggest that FLAWS is a good candidate for high resolution T1-weighted imaging and T1 mapping at the field strength of 7T.

5.3 Introduction
The increased signal available from 7T magnetic resonance (MR) imaging has significant clinical potential for the study of human brain structures, enabling improvements in resolution and/or signal to noise ratio of the acquired data [1]. However, 7T MR imaging is characterized by an increase in the transmitted ($B1^+$) and received ($B1^-$) bias fields, which affect image

quality and interpretation. To help address this limitation, the magnetization prepared two rapid gradient echoes (MP2RAGE) sequence was developed to reduce the $B1$ sensitivity of T1-weighted images [2]. This sequence is designed to acquire two gradient echo (GRE) images that are co-registered and combined to provide a T1-weighted image -named *MP2RAGE-uni*- that is free of $T2^*$ relaxation, proton density (M_0) and $B1^-$. In addition, T1 maps can be generated using lookup tables of the *MP2RAGE-uni* signal, enhancing the utility of the MP2RAGE sequence compared to the MPRAGE sequence for longitudinal and multi-center studies [3–5].

Marques et al. showed that the *MP2RAGE-uni* signal can be highly $B1^+$ dependent according to the parameters used to acquire the GRE images [2,6]. Thus, the reproducibility of the T1 mapping and cortical thickness measurements can be hampered by the increased transmitted bias field typical from 7T imaging [6,7]. To overcome this limitation, Marques et al. proposed a set of parameters to reduce the $B1^+$ sensitivity of the 7T MP2RAGE sequence, at the cost of limiting its resolution and contrast to noise ratio (CNR) [6]. In addition, MP2RAGE scans can be post-hoc $B1^+$ corrected to increase the reliability of T1 and cortical thickness measurements [6,7].

The two 3D datasets acquired in MP2RAGE have limited clinical utility [2]. Consequently, Tanner et al. proposed a new MP2RAGE optimization scheme, called fluid and white matter suppression (FLAWS), which was designed to acquire two co-registered 3D datasets with clinical relevance [8]. The FLAWS sequence provides i) a white matter (WM) suppressed contrast in the first 3D dataset and ii) a cerebrospinal fluid (CSF) suppressed contrast in the second 3D dataset, which we will refer to as *FLAWS1* and *FLAWS2,* respectively. In terms of clinical utility, the *FLAWS1* contrast facilitates the visualization of deep gray matter structures [8,9]. *FLAWS2* provides a standard T1-weighted anatomical contrast [10]. In addition, a gray matter (GM) specific contrast can be obtained by computing the voxel-wise minimum between *FLAWS1* and *FLAWS2.* This GM specific contrast is similar in purpose to the T2-weighted double inversion recovery (DIR) contrast [11], which is used to detect WM and intracortical lesions in multiple sclerosis (MS) [12]. These FLAWS properties suggest that this sequence has potential for the detection and segmentation of brain lesions [8,13,14]. The FLAWS sequence was also shown to be of interest to visualize basal ganglia structures [15,16] and to perform brain tissue segmentation [17].

Despite the potential clinical interest provided by the FLAWS sequence, its use was limited for 7T imaging as it could not provide a bias reduced T1-weighted image and its associated T1 map. Recent studies at 1.5T proposed a new combination image, named *FLAWS-hc*, to obtain a bias reduced T1-weighted contrast with the FLAWS sequence [9,18]. However, the possibility of measuring the T1 relaxation time with *FLAWS-hc* was not investigated.

In this context, the current study aimed at 1) optimizing the FLAWS sequence for $0.8\,mm$ isotropic resolution 7T acquisition with a FLAWS dedicated optimization method previously used at 1.5T [9]; 2) assessing if the *FLAWS-hc* combination image provides a T1-weighted contrast with reduced $B1$ sensitivity at 7T and 3) showing that the FLAWS sequence can be used to generate high resolution T1 maps with low $B1^+$ sensitivity at 7T.

5.4 Methods

5.4.1 FLAWS sequence optimization

The FLAWS sequence was optimized at the field strength of 7T using an optimization method previously used for FLAWS at 1.5T imaging [9]. This optimization method was designed to provide high CNR images with a suppression of the WM (respectively CSF) signal in *FLAWS1* (resp. *FLAWS2*), while ensuring that the signal of the basal ganglia structures, particularly the globus pallidus, is not suppressed in *FLAWS1*. In accordance with the previous FLAWS studies [8,9], the globus pallidus was used as a structure of reference in the current study to ensure that the WM signal suppression does not hamper the visualization of deep GM structures in *FLAWS1*, as FLAWS imaging intends to provide a good visualization of deep GM structures for DBS surgery planning [8,15].

The optimization was performed in two steps: 1) a profit function was maximized under constraints to select multiple pre-optimal parameter sets characterized by a high brain tissue signal in FLAWS images, except for the signals of WM in *FLAWS1* and CSF in *FLAWS2*, which were minimized; 2) the optimal set of parameters was extracted from the pre-optimal parameter sets by maximizing the sum of *FLAWS1* and *FLAWS2* brain tissue contrasts.

FLAWS1 and *FLAWS2* signals were simulated by solving the Bloch equations of the MP2RAGE sequence. Simulations were performed using *Mathematica (Wolfram Research, Inc, Champaign, IL, USA)*. The following T1 relaxation times were used to simulate FLAWS signals: $1050\ ms$ for WM, $1347\ ms$ for the globus pallidus, $1850\ ms$ for GM and $4000\ ms$ for CSF [2,19]. The proton densities of WM, the globus pallidus, GM and CSF were assumed to value 0.7, 0.72, 0.8 and 1, respectively.

The optimization was designed to allow FLAWS images to be acquired with $0.8\ mm$ isotropic resolution within 10 minutes. To avoid aliasing artifacts and to reduce the acquisition time, images were acquired in the sagittal direction with a matrix size of 300×300 and 192 slices. A slice partial Fourier of 6/8 was used to shorten the minimum first inversion time, thus allowing to suppress the WM signal in *FLAWS1* [8]. Increasing the sequence repetition time allows to increase the signal to noise ratio (SNR) of FLAWS images [8,9]. Therefore, the sequence repetition time was set to $5\ secs$ to maximize the SNR while ensuring an acquisition time of 10 minutes according to the resolution constraints. Parallel imaging was used to speed up the acquisition ($3x\ GRAPPA\ acceleration$).

The optimization was performed with a brute-force search to maximize the profit function and select the optimal parameter set. Sets were defined for a wide range of parameter combinations, with α_1 and α_2, the flip angles of the sequence, ranging from $3°$ to $13°$ (step-size $1°$); TI_1, the first inversion time, ranging from $0.26\ sec$ to $1.80\ sec$ (step-size $0.02\ sec$); TI_2, the second inversion time, ranging from $1.05\ sec$ to $4.47\ sec$ (step-size $0.02\ sec$); TR_{GRE}, the gradient echo repetition time, equals to $5.6\ msec$; TR_{Seq}, the sequence repetition time, equals to $5\ sec$ and N_{Ex}, the number of excitations, equals to 144 ($6/8 \times numberOfSlices$).

5.4.2 Contrast generation with the FLAWS sequence

The *FLAWS-uni* image was reconstructed by default by the MR system, with:

$$S_{uni} = \frac{Real({S1_C}^*\ S2_C)}{|{S1_C}^2| + |{S2_C}^2|} \qquad 5.1$$

Where $S1_C$ (resp. $S2_C$) denote the complex signal of *FLAWS1* (resp. *FLAWS2*), and $*$ designs the complex conjugate.

The signal of the FLAWS minimum image (*FLAWS-min*), characterized by the suppression of both WM and CSF signals, was computed as follow [8]:

$$S_{min} = \frac{\min(S1, S2)}{S1 + S2} \quad 5.2$$

With $S1$ and $S2$ the magnitude of the *FLAWS1* and *FLAWS2* signals, respectively. The signal of *FLAWS-hc* was computed using the following equation [18]:

$$S_{hc} = \frac{S1 - S2}{S1 + S2} \quad 5.3$$

Due to the design of the FLAWS sequence, the *FLAWS-uni*, *FLAWS-min* and *FLAWS-hc* signals are independent from the $T2^*$ relaxation, M_0 and $B1^-$ [2,18].

The contrast of *FLAWS-hc* is similar to the contrast of *FLAWS1*, with a suppression of the WM signal [18]. A bias reduced standard T1-weighted contrast can be obtained by computing the opposite of *FLAWS-hc*, named *FLAWS-hco*:

$$S_{hco} = \frac{S2 - S1}{S1 + S2} \quad 5.4$$

The reconstruction of the *FLAWS-min, FLAWS-hc* and *FLAWS-hco* images from the magnitude of the *FLAWS1* and *FLAWS2* signals leads to a loss of contrast compared to image reconstructions from complex signals. The contrast lost from the magnitude reconstruction was recovered using the sign information of the *FLAWS-uni* signal (refer to the supplementary materials for more information).

FLAWS-uni, FLAWS-min, FLAWS-hc and FLAWS-hco are characterized by an enhanced background noise [18] and were denoised by adding coefficients in the image combinations [20].

5.4.3 T1 mapping with the FLAWS sequence

Providing that *FLAWS-hc* is independent from the $T2^*$ relaxation, M_0 and $B1^-$ [18], the T1 relaxation time should be measurable with the FLAWS sequence using lookup tables of the *FLAWS-hc* signal. The *FLAWS-hc* signal was reconstructed offline using the magnitude of the *FLAWS1* and *FLAWS2* signals. This leads to T1 mapping ambiguities, as *FLAWS1* and *FLAWS2* signals with opposite signs would have the same intensity in *FLAWS-hc,* while they correspond to signals with different T1 relaxation times. The T1 mapping ambiguities induced by the *FLAWS-hc* signal were solved using the sign information of the *FLAWS-uni* signal (refer to the supplementary materials section “Contrast loss and T1 mapping ambiguities” and Supporting Information Figure 5.1 for more information).

5.4.4 Simulation experiments

The effect of $B1^+$ on the T1 measurements provided by the FLAWS sequence was assessed using Monte-Carlo experiments. The signals of *FLAWS1* and *FLAWS2* were simulated as follow:

$$\mathrm{S1} = f_1\left(\Gamma_{B1^+} \times \alpha_1, \Gamma_{B1^+} \times \alpha_2, TI_1, TI_2, TR_{GRE}, TR_{Seq}, N_{Ex}, t1\right) + \sigma_{\mathcal{N}1} \quad 5.5$$

$$\mathrm{S2} = f_2\left(\Gamma_{B1^+} \times \alpha_1, \Gamma_{B1^+} \times \alpha_2, TI_1, TI_2, TR_{GRE}, TR_{Seq}, N_{Ex}, t1\right) + \sigma_{\mathcal{N}2} \quad 5.6$$

With f_1 (resp. f_2) a function determined by solving the Bloch equations of the FLAWS sequence to simulate *FLAWS1* (resp. *FLAWS2*) signal at the center of the *k-space*. Γ_{B1^+} is a random variable following a gamma distribution tailored to fit the brain $B1^+$ values measured in the current study (refer to the supplementary materials for more information). The random variables $\sigma_{\mathcal{N}1}$ and $\sigma_{\mathcal{N}2}$ follow a Normal distribution with a mean of 0 and a standard deviation of $S2_{WM}/25$ to simulate FLAWS images with a SNR of 25.

Monte Carlo experiments were performed for every T1 value ranging from $900\,ms$ to $2500\,ms$ (step-size: $1\,ms$) by simulating 1000 FLAWS signals per T1 value. These Monte-Carlo experiments were used to compute the theoretical accuracy and precision of the FLAWS T1 mapping (mathematical equations provided in supplementary materials).

In order to decouple the effect of the SNR and the $B1^+$ on the T1 mapping, the theoretical accuracy and precision of the T1 measurements were respectively computed in three different simulation cases: case 1) signals simulated with a SNR of 25 and without $B1^+$ ($\Gamma_{B1^+} = 1$); case 2) signals simulated with an infinite SNR ($\sigma_{\mathcal{N}1} = \sigma_{\mathcal{N}2} = 0$) and with $B1^+$; and case 3) signals simulated with a SNR of 25 and with $B1^+$.

For comparison, the theoretical accuracy and precision of the MP2RAGE T1 mapping were computed by simulating Monte-Carlo experiments with the same $B1^+$ and noise distributions as the ones used to simulate FLAWS data.

5.4.5 *In-vivo* experiments

5.4.5.1 MRI acquisition

Experiments were performed on six healthy volunteers (age: 21-48 years old, 2 females) with a 7T whole body MRI research scanner (Siemens Healthcare, Erlangen, Germany) equipped with a 32 channel head coil (Nova Medical, Wilmington, USA). All experiments were performed under written informed consent and were approved by the institutional review board.

A $B1^+$ map was acquired for each volunteer using the SA2RAGE sequence [21]. Then, MP2RAGE and FLAWS images were acquired. The MP2RAGE sequence was acquired with parameters that had been optimized to obtain an *MP2RAGE-uni* signal with low $B1^+$ sensitivity [6]. The FLAWS parameters were those obtained from the optimization outlined in the current study. It should be noted that the MP2RAGE optimization [6] used in this study provided a lower resolution ($1mm$ isotropic) than the FLAWS optimization ($0.8mm$ isotropic). The parameters used for the SA2RAGE, MP2RAGE and FLAWS acquisitions are presented in Table 5.1.

5.4.5.2 FLAWS sequence optimization and contrast generation

The optimized 7T FLAWS sequence was qualitatively and quantitatively assessed using the *in-vivo* experiments on healthy volunteers. To be consistent with the qualitative assessments performed in the previous FLAWS optimization studies [8,9], the images acquired in the current study were reviewed to ensure that the separation between the external globus pallidus (*GPe*) and the internal globus pallidus (*GPi*) was clearly identified in *FLAWS1*. The quantitative assessment was performed by measuring the contrast (CN) and contrast to noise ratio per unit of time (CNR) between brain tissues in *FLAWS1* and *FLAWS2*. The CN and CNR were computed as follows:

Table 5.1. Proposed FLAWS sequence parameters for 7T imaging. The parameters used to acquire the MP2RAGE and SA2RAGE data in this study are also shown.

Sequence	FLAWS	MP2RAGE	SA2RAGE
TR/TE ($msec$)	$5000/2.04$	$6000/2.16$	$2400/0.95$
TI ($msec$)	$620/1430$	$800/2700$	$106/1800$
Flip angles	$4°/8°$	$3°/4°$	$6°/10°$
Matrix	300×300	240×240	64×64
Slices	192	160	48
Resolution (mm^3)	$0.8 \times 0.8 \times 0.8$	$1.0 \times 1.0 \times 1.0$	$4.0 \times 4.0 \times 4.0$
BW (Hz/px)	370	300	490
Orientation	$Sagittal$	$Sagittal$	$Sagittal$
FOV (mm^2)	240×240	240×240	256×232
$GRAPPA$	3	3	$None$
Slice partial Fourier	$6/8$	$6/8$	$6/8$
Scan time ($min: sec$)	$10: 02$	$10: 02$	$1: 28$

$$CN_{A/B} = \frac{|S_A - S_B|}{|S_A| + |S_B|} \quad 5.7$$

$$CNR_{A/B} = \frac{|S_A - S_B|}{\sqrt{\frac{\sigma_A^2 + \sigma_B^2}{2}}} \times \frac{1}{\sqrt{TR}} \quad 5.8$$

With S_A (resp. S_B) and σ_A (resp. σ_B) the mean and the standard deviation of a given tissue A (resp. B) and TR the sequence repetition time. The means and standard deviations of WM, GM and CSF were respectively measured in regions of interest (ROIs) manually drawn in the corpus callosum (splenium), the caudate nucleus (head) and the lateral ventricles. The SNR of WM was measured in *FLAWS2* using the following equation:

$$SNR = \frac{S2_W}{\sigma 2_W} \quad 5.9$$

With $S2_W$ and $\sigma 2_W$ the mean and the standard deviation of the WM signal in *FLAWS2*.

The CNs and CNRs between brain tissues of *FLAWS-uni*, *FLAWS-min* and *FLAWS-hco* were measured *in-vivo* and compared with the CNs and CNRs measured in *FLAWS1* and *FLAWS2*. The CN and CNR values of *FLAWS-hc* are not presented in this paper as they are equal to the CN and CNR values of *FLAWS-hco* ($S_{hc} = -1 \times S_{hco}$). The CNs and CNRs of *MP2RAGE-uni*, generated with the MP2RAGE sequence, were also computed. To compare the MP2RAGE-uni and FLAWS-hco CNRs, while *MP2RAGE-uni* and *FLAWS-hco* are characterized by different resolutions, a specific care was taken to ensure than no partial volume voxels were included in the ROIs used to compute the CNR.

5.4.5.3 T1 mapping

The SA2RAGE data was spatially normalized on the MP2RAGE and FLAWS data by registering the second 3D dataset to the second MP2RAGE and FLAWS 3D datasets. The registrations were performed using a block-matching rigid registration algorithm (Anima, RRID:SCR_017017, https://github.com/Inria-Visages/Anima-Public) [22,23]. The MP2RAGE data was spatially normalized on the FLAWS data using the same process.

MP2RAGE and FLAWS T1 maps were $B1^+$ corrected using the $B1^+$ map provided by the SA2RAGE sequence using the method described in [6]. *In-vivo* T1 relaxation times of white matter, putamen, caudate nucleus and cortical gray matter were measured by manually drawing ROIs within the MP2RAGE and FLAWS T1 maps. For more information about the selection of the ROIs, please refer to [24].

MP2RAGE and FLAWS data were segmented using a similar approach as in [7]. First, the MP2RAGE and FLAWS second 3D datasets were bias corrected using the N4 algorithm [25]. Then, the bias corrected images were skull-stripped using *FSL-Bet2* [26] and the brain masks were used to remove all non-brain tissues in *MP2RAGE-uni* and *FLAWS-hco*. Finally, the skull-stripped *MP2RAGE-uni* and *FLAWS-hco* images were segmented with *FreeSurfer 6.0* [27].

The Pearson's correlation between the MP2RAGE and FLAWS T1 measurements was computed for every T1 measured within brain tissues (CSF excluded) on the healthy volunteers. The average *in-vivo* precision of the T1 mapping (mathematical equation provided in supplementary materials) was computed within the WM and cortical GM segmentations provided by *Freesurfer*. The effect of the $B1^+$ on the MP2RAGE and FLAWS T1 mapping was assessed *in-vivo* by measuring the Pearson's correlation between T1 and $B1^+$ maps within the WM and cortical GM segmentations provided by *FreeSurfer*.

5.5 Results

5.5.1 Sequence optimization

The FLAWS sequence parameters optimized in the current study are presented in Table 5.1. The *FLAWS1* (first 3D dataset, WM suppressed) and *FLAWS2* (second 3D dataset, CSF suppressed) signals simulated with this optimized set of parameters are shown in Figure 5.1a. In *FLAWS1,* most of the WM signal is successfully suppressed, with strong signals obtained from the globus pallidus, GM and CSF. The *FLAWS2* signal is successfully characterized by a strong CSF suppression, resulting with high signal for WM and GM and good contrast between them.

An example of FLAWS images acquired at 7T with the set of parameters optimized in this study is shown in Figure 5.2. From a qualitative point of view, the *FLAWS1* and *FLAWS2* contrasts acquired at 7T in the current study look similar to the contrasts obtained with previous optimizations of the sequence at both 1.5T and 3T [8,9]. A time of flight effect was found in FLAWS images, making the blood vessels appear hyper-intense, as depicted in Figure 5.2b. However, the blood hyper-intensity was found to vary with blood flow and could not be used to generate MR angiographies. A qualitative assessment validated the proposed 7T sequence parameters to visualize the basal ganglia in *FLAWS1* images, which provide a clear separation between the *GPe* and the *GPi* as shown in Supporting Information Figure 5.2.

The values of the brain tissue contrasts measured *in-vivo* in the current study are reported in Table 5.2. For comparison, the brain tissue contrasts measured in the same ROIs for the 1.5T and 3T FLAWS optimizations are also reported [8,9]. The CN values obtained in the current study agree with those obtained for the 1.5T and 3T studies. The average SNR of WM in *FLAWS2* is equal to 25 ± 2 in the current study.

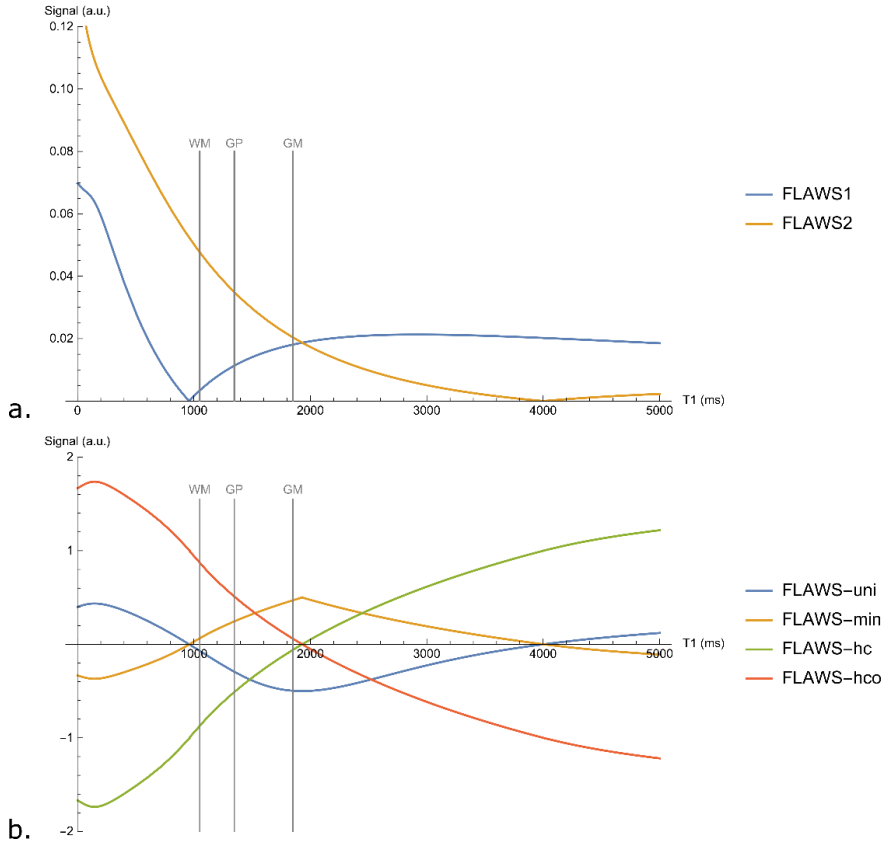

Figure 5.1. Simulations of the acquired (a) and reconstructed (b) FLAWS signals with the parameters optimized in the current study. WM: white matter; GP: globus pallidus; GM: gray matter.

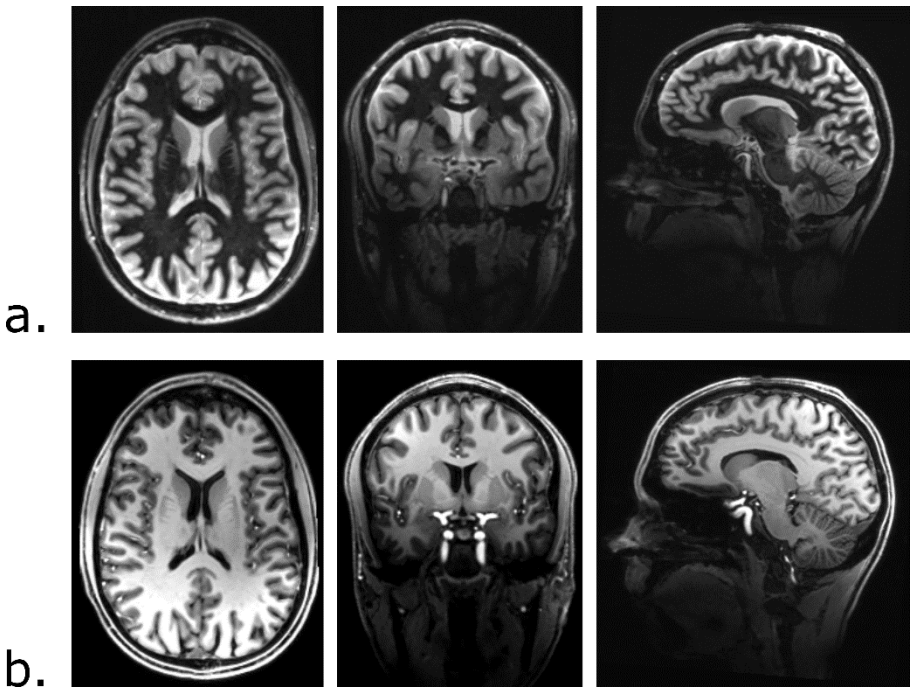

Figure 5.2. Axial (left), coronal (center) and sagittal (right) images of FLAWS1 (a) and FLAWS2 (b) acquired at 7T on one healthy volunteer with the set of parameters presented in Table 5.1.

5.5.2 Contrast generation with the FLAWS sequence

Simulations of the bias reduced *FLAWS-uni*, *FLAWS-min*, *FLAWS-hc* and *FLAWS-hco* signals are shown in Figure 5.1b for the optimization proposed in the current study. Simulations indicate that *FLAWS-uni* is characterized by a low GM signal compared to its WM and CSF signals, thus suggesting that it provides a GM suppressed contrast instead of providing the standard T1-weighted contrast typical from *MP2RAGE-uni*. *FLAWS-min* provides a high GM signal compared to the signals of WM and CSF. In accordance with previous theoretical experiments performed at 1.5T [9], the signal of the 7T *FLAWS-hc* combination image is characterized by a WM suppressed signal, with an increased contrast between GM and CSF compared to *FLAWS1*. Similarly, *FLAWS-hco* provides a CSF suppressed signal with an increased contrast between WM and GM compared to *FLAWS2*. The assumptions deduced from signal simulations were confirmed by *in-vivo* imaging, as shown in Figure 5.3. The bias field reduction provided *in-vivo* by *FLAWS-uni*, *FLAWS-min*, *FLAWS-hc* and *FLAWS-hco* is noteworthy compared to FLAWS1 and FLAWS2 in Figure 5.3. This bias field reduction was further highlighted in Supporting Information Figure 5.3.

Table 5.2. In-vivo measurements of the contrast (CN) of FLAWS images acquired at 7T with the set of parameters presented in Table 5.1. For comparison, the values measured in the work by Beaumont et al. at 1.5T [9] and Tanner et al. at 3T [8] are also reported. The CN values of the FLAWS optimization proposed for 7T imaging are in agreement with the FLAWS CN obtained at 1.5T and 3T.

	FLAWS1			FLAWS2		
Contrast	1.5T	3T	7T	1.5T	3T	7T
WM/GM	0.69 (0.59-0.69)	0.59 (0.51-0.69)	0.68 (0.58–0.72)	0.23 (0.19-0.28)	0.15 (0.13-0.16)	0.25 (0.21–0.31)
WM/CSF	0.75 (0.67-0.89)	0.68 (0.62-0.77)	0.82 (0.77–0.85)	0.88 (0.82-0.93)	0.83 (0.68-0.89)	0.81 (0.76–0.86)
GM/CSF	0.12 (0.08-0.19)	0.16 (0.13-0.17)	0.32 (0.29–0.34)	0.81 (0.72-0.89)	0.78 (0.60-0.86)	0.70 (0.65–0.77)

WM: White Matter, GM: Gray Matter, CSF: Cerebrospinal Fluid. CN measurements were performed in the corpus callosum (splenium) for WM, caudate nucleus (head) for GM and lateral ventricle for CSF. The CN range is presented in parentheses.

The CN and CNR measured in *FLAWS1*, *FLAWS2*, *FLAWS-uni*, *FLAWS-min*, *FLAWS-hco* and *MP2RAGE-uni* are reported in Table 5.3. The results of the CN and CNR analysis show quantitatively that *FLAWS-uni* provides a GM suppressed contrast, with high CN and CNR values measured for WM/GM and GM/CSF compared to the CN and CNR values measured for WM/CSF. Similarly, the high CNR values obtained for WM/GM and GM/CSF compared to WM/CSF in *FLAWS-min* confirm quantitatively that *FLAWS-min* provides a GM-specific contrast. In agreement with previous studies performed at 1.5T [9,18], *FLAWS-hco* is characterized by an improved contrast with respect to *FLAWS1* and *FLAWS2*, with a high CNR between brain tissues. In addition, *FLAWS-hco* is characterized by an enhanced CN compared to *MP2RAGE-uni*. *FLAWS-hco* also provides a higher CNR for WM/CSF and GM/CSF compared to *MP2RAGE-uni.* The WM/GM CNR measured in *FLAWS-hco* was close to the one measured in *MP2RAGE-uni*. The contrast enhancement provided by *FLAWS-hco* is noteworthy when compared to *MP2RAGE-uni*, as shown in Supporting Information Figure 5.4.

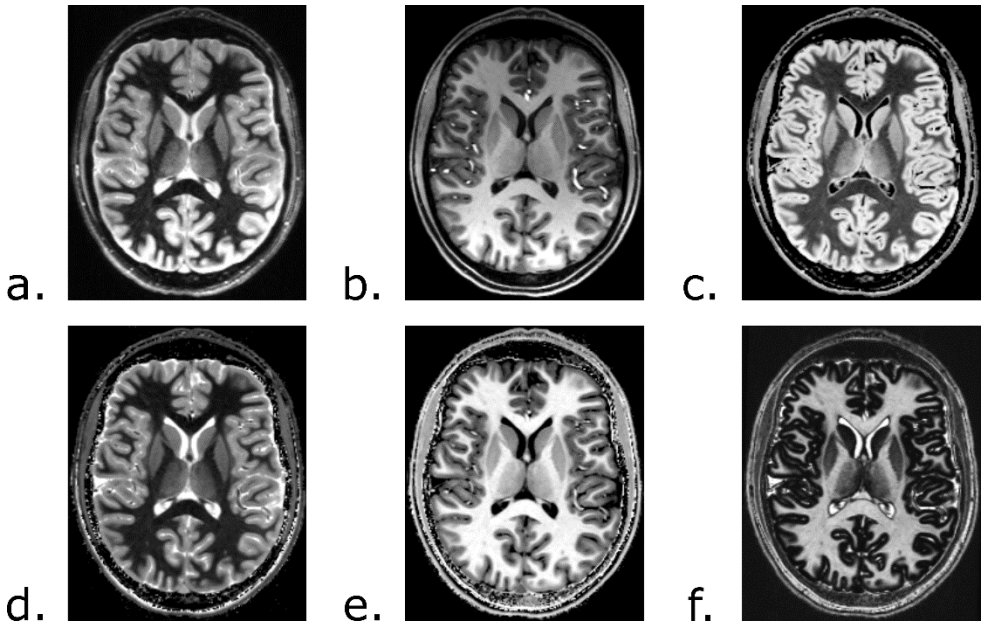

Figure 5.3. Example of the different contrasts obtained with FLAWS imaging at 7T. a) FLAWS1. b) FLAWS2. c) FLAWS-min. d) FLAWS-hc. e) FLAWS-hco. f) FLAWS-uni. FLAWS-min, FLAWS-hc, FLAWS-hco and FLAWS-uni were denoised by adding coefficients in the image combinations [20].

Table 5.3. Average contrast (CN) and contrast to noise ratio (CNR) measured in-vivo in FLAWS images acquired at 7T with the set of parameters presented in Table 5.1. The average CN and CNR of the MP2RAGE images acquired in this study are also shown.

		FLAWS1	*FLAWS2*	*FLAWS-uni*	*FLAWS-min*	*FLAWS-hco*	*MP2RAGE-uni*
CN	WM/GM	0.68 (0.58–0.72)	0.25 (0.21–0.31)	0.71 (0.63 – 0.77)	0.71 (0.62 – 0.76)	0.53 (0.47 – 0.58)	0.29 (0.25 – 0.31)
	WM/CSF	0.82 (0.77–0.85)	0.81 (0.75–0.86)	0.22 (0.19 – 0.25)	1.00 (1.00 – 1.00)	1.00 (1.00 – 1.00)	0.74 (0.68 – 0.82)
	GM/CSF	0.32 (0.29–0.34)	0.70 (0.63–0.77)	0.81 (0.76 – 0.85)	1.00 (1.00 – 1.00)	1.00 (1.00 – 1.00)	0.58 (0.49 – 0.68)
CNR	WM/GM	4.9 (3.6 – 5.9)	5.0 (4.0 – 6.1)	6.5 (5.2 – 7.8)	5.5 (4.6 – 6.1)	5.5 (4.6 – 6.1)	4.9 (3.7 – 6.4)
	WM/CSF	7.9 (4.6 – 9.7)	10.3 (7.5 – 13.9)	2.7 (2.0 – 3.2)	3.1 (2.3 – 3.7)	14.7 (12.8 – 16.6)	6.6 (5.4 – 8.1)
	GM/CSF	4.1 (2.6 – 5.1)	5.6 (4.4 – 7.0)	6.6 (5.6 – 8.2)	6.9 (5.6 – 8.5)	10.3 (8.2 – 12.0)	3.7 (2.4 – 4.6)

WM: White Matter, GM: Gray Matter, CSF: Cerebrospinal Fluid. CN and CNR measurements were performed in the corpus callosum (splenium) for WM, caudate nucleus (head) for GM and lateral ventricle for CSF. Ranges of *CN and CNR* are presented in parentheses.

5.5.3 T1 mapping

Simulations of the *MP2RAGE-uni* and *FLAWS-hc* signals affected by $\pm 40\ \%$ $B1^+$ inhomogeneities indicated that *FLAWS-hc* is robust to $B1^+$ inhomogeneities for the T1 range of WM and GM signals, as shown in Supporting Information Figure 5.5. However, the sensitivity of the *FLAWS-hc* signal to $B1^+$inhomogeneities increases for short ($< 1000\ ms$) and long ($> 2000\ ms$) T1 relaxation times. Specifically, the FLAWS T1 mapping theoretical error due to $\pm 40\ \%$ $B1^+$ inhomogeneities ($4.3\ \%$ for a T1 of $2000\ ms$ and $12.5\ \%$ for a T1 of $2500\ ms$) is higher than the one obtained from MP2RAGE optimized for reduced $B1^+$ sensitivity ($3.2\ \%$ for a T1 of $2000\ ms$ and $4.4\ \%$ for a T1 of $2500\ ms$). The T1 mapping

theoretical error induced by ± 40 % $B1^+$ inhomogeneities is however lower in FLAWS (4.3 % for a T1 of $2000\ ms$ and 12.5 % for a T1 of $2500\ ms$) than in the MP2RAGE protocol optimized for high resolution and high contrast imaging (16.8 % for a T1 of $2000\ ms$ and 24.7 % for a T1 of $2500\ ms$), while FLAWS is characterized by a higher resolution ($0.8\ mm$ isotropic) than this MP2RAGE protocol ($0.85\ mm$ isotropic) [6].

The high theoretical accuracy and precision of the T1 maps obtained with the FLAWS and MP2RAGE sequences can be seen in Table 5.4. The results show that both the SNR and $B1^+$ impact the accuracy and precision of the T1 mapping. In all experiments, the average accuracy and precision of the FLAWS T1 mapping were close to the ones of the MP2RAGE T1 mapping and were above 90 % for the T1 range of brain tissues ($900\ ms - 2500\ ms$).

Table 5.4. Accuracy and precision of the T1 measurements provided by the MP2RAGE sequence with low B1+ sensitivity and by the FLAWS sequence, according to different values of the signal to noise ratio (SNR) and to the effect of the $B1^+$ on the signal.

Bias	SNR	Sequence	Accuracy (%)	Precision (%)
No $B1^+$	25	MP2RAGE	93.7	92.1
		FLAWS	95.3	94.1
$B1^+$	$+\infty$	MP2RAGE	98.5	99.2
		FLAWS	96.4	97.8
	25	MP2RAGE	90.0	86.8
		FLAWS	91.9	90.2

Examples of *in-vivo* T1 maps –without post-hoc correction– and $B1^+$ maps obtained with the FLAWS, MP2RAGE and SA2RAGE sequences are shown in Figure 5.4. From a qualitative point of view, the T1 map provided by the FLAWS sequence looks like the MP2RAGE T1 map and does not seem to be hampered by the $B1^+$. The difference between the MP2RAGE and FLAWS T1 maps –without post-hoc correction– appears to be mainly due to the resolution difference between the scans, as shown in Supporting Information Figures 5.6 and 5.7.

The effect of the post-hoc correction on the *in-vivo* FLAWS T1 measurements appears to be negligible for most of the brain tissues, except for long T1 relaxation times like cortical GM, as shown in Table 5.5. A slightly higher T1 change was found in brain tissues regarding the $B1^+$ correction of MP2RAGE T1 measurements, except for long T1 relaxation times like cortical GM. The $B1^+$ corrected T1 measurements provided by the FLAWS sequence were in concordance with the ones provided by the MP2RAGE sequence optimized for low $B1^+$ sensitivity ($r = 0.91$). In addition, the $B1^+$ corrected FLAWS T1 measurements performed in this study provided results close from T1 measurements performed in similar ROIs by T1 curve fitting of MPRAGE data acquired at multiple inversion times in a previous study [24].

The average precision of the FLAWS *in-vivo* T1 mapping, computed within the WM and cortical GM segmentations after $B1^+$ correction ($prec_{WM} = 86.3\% \pm 0.5\%;\ prec_{GM} = 87.8\% \pm 0.5\%$), was close to the one computed on MP2RAGE T1 maps after $B1^+$ correction ($prec_{WM} = 87.9\% \pm 0.3\%; prec_{GM} = 83.8\% \pm 3.1\%$).

The average *in-vivo* T1 values –without post-hoc correction– measured with MP2RAGE and FLAWS within the WM and cortical GM segmentations of one volunteer were reported as a function of $B1^+$ in Figure 5.5a and 5.5b. The effect of the $B1^+$ on MP2RAGE and FLAWS T1 mapping appears to be negligible for $B1^+$ values within the $50\% - 100\%$ range for all

volunteers. However, the T1 values tend to diverge outside of this range. The divergence in the T1 measurements was found to increase when the number of voxels per $B1^+$ value decreases, as shown in Figure 5.5c and 5.5d. Across all the volunteers, 13.0% and 19.6% of the MP2RAGE WM and cortical GM voxels were characterized by a $B1^+$ value outside of the $50\% - 100\%$ range. The rate of voxels outside of the $50\% - 100\%$ $B1^+$ range was similar in FLAWS images (12.4% for WM and 17.0% for cortical GM). A qualitative assessment indicated that the voxels with a $B1^+$ value under 50% of the nominal flip angles were located near the ear canals and the frontal sinuses or were located in the inferior brain regions, where $B1^+$ is characterized by a strong signal reduction in the z direction (example available in Supporting information Figure 5.8). The voxels responsible for the T1 mapping divergence for $B1^+$ values over 100% of the nominal flip angles were found to be voxels misclassified at tissue boundaries (due to small errors in skull-stripping and segmentations, example available in Supporting information Figure 5.9).

Table 5.5. Mean and standard deviation T1 values measured in-vivo on 6 healthy volunteers at 7T using the FLAWS sequence and the MP2RAGE sequence with low B1+ sensitivity. T1 values are reported with ($B1^+$ $corr$) and without (Raw) post-hoc $B1^+$ correction. T1 values from the literature are also reported [24]. The T1 values measured with FLAWS did not change after post-hoc correction, except for tissues with long T1 relaxatin times, as cortical GM.

	FLAWS		MP2RAGE		Wright et al.
	Raw	$B1^+$ $corr$	Raw	$B1^+$ $corr$	$B1^+$ $corr$
White matter	$1076 \pm 40\ ms$	$1071 \pm 44\ ms$	$1123 \pm 41\ ms$	$1110 \pm 41\ ms$	$1130 \pm 100\ ms$
Caudate nucleus	$1617 \pm 83\ ms$	$1615 \pm 80\ ms$	$1607 \pm 74\ ms$	$1598 \pm 74\ ms$	$1684 \pm 76\ ms$
Putamen	$1569 \pm 78\ ms$	$1569 \pm 75\ ms$	$1590 \pm 70\ ms$	$1578 \pm 68\ ms$	$1643 \pm 167\ ms$
Cortical gray matter	$1995 \pm 128\ ms$	$1941 \pm 96\ ms$	$1983 \pm 134\ ms$	$1954 \pm 153\ ms$	$1939 \pm 150\ ms$

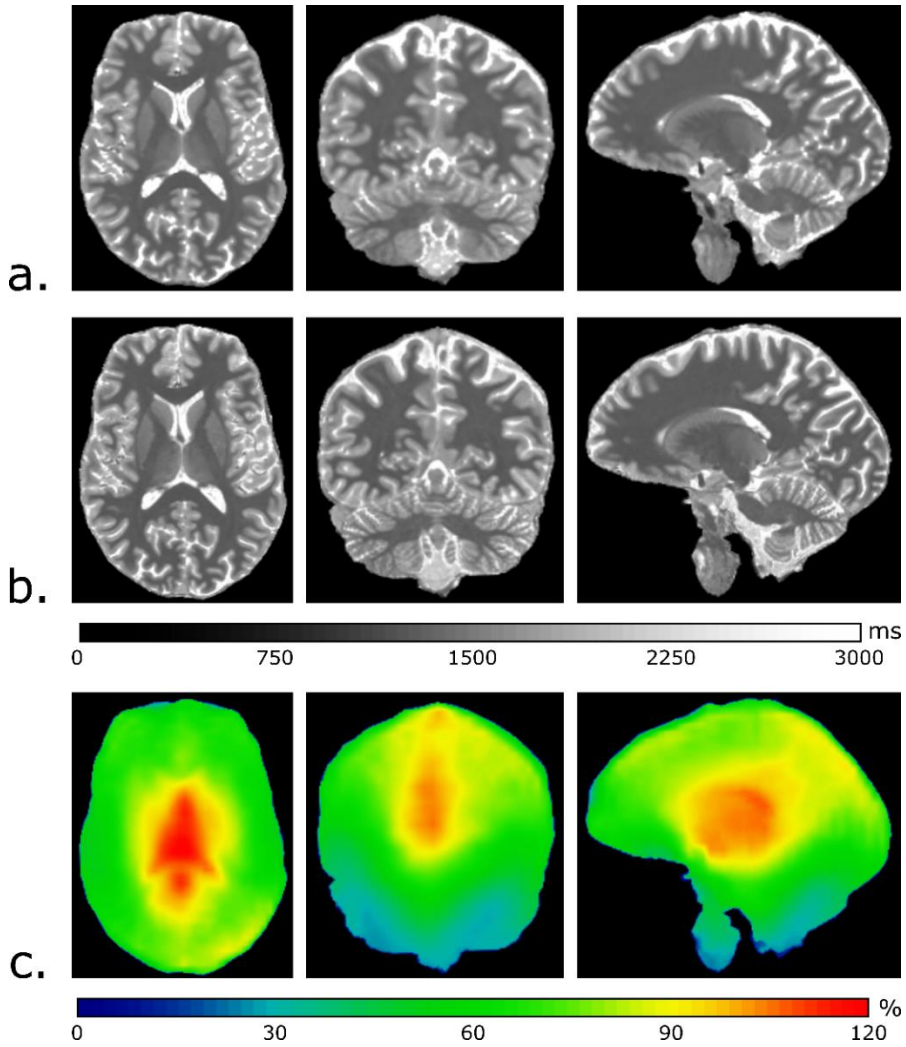

Figure 5.4. T1 Maps –without post-hoc $B1^+$correction– acquired with the MP2RAGE sequence optimized for low $B1^+$ sensitivity (a) and with the FLAWS sequence optimized in this study (b). The $B1^+$ map acquired with the SA2RAGE sequence on the same volunteer is also shown (c). The $B1^+$ values are displayed as a percentage of the nominal sequence flip angles. From a qualitative point of view, the FLAWS and MP2RAGE T1 maps are similar and do not appear to be sensitive to $B1^+$.

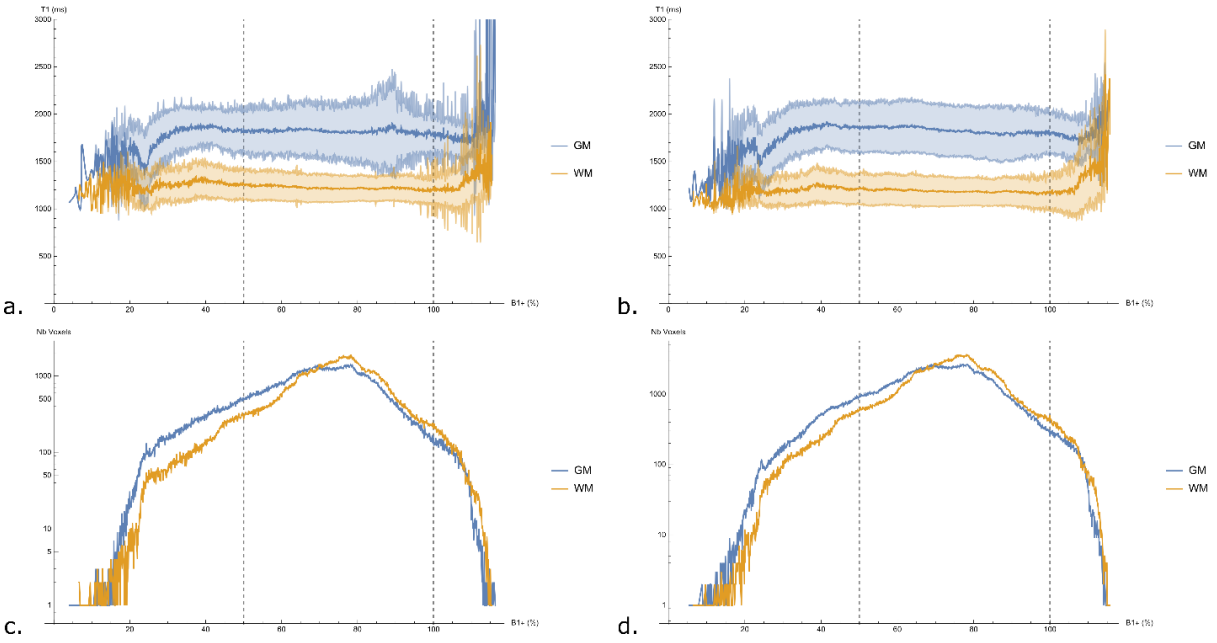

Figure 5.5. Effect of the transmitted bias field ($B1^+$) on T1 measurements –without post-hoc correction– performed in-vivo within WM and cortical GM segmentations of one volunteer with the MP2RAGE (a,c) and FLAWS (b,d) sequences. First row: average (dark color) and standard deviation (light color) of the WM and cortical GM MP2RAGE (a) and FLAWS (b) T1 values as a function of $B1^+$. Second row: number of voxels within the MP2RAGE (c) and FLAWS (d) WM and cortical GM segmentations as a function of $B1^+$. The $B1^+$ values are displayed as a percentage of the nominal sequence flip angles.

The average correlation between the T1 relaxation time –measured without post-hoc correction– and the $B1^+$ was weak within the WM and cortical GM segmentations for both MP2RAGE ($r_{WM} = -0.051 \pm 0.017$; $r_{GM} = -0.027 \pm 0.045$) and FLAWS ($r_{WM} = -0.026 \pm 0.021$; $r_{GM} = 0.081 \pm 0.038$). The correlation remains weak when computed on voxels belonging to the $50\% - 100\%$ $B1^+$ range within MP2RAGE ($r_{WM} = -0.040 \pm 0.040$; $r_{GM} = -0.040 \pm 0.036$) and FLAWS ($r_{WM} = -0.027 \pm 0.041$; $r_{GM} = -0.097 \pm 0.036$) segmentations. The bias correction of the T1 maps slightly decreases the correlation between the T1 relaxation time and the $B1^+$ within the $50\% - 100\%$ range for both MP2RAGE ($r_{WM} = -0.011 \pm 0.035$; $r_{GM} = -0.013 \pm 0.027$) and FLAWS ($r_{WM} = -0.024 \pm 0.040$; $r_{GM} = -0.029 \pm 0.027$).

5.6 Discussion

5.6.1 Sequence optimization

The FLAWS sequence was optimized at the field strength of 7T for high resolution ($0.8\,mm$ isotropic) imaging using a method previously used to optimize the sequence at 1.5T [9]. The 1.5T optimization process was customized to adapt the T1 relaxation times, the sequence acquisition time and image resolution for 7T imaging. As the optimization method is based on simulations of brain tissue signals using the Bloch equations, the outcome of the optimization depends on the choice of the T1 relaxation times used to simulate the signals [9]. To increase the consistency between the FLAWS and MP2RAGE optimizations, the T1 relaxation times used to optimize the FLAWS sequence were the same as the ones used to optimize the MP2RAGE sequence at 7T in a previous study [2].

Simulations of FLAWS signals with the parameters optimized in this study indicate that the WM signal suppression is not perfect in *FLAWS1*. In a previous study performed at 3T, Tanner

et al. showed that the WM signal should not be perfectly suppressed in *FLAWS1* to ensure a good visualization of deep GM structures [8].

The optimization method employed in this study was designed to provide a set of parameters allowing to acquire 7T FLAWS images characterized by 1) a contrast similar to the one obtained with the 3T FLAWS sequence optimization [8,9]; and 2) a good visualization of deep GM structures in FLAWS1. Qualitative and quantitative *in-vivo* experiments showed that the optimization performed in this study provided images with a contrast similar to the one obtained in previous studies conducted at 1.5T and 3T [8,9]. In addition, the separation between the *GPe* and the *GPi* –identified as a typical metric used to assess the quality of the basal ganglia visualization in *FLAWS1* [8,9]– was clearly visible in the *FLAWS1* images acquired with the set of parameters optimized in the current study.

5.6.2 Contrast generation with the FLAWS sequence

The current study shows that *uni*, the image combination used to generate a bias reduced standard T1-weighted contrast with MP2RAGE data, cannot provide a similar contrast with the proposed 7T FLAWS optimization. However, another image combination, named *FLAWS-hco*, was recently introduced at 1.5T to generate a bias reduced standard T1-weighted contrast with the FLAWS sequence [9]. Signal simulations, as well as qualitative and quantitative *in-vivo* assessments, showed that *FLAWS-hco* provides a bias reduced standard T1-weighted contrast for the FLAWS optimization proposed for 7T imaging. In addition, it was shown that the *FLAWS-hco* images acquired in the current study were characterized by an increased brain tissue CN, CNR and resolution compared to the *MP2RAGE-uni* images acquired with parameters optimized for low $B1^+$ sensitivity. Signal simulations, qualitative and quantitative *in-vivo* assessments also showed that bias reduced WM suppressed, GM suppressed and GM specific contrasts can be generated with 7T FLAWS imaging, thus allowing to provide more contrasts than the ones currently provided by the MP2RAGE sequence.

It should be noted that different MP2RAGE optimizations provide images with better CNR and resolution than the MP2RAGE optimization employed in the current study [6]. However, these optimizations provide data with high $B1^+$ sensitivity and could not be used as references to assess the $B1^+$ sensitivity of the FLAWS optimization proposed in the current study.

5.6.3 T1 mapping

The current study shows that the *FLAWS-hc* signal can be used to measure the T1 relaxation time. The theoretical accuracy and precision of the FLAWS T1 mapping were compared to the ones of the MP2RAGE T1 mapping in terms of robustness to noise and $B1^+$. The consistency between the theoretical and *in-vivo* experiments was ensured by simulating MP2RAGE and FLAWS signals with noise and $B1^+$ distributions determined from the *in-vivo* data acquired in this study.

Simulation experiments suggest that the proposed 7T FLAWS optimization can be used for accurate T1 mapping with a low $B1^+$ sensitivity and provides a theoretical accuracy and precision in agreement with the ones provided by the MP2RAGE sequence optimized for low $B1^+$ sensitivity for the T1 range of WM and GM tissues. These theoretical assumptions were supported by *in-vivo* experiments showing that the FLAWS T1 mapping provides T1 measurements in agreement with the ones provided by other established T1 mapping methods at 7T [2,24]. In addition, the harmony observed between the *in-vivo* FLAWS and

MP2RAGE T1 mapping precisions further validated the possibility of measuring T1 relaxation times with the FLAWS sequence.

The small *in-vivo* T1 change noticed between the raw and post-hoc corrected T1 measurements provided by the MP2RAGE and FLAWS sequences suggests that the FLAWS T1 mapping is characterized by a low $B1^+$ sensitivity for most of the brain tissues. The weak correlation between the $B1^+$ and T1 values –without post-hoc correction– measured within WM and cortical GM segmentations with MP2RAGE and FLAWS further demonstrated the low $B1^+$ sensitivity provided by the FLAWS optimization proposed in this study. However, it was shown that the FLAWS T1 mapping is hampered by $B1^+$ in cortical GM. Simulations of the *FLAWS-hc* signal hampered by $B1^+$ inhomogeneities of $\pm 40\ \%$ indicated that the $B1^+$ dependency of the FLAWS T1 mapping increases for short ($< 1000\ ms$) and long ($> 2000\ ms$) T1 relaxation times, thus, explaining the increased $B1^+$ dependency of cortical GM, which is characterized by a long T1 relaxation time compared to WM and deep GM. This increased dependency to $B1^+$ for cortical GM signals was also found in the MP2RAGE T1 mapping.

In agreement with previous studies conducted with MP2RAGE at 7T [6,7], the current study showed that the MP2RAGE T1 maps can be post-hoc corrected to remove the remaining bias in MP2RAGE data. The decreased correlation noticed between $\mathrm{B1}^+$ and T1 for the FLAWS sequence after $B1^+$ correction indicates that the method previously proposed by Marques et al. [6] to correct the $B1^+$ in *MP2RAGE-uni* can also be used to correct the $B1^+$ in *FLAWS-hc*. In a recent study, Haast et al. assessed the effect of $B1^+$ on multi-center MP2RAGE T1 mapping and morphometry at 7T [28]. The authors advised to use MP2RAGE sequence parameters optimized for low $B1^+$ sensitivity to improve the robustness of multi-center analysis, except when a good visualization of deep GM is required. To the best of our knowledge, the current study is the first that proposes a sequence optimization allowing to acquire T1-weighted scans and T1 maps characterized by a low $B1^+$ sensitivity while providing a good visualization of deep GM structures. Therefore, the results of the current study highlight the interest of FLAWS imaging to study deep GM in multi-center studies conducted at 7T.

This study shows that the T1 relaxation times measured within WM and cortical GM segmentations tend to diverge for $B1^+$ values outside of the $50\% - 100\%$ nominal flip angle range. A qualitative assessment showed that the low $B1^+$ values were measured in the inferior brain regions, where the adiabatic condition of the inversion pulse might not be reached. This issue has already been reported in previous studies [6,7] and can be mitigated by placing dielectric pads near the temporal lobes [29]. Indeed, a previous study conducted with the MP2RAGE sequence showed that the use of dielectric pads allows to increase the $B1^+$ by up to $50\ \%$ of the nominal flip angle near the cerebellum and the temporal lobes at 7T [30]. Low $B1^+$ values were also found near the frontal sinuses and the ear canals. The presence of these low $B1^+$ values could be explained by off-resonance frequency effects that are commonly found near the frontal sinuses and ear canals in $B1^+$ mapping techniques [31,32]. The high $B1^+$ values that led to a divergence of the T1 measurements within the WM and cortical GM segmentations were only noticed in voxels that were misclassified as belonging to the WM or cortical GM segmentations. In addition, high $B1^+$ values were measured in deep GM structures (see Figure 5.4c), where the effect of the $B1^+$ correction on FLAWS T1 mapping was shown to be negligible. Therefore, the T1 divergence reported for high $B1^+$ value in the current study was not considered as a failure of the MP2RAGE and FLAWS T1 mapping methods.

5.6.4 Limitations

The current study has several limitations. First, the MR experiments were performed on a small number of healthy volunteers and FLAWS imaging on a larger patient cohort would be necessary to assess the potential clinical interest provided by the multiple FLAWS contrasts for 7T imaging. In addition, the signals of *FLAWS1* and *FLAWS2* being dependent upon the number of slices, a new optimization of the FLAWS sequence would be necessary to increase the scan resolution. Moreover, the bias reduced *FLAWS-min, FLAWS-hc* and *FLAWS-hco* combination images, as well as the FLAWS T1 mapping, are not yet readily available on the MRI console. The code used to generate the FLAWS contrasts and perform the FLAWS T1 mapping is however available on Github (*https://github.com/jerbeaumont/FLAWS-Tools*). Finally, the B1+ dependency of the FLAWS T1 mapping increases for long T1 and as such, a B1+ post-hoc correction of the FLAWS T1 maps is necessary to study tissues with long T1 relaxation times, such as brain lesions.

5.6.5 Conclusion

In conclusion, this study proposes a new optimization of the FLAWS sequence to provide multiple T1-weighted contrasts with reduced $B1$ sensitivity that might be of interest for high resolution ($0.8\ mm$ isotropic) 7T imaging. It was shown that the proposed FLAWS optimization provides high-resolution T1 maps with low $B1^+$ sensitivity, thus overcoming the limitations of the MP2RAGE sequence optimized for low $B1^+$ sensitivity in terms of CNR and resolution. These results suggest that FLAWS is a good candidate for T1-weighted imaging and T1 mapping at the field strength of 7T.

5.7 Supplementary materials

5.7.1 Contrast loss and T1 mapping ambiguities

The FLAWS-hc signal was computed offline using the following equation:

$$S_{hc} = \frac{S1 - S2}{S1 + S2} \qquad 5.10$$

With $S1$ (resp. $S2$) the magnitude of the *FLAWS1* (resp. *FLAWS2*) signal. A loss of contrast is noticed in *FLAWS-hc* when the complex *FLAWS1* and *FLAWS2* signals are changing of sign (Supporting Information Figure 5.1). This contrast loss can be recovered using the *FLAWS-uni* signal, which is sensitive to the sign change of the *FLAWS1* and *FLAWS2* signals:

$$S_{uni} = \frac{Real(S1_C^*\, S2_C)}{\left||S1_C|\right|^2 + \left||S2_C|\right|^2} \qquad 5.11$$

With $S1_C$ (resp. $S2_C$) the *FLAWS1* (resp. *FLAWS2*) complex signal and $*$ designing the complex conjugate.

The *FLAWS-uni* signal changes twice of sign on the T1 range of 7T brain tissues for the proposed FLAWS optimization (Supporting Information Figure 5.1), with: i) $S_{uni} \geq 0$ when $S1_C \geq 0$ and $S2_C \geq 0$; ii) $S_{uni} \leq 0$ when $S1_C < 0$ and $S2_C \geq 0$; and iii) $S_{uni} > 0$ when $S1_C < 0$ and $S2_C < 0$. The cases i) and iii) can be easily differentiated using the magnitude of the *FLAWS1* and *FLAWS2* signals, as $S1 < S2$ for every T1 relaxation times in case i) and $S1 > S2$ for every relaxation time in case iii). Then, the *FLAWS-hc* contrast loss is recovered by inverting its signal about the $S_{hc} = -1$ and $S_{hc} = 1$ axis in cases i) and iii), respectively:

$$S_{hcFullRange} = \begin{cases} -2 - S_{hc} & when\ S_{uni} \geq 0\ and\ S1 < S2 \\ S_{hc} & when\ S_{uni} \leq 0 \\ 2 - S_{hc} & when\ S_{uni} > 0\ and\ S1 > S2 \end{cases} \quad 5.12$$

Similarly, the *FLAWS-min* and *FLAWS-hc* contrast loss is recovered using the following equations:

$$S_{hcoFullRange} = \begin{cases} 2 - S_{hco} & when\ S_{uni} \geq 0\ and\ S1 < S2 \\ S_{hco} & when\ S_{uni} \leq 0 \\ -2 - S_{hco} & when\ S_{uni} > 0\ and\ S1 > S2 \end{cases} \quad 5.13$$

$$S_{minFullRange} = \begin{cases} -S_{min} & when\ S_{uni} \geq 0\ and\ S1 < S2 \\ S_{min} & when\ S_{uni} \leq 0 \\ -S_{min} & when\ S_{uni} > 0\ and\ S1 > S2 \end{cases} \quad 5.14$$

The contrast loss recovery of the *FLAWS-hc, FLAWS-hco* and *FLAWS-min* signals is shown in Figure 5.1.

The FLAWS T1 mapping was performed using lookup tables of the *FLAWS-hc* signal. Since *FLAWS-hc* is reconstructed from the magnitude of the *FLAWS1* and *FLAWS2* signals, T1 mapping ambiguities arise when *FLAWS-hc* intensities could be obtained from signals corresponding to two different T1 relaxation times (refer to Supplementary Figure 5.1). T1 mapping ambiguities were solved by building three different *FLAWS-hc* lookup tables, covering the range of T1 relaxation times of the *FLAWS-uni* sign cases. Then, the choice of the appropriate lookup table for *FLAWS-hc* T1 mapping is determined by using the same conditions as the ones used to recover the contrast loss in *FLAWS-hc* (equation *5.12*).

5.7.2 $\boldsymbol{B1^+}$ distribution fitting

To simulate FLAWS signals consistent with the *in-vivo* signals measured in the current study, the $B1^+$ distribution of brain tissues at 7T was modeled from the data acquired in the current study.

The *in-vivo* $B1^+$ brain values were extracted as follow: i) $B1^+$ map were spatially normalized on FLAWS images for all volunteers. The spatial normalization was performed using a rigid registration algorithm provided by the Anima software[1]; ii) the $B1^+$ maps were brain masked by skull-stripping the *FLAWS2* images with FSL-BET2[2].

Multiple statistical distributions (Skew Normal, Gamma, Rice, Chi-Square, Weibull, Rayleigh, …) were fitted to the *in-vivo* $B1^+$ brain distribution by maximizing their log-likelihood. Then, the statistical distribution that best fits the *in-vivo* distribution was determined by minimizing the Akaike information criterion. The results of the analysis indicate that the brain $B1^+$ values measured in the current study follow a Gamma distribution with the following parameters: $\alpha = 1.5$, $\beta = 0.72$, $\gamma = 3.4$ and $\mu = -0.075$.

[1] Anima, RRID:SCR_017017, https://github.com/Inria-Visages/Anima-Public
[2] FSL, https://fsl.fmrib.ox.ac.uk/fsl

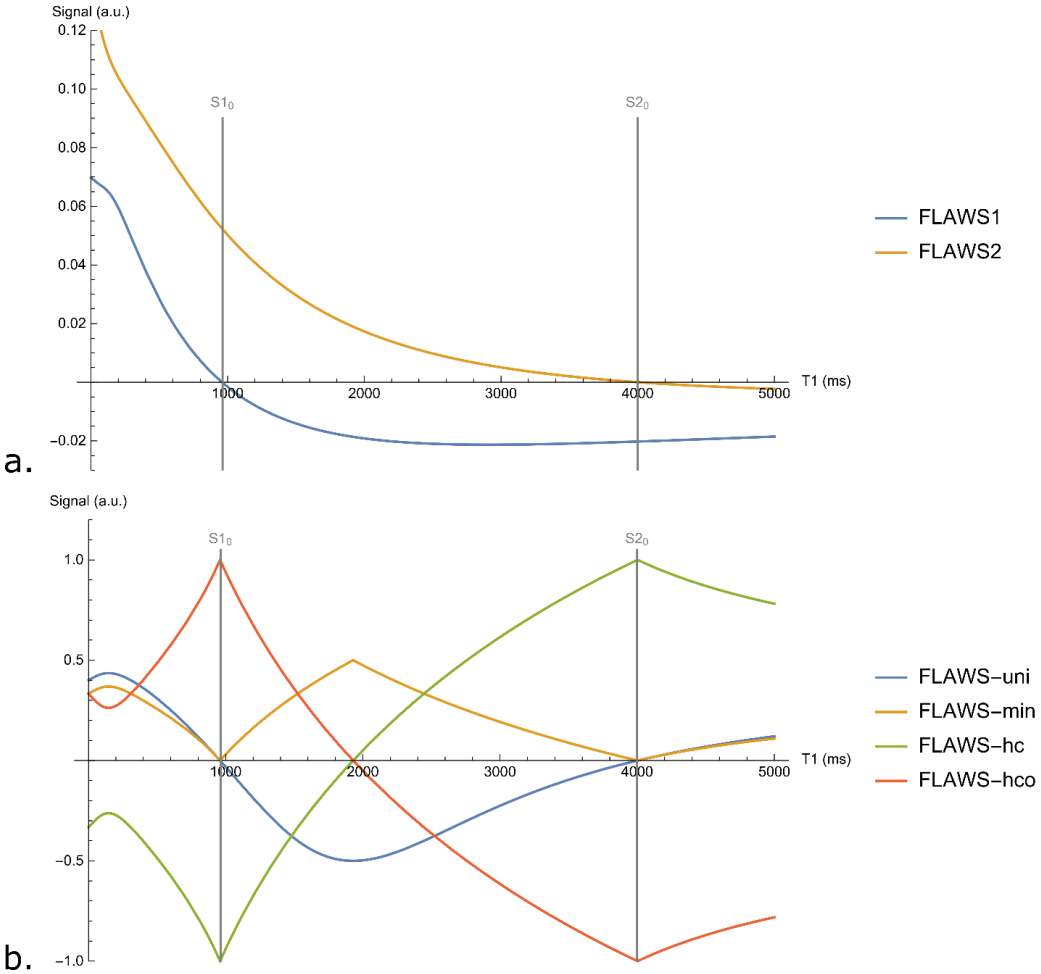

Supporting Information Figure 5.1. Simulations of the FLAWS1 and FLAWS2 real parts of the complex signals (a). Simulations of the reconstructed FLAWS signals are shown in b. $S1_0$: sign change in FLAWS1. $S2_0$: sign change in FLAWS2. The sign of FLAWS-uni is linked to the sign change of FLAWS1 and FLAWS2. A loss of contrast is noticed in FLAWS-hc, FLAWS-hco and FLAWS-min at every sign change ($S1_0$,$S2_0$).

5.7.3 T1 mapping theoretical accuracy and precision

The theoretical accuracy and precision of the T1 mapping were defined as follow:

$$accuracy_{th} = 1 - \frac{1}{M_{t1} - m_{t1} + 1} \sum_{t1=m_{t1}}^{M_{t1}} \frac{\mu_{\Delta t1}}{t1} \qquad 5.15$$

$$precision_{th} = 1 - \frac{1}{M_{t1} - m_{t1} + 1} \sum_{t1=m_{t1}}^{M_{t1}} \frac{\sigma_{\widehat{t1}}}{t1} \qquad 5.16$$

$$\mu_{\Delta t1} = \frac{1}{N_e} \sum_{e=0}^{N_e-1} \left| t1 - \widehat{t1(e)} \right| \qquad 5.17$$

$$\sigma_{\widehat{t1}} = \sqrt{\frac{1}{Ne}\sum_{e=0}^{N_e-1}\left(\mu_{\widehat{t1}} - \widehat{t1(e)}\right)^2} \quad 5.18$$

$$\mu_{\widehat{t1}} = \frac{1}{N_e}\sum_{e=0}^{N_e-1}\widehat{t1(e)} \quad 5.19$$

With m_{t1} (resp. M_{t1}) the minimum (resp. maximum) T1 value used to generate the Monte-Carlo experiments, N_e the number of Monte-Carlo experiments, $t1$ the T1 value used to simulate a given Monte-Carlo experiment e and $\widehat{t1(e)}$ the T1 value estimated from a given Monte-Carlo experiment e.

5.7.4 T1 mapping *in-vivo* precision

The average *in-vivo* precision of the WM (resp. cortical GM) T1 mapping was computed as:

$$precision_{WM} = 1 - \frac{\sigma T1_{WM}}{\mu T1_{WM}} \quad 5.20$$

With $\mu T1_{WM}$ (resp. $\mu T1_{GM}$) and $\sigma T1_{WM}$ (resp. $\sigma T1_{GM}$) the average and standard deviation of the T1 measurements within the WM (resp. cortical GM) segmentation.

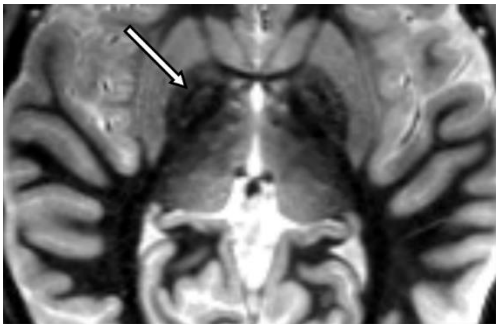

Supporting Information Figure 5.2. Visualization of the separation between the internal and the external globus pallidus in FLAWS1. The separation is indicated by the white arrow.

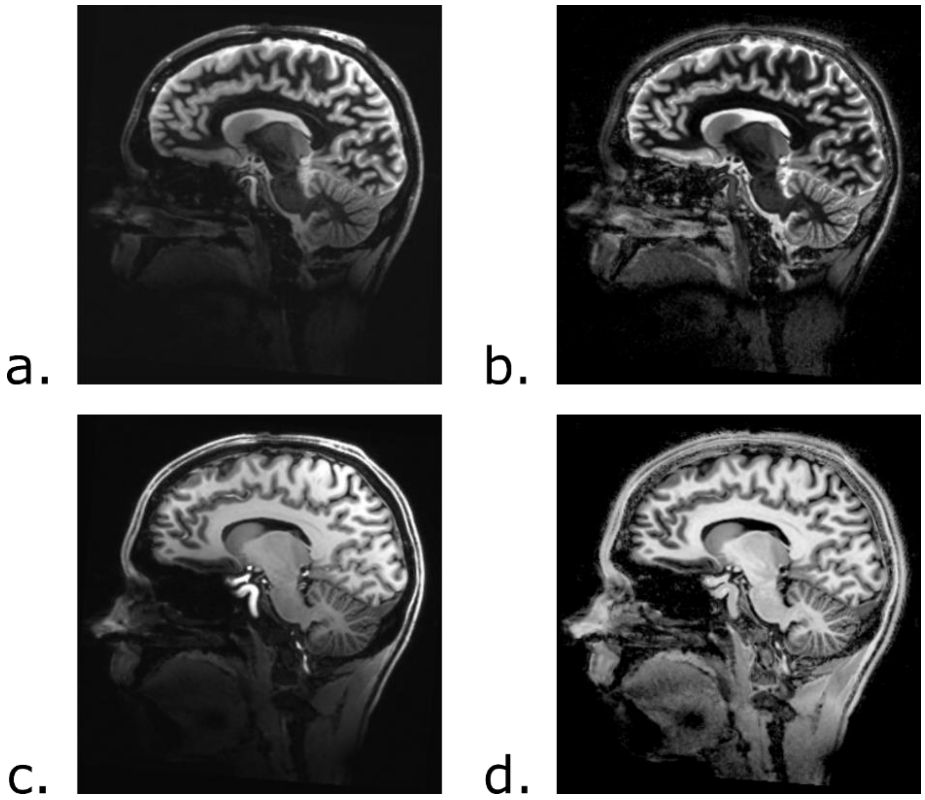

Supporting Information Figure 5.3. Illustration of the bias field reduction provided by FLAWS-hc (b) and FLAWS-hco (d) compared to FLAWS1 (a) and FLAWS2 (c).

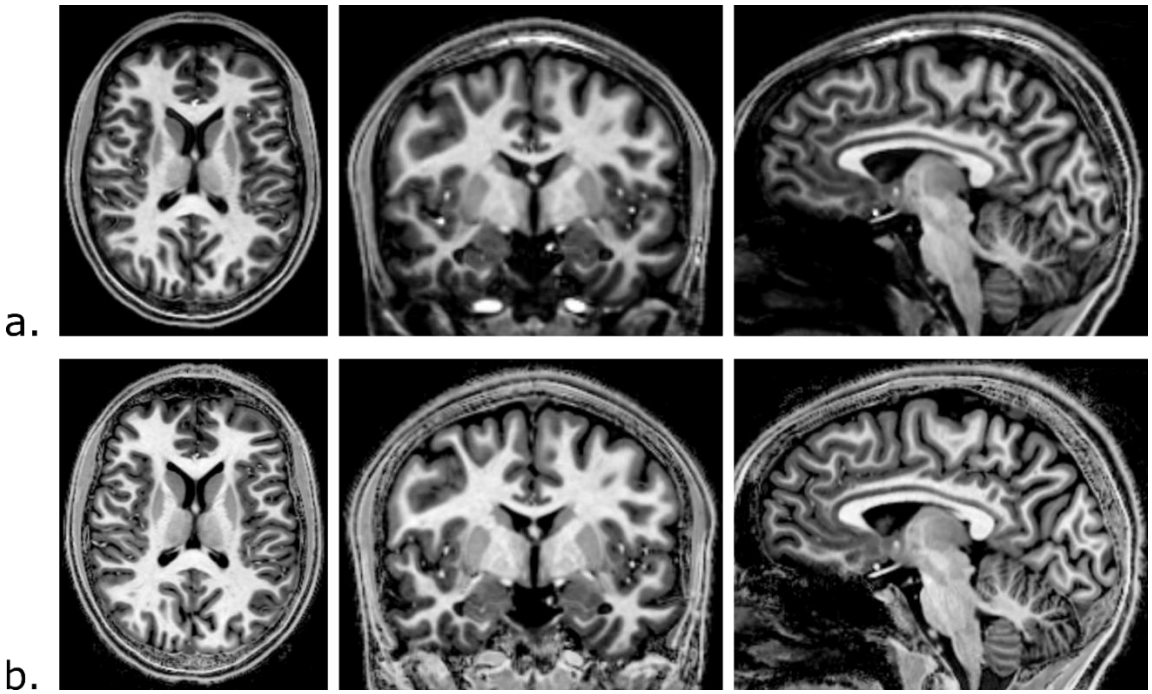

Supporting Information Figure 5.4. Example of axial, coronal and sagittal images of MP2RAGE-uni (a) and FLAWS-hco (b). The increased contrast and resolution provided by FLAWS-hco is noteworthy.

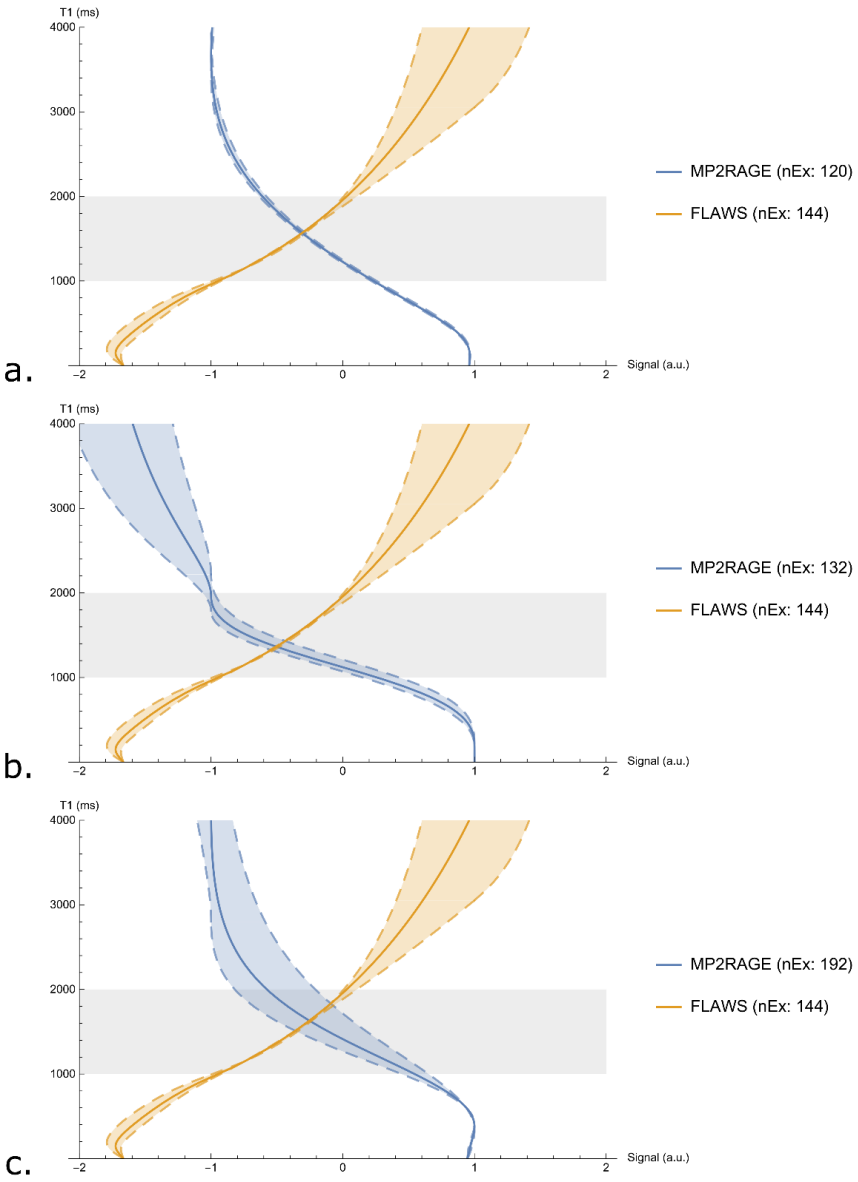

Supporting Information Figure 5.5. T1 relaxation time as a function of MP2RAGE-uni (blue line) and FLAWS-hc (orange line). The comparison is performed for MP2RAGE signals from the reduced $B1^+$ MP2RAGE optimization (a), the high WM/GM contrast MP2RAGE optimization (b) and the high resolution MP2RAGE optimization (c) presented in Marques et al, Plos one, 2013 [6]. The dashed lines show the signals affected by $\pm 40\%$ $B1^+$ inhomogeneities. This figure shows that FLAWS-hc is robust to $B1^+$ inhomogeneities for the T1 range of WM and GM signals (gray zone). However, the sensitivity of the FLAWS-hc signal to $B1^+$inhomogeneities increases for short ($< 1000\ ms$) and long ($> 2000\ ms$) T1 relaxation times. It should be noted that the proposed FLAWS optimization allows to maintain a reduced $B1^+$ sensitivity for FLAWS-hc signals acquired with a high number of excitations ($nEx = 144$) compared to the MP2RAGE optimizations previously proposed at 7T for high WM/GM contrast ($nEx = 132$, b) or high ($0.65\ mm$ isotropic) resolution ($nEx = 192$, c). The MP2RAGE-uni signal was plotted on the [-1;1] range to allow a comparison with the FLAWS-hc signal. The full range MP2RAGE-uni signal was recovered using the division image for the high WM/GM contrast protocol, as suggested in [6].

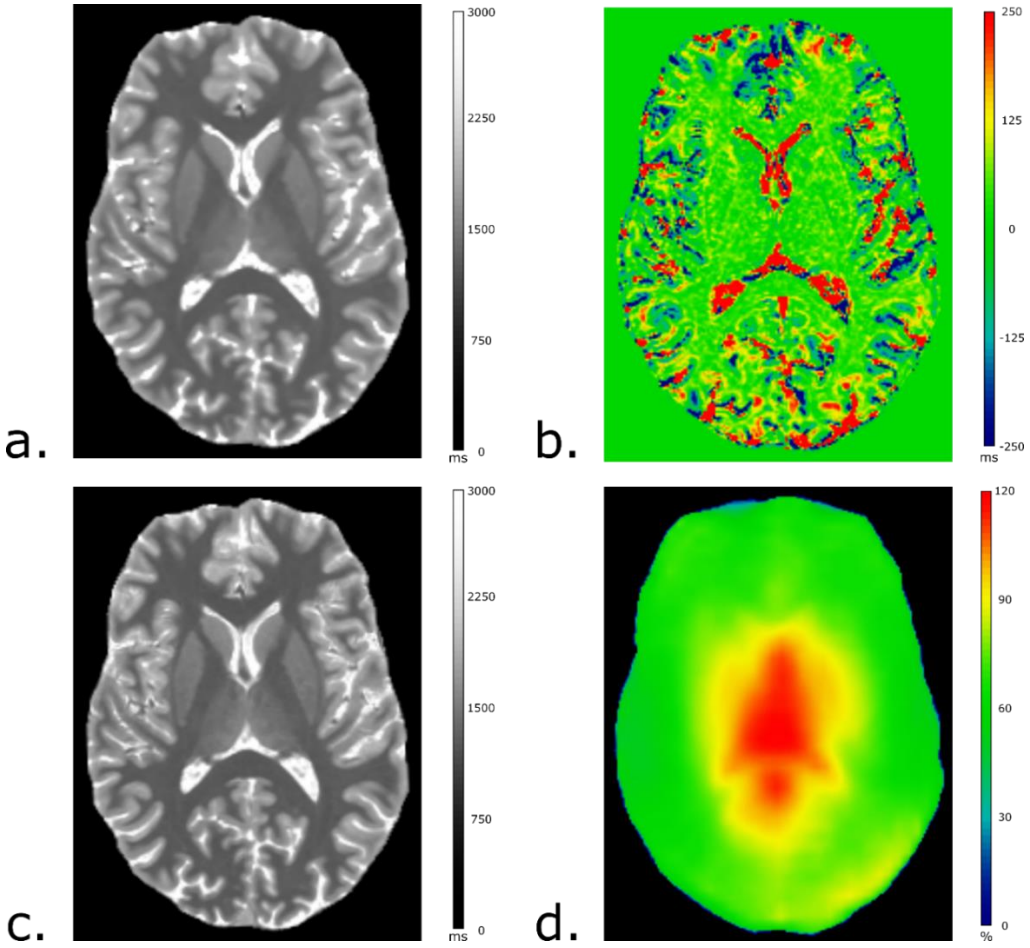

Supporting Information Figure 5.6. Example of MP2RAGE (a) and FLAWS (c) T1 maps without post-hoc correction. The difference between the T1 maps (b) appears to be mostly due to the T1 measurements of the CSF. A qualitative assessment suggested that most of the differences found for WM and GM tissues were due to the resolution difference between the two scans, as illustrated in the zoomed-in version of this figure presented in Supporting Information Figure 5.7. The difference between the MP2RAGE and FLAWS T1 maps did not appear to be mainly impacted by the changes in the $B1^+$ map (d).

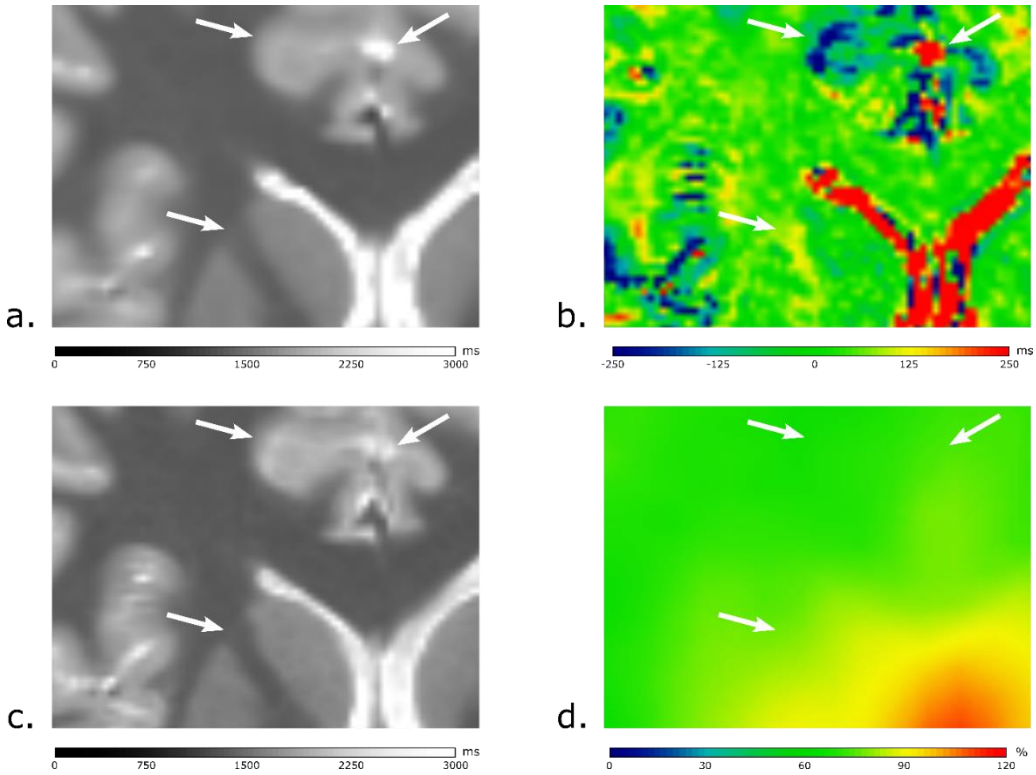

Supporting Information Figure 5.7. Example of MP2RAGE (a) and FLAWS (c) T1 maps without post-hoc correction. The difference between the MP2RAGE and FLAWS T1 values (b) appears to be mostly due to the resolution difference between the scans, as highlighted by the white arrows. Top left arrow: negative difference (b) between the MP2RAGE (a) and FLAWS (c) T1 maps due to the presence of GM/CSF partial volume voxels in the FLAWS T1 map. Top right arrow: positive difference (b) between the MP2RAGE (a) and FLAWS (c) T1 maps due to the increased number of CSF voxels in the MP2RAGE T1 map. Bottom left arrow: positive difference (b) between the MP2RAGE (a) and FLAWS (c) T1 maps due to the increased partial volume effect between the basal ganglia structures and surrounding WM in the MP2RAGE scan.

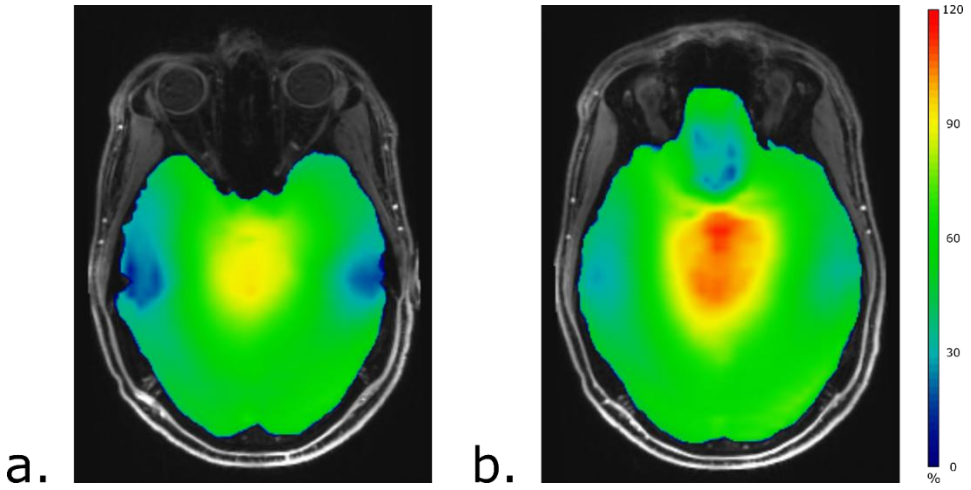

Supporting Information Figure 5.8. $B1^+$ map overlaid on FLAWS2 to show that low $B1^+$ values were found in the inferior brain regions and near the hear canals (a) and frontal sinuses (b).

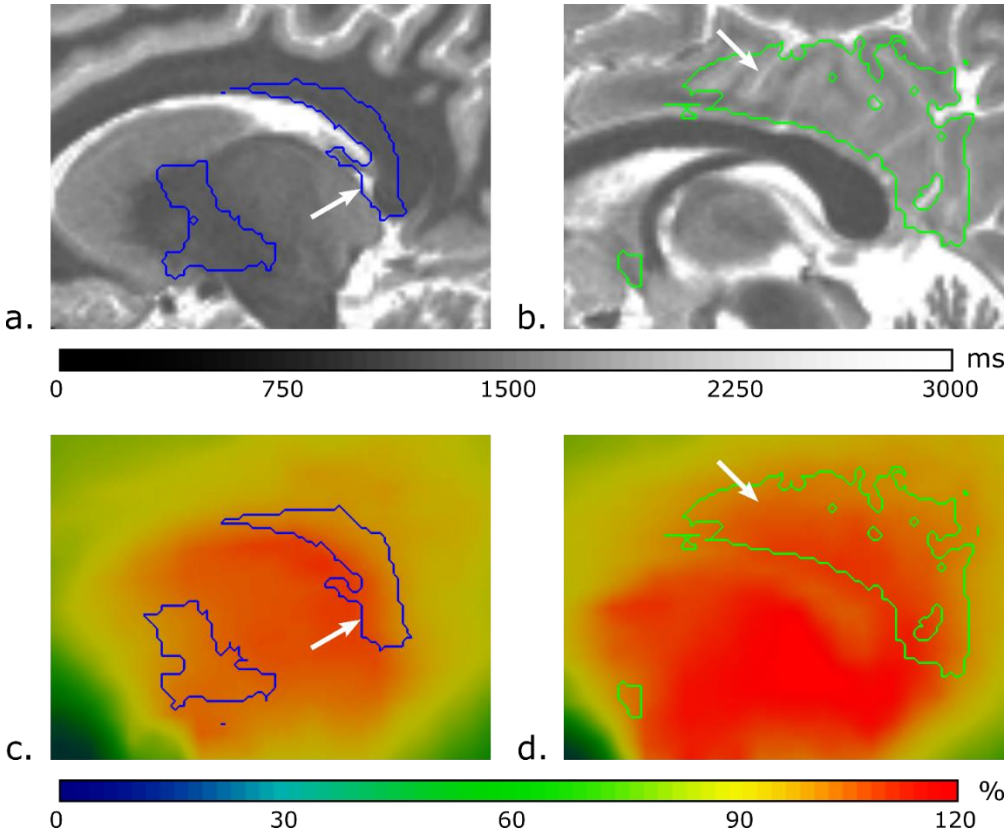

Supporting Information Figure 5.9. Sagittal slices of a FLAWS T1 map without post-hoc correction (a,b). The corresponding slices of the $B1^+$ map are also shown (c,d). The blue ROI (a,c) delineates the WM segmentation for $B1^+$ values above $100\,\%$ of the nominal flip angle. The green ROI (b,d) delineates the cortical GM segmentation for $B1^+$ values above $100\,\%$ of the nominal flip angle. The white arrows design segmentation error (here, inclusion of CSF voxels in the WM and cortical GM segmentations). A qualitative assessment suggested that the WM and cortical GM T1 measurements remains stable for $B1^+$ values above $100\,\%$ of the nominal flip angle, thus indicating that the T1 mapping divergence found for high $B1^+$in Figure 5.5 is likely due to segmentation errors (highlighted by the white arrows here).

5.8 References

[1] Trattnig S, Springer E, Bogner W, Hangel G, Strasser B, Dymerska B, et al. Key clinical benefits of neuroimaging at 7 T. Neuroimage 2018;168:477–89. doi:10.1016/j.neuroimage.2016.11.031.

[2] Marques JP, Kober T, Krueger G, van der Zwaag W, Van de Moortele P-F, Gruetter R. MP2RAGE, a self bias-field corrected sequence for improved segmentation and T1-mapping at high field. Neuroimage 2010;49:1271–81. doi:10.1016/j.neuroimage.2009.10.002.

[3] Okubo G, Okada T, Yamamoto A, Kanagaki M, Fushimi Y, Okada T, et al. MP2RAGE for deep gray matter measurement of the brain: A comparative study with MPRAGE. J Magn Reson Imaging 2016;43:55–62. doi:10.1002/jmri.24960.

[4] Kober T, Granziera C, Ribes D, Browaeys P, Schluep M, Meuli R, et al. MP2RAGE Multiple Sclerosis Magnetic Resonance Imaging at 3 T. Invest Radiol 2012;47:346–52. doi:10.1097/RLI.0b013e31824600e9.

[5] Simioni S, Amarù F, Bonnier G, Kober T, Rotzinger D, Du Pasquier R, et al. MP2RAGE provides new clinically-compatible correlates of mild cognitive deficits in relapsing-remitting multiple sclerosis. J Neurol 2014;261:1606–13. doi:10.1007/s00415-014-7398-4.

[6] Marques JP, Gruetter R. New Developments and Applications of the MP2RAGE Sequence - Focusing the Contrast and High Spatial Resolution R1 Mapping. PLoS One 2013;8:e69294. doi:10.1371/journal.pone.0069294.

[7] Haast RAM, Ivanov D, Uludağ K. The impact of B1+ correction on MP2RAGE cortical T_1 and apparent cortical thickness at 7T. Hum Brain Mapp 2018;39:2412–25. doi:10.1002/hbm.24011.

[8] Tanner M, Gambarota G, Kober T, Krueger G, Erritzoe D, Marques JP, et al. Fluid and white matter suppression with the MP2RAGE sequence. J Magn Reson Imaging 2012;35:1063–70. doi:10.1002/jmri.23532.

[9] Beaumont J, Saint-Jalmes H, Acosta O, Kober T, Tanner M, Ferré JC, et al. Multi T1-weighted contrast MRI with fluid and white matter suppression at 1.5 T. Magn Reson Imaging 2019;63:217–25. doi:10.1016/J.MRI.2019.08.010.

[10] Mugler JP, Brookeman JR. Three-dimensional magnetization-prepared rapid gradient-echo imaging (3D MP RAGE). Magn Reson Med 1990;15:152–7.

[11] Redpath TW, Smith FW. Use of a double inversion recovery pulse sequence to image selectively grey or white brain matter. Br J Radiol 1994;67:1258–63. doi:10.1259/0007-1285-67-804-1258.

[12] Geurts JJG, Pouwels PJW, Uitdehaag BMJ, Polman CH, Barkhof F, Castelijns JA. Intracortical Lesions in Multiple Sclerosis: Improved Detection with 3D Double Inversion-Recovery MR Imaging. Radiology 2005;236:254–60. doi:10.1148/radiol.2361040450.

[13] Urushibata Y, Kuribayashi H, Fujimoto K, Kober T, Grinstead JW, Isa T, et al. Advantages

of fluid and white matter suppression (FLAWS) with MP2RAGE compared with double inversion recovery turbo spin echo (DIR-TSE) at 7T. Eur J Radiol 2019;116:160–4. doi:10.1016/j.ejrad.2019.04.019.

[14] Chen X, Qian T, Kober T, Zhang G, Ren Z, Yu T, et al. Gray-matter-specific MR imaging improves the detection of epileptogenic zones in focal cortical dysplasia: A new sequence called fluid and white matter suppression (FLAWS). NeuroImage Clin 2018;20:388–97. doi:10.1016/J.NICL.2018.08.010.

[15] Bannier E, Gambarota G, Ferre J-C, Kober T, Nica A, Chabardes S, et al. FLAWS imaging improves depiction of the thalamic subregions for DBS planning in epileptic patients. Int. Soc. Magn. Reson. Med., 2018.

[16] Martin-Bastida A, Ward RJ, Newbould R, Piccini P, Sharp D, Kabba C, et al. Brain iron chelation by deferiprone in a phase 2 randomised double-blinded placebo controlled clinical trial in Parkinson's disease. Sci Rep 2017;7:1398. doi:10.1038/s41598-017-01402-2.

[17] Wang Y, Wang Y, Zhang Z, Xiong Y, Zhang Q, Yuan C, et al. Segmentation of gray matter, white matter, and CSF with fluid and white matter suppression using MP2RAGE. J Magn Reson Imaging 2018;48:1540–50. doi:10.1002/jmri.26014.

[18] Beaumont J, Saint-Jalmes H, Acosta O, Kober T, Tanner M, Ferré J-C, et al. High Contrast T1-Weighted MRI with Fluid and White Matter Suppression Using MP2RAGE. IEEE Int. Symp. Biomed. Imaging, Venice, Italy: 2019, p. 701–4.

[19] Rooney WD, Johnson G, Li X, Cohen ER, Kim S-G, Ugurbil K, et al. Magnetic field and tissue dependencies of human brain longitudinal1H2O relaxation in vivo. Magn Reson Med 2007;57:308–18. doi:10.1002/mrm.21122.

[20] O 'brien KR, Kober T, Hagmann P, Maeder P, Marques J, Lazeyras F, et al. Robust T1-Weighted Structural Brain Imaging and Morphometry at 7T Using MP2RAGE 2014;9:e99676. doi:10.1371/journal.pone.0099676.

[21] Eggenschwiler F, Kober T, Magill AW, Gruetter R, Marques JP. SA2RAGE: A new sequence for fast B1+-mapping. Magn Reson Med 2012;67:1609–19. doi:10.1002/mrm.23145.

[22] Commowick O, Wiest-Daessle N, Prima S. Block-matching strategies for rigid registration of multimodal medical images. 2012 9th IEEE Int. Symp. Biomed. Imaging, IEEE; 2012, p. 700–3. doi:10.1109/ISBI.2012.6235644.

[23] Ourselin S, Roche A, Prima S, Ayache N. Block Matching: A General Framework to Improve Robustness of Rigid Registration of Medical Images, Springer, Berlin, Heidelberg; 2000, p. 557–66. doi:10.1007/978-3-540-40899-4_57.

[24] Wright PJ, Mougin OE, Totman JJ, Peters AM, Brookes MJ, Coxon R, et al. Water proton T 1 measurements in brain tissue at 7, 3, and 1.5T using IR-EPI, IR-TSE, and MPRAGE: results and optimization. Magn Reson Mater Physics, Biol Med 2008;21:121–30. doi:10.1007/s10334-008-0104-8.

[25] Tustison NJ, Avants BB, Cook PA, Zheng Y, Egan A, Yushkevich PA, et al. N4ITK: improved N3 bias correction. IEEE Trans Med Imaging 2010;29:1310–20.

doi:10.1109/TMI.2010.2046908.

[26] Jenkinson M, Beckmann CF, Behrens TEJ, Woolrich MW, Smith SM. FSL. Neuroimage 2012;62:782–90. doi:10.1016/j.neuroimage.2011.09.015.

[27] Fischl B. FreeSurfer. Neuroimage 2012;62:774–81. doi:10.1016/j.neuroimage.2012.01.021.

[28] Haast RA, Lau JC, Ivanov D, Menon RS, Uludağ K, Khan AR. Effects of MP2RAGE B1+ sensitivity on inter-site T1 reproducibility and morphometry at 7T. BioRxiv 2020:2020.02.13.947382. doi:10.1101/2020.02.13.947382.

[29] Teeuwisse WM, Brink WM, Webb AG. Quantitative assessment of the effects of high-permittivity pads in 7 Tesla MRI of the brain. Magn Reson Med 2012;67:1285–93. doi:10.1002/mrm.23108.

[30] O'Brien KR, Magill AW, Delacoste J, Marques JP, Kober T, Fautz H-P, et al. Dielectric pads and low- B1+ adiabatic pulses: Complementary techniques to optimize structural T_1 w whole-brain MP2RAGE scans at 7 tesla. J Magn Reson Imaging 2014;40:804–12. doi:10.1002/jmri.24435.

[31] Duan Q, van Gelderen P, Duyn J. Improved Bloch-Siegert based B_1 mapping by reducing off-resonance shift. NMR Biomed 2013;26:1070–8. doi:10.1002/nbm.2920.

[32] Wang J, Mao W, Qiu M, Smith MB, Constable RT. Factors influencing flip angle mapping in MRI: RF pulse shape, slice-select gradients, off-resonance excitation, andB0 inhomogeneities. Magn Reson Med 2006;56:463–8. doi:10.1002/mrm.20947.

Conclusion

Contribution

The work presented in this thesis proposes an optimization methods based on magnetic properties of brain tissues and simulations of the FLAWS signals to provide FLAWS sequence parameters. This optimization method provided FLAWS sequences parameters at 1.5T and 7T. The 1.5T and 7T optimizations were validated with theoretical and *in-vivo* experiments (Chapters 4 and 5).

A new combination of the FLAWS signals was proposed in this thesis to generate T1-weighted images that are roughly independent from the proton density, the $T2^*$ relaxation time as well as the $B1^-$ field inhomogeneities. These images provide either a WM-suppressed or a CSF-suppressed signal and are characterized by a high brain tissue CNR. The properties of the new FLAWS combination images, *FLAWS-hc* and *FLAWS-hco*, were validated at 1.5T and 7T with theoretical and *in-vivo* experiments (Chapters 3, 4 and 5).

The work presented in this thesis proposes a method to perform T1 mapping with the FLAWS sequence (Chapter 5). This method was validated with phantom experiments at 3T (section 2.9). It was shown that the FLAWS T1 mapping method allows for the generation of high resolution T1 maps characterized by a reduced $B1^+$ sensitivity at 7T (Chapter 5). The results obtained at 7T suggest that the FLAWS sequence could replace the MP2RAGE sequence for brain imaging studies performed at 7T since it provides more T1-weighted contrasts characterized by a reduced $B1$ sensitivity than the MP2RAGE sequence. In addition, it was shown that the FLAWS sequence overcomes the CNR and resolution limitations of the MP2RAGE sequence regarding the generation of T1 maps with reduced $B1^+$ sensitivity.

The work presented in this thesis resulted in the publication of two journal papers (Chapters 4 and 5) and one conference papers (Chapter 3).

Limitations

The FLAWS optimization method presented in this thesis depends on the resolution and the choice of the brain tissues T1 relaxation times. Therefore different FLAWS sequence parameters can be obtained according to the T1 relaxation times and resolution chosen for the optimization. In addition, the resolution of the FLAWS images in the sagittal plane is limited since an important number of excitations per TR would not allow for the suppression of the WM signal in FLAWS1.

The $B1^+$ sensitivity of the FLAWS T1 mapping increases with the T1 relaxation times. Therefore, the FLAWS T1 maps need to be corrected for $B1^+$ inhomogeneities to allow accurate T1 mapping of tissues characterized by a long T1 relaxation time, such as brain lesions.

The work presented in this thesis has only been validated on healthy volunteers. A validation on patients would be necessary prior to use this work in clinical applications. In addition, the

FLAWS sequence acquisition time is long, thus limiting the use of the FLAWS sequence in clinical routine applications.

Perspectives.

The generation of the *FLAWS-hc* and *FLAWS-hco* combination images has been implemented in the "Work-in-progress package #925B-VE11C" that makes the *FLAWS-hc* and *FLAWS-hco* images directly available on the Siemens MR scanners equipped with the package, thus facilitating the use of the work presented in this thesis in neuroimaging studies.

The FLAWS sequence was re-optimized for 3T imaging to increase its sagittal field of view (parameters presented in section 2.8). This new protocol has been included in the brain imaging protocol of the "Prospective Imaging Study of Ageing: Genes, Brain and Behavior" (PISA) on a subset of 30 subjects with brain lesions due to ageing. These subjects will be imaged with multiple MR sequences, including the FLAIR and MP2RAGE sequence. The data acquired will allow to compare the performances of the FLAWS sequence with the FLAIR sequence in terms of lesion detection and segmentation. A comparison between the MP2RAGE and FLAWS data will also be performed to further validate the FLAWS T1 mapping method on aged subjects with brain lesions. In addition, a collaboration with the "Ecole Polytechnique Federale de Lausanne" started with the LTSI and the AEHRC to assess the interest of the work presented in this thesis regarding the FLAWS sequence for multiple sclerosis lesions segmentation at 3T. This collaboration may allow for a validation of the work presented in this thesis on patient data.

Finally, the work presented in this thesis resulted in a collaboration with "Siemens Healthineers" to provide an optimization of the FLAWS sequence with compressed sensing at 3T. This new FLAWS sequence optimization will allow for the shortening of the sequence acquisition time to facilitate the use of FLAWS imaging in clinical practice. The FLAWS sequence optimization method presented in this thesis has been used to determine a set of parameters for 6 mins FLAWS imaging at 3T. Preliminary results are presented in Figure 6.1. Further experiments will however be required to validate the optimization.

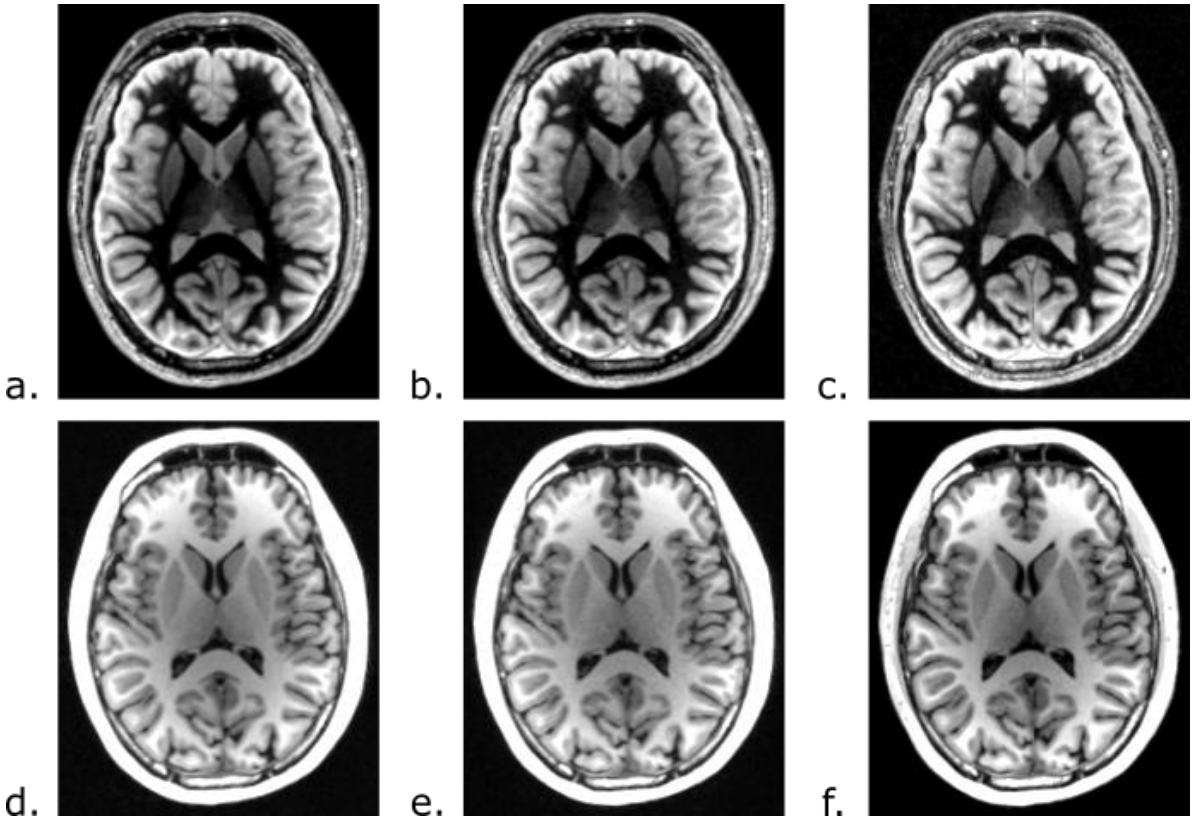

Figure 6.1. Preliminary results obtained for the compressed sensing optimization of the FLAWS sequence at 3T with a 64-channel head coil. Examples of FLAWS1 (a, b, c) and FLAWS2 (d, e, f) images are presented. a,d: FLAWS acquired with full k-space sampling (20 mins); b,e: FLAWS acquired with a GRAPPA parallel acquisition with an acceleration factor of 3 (8 mins); c,f: FLAWS acquired with compressed sensing (6 mins).

Annex

List of publications

Peer-reviewed journal papers

Beaumont J, Gambarota G, Saint-Jalmes H, Acosta O, Ferré J, Raniga P, et al. High-resolution multi T1–weighted contrast and T1 mapping with low B1+ sensitivity using the fluid and white matter suppression (FLAWS) sequence at 7T. Magn Reson Med 2020:mrm.28517. doi:10.1002/mrm.28517.

Beaumont J, Saint-Jalmes H, Acosta O, Kober T, Tanner M, Ferre JC, Salvado O, Fripp J and Gambarota G. Multi T1-weighted contrast MRI with fluid and white matter suppression at 1.5 T. Magn. Reson. Imaging 2019;63:217–225 doi: 10.1016/J.MRI.2019.08.010.

In preparation for submission to Magnetic Resonance in Medicine: **Beaumont J**, Fripp J, Raniga P, Acosta O, Ferre JC, McMahon K, Trinder J, Kober T and Gambarota G. FLAWS acquisition time reduction using a Cartesian phyllotaxis readout and a compressed sensing reconstruction at 3T.

Submitted to Plos One: **Beaumont J**, Gambarota G, Prior M, Fripp J and Reid L. Avoiding Data Loss: Synthetic MRIs generated from diffusion imaging can replace corrupted structural acquisitions for Freesurfer-seeded tractography. Plos One

Peer-reviewed conference papers

Beaumont J, Acosta O, Raniga P, Gambarota G and Fripp J. Towards a generalization of the MP2RAGE partial volume estimation model to account for B1+ inhomogeneities at 7T. In: IEEE International Symposium on Biomedical Imaging. Online; 2021.

Beaumont J, Saint-Jalmes H, Acosta O, Kober T, Tanner M, Ferre JC, Salvado O, Fripp J and Gambarota G. High Contrast T1-Weighted MRI with Fluid and White Matter Suppression Using MP2RAGE. In: IEEE International Symposium on Biomedical Imaging. Venice, Italy; 2019. pp. 701–704.

Abstracts in international conferences

Beaumont J, Gambarota G, Saint-Jalmes H, Acosta O, Raniga P, Salvado O, Fripp J, High resolution T1 mapping with reduced B1+ sensitivity using the FLAWS sequence at 7T. Int. Soc. Magn. Reson. Med. 2020. Paris, France; 2020.

Beaumont J, Gambarota G, Saint-Jalmes H, Acosta O, Ferré J.C., Raniga P, Salvado O, Fripp J, High resolution multi T1-weighted contrast with reduced B1 sensitivity using the FLAWS sequence at 7T. Int. Soc. Magn. Reson. Med. 2020. Paris, France; 2020.

Beaumont J, Gambarota G, Saint-Jalmes H, Acosta O, Salvado O, Fripp J, Effect of the transmitted bias-field on partial volume estimation of MP2RAGE data at 7T. Alzheimer's Association International Conference (AAIC) Satellite Symposium. Sydney, Austalia; 2019.

UNIVERSITÉ DE RENNES 1

Titre : Vers de nouvelles méthodes permettant l'acquisition d'images multi-contrastes pondérées T1 et de cartographies des temps de relaxation T1 avec la séquence d'imagerie par résonance magnétique FLAWS.

Mots clés : Cerveau, IRM, FLAWS, multi-contraste, cartographie T1

Résumé : La séquence d'imagerie cérébrale par résonance magnétique FLAWS fourni deux images pondérées T1 respectivement caractérisées par une suppression du signal de substance blanche et du signal du liquide céphalorachidien. Le minimum entre ces deux images fourni une image spécifique de la substance grise.
Au commencement de cette thèse, la séquence FLAWS était uniquement disponible pour de l'imagerie 3T. Dans cette thèse, nous proposons une méthode d'optimisation basée sur la maximisation d'une fonction de profit sous contraintes et sur des informations à priori sur les temps de relaxation T1 des tissus cérébraux afin de déterminer les paramètres de la séquence FLAWS.
Cette méthode fut utilisée afin de proposer des paramètres permettant l'acquisition de la séquence FLAWS à 1.5T et 7T.
Une nouvelle combinaison des signaux FLAWS fut proposée afin de générer des images pondérées T1 caractérisées par une sensibilité réduite aux inhomogénéités du champ magnétique B1. De plus, cette nouvelle combinaison des signaux FLAWS fut utilisée pour générer des cartographies T1 des tissus cérébraux. Nous montrons que ces cartographies T1 sont caractérisées par une sensibilité réduite aux inhomogénéités du champ magnétique de transmission.
Les méthodes présentées dans cette thèse furent validées par des expériences d'imageries sur un fantôme à 3T et sur des volontaires sains à 1.5T et 7T.

Title: Towards new means of performing multi T1-weighted contrast and imaging and T1 mapping with the FLAWS magnetic resonance sequence.

Keywords : Brain, MRI, FLAWS, multi-contrast, T1 mapping

Abstract: The FLAWS brain magnetic resonance imaging sequence provides two co-registered T1-weighted contrasts characterized by a suppression of the white matter and cerebrospinal fluid signals, respectively. The computation of the minimum between these two images provides a GM-specific contrast.
The contrasts provided by the FLAWS sequence are of interest for deep brain stimulation surgery planning applications and for brain lesion detection.
When this thesis started, the FLAWS sequence was only available for 3T imaging. The work presented in this thesis proposes an optimization method based on the maximization of a profit function under constraints and prior information about the brain tissues T1 relaxation times to determine FLAWS sequence parameters. This method was used to propose sets of FLAWS sequence parameters for 1.5T and 7T imaging.
A new combination of the FLAWS signals is proposed to generate T1-weighted images characterized by a reduced sentisitivity to the B1 magnetic field inhomogeneities. In addition, this new combination of the FLAWS signals was used to generate T1 maps of the brain tissues. We show that the FLAWS T1 maps are characterized by a reduced sensitivity to the transmitted magnetic field inhomogeneities.
The methods presented in this thesis were validated by performing experiments on a phantom at 3T and on healthy volunteers at 1.5T and 7T.